

**NUMERICAL AND EXPERIMENTAL MODELLING OF
FLOW AND KINETIC PROCESSES IN SERPENTINE
DISINFECTION TANKS**

A thesis submitted to Cardiff University

in candidature for the degree of

Doctor of Philosophy

by

Athanasios Angeloudis

Division of Civil Engineering, Cardiff School of Engineering

Cardiff University, 2014

ACKNOWLEDGEMENTS

The completion of this study would not have been possible without certain people and organisations to whom I would like express my acknowledgements and gratitude:

- To Professor Thorsten Stoesser who supervised this project, whilst allowing me to pursue and develop my own ideas. Professor Stoesser has been my mentor during this period, and for his guidance and feedback I am grateful and indebted.
- To Professor Roger A. Falconer who encouraged me to join the Hydro-environmental Research Centre at Cardiff University. Professor Falconer has provided me with invaluable advice and support over the course of this study.
- To CH2M Hill group for the financial support through the CH2M Hill – Cardiff University collaboration.
- To the staff and students of the Hydro-environmental Research Centre at Cardiff University for their support and guidance.
- To my family and friends, within Cardiff and beyond, for their support and understanding.

NUMERICAL AND EXPERIMENTAL MODELLING OF FLOW AND KINETIC PROCESSES IN SERPENTINE DISINFECTION TANKS

Athanasios Angeloudis

ABSTRACT

New water directives impose strict regulations to reduce the footprint of treatment operations and contaminant levels, which suggest a performance review of water treatment facilities, including disinfection contact tanks. Serpentine contact tank units suggest plug flow to be the optimal hydrodynamic condition at which disinfection performance is maximized. However, previous studies indicate that flow exhibits a residence time distribution (RTD) which can be significantly distorted from what is dictated by plug flow. Over the years, there has been rising concern over the impact of such digressions from optimal hydraulic conditions on microbe inactivation and the regulation of potentially carcinogenic Disinfection By-Products (DBPs).

With the growth of computing power and the advancement of computational models, the potential of contact tank water disinfection optimization by means of numerical modelling techniques can be assessed. In this study, Acoustic Doppler Velocity (ADV) and fluorescent tracer dye measurement campaigns are carried out to assess the hydraulic efficiency of a serpentine contact tank physical model and evaluating appropriate indicators. Then, three-dimensional Computational Fluid Dynamics (CFD) models are set up to simulate the hydrodynamic and solute transport processes for a variety of contact tank geometries examining the effects of inlet design, baffling configuration and tank scale. The simulation capability to reproduce the actual conditions is attested through comparisons against available laboratory results. The CFD approach is subsequently refined with appropriately selected kinetic models, describing the processes of disinfectant decay, pathogen inactivation and DBP formation.

Results highlight that computational models can become invaluable tools for the simulation of disinfection processes as they can reproduce the conditions encountered experimentally to a satisfactory extent. Moreover, the optimization of hydraulic efficiency, as studied numerically, facilitates more uniform disinfectant contact time which corresponds to greater levels of pathogen inactivation and a more controlled by-product accumulation.

Keywords: Chlorine contact tank; Mathematical modelling; Physical experimentation; Computational fluid dynamics; Disinfection by-products; Water disinfection; Hydraulic Efficiency; Froude – Reynolds Conflict; RANS Modelling

TABLE OF CONTENTS

Acknowledgements	i
Abstract	ii
Table of Figures	v
List of tables	xi
Chapter 1: Introduction	1
1 Introduction	2
Chapter 2: Literature Review	6
2.1 Introduction	7
2.2 Contact tank design aspects.....	7
2.3 Residence time distribution curves and hydraulic efficiency.....	13
2.4 Mathematical models of disinfection kinetics.....	17
2.5 Advances in contact tank computational fluid dynamics modelling.....	22
2.6 Review Summary	33
Chapter 3: Experimental Methods	35
3.1 Introduction	36
3.2 Laboratory model	36
3.3 Acoustic Doppler Velocimetry.....	41
3.4 Tracer experimentation.....	48
3.5 Chapter summary	56
Chapter 4: Numerical Modelling Governing Equations and Methods.....	57
4.1 Introduction	58
4.2 Numerical modelling equations.....	58
4.3 Numerical methods.....	70
4.4 Chapter summary	79

Chapter 5: Experimentation Results	80
5.1 Introduction	81
5.2 Hydrodynamic Characteristics of CT-1	81
5.2 Tracer Analysis of CT-1	95
5.3 Chapter summary	105
Chapter 6: Numerical Simulations	107
6.1 Introduction	108
6.2 Contact tank numerical model setup	108
6.3 Numerical result validation	110
6.4 Applications of CFD Modelling in CTs	119
6.5 Chapter summary	132
Chapter 7: Disinfection kinetics	134
7.1 Introduction	135
7.2 Kinetics of Interest	135
7.3 Analysis of kinetics through CFD modelling	138
7.4 Chapter summary	152
Chapter 8: Concluding Remarks	155
8.1 Summary	156
8.2 Contribution to contact tank research	156
8.3 Recommendations for future investigations	160
8.4 Publications related to this work	162
References	163
Nomenclature	176
Abbreviations	180

TABLE OF FIGURES

Figure 2.1 Examples of CCTs encountered in the literature, including: a) Embsay Contact Tank, Yorkshire, UK (Teixeira, 1993), b) CCT in Athens, Greece (Stamou, 2002) and c) Calgary Glenmore Water Treatment Plant, Northeast Clear Well (Yu et al., 2010)	10
Figure 2.2 Examples of a comparison amongst normalised tracer curves, including results for idealised flow patterns Plug Flow and Complete Mixing, as well as the Plug Flow with Dispersion condition estimated for a prototype CT assessed experimentally by Rauen (2005) and results of tests obtained in that study for distinct prototype configurations. The plots show: a) Residence Time Distribution (RTD) curves; and b) F-curves. $E(\theta)$ is the normalized tracer concentration, $F(\theta)$ is the accumulated tracer mass and θ is the normalized time. For Plug Flow, $E(\theta) \rightarrow \infty$ for $\theta=1.0$, while for Complete Mixing the RTD curve is described by $E(\theta)=e^{-\theta}$, so that $E(\theta) \rightarrow 0$ as $\theta \rightarrow \infty$.	14
Figure 3.1 Hydraulic Circuit Diagram	36
Figure 3.2 Three-Dimensional sketch of CT-1	38
Figure 3.3 Plan View of CT-1 and main dimensions.....	38
Figure 3.4 Cross-Section of CT-1 halfway through the 1st Compartment	39
Figure 3.5 (a) Schematic view of laboratory model tank configuration including vectors indicating main streamwise flow direction ; (b) channel inlet and compartment 1 cross-section (dimensions in mm). Experimental data sampling points are illustrated in both sketches.	40
Figure 3.6 Baffling Configurations examined in previous studies (adopted from Rauen, 2005): (a) MS1, (b) MS2, (c) MS3 and (d) CT-O.....	41
Figure 3.7 Representation of a 3-receiver ADV probe, its sampling volume and acoustic pulses (adopted from Chanson, 2008).....	43
Figure 3.8 Unfiltered ADV data series obtained during data acquisition at a sampling point in compartment 1. (a) Horizontal (U), Transverse (V) and Vertical (W) velocity	

fluctuations. The mean value of each velocity is indicated by the straight line; (b) Signal-to-Noise Ratio and (SNR) average correlation percentage (COR).....	45
Figure 3.9 Root Mean Squared profiles of: (a) Mean (U), and (b) Turbulent (u') Horizontal Velocities	47
Figure 3.10 Calibration Curve and Readings for known concentrations for each of the 3 fluorometers.	50
Figure 3.11 (a) C_{pulse} curve from a black box experiment with an injection concentration of 4ppt at the inlet. Corresponding curves after the analysis: (b) Residence Time Distribution (RTD) Curve and (c) Flow – Through (FTC) Curve.....	52
Figure 3.12 Reproducibility of RTD curves: (a) C_{pulse} curves for 3 experiments at the outlet and (b) corresponding normalized RTD curves.....	54
Figure 4.1 Examples of structured Finite Volume Method discretization grids (a) 3-D uniform computational grid and (b) plan view of non-uniform computational mesh.....	71
Figure 4.2 Flow Chart illustrating the sequence of operations performed for the acquisition of Flow and Disinfection Predictions	78
Figure 4.3 Different mesh resolution examples produced from the grid generator program.....	78
Figure 5.1 Streamlines and vectors indicating the flow pattern and normalised velocity magnitude as observed from the ADV investigation in each of the 8 compartments of CT-1. The longitudinal profiles are taken from the centreline of the compartments and are plotted as viewed from the east side of the tank defined in Figure 3.5.....	82
Figure 5.2 Flow pattern of compartment 1 at the horizontal plane of $z/H_t = 0.5$. This is further illustrating the hydrodynamic complexity downstream of the inlet when combined with the vertical recirculation zone of figure 5.1(a).....	83
Figure 5.3 (a) Compartment 1 and (b) compartment 2 recirculation zones in x-z planes . Based on the obtained flow pattern the vertical recirculation zone occupying the majority of compartment 1 volume also expands to the first half of compartment 2 and	

results in a subsequent dead zone in the second half of the compartment. The profiles are plotted as viewed from the east side of the tank defined in Figure 3.5...84

Figure 5.4 Main CT flow patterns in 3-D sketch form a) 1st and 2nd Compartments: White arrows correspond to flow in the 1st compartment and dark grey in the 2nd. b) 2nd and 3rd Compartments; white arrows represent the 3rd compartment flow and dark grey the 2nd .c) System plan view including the main flow streamline and 2-D recirculation zones.85

Figure 5.5 Normalized velocity measurements plotted with respect to the tank length. (a) Horizontal velocities where the positive values are towards the flow direction (streamwise), (b) transverse velocities and (c) magnitude of vertical velocity measurements. The dashed line implies the plug flow velocity magnitude. Vertical grid lines indicate the different compartments.86

Figure 5.6 Vertical profiles of U/U_b in the centre of each compartment. Positive velocities follow the streamwise direction in each compartment. The theoretical plug flow velocity profile is presented for comparison.....87

Figure 5.7 Plug Flow deviation coefficient with respect to compartment number89

Figure 5.8 Normalised turbulence kinetic energy (k/U_b^2) along the tank, calculated from the RMS fluctuations of velocity obtained from the ADV experimentation89

Figure 5.9 Normalised mean velocities measured in this study (on the left) and Rauen (2005) (right) for: a) Vector plot of the resultant velocity field; b) horizontal velocity (U/U_b) and c) vertical velocity (W/U_b) contour plots.92

Figure 5.10 Mean flow and turbulent parameters graphical comparison a) velocity vector plots, b) contour plot of turbulent intensity u'/U_b , c) w'/U_b and d) Reynold's stress uw/U_b^293

Figure 5.11 Correlation of (a) mean velocity and (b) turbulence intensity results with the available data of Shiono and Teixeira (2000)95

Figure 5.12 Residence Time Distribution (RTD) curves for each compartment normalized with respect to the theoretical retention time T96

Figure 5.13 RTD curves vs Compartment flow patterns. a) 1st compartment, b) 2nd compartment, c) 3rd Compartment, d) 8th Compartment. Fluorescence peaks indicating flow recirculation are marked in the 1st compartment RTD Curve.....	97
Figure 5.14 Vertically Averaged F curves for sampling points at compartments 1, 2, 3 and 8 as measured experimentally. Specifically for the compartment 8 F curve, t_{10} and t_{90} values are indicated to demonstrate how they are obtained for HEI calculation.....	99
Figure 5.15 HEI indicators as a function of distance from the inlet (here in terms of compartment number) obtained experimentally. The hydraulic performance of the tank is indicated for each HEI ranging between poor, compromising, acceptable and excellent. Grey data points indicate results which are influenced by tracer mass re-appearance.....	100
Figure 5.16 Dispersion Index with respect to tank length to width ratio (β) according to the tracer experiments of the present work, Marske and Boyle (1973), Teixeira (1993) and Rauen (2005).....	101
Figure 5.17 Theoretical and Dispersion Calibrated RTD curve predictions against experimental measurements: (a) 1st compartment, (b) 2nd compartment and (c) 8th Compartment.....	103
Figure 5.18 Deviation between measured (d_M) and theoretical (d_T) dispersion number prediction. The compartment number of the measured dispersion numbers is indicated in the figure.	103
Figure 6.1 3-D Mesh (MM) used for hydrodynamic and solute transport simulations	109
Figure 6.2 Normalised (a) Streamwise velocity (U/U_b) and (b) turbulence kinetic energy (k/U_b^2) data available from simulations with the FM mesh and experimentally.	111
Figure 6.3 (a) Profiles of the streamwise velocity and (b) profiles of the turbulent kinetic energy k in the centre of the 1st(left), 2nd (middle) and 8th (right) compartment	112
Figure 6.4 Comparison of horizontal profiles of (a) streamwise velocity and (b) turbulence kinetic energy against available experimental data at 3 different vertical planes ($z/H_t = 0.05, 0.50$ and 0.95) where $x/W_t = 0.50$	113

Figure 6.5 (a) Velocity vectors in the centre-plane of Compartments 1 (first row left),2 (first row right), 3(second row left) and 8 (second row right). The blue vectors represent the CT-S-FM simulation results and the black vectors represent the ADV (CT-EXP) data (b) Horizontal profile of flow at mid-depth ($z/H_t = 0.50$) for CT-S-FM streamlines and CT-EXP measurement vectors in compartment 1.....	114
Figure 6.6 RTD curves produced at the outlet for experimental and computational data. Further refinement of the computational grid does not produce noticeable difference.	115
Figure 6.7 RTD curves produced for experimental and computational data (FM) at compartments (a) 1, (b) 2, (c) 3, and (d) 8: experimental RTDs (left), computational RTDs (right).....	116
Figure 6.8 Cumulative tracer distribution (F) in compartments 1, 2, and 8 as produced experimentally and computationally.....	118
Figure 6.9 Simulation HEI prediction and comparison against experimental results from Chapter 5.....	118
Figure 6.10 CFD predictions of Outlet (a) E_θ and (b) F curves for the different baffling configurations examined experimentally by Rauén (2005) and (Angeloudis et al., 2014).....	120
Figure 6.11 Streamwise velocity profiles in the 1st (a) 2nd (b) 4th (c) and 7th (d) compartment for original inlet (CT-1), half depth inlet (HDI) and full depth inlet (FDI) configurations.....	123
Figure 6.12 3-D and plan view visualization of fluid flow using streamtraces in (a)CT-S (b) HDI and (c) FDI design models respectively. The streamtraces are coloured with regards to their velocity magnitude.....	124
Figure 6.13 Contour profiles of tracer distribution in the initial at $t = 10,30,50,70, 150$ and 300 sec following injection (a) Current configuration simulation (CT); (b) Half Depth Inlet (HDI) configuration; (c) Full Depth Inlet (FDI) configuration.....	125
Figure 6.14 F curves of CT-S, FDI and HDI for compartments (a)1, (b) 2, (c) 8.	126

Figure 6.15 HEI indicator prediction across the CT model computational domain. Flow path normalized with respect to the compartment number for σ^2 , t_{10} , t_{90} and Mo . Results from the three different inlet configurations (CT-1,HDI and FDI) are reported illustrating the efficiency improvement shown by each of the indicators. Unreliable results due to tracer recirculation are highlighted in grey marker	128
Figure 6.16 Mean flow and turbulent parameters graphical comparison. Normalised velocity (U/U_b , W/U_b) vector plots and Normalized Turbulent kinetic energy (k/U_b^2) contour plots in the centerline of compartment 1 for (i) CT-1 experimental measurements, (ii) Numerical simulation of CT-1, (iii) Simulation up-scaled (6:1) CT-6 model.....	130
Figure 6.17 Vertical profiles of a) U/U_b and b) k/U_b^2 in compartments 1, 2 and 8 as measured experimentally in CT-1 and computationally in CT-6. Positive are considered the velocities that follow the streamwise direction in each compartment.	131
Figure 7.1 <i>G.Lamblia</i> concentration RTD curves; (a) Results for different CT designs and (b) comparison with conservative tracer curves.....	142
Figure 7.2 Chlorine concentration RTD curve comparison against conservative tracer results from Chapter 6; (a) E_θ and (b) cumulative F curves.....	144
Figure 7.3 Outlet by-product concentration RTDs; (a) TTHM concentration-time and (b) normalised (TTHM and conservative) E_θ curves	144
Figure 7.4 Contour plots of Disinfectant Distribution, <i>G.lamblia</i> Inactivation and total Trihalomethane formation as predicted from the CFD simulation of the disinfection processes for each of the CT designs . The plots are obtained at half-depth, i.e. $z/H = 0.50$	147
Figure 7.5 Disinfection Performance with respect to contact time based on computational cells of CFD simulations: (a) Chlorine Concentration (C_{Cl}), (b) <i>G.lamblia</i> Survival Ratio (N/N_0) (c)Total Trihalomethane (TTHM) formation. The figure indicates that despite disinfection occurring under identical conditions of operation and water quality, the CT geometrical differences have a distinctive impact on the kinetics.....	149

LIST OF TABLES

Table 2.1 Hydraulic Efficiency Indicator (HEI) values associated with the normalised tracer curves shown in Figure 2.2 (Rauen et al., 2012).....	17
Table 2.2 Turbulence models used in CFD modelling studies of CTs, with sources indicated in brackets for further information on specific model formulations.	25
Table 3.1 REC values for Outlet Tracer Experiments	53
Table 3.2 Definition of time-specific parameters	55
Table 3.3 Hydraulic Efficiency Indicator Definition	55
Table 5.1 Calculation of mean plug flow deviation coefficient for the vertical profiles of Figure 5.6 b	88
Table 5.2 Morrill index (M_o) as predicted by using the theoretical model and as obtained experimentally in tabulated form.	104
Table 6.1 Mesh Resolutions of numerical models.	109
Table 6.2 Outlet Experimental and Computational HEIs obtained for different Baffling Configurations.....	121
Table 6.3 Disinfection Indicators at the Outlet for different inlet configurations of the laboratory model.	127
Table 6.4 Model parameters according to geometric and dynamic similarity.....	129
Table 6.5 Theoretical, Experimental and CFD prediction of Morrill Index (M_o).....	131
Table 7.1 Water Quality Parameters Input.....	138
Table 7.2 <i>G.Lamblia</i> tracer mass loss during the experiment and RTD peak time (t_p) for conservative and reactive tracer respectively.....	142
Table 7.3 Cl_2 and TTHM mass recovered at CT Outlets	145
Table 7.4 Average Values of <i>G.Lamblia</i> Survival Ratio and TTHM Concentration with respect to mean residence time.	151
Table 7.5 Estimation of <i>G.Lamblia</i> N/N_0 and TTHM at the outlet for t_{10} and t_{90} with the aid of regression analyses of CFD results extracted from Figure 7.5 (e.g. Table 7.4)..	151

CHAPTER 1

INTRODUCTION

1 INTRODUCTION

The total volume of water in the world remains constant and is recycled according to the hydrological cycle. Drinking water is regarded as one of the fundamental elements of life and a satisfactory supply must be accessible to all. However, water security is under pressure by the significant growth of population coupled with their rapid shift from rural to urban areas. Climate changes, pollution and phenomena such as droughts can have further detrimental impacts on the water supply quality and availability. The rising demand for water in the near future could contribute to water scarcity, leading to potential implications for water access, quality and hygiene (UNESCO, 2012). By taking the above factors into consideration, careful water resource management is crucial to sustainably address the increasing water demands.

Potable water supplies are derived from either surface or groundwater sources. In its original form they contain organic and inorganic substances. These substances may exceed the standards for colour, taste and odour, hardness, turbidity, pathogen level and suspended matter, making it unsuitable for direct consumption. As a result, treatment is required in order to improve the quality of water, which depends upon the current condition of the water and the standards that need to be met prior to its distribution and usage. The standards can vary significantly spatially, where in less-developed countries they only require adherence to the basic international guidelines (WHO, 2011). In contrast, water directives in developed countries impose strict regulations to reduce contaminant levels as well as the footprint of treatment.

Historically, the first drinking water standards can be traced back to even 4000 years ago. In those civilizations, people used techniques such as boiling, thus improving the quality of water. Hippocrates (460 to 354 BC) stated that “water contributes to health” (AWWA, 1990) and strived to identify water-sources that seemed beneficial when consumed. The drinking water quality was later made particularly significant over the 18th century when a correlation was made between water and the spread of various epidemics. At present, the treatment of water occurs in specially designed facilities, where the water is subject to processes like flocculation, filtration, storage and disinfection, prior to being distributed to the public via water supply networks.

The thesis is focusing on the investigation of disinfection of drinking water, one of the primary aspects of the water treatment process, and the corresponding facilities where it

is normally undertaken. Disinfection is a process designed for the inactivation of pathogenic micro-organisms, thus preventing the transmission of waterborne diseases. The disinfection of water supply occurs through contact with suitable concentrations of disinfectant for a sufficiently long period. This period is referred to as the contact time and is typically in the region of 30 to 60 minutes for chlorination of potable water in contact tanks (CTs), depending on the incoming water quality and disinfectant dosage. Treatment processes that precede disinfection can also achieve pathogen reduction, even though that is not their primary objective. The most common form of water disinfection is by chlorination, even though other methods are used, such as: ozonation, ultraviolet (UV) radiation and, in the past, through the addition of potassium permanganate to water (AWWA, 1990).

Despite the growing implementation of ozone and UV-based facilities, chlorine CTs still constitute an integral component of water treatment systems worldwide. Presently, the extensive use of chlorine-based disinfection is due to a range of advantages, including: ease of handling, measurement and control, low cost of installation and, most importantly, the controlled concentration of chlorine residual after treatment. Residual chlorine prevents recontamination of the water supply in the distribution system and is sometimes added to the treated waters of ozone or UV-based plants (Brown et al., 2011).

However, the use of chlorine for drinking water disinfection has been a cause of concern because of the formation of potentially carcinogenic compounds, namely Disinfection By-Products (DBPs), which arise from excess residual chlorine in CTs. Epidemiological studies have proven an association between chlorinated water consumption and colon and rectal cancer in laboratory animals, while others have resulted in associations to reproductive and developmental anomalies in laboratory animals (Brown et al., 2011). A number of studies have been undertaken to identify the health effect of chlorinated water and DBPs on humans, but the findings do not yield a conclusive result (Nieuwenhuijsen et al., 2008; Yang et al., 2000). Nonetheless, concerns have led to the regulation of DBP formation, through approaches such as the adoption of stringent maximum contaminant levels (MCLs) and the use of alternative disinfectants. It is argued (Singer, 1994) that such suggestions face the following issues: firstly, MCLs may compromise the virus and bacterial inactivation of disinfection and, secondly, other disinfectants have their respective attendant problems.

The formation of DBPs can be attributed to the excess use of chlorine in inefficient disinfection CTs. It is considered that improvements in the hydraulic performance of CTs can substantially mitigate these issues by leading to a maximization of disinfection efficiency, minimisation of operational costs and regulation of DBP formation without compromising the quality of the finished water (Teixeira, 1993). Such modifications must take into consideration the following major elements: chlorine and source water chemistry, chlorine decay kinetics, microbial inactivation kinetics and CT hydrodynamic and solute transport processes.

The hydraulic design of CTs has traditionally been based on the assumption that the contact time for all fluid elements corresponds to the theoretical hydraulic residence time, i.e. assuming plug flow conditions. According to the British Standards, “it will normally be a pipeline or a serpentine chamber” (BSI,2003). The CT size and geometry, inlet and outlet configurations, the introduction and orientation of baffles and diffusers can all be determinant factors on the actual flow within the chamber and its resemblance to ideal conditions.

The optimisation practice of poorly designed tanks commenced with experimental studies undertaken in the 1960s and 1970s, which involved mainly two types of studies, namely in-situ “black box” tracer tests and laboratory physical modelling. The former has traditionally been conducted to diagnose the hydraulic performance of existing CTs, typically based on results such as Residence Time Distribution (RTD) curves and values of the Hydraulic Efficiency Indicators (HEIs) at the tank outlet. The latter has been useful in trial and error testing of the impact of certain design modifications on those results, with suggestions for later improvements of the field scale unit. In the 1980s mathematical and numerical modelling studies started to be used to assist CT investigations, offering a greater level of detail in a more cost-effective manner than equivalent experimentally-based investigations.

With the growth of computing power and the advance of computational models, the 1990s saw the development and application of Computational Fluid Dynamics (CFD) tools to simulate the hydraulic performance of CTs, sometimes independently of experimentation, other than by using available data to calibrate and validate modelling predictions. This has led to the current scenario of CFD models being invaluable assistive tools in optimisation studies of CTs, with the experimentation practice

continuing to allow for specific diagnostics and to supply data for the calibration and validation of CFD modelling results. The vast majority of CT modelling studies published to date has focused on simulating CT hydrodynamic and conservative solute transport processes. The chlorination kinetics and Disinfection By-Product (DBP) formation have rarely been contemplated in computer modelling studies of CTs. Commercially available CFD models have not been applied with this purpose, while research studies undertaken using open source codes to produce tailor-made applications are rare.

Aspects that motivated this study include (i) the need to provide numerical modellers with experimental data, (ii) understanding the impact of scale when studying small-scale physical models, (iii) quantifying the influence of certain CT design characteristics on overall disinfection efficiency (iv) the implementation of state of the art chlorination kinetics and DBP formation models into three-dimensional CFD tools that can assist modern design or retrofit of CTs for improved performance.

Chapter 2 reports on relevant research outcomes and how these have been included (or not) in modelling studies targeted at providing subsidies for the design optimisation of CTs. The content aims for a thorough identification of potential further developments to the CT modelling practices. Chapter 3 details the associated methodology implemented for the experimental investigation in a small-scaled contact tank. Chapter 4 describes the numerical methods employed in this study to simulate hydrodynamics and solute transport in contact tanks, providing an overview of the governing equations, assumptions, considerations and solution methods. Results and analyses of the physical experimentation are expanded in Chapter 5, which are essential for the validity and setup of CT computational models in general. Chapter 6 assesses the credibility of the numerical model to reproduce the experimental findings, and evaluates the impact of CT design modifications on hydraulic efficiency. The refinements of the CFD code to simulate disinfection kinetic processes are discussed on Chapter 7, supplemented with numerical results illustrating the potential of such simulations to disinfection chamber design practises. In Chapter 8 the main conclusions of this study are highlighted and CT research areas which would benefit from additional investigation are recommended.

CHAPTER 2

LITERATURE REVIEW

2.1 INTRODUCTION

This chapter describes advances and challenges encountered in contemporary research on chlorine Contact Tanks (CTs), based on a critical review of the international literature. It provides the framework for the development of this work by identifying aspects requiring further investigation. It highlights the multi-disciplinary nature of performance analyses of CTs, which has been examined through detailed physical and/or numerical modelling studies, in association with appropriate hydro-kinetic models that reflect current knowledge and understanding of the chemistry of drinking water disinfection by chlorination. The chapter begins with an overview of the practices with respect to contact tank design in section 2.2 and the availability of experimental data. Standard ways of CT performance assessment are detailed in section 2.3 and presents results from previous studies undertaken in the same experimentation tank of Chapter 3 for completeness. The chemistry of chlorination is examined in section 2.4, mainly from a numerical point of view, describing models that are developed to simulate disinfection kinetics. Section 2.5 presents the advances in CFD modelling practices of contact tanks with respect to the flow hydrodynamics, solute transport and the incorporation of kinetics.

2.2 CONTACT TANK DESIGN ASPECTS

The hydraulic design of CTs has traditionally been based on the assumption that the contact time for all fluid elements corresponds to the theoretical hydraulic residence time (T) of a given tank (Falconer and Tebbutt, 1986), which can be estimated as $T=V/Q$, where V is the volume of the CT and Q is the discharge. In Chemical Reaction Engineering (Levenspiel, 1999), this assumption has been associated with the theoretical/idealised flow pattern, known as ‘Plug Flow’, in which all elements of fluid passing through a flow reactor do so uniformly, in parallel paths from the inlet to the outlet sections of the tank, i.e. without undergoing longitudinal dispersion. The other theoretical/idealised flow pattern is known as ‘Complete Mixing’ and its characterising assumption is the instantaneous mixing of all incoming fluid elements with the fluid already in the reactor, thereby representing maximum dispersion. In practice, the flow pattern in flow reactors is always non-ideal. Even in optimally designed CTs, Plug Flow cannot be achieved due to the occurrence of viscous (wall) effects and turbulence, which inevitably induce a degree of dispersion of fluid elements. Hence, for any

particular CT (existing or planned) it is important to assess how much the flow conditions resemble Plug Flow and to take some measure of the departure from it into consideration when estimating the tank design disinfection efficiency, and other chemical reaction parameters. For this reason, Falconer and Tebbutt (1986) considered these effects in establishing a reference flow pattern for analyses of the hydraulic efficiency of an existing CT. Such a more realistic reference flow pattern can be referred to as ‘plug flow with dispersion’.

A number of studies were carried out between the 1960s and 1980s to investigate the impacts of different setups of existing CTs on their hydraulic performance, typically by using tracer experimentation techniques (e.g. Louie and Fohrman, 1968; Marske and Boyle, 1973; Trussell and Chao, 1977; Hart, 1979; Hart and Vogiatzis, 1982; Thayany, 1984; Falconer and Tebbutt, 1986). These studies have set the foundations for a more rational approach to the design of CTs, by identifying key parameters that have a significant impact on the hydraulic efficiency of such tanks. Such studies have shown that the extent of deviation from the target flow pattern depends strongly on constructive features, such as: the geometry of the tank, the use of flow-modifier structures, such as baffles, their orientation and inlet and outlet configurations. The length-to-width ratio of the flow (β , L/W) has been identified by Marske and Boyle (1973), and later confirmed by Thackston et al. (1987), as one of the key design parameters, where a β value of 40 has been associated with the achievement of good CT hydraulic performance. This is usually obtained in a long narrow chamber, such as a pipeline or in a baffled tank with a serpentine-like flow path. Furthermore, the disposition of baffles along the longitudinal direction of a CT has been associated with the occurrence of better hydraulic performance than with cross baffling (Marske and Boyle, 1973; Teixeira, 1993).

The location and relative size and orientation of the inlet and outlet sections in a CT can also influence the occurrence of recirculating flow zones in the horizontal and/or vertical planes, which Levenspiel (1999) refers to as ‘stagnant regions’. Previous studies have shown that these conditions can be very detrimental to the hydraulic performance of CTs, as they contribute to increasing the degree of mixing in the tank. These regions tend to retain fluid elements in the tank for a longer period of time than T . Furthermore, as shown by Thackston et al. (1987), the occurrence of recirculating flow structures is normally concurrent with the presence of advective flow paths, in which the average

flow speed is faster than the cross-sectional mean velocity, U_b , obtained for an ideal flow as $U_b = Q/A$, where A is the cross-sectional wetted area. Successive advective flow paths usually form the main streamwise flow trajectory through a CT and fluid elements being transported there usually remain in a CT for a shorter period of time than T , thereby characterising the phenomenon of short circuiting. The advective flow also usually creates and drives the flow recirculation zones by way of flow separation, adverse pressure gradients, shear and viscous effects. It follows that the degree of occurrence of short circuiting and enhanced mixing is proportional to the level of longitudinal dispersion observed in a tank.

In terms of full scale CTs, different sizes have been reported in the literature, such as the relatively small Embsay Contact Tank, located in Yorkshire, UK (Teixeira, 1993), measuring $16\text{m} \times 7.5\text{m} \times 4.8\text{m}$, and the larger Elan Contact Tank, which measured $91\text{m} \times 46\text{m} \times 2.5\text{m}$ and has been used to treat water supplied to much of the city of Birmingham, UK (Thayanity, 1984; Falconer and Tebbutt, 1986). CTs have sometimes been built in available spaces in water treatment works, upgrading their capacity to meet a growing urban demand. As a result, tanks can vary significantly in shape, as shown by Marske and Boyle (1973), Liem et al. (1999), Stamou (2002), Yu et al. (2010) and illustrated in Figure 2.1. Nonetheless, the recommended design shape of CTs has a rectangular plan view, where baffles are inserted to induce a serpentine-like flow path from the inlet to the outlet sections. The inlet and outlet devices are usually pipes or culverts.

Modern design or retrofitting practices of CTs typically involve attempts to mitigate the operation of poorly performing tanks, as drinking water regulations become stricter and there are pressures to reduce the carbon footprint of water treatment plant operations. As mentioned earlier (Teixeira, 1993), the purposes of hydraulic optimisation studies of CTs are usually threefold, including: i) to maximise the disinfection efficiency; ii) to minimise the usage of disinfectants and other chemicals to achieve the maximum disinfection efficiency; and iii) to minimise the formation of Disinfection By-Products. This knowledge has been reflected in the application of the hydrokinetic modelling concept when estimating the disinfection efficiency of CTs.

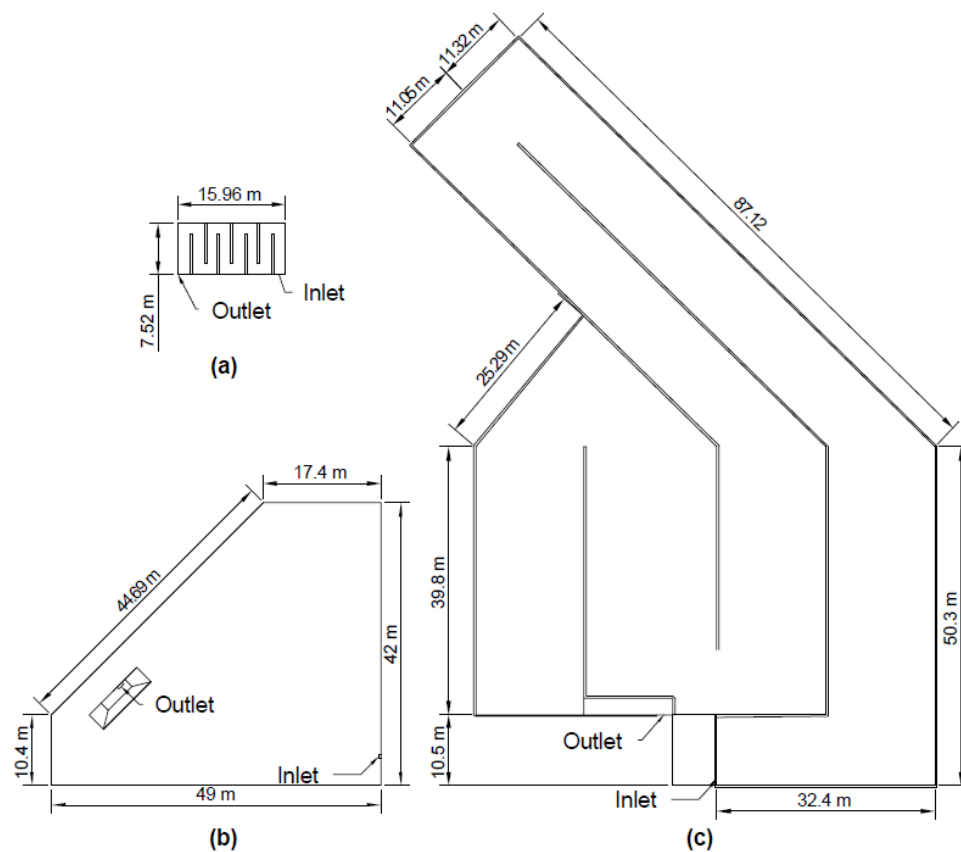


Figure 2.1 Examples of CCTs encountered in the literature, including: a) Embsay Contact Tank, Yorkshire, UK (Teixeira, 1993), b) CCT in Athens, Greece (Stamou, 2002) and c) Calgary Glenmore Water Treatment Plant, Northeast Clear Well (Yu et al., 2010)

A distinguished example is provided by the U.S. Environmental Protection Agency, which promulgated the Surface Water Treatment Rule (SWTR) in 1989 (Singer, 1994). Ultimately, SWTR established certain standards of inactivation for bacteria and viruses, essential to ensure safe potable water and attempts to regulate the chlorine residual in the distribution system. With respect to CT design, SWTR suggests the Ct (concentration \times time) concept. This requires water to be in contact with a certain concentration of disinfectant for a sufficient time so as to provide desirable degrees of inactivation for different water-quality conditions and disinfectants (Singer, 1994). In practice, disinfection is achieved when its Ct value exceeds the reference value for similar conditions. There have been discussions which concede that the use of the theoretical retention time T to determine Ct values is flawed since it does not take into consideration the hydraulic efficiency of the unit. In order to rectify this, guidelines recommend the use of the parameter t_{10} (Johnson, 1998). This is normally obtained by tracer studies and represents the time for 10% of the injected tracer mass to pass through the outlet of the tank. Another typical example is the chemical reaction model of Wehner and Wilhelm (Levenspiel, 1999). These concepts involve parameters associated

with the chemical kinetics and, importantly, with the CT hydraulic performance, by taking into account the effects of longitudinal dispersion rather than simply assuming that the contact time equals T . The application of such models depends on the determination of Hydraulic Efficiency Indicators (HEIs), which is the subject of the following section.

Most of the experimentation work on CTs conducted to date has made use of scaled CT models, since experiments on site cannot always be cost-efficient and may disrupt water treatment processes. Unfortunately, the representation of mixing processes in scaled models can be problematic as a physical hydraulic model is constructed by scaling either the Froude or Reynolds number, but not both. This leads to an overestimation of bed-generated turbulence, but an underestimation of bed friction effects (Falconer and Liu, 1988). Scale effects in model CTs have been assessed experimentally by Rauen (2001). Key effects observed included the loss of dynamic similitude between the prototype and model beyond a certain reduction ratio and challenges to mimic a prototype's Disinfection Efficiency in the bench scale models. Impacts such as these can create problems, e.g. for transferring a CFD model calibrated and validated using prototype data to simulate full scale CTs. It follows that appropriate consideration should be given to possible scale effects, such as on the turbulence levels vis-à-vis the choice of a turbulence closure scheme in a CFD modelling study.

Other than conventional tracer experiments, technological advancements have provided researchers with sophisticated experimentation equipment, such as Laser Doppler Anemometry (LDA) and Acoustic Doppler Velocimetry (ADV). Techniques such as these have enabled the acquisition of detailed three-dimensional (3-D) velocity measurements in model CTs, which have been used to assess turbulence levels in the tanks and reveal details about the occurrence of flow features, such as recirculating flow zones. For instance, Teixeira (1993) assessed a model serpentine CT, divided into eight compartments and an open channel as the inlet device, which was positioned in the top part of the inlet wall in the first compartment of the tank. The experimental results showed that the flow field was 3-D in a large proportion of the tank, with relatively high turbulence levels near the inlet section, baffle lees, in the transitional zone between two compartments and near recirculating flow regions (Shiono and Teixeira, 2000).

Rauen (2005) investigated the impact of five distinct baffling arrangements and two types of inlet devices on the hydrodynamic and solute transport processes in a model CT. The starting setup of this model tank comprised eight compartments and a channel inlet device, bearing similarities with the setup assessed by Teixeira (1993). ADV measurements were made to characterise the flow field, with particular emphasis on the vertical and horizontal flow recirculation structures formed in key regions of the tank under its various configurations. The results thus obtained were contrasted with the findings of Teixeira (1993) in terms of the progression of the 3-D flow effects through compartments, with an overall similarity being observed in the pattern of vertical non-uniformity of the flow field in different compartments. Regions with 2-D flow recirculation were characterised in terms of their size and turbulence levels (Rauen et al., 2008). Different CT setups were also assessed using fluorescent tracer techniques at the tank outlet and interpreted in relation to the idealised flow patterns.

Asraf-Snir and Gitis (2011) proceeded to fluorescent labelling of microorganisms and conducted reactive tracer experiments in a bench scale reactor. It was argued that analyses thus far sufficed on hydraulic indices to quantify efficiency, despite the need to disinfect the microorganisms. The technique evaluated the tank performance at the outlet by also taking into consideration the disinfection kinetics as the microorganisms reacted with the chlorine that was constantly pumped with the inflow.

The research and development of ozone contactors is another source of information, as they are designed according to the same principles when it comes to baffling configurations. Analyses (Kim, 2007; Kim et al., 2010a) using three-dimensional laser induced fluorescence, indicated that flow irregularities such as short-circuiting and dead zone formation are prevalent as flow meanders around baffles in disinfection contactors. These investigations concluded that the compartment width can be a determinant parameter with regards to hydraulic efficiency.

These experimental studies have led to insights being obtained about the effects of hydrodynamic processes on the dispersive transport and mixing of fluid elements in CTs, besides providing datasets for the calibration and verification of CFD modelling predictions.

2.3 RESIDENCE TIME DISTRIBUTION CURVES AND HYDRAULIC EFFICIENCY

RTD curves and HEIs are useful tools for diagnosing the hydraulic efficiency of CTs in comparison to the idealised flow pattern. The hydraulic performance of existing CTs has historically been assessed using tracer techniques, as can be seen in a number of earlier studies (e.g. Louie and Fohrman, 1968; Marske and Boyle, 1973). This method usually consists of monitoring the outlet concentration of a substance (tracer) injected in a controlled manner, typically as a slug at the inlet section, and which can alter some measurable characteristic of the fluid, such as its colour, fluorescence intensity or concentration of a given chemical, but otherwise behaves in a similar manner to the fluid while in the tank. The tracer monitoring data can be acquired and processed using automated systems (e.g. Teixeira et al., 2002). The duration of the monitoring period, the sampling frequency and the choice of sampling site should be adequately set to allow for the correct characterisation of the passage of the injected tracer mass. The typical monitoring output is a time series of tracer concentration values at the outlet, i.e. $c(t)$, calculated from the measured variation of a fluid property (e.g. fluorescence) through the use of calibration functions, obtained separately. The data processing stage usually involves three steps in a typical hydraulic efficiency assessment, such as:

- i. Normalise the concentration data and the corresponding monitoring times (such as based on Coker, 2001) to obtain non-dimensional quantities;
- ii. use the normalised results, plot the RTD curve, which represents the age distribution of elements of fluid in the flow reactor and can be used in qualitative hydraulic efficiency assessments, with this step also including the plotting of the accumulated tracer curve (F-curve); and
- iii. compute the relevant HEIs for the assessment, which can be used in a semi-quantitative analysis of the hydraulic performance (see Stamou and Noutsopoulos, 1994).

For the first step above, the time values are divided by T , giving the non-dimensional time parameter θ , where $\theta = t/T$. The non-dimensional tracer concentration values, $C(\theta)$, are calculated as:

$$C(\theta) = \frac{c(t)}{c_0} \quad (2.1)$$

where $c(t)$ is the tracer concentration recorded as a function of time t and C_0 is the average tracer concentration in the tank, such that $C_0 = M/V$, where M is the injected tracer mass. It is then necessary to compute the tracer mass recovery parameter, REC as:

$$REC = \sum C(\theta)\Delta\theta \quad (2.2)$$

where $\Delta\theta$ is the normalised time interval. Stamou and Adams (1988) suggested that the REC values associated with conservative tracer experiments should lie in the range 0.85 to 1.15, for the sake of confidence in the information contained in the whole RTD curve. Thus, REC also provides a quality indication of the experimental data, as values situated outside the recommended range suggest a problem in the planning or execution of the experiment and/or that the tracer underwent reactions over the course of the test, i.e. behaved as a non-conservative substance. The values of $C(\theta)$ can then be divided by REC to generate the time series of the normalised concentration $E(\theta)$, such as:

$$E(\theta) = \frac{c(\theta)}{REC} \quad (2.3)$$

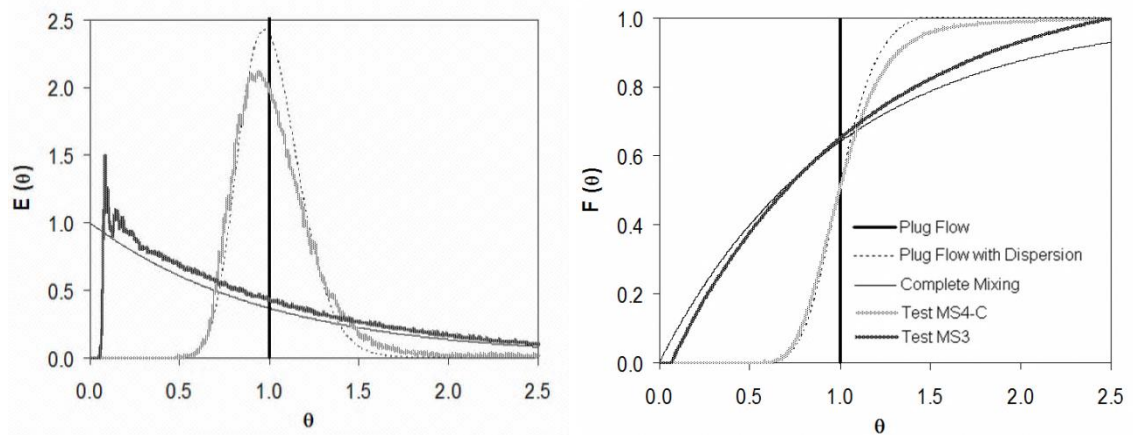


Figure 2.2 Examples of a comparison amongst normalised tracer curves, including results for idealised flow patterns Plug Flow and Complete Mixing, as well as the Plug Flow with Dispersion condition estimated for a prototype CT assessed experimentally by Rauen (2005) and results of tests obtained in that study for distinct prototype configurations. The plots show: a) Residence Time Distribution (RTD) curves; and b) F-curves. $E(\theta)$ is the normalized tracer concentration, $F(\theta)$ is the accumulated tracer mass and θ is the normalized time. For Plug Flow, $E(\theta) \rightarrow \infty$ for $\theta=1.0$, while for Complete Mixing the RTD curve is described by $E(\theta)=e^{-\theta}$, so that $E(\theta) \rightarrow 0$ as $\theta \rightarrow \infty$.

The results of $E(\theta)$ vs. θ can in turn be used to plot the RTD curve of the experiment, which has a unit area. The so-called F-curve (Levenspiel, 1999) is obtained by integrating the corresponding RTD curve, thereby representing the accumulated tracer mass that passed through the monitoring section as a function of the normalised time, i.e. $F(\theta)$. A key advantage of using the normalised RTD and F curves is that they allow for direct comparisons of results obtained in different experiments, such as for different

baffling arrangements in a given CT or between distinct units. An example of such a comparison is shown in Figure 2.2, as adopted from Rauen et al. (2012).

It may be noted in Figure 2.2 that the curves for Tests MS4-C and MS3 were obtained in the same CT model tank, but using distinct baffling arrangements, with $\beta \approx 40$ and 1.5 respectively. Normalised concentration results for the RTD curve associated with the plug flow with dispersion condition were calculated following Levenspiel (1999), as:

$$E(\theta) = \frac{1}{\sqrt{4\pi d}} \frac{1+1/\theta}{\sqrt{\theta}} e^{\left[-\frac{(1-\theta)^2}{4\theta d}\right]} \quad (2.4)$$

where d is the dispersion number, which can be calculated from the HEI results or as $d = D_L/(U_0L)$, where D_L is the longitudinal dispersion coefficient and L is the length of the CT, or the mean flow path length if baffles are included.

Qualitative analyses of the hydraulic performance of CTs based on normalised curves such as shown in Figure 2.2 usually involve an assessment of the degree of similarity between the results obtained for a given tank and the corresponding reference curve, i.e. for plug flow or plug flow with dispersion. When two or more conditions are contrasted, for example, different baffling arrangements for a given CT, then the aim of the analysis is usually to find the condition that gave the closest results to the reference curve, in order to determine the condition with the highest hydraulic efficiency from those tested. This type of analysis is usually complemented by a semi-quantitative analysis based on the HEIs.

The HEIs can be generally classified as short circuiting or mixing indicators, depending on the phenomenon which a particular indicator is intended to represent (Teixeira and Siqueira, 2008). The literature on tracer techniques applied to hydraulic efficiency assessments of flow reactors includes a large number of HEIs. For instance, the analysis made by Marske and Boyle (1973) involved the combined use of seven of these parameters, which in some occasions led to conflicting conclusions. Those authors identified the dispersion index (σ^2) as the most reliable and reproducible HEI in their investigation calculated as:

$$\sigma^2 = \frac{\sigma_t^2}{t_g^2} \quad (2.5)$$

where σ_r^2 is the variance of the RTD curve and t_g is the time to the centre of mass of the RTD curve. This indicator was introduced by Thirumurthi (1969) and can be calculated from the variance of the RTD curve. More recently, Teixeira and Siqueira (2008) tested the performance of a number of HEIs under a greater range of mixing levels in a comparative analysis of the hydraulic efficiency of scaled water treatment units. Their results showed that only a few of them were statistically robust and fit for purpose. The HEIs that were identified by those authors as having adequate performance and reliability levels are:

- for short circuiting, the indicator t_{10}/T (θ_{10}), which corresponds to the normalised time since injection for the passage of 10% of the injected tracer mass through the monitoring section;
- for mixing, the indicators Mo (Morrill index) and σ^2 , which can be defined as $Mo = \theta_{90}/\theta_{10}$, where θ_{90} is the normalised time since injection for the passage of 90% of the injected tracer mass through the monitoring section.

The use of Mo has been recommended, in particular, for situations with very low mixing levels, i.e. approaching Plug Flow, when a relatively small change in σ^2 can appear large, in percentage terms, because of the corresponding very low values of this indicator (Teixeira and Siqueira, 2008). Furthermore, it is deemed important to include σ^2 in performance analyses of CTs due to its link with the dispersion number, d , which appears in the first order reaction equation, as shown in Equation (2.4). CTs can typically be classified as closed vessels, in the sense described by Levenspiel (1999), so that σ^2 and d can be associated through the expression:

$$\sigma^2 = 2d - 2d^2 \left(1 - e^{-1/d}\right) \quad (2.6)$$

which can be solved iteratively for d . It has also been associated to the parameter β through a power law equation, with relatively high determination coefficients (Teixeira, 1993), such as $\sigma^2 = a_1 \beta^b$, where a_1 and b are coefficients that depend on the geometrical and hydraulic characteristics of the CT.

The range of variation of each of the above HEIs and of d is limited by the corresponding values calculated for the idealised flow patterns, as shown in Table 2.1,

which also includes the values obtained from the three other normalised curves shown in Figure 2.2.

Table 2.1 Hydraulic Efficiency Indicator (HEI) values associated with the normalised tracer curves shown in Figure 2.2 (Rauen et al., 2012)

HEI	PF	PFwD	MS4-C	MS3	CM
t_{10}/T	1.0	0.81	0.78	0.16	0.11
Mo	1.0	1.52	1.69	11.5	22.8
σ^2	0.0	0.027	0.055	0.539	1.0
d	0.0	0.014	0.029	0.451	$\rightarrow\infty$

In semi-quantitative analyses of the hydraulic performance of CTs using HEIs, one is usually interested in evaluating how close the result obtained for a given HEI is to the corresponding value associated with the plug flow or plug flow with dispersion flow pattern, considering the theoretical range of variation of that HEI. Deviation coefficients can be used to quantify variations in these indicators e.g. due to a setup change. However, this type of analysis cannot usually be deemed fully quantitative because the phenomena represented by the HEI, i.e. short circuiting and mixing, or indeed the hydraulic efficiency, are not directly quantifiable. It follows that if the value of a given HEI, say the mixing indicator Mo, was found to be twice as high in a certain situation as in another, the same cannot be said about the mixing levels. Thus, an analysis of Table 2.1 shows that the HEI results obtained for setup MS4-C were much closer to the corresponding values for plug flow with dispersion than to the corresponding values for complete mixing, while the opposite is true for setup MS3. It would then be concluded that the former setup is more appropriate as a CT than the latter, since the corresponding short circuiting and mixing levels, as indicated by the HEIs, are more closely associated with those found under the plug flow with dispersion condition. If attempts were to be made to improve further the hydraulic performance of that particular CT, attention should be paid to two key aspects, namely, that the plug flow with dispersion results (and not plug flow) should provide the target and, secondly, the expected improvement for the CT in terms of the disinfection efficiency and mitigation of the formation of disinfection by-products.

2.4 MATHEMATICAL MODELS OF DISINFECTION KINETICS

The inactivation of micro-organisms within CTs is not the only type of chemical reaction of interest. The decay of chlorine has to be considered since changes in the

levels of disinfectant influence rates of pathogen inactivation. In addition, regulations require standard chlorine concentrations in the finished water. This provides another incentive for modelling the reactions and the remaining concentrations of chlorine. Recent concern regarding DBPs also presents a new challenge of modelling their formation within the tank. Indicators of such kinetics can be a significant aid for the design and evaluation of CT facilities. Unfortunately, simulating chemical reactions can become complicated because they are affected by a wide range of factors, such as: the chemical composition of water, temperature, initial disinfectant concentrations, pH and maintaining the disinfectant concentration for a certain time.

2.4.1 Chlorine Decay

Chlorine is typically injected in water treatment applications in the form of gas under pressure or as a solution of sodium hypochlorite or calcium hypochlorite. Besides acting as an antimicrobial agent, chlorine reacts with both organic and inorganic substances, leading to a process of decay. Details of such reactions are outlined by Deborde and von Gunten (2008). The reaction with water in the case of gaseous chlorine can be described by:



Similar reactions tend to occur with the other solutions. Hypochlorous acid (HOCl), in turn, is weak in the sense that it tends to undergo partial dissociation. It is often desirable to retain conditions that enable a predominance of the Hypochlorous acid due to its higher disinfection efficiency, as described by Brown *et al.* (2011). The standard first order decay model can be written as (Chick, 1908):

$$C = C_0 e^{-k_b t} \quad (2.8)$$

where t is here expressed in hours, C_0 is the initial disinfectant concentration (for $t = 0$) expressed in mg/l, k_b is the bulk first order decay constant, which is typically in the range of 0.02 to 0.74 h⁻¹ and varies mainly with temperature, organic content and the initial chlorine concentration (Powell *et al.*, 2000), in addition to the cumulative concentration of chlorine applied to the water (Courtis *et al.*, 2009). Other than this approach, there have been documented second-order (with respect to chlorine and to chlorine and another reactant) and parallel first-order rate reactions with respect to chlorine (Brown *et al.*, 2011). It is agreed that chlorine decay could be more accurately

represented as the sum of two first order reactions that describe the initially rapid decay, followed by slower reactions. For instance, Brown *et al.* (2010) reported a decrease of up to 31% of the initial free chlorine concentration in only the first 5 min of the 4 h tests. An example of such a model was given by Haas and Karra (1984):

$$C = C_0 z e^{-k_{bf}t} + C_0(1 - z)e^{-k_{bs}t} \quad (2.9)$$

where k_{bf} is the decay rate for fast reactants and k_{bs} is the equivalent term for slow reactants, both expressed in h^{-1} , while z is the ratio of fast to slow reactions.

2.4.2 Microorganism Inactivation

A number of researchers have previously developed models to describe inactivation processes (Haas & Karra, 1984; Haas et al., 1995). A simple approach is the Chick–Watson model (Chick, 1908; Watson, 1908), where the inactivation rate of a microorganism is dependent upon the concentration of the disinfectant and contact time and is normally given as

$$N = N_0 e^{-k' C^n t} \quad (2.10)$$

where k' is an empirical constant and n the average number of disinfectant molecules required to inactivate a single micro-organism and C is the disinfectant concentration (mg/l). The differential form of the above equation provides the rate of pathogen inactivation as:

$$\frac{\partial N}{\partial t} = -k' C^n N \quad (2.11)$$

which is considered a robust model for the disinfection rates of various pathogens. Assuming first order reaction kinetics, the Disinfection Efficiency (DE) of a contactor can be estimated using an adapted form of Wehner and Wilhelm's equation (Levenspiel, 1999), such as:

$$DE = 1 - \frac{4\alpha e^{1/2d}}{(1+\alpha)^2 e^{\alpha/2d} - (1-\alpha)^2 e^{-\alpha/2d}} \quad (2.12)$$

$$\alpha = \sqrt{1 + \kappa T d} \quad (2.13)$$

where DE can vary between 0 (no disinfection) and 1 (full disinfection) and α is a dimensionless group that includes the reaction rate and dispersion effects, where κ is the first order rate constant of inactivation and can be obtained using the Chick-Watson model (Gyürék and Finch, 1998), such as:

$$\kappa = k' C^n \quad (2.14)$$

It may be noted that the higher the value of d entered in Equation (2.12), then the lower the value of DE obtained, with other parameters being kept constant. This type of response correctly reflects the knowledge that the CT process performance is usually detrimentally impacted on by an enhanced degree of longitudinal dispersion in the tank, as caused by short circuiting, since the corresponding fluid elements typically leave a tank earlier than the design contact time. However, due to the non-linear nature of the model the impact of a variation in d on the DE depends on how hydraulically efficient the tank already is. Such models were applied by Stevenson (1995) and Johnson et al. (1998) to estimate the influence of the dispersion number on the disinfection efficiency of a number of CT configurations. Both studies showed that improving the hydraulic performance of a CT beyond a certain level did not significantly increase its overall disinfection efficiency, which indicated that hydraulic optimisation must be considered together with process performance. For instance, as pointed out by Trussell and Chao (1977) reducing d from 0.1 to 0.01 leads to an improvement of 60% in DE , while a further reduction in d to 0.001 only results in a further DE improvement of 6%.

A noteworthy variation of the Chick-Watson law has been reported by Hom (1972), who incorporated a parameter m which empirically describes the deviation of the disinfection from first order kinetics:

$$\frac{\partial N}{\partial t} = -k' m C^n N t^{m-1} \quad (2.15)$$

The inactivation rate of Hom's model has been successfully validated against experimental studies of *G. Lamblia* (Haas et al. 1995) and *Cryptosporidium* (Finch et al., 1993) inactivation.

2.4.3 By-Product Formation

The reactions between chlorine and organic and inorganic matter often lead to the formation of DBPs. General awareness and understanding of these reactions have

improved considerably since their first connections with health issues in 1976, but there is still a lot of uncertainty over this issue, which is still one of the main challenges for the water sector (EWP/WssTP, 2011). An example of the limited knowledge is the fact that the formation of 50% of total organic halide produced during chlorination still cannot be explained (Brown *et al.*, 2011). Even so, predictive models that describe DBPs have been developing for some time. They estimate concentrations of specific DBPs based on the contact time, chemical composition of water (e.g. organic matrix, bromide concentrations) and the disinfection conditions (e.g. pH, temperature, disinfectant concentrations). The most significant DBPs for chlorination according to our current knowledge include: trihalomethanes (THMs) with the largest concentrations, followed by haloacetic acids (HAAs), then haloacetonitrile (HAN) and inorganic compounds (Sadiq and Rodriguez, 2004). The study of Singer (1994) on the regulation of DBPs in drinking water listed key equations that predict concentrations of major DBPs for the Water Treatment Simulation Program of the U.S. EPA, including, for example:

$$TTHM = 0.00306[(TOC)(UV_{254})]^{0.44}(Cl_2)^{0.409}(T_e)^{0.665}(pH - 2.6)^{0.715} \\ \times (Br + 1)^{0.036}(t)^{0.265} \quad (2.16)$$

$$DCAA = 0.605(TOC)^{0.291}(UV_{254})^{0.726}(Cl_2)^{0.480}(T_e)^{0.665}(Br + 1)^{-0.568}(t)^{0.239} \quad (2.17)$$

$$TCAA = 87.182(TOC)^{0.355}(UV_{254})^{0.901}(Cl_2)^{0.881}(pH - 2.6)^{-1.732}(T_e)^{0.665} \\ \times (Br + 1)^{-0.679}(t)^{0.239} \quad (2.18)$$

where *TTHM* is the total trihalomethanes concentration in µg/l, *DCAA* is the dichloroacetic acid concentration in µg/l, *TCAA* is the trichloroacetic acid concentration in µg/l, *TOC* is the total organic carbon concentration in mg/l, *UV₂₅₄* is the ultraviolet absorbance at 254 nm in cm⁻¹, *Cl₂* is the chlorine dosage in mg/l, *T_e* is the temperature in °C, and *Br* is the bromide ion concentration in mg/l. This type of semi-empirical models for THM formation was first proposed by Amy *et al.* (1987) but its applicability is impaired by its reliance on costly data collection and analysis, dependency on specific site and operational conditions and the non-inclusion of other important controlling parameters (Brown *et al.*, 2010).

Research on the prediction of DBP formation has expanded since then. In their review, Sadiq and Rodriguez (2004) list the development and application of numerous

mathematical models that predict concentrations of various DBPs under a range of field and laboratory studies. More recently, a simple, yet robust model for *TTHM* formation was proposed by Brown et al. (2010), which reads:

$$TTHM = k_{tc}(C_0 - C) \quad (2.19)$$

where k_{tc} expressed in terms of $\mu\text{g TTHM/l}$ per mg chlorine/l , is the coefficient of proportionality between *TTHM* production and chlorine consumption, which is an easily measured parameter in a water treatment or distribution system. Future research may lead to the development of similar models for other DBPs, which can be of significance when it comes to operational purposes of water treatment and management of water quality. They can be used to assess the health risk of water treatment facilities under current operation and for estimating the impact of DBP regulations. However, in practical CT applications it is necessary to account for the flow and solute transport processes that govern the occurrence of stagnant regions, in particular, due to their higher potential for DBP formation relative to other regions of a given tank, induced by a relatively high average contact time. This could be achieved using CFD models.

2.5 ADVANCES IN CONTACT TANK COMPUTATIONAL FLUID DYNAMICS MODELLING

Advances in CFD modelling and computing power have enabled the development of models that can simulate the flow and solute transport processes in CTs with considerable detail. The recent attention to CFD modelling can be easily justified. As mentioned earlier, physical models are characterized by an inability to simultaneously scale both the turbulence and the decay rates, which means that model predictions will not reflect prototype conditions, and in certain cases (e.g. recirculation zones) the results can be in serious error. In CFD models, on the other hand, all parameters are modelled at prototype dimensions, thus the turbulence, chemical and biological processes and decay rates are not distorted by scaling (Falconer, 1990). Numerical models have the added advantages of being cost-effective, easily adjustable and flexible.

CFD models apply numerical schemes to solve the governing mathematical equations applicable to a wide range of problems in fluid mechanics. By observation, CT simulation requires models that represent the hydrodynamic and solute transport

processes in 2-D or 3-D. Numerical modelling methods used in CT simulations are outlined below and further details about specific models can be found in the literature.

2.5.1 Hydrodynamics

The hydrodynamic processes in CTs are governed by the mass and momentum Navier-Stokes (N-S) equations. The water is generally treated as an incompressible fluid and the influence of Earth's rotation can be disregarded in typical CT simulations, due to the relatively small scale of the problem being considered. Temperature changes are also usually unimportant within the time scale of simulations and boundary conditions of a problem, which allows the continuity and momentum equations to be uncoupled from the energy equation by assuming a constant viscosity and treating pressure as an ordinary variable (i.e., disregarding its thermodynamic nature). Expressed in Eulerian, rectangular coordinates, the simplified unsteady continuity and momentum equations can be written in Cartesian tensor notation as:

$$\frac{\partial U_i}{\partial x_i} = 0 \quad (2.20)$$

$$\frac{\partial U_i}{\partial t} + U_j \frac{\partial U_i}{\partial x_j} = -\frac{1}{\rho} \frac{\partial p}{\partial x_i} + \nu \frac{\partial^2 U_i}{\partial x_i^2} \quad (2.21)$$

where U_i is the time-averaged velocity component in the i -direction (subscripts $i, j=1,2,3$ express the three spatial directions x, y, z), ρ and ν are the fluid specific mass and kinematic viscosity respectively, t is the time and p is the pressure. Unsteady conditions in CTs are usually associated with the variation of water levels and input or output discharge. This can be of interest in long term simulations, e.g. of a daily supply-demand cycle of a service reservoir, as conducted by Zhang *et al.* (2011). However, obtaining a steady state flow field solution is usually the aim of CFD simulations undertaken to assess the hydraulic performance of a CT under certain operational conditions. It follows that the transient term can usually be dropped from the momentum equations and the resulting set solved for as an elliptic, vis-à-vis a parabolic problem.

As pointed out by Rodi (1993), the N-S equations cannot currently be analytically solved for flows of practical relevance, such as in CTs. Hence, statistical approaches have been used to resolve explicitly the scales of flow and provide a closure model for the effects of turbulent micro-scales upon resolved scales (Wang and Falconer, 1998a).

The most common approaches used for the establishment of appropriate resolved scale N-S equations are the Reynolds-Averaged Equations and Large Eddy Simulation (LES) models. Due to the non-linearities that characterize the N-S equations, unknown correlations are produced upon the application of statistical approaches. These unknown quantities can be translated into the Reynolds and sub-grid scale (SGS) stresses respectively, which relate to the turbulence characteristics of the flow. Accurate determination of these values is necessary for a reliable hydrodynamic model. As a result, the development of accurate turbulence models has been the subject of CFD research in general. Turbulence models have been developed that vary from simplified zero-equation models (e.g. constant eddy viscosity) to more sophisticated models that can be more accurate, but computationally more demanding (Rodi, 1993). Consequently, research on the hydrodynamics of CTs has been conducted to investigate the performance of different turbulence models and their ability to simulate practical conditions in such tanks, as illustrated in Table 2.2. Peplinski and Ducoste (2002) assessed the sensitivity of CFD modelling predictions to the variation of the turbulence modelling approach and concluded that it is one of the strongest factors governing the outcome of the modelling predictions.

Boundary conditions for the N-S equations as applied to simulate CT hydrodynamics are typically of the Dirichlet and Neumann types, which correspond to the specification of values and prescription of the zero gradient condition for parameters respectively (Roache, 1998). It can be noted that the free surface is usually deemed to be horizontally flat, as little improvement can be derived from resolving the water-air interface exactly (Zhang *et al.*, 2011). This assumption contributes to improve the cost-effectiveness of the hydrodynamic simulations of CTs. In addition, the surface can be treated as a frictionless boundary, which leads to the application of the free slip condition. By contrast, the no-slip condition is usually prescribed for solid surfaces. It can be noted that a semi-slip condition in which the boundary roughness scale value can be calibrated may lead to better agreement with hydrodynamic data in some occasions. This boundary condition does not appear to have been tested in CT simulations.

Table 2.2 Turbulence models used in CFD modelling studies of CTs, with sources indicated in brackets for further information on specific model formulations.

Turbulence Models	CT References	CFD Code
Mixing Length (Fischer, 1973)	Wang and Falconer (1998a)	CONTANK
	Wang et al. (2003)	CONTANK
	Rauen (2005)	STRATUS
SGS stress (Smagorinsky, 1963)	Wang and Falconer (1998a)	CONTANK
	Kim et al. (2009)	Hydro3D-GT
	Kim et al. (2010)	Hydro3D-GT
	Kim et al. (2013a)	Hydro3D-GT
	Zhang et al. (2013)	OpenFOAM
Standard k- ϵ (Rodi, 1993)	Wang (1995)	CONTANK
	Wang and Falconer (1998)	CONTANK
	Cockx et al. (1999)	ASTRID
	Zhang et al. (2000)	CONTANK
	Peplinski and Ducoste (2002)	PHOENICS
	Wang et al. (2003)	CONTANK
	Huang et al. (2004)	FLUENT
	Rauen (2005)	STRATUS
	Khan et al. (2006)	CFX
	Templeton et al. (2006)	FLUENT
	Gualtieri (2007)	Multiphysics
	Stamou (2008)	CFX
	Xu (2010)	FLUENT
	Wilson and Venayagamoorthy (2010)	FLUENT
	Kim (2011)	SSIIM
Lee et al. (2011)	CFX	
Wols et al. (2011)	FINLAB	
Zhang et al. (2013)	OpenFOAM	
Kim et al. (2013b)	SSIIM	
Low Reynolds k- ϵ (Lam and Brethorst, 1981; Launder and Sharma, 1974)	Rauen (2005)	STRATUS
	Greene et al. (2004)	CFX
	Rauen et al. (2008)	STRATUS
k- ω model (Menter, 1994)	Zhang et al. (2011)	FLUENT

Hydrodynamic modelling of contact tanks commenced long after initial experimental studies. One of the first documented numerical model studies solely related to chlorine CTs was undertaken by Falconer and Liu (1987). They applied a version of the Depth Integrated Velocities And Solute Transport (DIVAST) model, which is based on a finite difference discretisation scheme and the Alternating Direction Implicit (ADI) solution method to create a 2-D depth integrated model (2-D-H). The model was used to simulate the hydrodynamic conditions of the Elan Contact Tank, which was the topic of two earlier experimental studies (Thayanity, 1984; Falconer and Tebbutt, 1986). The 2-D flow patterns for the tank were studied through previous experiments that monitored the route of neutrally buoyant floats within the tank (Falconer and Tebbutt, 1986). A comparison of results gave rise to disparities attributed to three dimensional flow features that could not adequately be represented in a 2-D model.

Following these studies, the refinement of similar depth averaged models has been a core issue since there is an encouraging similarity between the simulation results and CT flow when near plug flow conditions exist. The research on 2-D-H models largely aims at reducing inaccuracies by testing more sophisticated turbulence models (Wang, 1995; Wang and Falconer, 1998a). For instance, out of the mixing length model, depth integrated k- ϵ model and the Smagorinsky model (1963), the latter one seemed to be quite satisfactory for the simulation of the turbulence structure for advection domination effects (Wang and Falconer, 1998a). On the other hand, even though the depth integrated k- ϵ model underestimated the cross-sectional velocity, it produced accurate predictions of the flow patterns, allowing for the estimation of the location and magnitude of stagnant regions and the advective flow paths.

Hannoun and Boulos (1997) successfully applied a CFD code using the finite volume method to provide the distribution of water quality parameters within water storage and disinfection facilities. Their work is of particular significance since the model developed was 3-D, which represented a significant step forward in the simulation of chlorine CTs.

Research associated with the finite volume method was undertaken by Rauen (2005), who developed a chlorine CT-specific CFD code that performed 2-D and 3-D simulations. The model applied the SIMPLER numerical procedure that was developed by Patankar (1980) to discretise the N-S equations. Two different methods of turbulence modelling were reported, namely a mixing length approach and a version of the low

Reynolds number k - ϵ model (Lam and Bremhorst, 1981). Refinements were made to the near wall representation of the c_μ parameter of the k - ϵ model, so that the near wall region and the location and magnitude of 2-D recirculating flow structures could be correctly predicted, albeit at the expense of computational time. The results were compared with hydrodynamic data acquired in a model CT and the ensuing analyses suggested that the low Reynolds number k - ϵ model yielded realistic representations of the short-circuiting and mixing levels within the tank, in which low to moderate turbulence levels occurred. The performance of this approach has not been validated for field scale conditions, where higher Reynolds numbers are encountered – although these models tend to the standard k - ϵ in fully turbulent regions. However, the standard k - ϵ model could be sufficient for the larger field scale tanks, where near wall profiles do not dominate the flow conditions within the unit. This example illustrates how great care needs to be taken when selecting a turbulence model depending on the scale of the problem.

A number of 3-D applications of the low Reynolds number k - ϵ model were made by Rauen (2005) but fully converged hydrodynamic results could not always be achieved at the time, due to the excessively long computational time required for the completion of simulations in a single processor desktop computer, of two weeks or more in some cases. However, it should be pointed out that comparable detailed LES runs for baffled contact tanks could be up to 14 times slower than the corresponding simulations using the Reynolds Averaged N-S modelling approach, as shown by Kim et al. (2010b). This was also partly due to the relatively slowly converging nature of simulations with iterative models, such as based on the SIMPLE family of algorithms, compared to more direct solution approaches. With the further development of parallel processing techniques and the growing availability of multi-core and cluster computers, this option may become more feasible for practical simulations of interest, e.g. to water supply companies, if justified in terms of the level of flow field detail required vis-à-vis the flow regime and other characteristics of the CT. However, existing codes need to be parallelised. It may also be noted that fully 3-D simulations, which are typically more time consuming than 3-D layer integrated or 2-D simulations, allow for the prediction of a hydrodynamic pressure distribution in the vertical direction, rather than assuming a hydrostatic pressure distribution. Thus, the use of fully 3-D simulations should be justified by the occurrence, in the CT of interest, of relatively strong vertical

accelerations, which is normally associated with the occurrence of vertically reversed flow structures, as measured by Teixeira (1993) and Rauen (2005). This is not an uncommon feature of CTs, at least in some regions of the flow field, and is usually induced by inappropriately designed but commonly used inlet and outlet pipes and culverts.

The study of Kim et al. (2010b) reported results of an LES three-dimensional simulation of a small-scale serpentine ozone contactor. These results indicated a satisfactory performance in reproducing the flow conditions and appeared comparable in terms of hydrodynamics with the mean predictions of RANS simulations. The associated RANS simulations were performed using the conventional k - ϵ turbulence model and were considerably less computationally demanding. More recently, Zhang et al. (2013) reproduced the results of the study using both LES and RANS simulations reaffirming the performance of both approaches.

The numerical model studies mentioned so far have been conducted using research CFD models. In addition, commercially available CFD packages have been used in a number of investigations of CT hydrodynamics, which were typically aimed at diagnosing the hydraulic performance of existing CTs and assessing the impact of design modifications. Examples have included alterations to the number of baffles and, hence, the β value (Templeton et al., 2006; Gualtieri, 2006; Gualtieri, 2007; Xu, 2010; Amini et al., 2011), testing alternative baffling arrangements (Stamou, 2002 and 2008) and other flow modifier structures in chlorine and ozone CTs of similar geometry (Cockx et al. 1999; Huang et al., 2002; Huang et al, 2004; Wols et al., 2010; Lee et al., 2011).

Greene et al. (2004) used a commercially available CFD package equipped with the low Reynolds number k - ϵ model of Launder and Sharma to assess the impact of fine and coarse baffle configurations respectively near the inlet region on the overall performance of an existing CT. Their hydrodynamic results were not validated due to a lack of the corresponding data, which is usually not obtainable in full scale CCTs due to operational and safety constraints (Greene, 2002). The subsequently obtained solute transport results, when compared with the corresponding data suggested that the hydrodynamic model may have overestimated the strength of the advective flow paths. It is unclear whether such a shortcoming was induced by the low Reynolds number k - ϵ model used or caused by other issues with the hydrodynamic model. Further research

could be conducted to contrast the performance of different turbulence approximations when simulating CT hydrodynamics, particularly in conditions of low to moderate turbulence levels, such as the ones encountered at the prototype scale.

The validation of hydrodynamic predictions obtained using available CFD software, when conducted, have been based on the datasets obtained by Teixeira (1993) and Rauen (2005) for prototype CTs (e.g. Khan et al., 2006; Rauen et al., 2008) and predominantly relied on reproducing the velocity field. Validation of turbulence characteristics such as turbulent kinetic energy has yet to be reported in the published literature even though it is highly influential to the simulation of solute transport. Due to the limited availability of hydrodynamic data, calibration and validation studies of CFD modelling predictions are usually undertaken for the ensuing tracer transport results. Some implications of this practice are discussed further in the following section.

2.5.2 Solute Transport

The governing equation for solute transport processes is the advection-diffusion equation, which can be written in indicial form as:

$$\frac{\partial \phi}{\partial t} + u_i \frac{\partial \phi}{\partial x_i} = D \frac{\partial^2 \phi}{\partial x_i \partial x_j} + S_\phi \quad (2.22)$$

where ϕ is a scalar quantity (e.g. disinfectant or pollutant concentration), D is the scalar molecular diffusivity and S_ϕ is a volumetric source term.

The advection-diffusion equation can be solved in a similar manner to the momentum equations (Rodi, 1993). From (2.22) it can be seen that solute transport is dependent on the results of the hydrodynamic model, as the velocity field and turbulence distribution parameters must be imported into the solute transport model. When it comes to CTs, a transport model allows for simulating the transport and mixing processes within the unit. Amongst the typical outputs of interest is the concentration of disinfectants, micro-organisms or tracers with respect to time, as well as the RTD and F curves and HEI values. In turn, that output can be converted into information that reflects the efficiency of the tank.

The modelling of the advective terms using finite difference methods has been problematic with respect to accuracy, stability and simplicity (Wang and Falconer,

1998b). In order to overcome the difficulties associated with these obstacles, upwind schemes have largely been employed. Methods of this kind found in the literature include the first-order upwind scheme, the Quadratic Upstream Interpolation for Convective Kinematics (QUICK) scheme, the third-order upwind difference scheme (Wang and Falconer, 1998b; Wang et al., 2003). The higher order approximations produced by the QUICK scheme have improved stability from a central difference scheme and can accurately represent the advective terms (Wang and Falconer, 1998b), particularly in relatively coarse grids. A detailed analysis of how this method is applied was published by Falconer and Liu (1987). The Hybrid Linear/Parabolic (Zhu, 1991) method was successfully deployed for the modelling of advective terms in baffled ozone contactors (Kim, 2011; Kim et al, 2013) but has yet to be reported in chlorine CTs.

A study where the primary concern was solute transport in CTs was published by Falconer and Ismail (1997), in which a 2-D-H semi-time-centred implicit QUICK scheme was used to simulate the tracer transport in a scaled serpentine CT. RTD curves were plotted according to tracer injection simulations, thus enabling comparisons with experimentation results. The results matched well in regions where the flow was uniform over the depth, i.e. largely 2-D in nature. Based on the literature, the QUICK method has yet to be applied in a 3-D model.

Rauen (2005) conducted 2-D and 3-D solute transport modelling based on the finite volume method and with the fifth order power law (Patankar, 1980) scheme to account for the advection-diffusion fluxes. A CT model tank with 2-D flow assessed experimentally by Rauen (2001) was simulated, as well as various setups of the CT model tank with 3-D flow assessed experimentally in the same study. The 2-D solute transport results agreed well with the laboratory tracer data, suggesting the appropriateness of a 2-D modelling approach for the particular design, but the 3-D results showed an underestimation of the levels of mixing and short-circuiting compared to laboratory measurements when using the low Reynolds $k-\epsilon$ turbulence model. The turbulent Schmidt number (Sc) was also varied in that study and had a significant impact on the solute transport results. It is known that Sc is directly associated with the turbulent diffusivity (Kim et al., 2010), so that it is an influential parameter when it comes to the solution of the advection-diffusion equation in contact tanks (Peplinski and Ducoste, 2002). Further research on the solute transport modelling of CTs could focus

on the determination of Sc under different conditions (e.g. CT size, flow conditions, solute type), which would contribute to improving the accuracy of CFD models of the solute transport processes in CTs. The suitability of using a gradient diffusion hypothesis altogether which relies on the Sc parameter was argued by Kim et al. (2013b), where it was considered that such a simplistic approach can be accurate only under specific circumstances without calibration. The Sc was found to depend on the geometry yielding accurate predictions for narrow compartments with the standard value of 1.0, while it had to be lowered substantially for wider compartments.

In the absence of experimental hydrodynamic data, Kim et al. (2010) based the validation of the LES simulation on comparisons between simulated tracer transport and the 3D-LIF data of Kim et al. (2010). With respect to the RANS simulations, poor agreement was produced against the actual readings. However, when Zhang et al. (2013) examined the results of the study, a revisited RANS approach produced results which were on par with the accuracy of the LES and the 3D-LIF experimentation. Subsequent CFD analyses (Kim et al., 2013a; Kim et al., 2013b) reaffirmed that baffle spacing is a critical parameter in the design of serpentine disinfection tanks and should ideally converge to the dimensions of the inlet device for optimal disinfection performance.

Commercially available CFD packages have also been used to assess CT solute transport performance. These studies typically resolved the advective-diffusion equation in 2-D (e.g. Templeton et al., 2006; Gualtieri, 2006; Gualtieri, 2007; Xu, 2010) or 3-D (e.g. Cockx et al., 1999; Huang et al., 2004; Khan et al., 2006; Stamou, 2008; Amini et al., 2011) simulations to obtain the tracer and/or chlorine concentration results for CTs. Simulations of tracer studies are typically undertaken for a slug injection, with the outlet RTD curve and HEI results of the corresponding tanks being generated and compared with available data.

It has been noted that the majority of CFD modelling studies of CTs have only reported the validation of modelling predictions against outlet tracer or chlorine concentration data, as available for the CTs simulated. Obtaining agreement in terms of the outflow solute concentration results is indicative of adequate hydrodynamic modelling and correct prediction of flow and mixing processes in the CTs, but it is not necessarily a guarantee of it. This is because similar outflow RTD curves, for instance, can be

associated with significantly different flow fields in reactors, as shown by Levenspiel (1999). Hence, whenever possible, comparisons with hydrodynamic data that represents the types of flow features encountered in a CT of interest should be performed and reported. Alternatively, the validation of RTD curves obtained in CTs – in addition to outflow results – can contribute to increase the level of confidence in the modelling predictions, as proposed by Teixeira et al. (2004). In this case, the selection of sampling stations internal to the flow field should be carefully conducted, and possibly assisted by preliminary CFD simulations of the CT of interest, to account for the relative contributions of key flow features – such as stagnant regions and advective flow paths – to the solute transport results thus obtained. Such methodology still requires further experimental confirmation and does not eliminate the problem of sampling in the operating tanks but can potentially enhance the calibration and validation practice of CFD models of CTs.

2.5.3 Disinfection Kinetics

The hydraulic efficiency examined by hydrodynamic and conservative tracer analyses can provide a reasonable estimate of the expected performance of the contact tank; however, these cannot predict disinfection specific parameters such as optimum disinfectant dosage or bacteria survival level, i.e. invaluable information for the operation and design of field-scale tanks. Several research studies in the recent literature have acknowledged this issue.

Greene (Greene, 2002; Greene et al., 2004; Greene et al., 2006) used the SIMPLEC finite volume method (a variant of the SIMPLE method) to resolve the advective-diffusion equation and also included models to account for the disinfectant decay and bacteria inactivation, which were used to estimate the Disinfection Efficiency of the unit. The model overestimated the output micro-organism levels when lower dispersion was observed. This finding has not been reported previously or ever since, and contradicts the theory that lower dispersion leads to greater disinfection. Wols et al. (2010) investigated several evaluation methods of disinfection performance in a baffled ozone CT using two-dimensional simulations also departing from the standard of calculating HEIs at the outlet. Zhang et al. (2011) simulated chlorine transport and decay in a CT through a user defined function within a commercially available CFD model, which impacted the source term S_ϕ solved for the chlorine concentration.

Predictions thus obtained for outlet chlorine distributions were accurate to $\pm 5\%$ of measured data. The model was then applied to estimate the spatial distributions of the local mean residence time of chlorine in the CT, which is a useful result for estimating the formation of DBPs, although this was not contemplated in their study.

The only CFD modelling study found dealing with the incorporation of available equations to describe the disinfectant decay, consumption rate and DBP formation in chlorine CTs was that of Zhang *et al.* (2000). A modified version of DIVAST, which was refined by Wang (1995), was used to simulate the chlorine kinetics and estimate the distribution of DBPs in the CT model tank of Teixeira (1993). The corresponding predictions could not be verified due to the lack of water quality data for the tank, as datasets on DBP formation in CTs appear to be scarce. Moreover, the suitability of a depth-averaged model for the simulation of that CT is questionable, as the particular inlet and outlet configurations correspond to extensive three-dimensionality as highlighted by the study of Shiono and Teixeira (2000). Recent advances on the mathematical modelling of chlorine decay, bacterial inactivation and DBP formation have yet to be incorporated into CFD models of the CT processes. That potential could be further explored, so that modern requirements of CT design and performance optimisation would be adequately assisted by suitable modelling tools. Any such studies undertaken in the absence of suitable calibration and validation data might include sensitivity analyses of the response of modelling predictions to the variation of input parameters, complexity of governing equations and numerical aspects, as this could inform the determination of uncertainty in modelling predictions thus made.

2.6 REVIEW SUMMARY

In this chapter a critical appraisal of design considerations, experimental research and numerical modelling techniques commonly used in chlorine CT studies was conducted, based on a review of the international scientific literature. At first, the main concepts and strategies adopted for the design and operation of CTs at water treatment works were introduced and particular focus was given on the derivation and analysis of RTD curves, determinant for the evaluation of disinfection performance using HEIs.

A historical perspective on modelling practices was described and possibilities for further research and modelling development were identified. Initially, the calibration and validation of CFD modelling predictions for CT hydrodynamics suffer from the

scarcity of data. Available experimental data on hydrodynamics is currently limited and has so far been used in simulation validations with respect to the velocity field (Khan et al., 2006) but not for the observed turbulence characteristics (e.g. Shiono and Teixeira, 2000). Other reports of numerical modelling in CTs to a significant extent are validated against outlet RTD curves which can be a source of uncertainty as argued by Levenspiel (1999). However, characterization of the hydrodynamic influence on solute transport might mitigate this uncertainty through a better understanding of the mixing processes in CTs.

The main kinetic processes of interest for chlorine disinfection are outlined as chlorine decay, pathogen inactivation and DBP formation. Representative mathematical models developed to describe such processes were investigated with regard to the extent to which they have (or not) been incorporated into numerical modelling studies towards the development of integrated hydro-kinetic tools for the optimization of CT facilities. An additional concern encountered is the necessity to expand the modelling capacity to 3-D simulations as the conditions found in CTs are often beyond two dimensions.

The sensitivity of CFD model predictions to the variation of modelling components, such as the type of advection-diffusion scheme, turbulence model and boundary conditions, needs to be better established for relevant ranges of operational conditions of CTs, including prototype tanks that may be subjected to scale effects;

Detailed simulations using three-dimensional CFD models with fine mesh resolution can take advantage of parallel processing techniques but existing codes developed for CT research need to be parallelised; state of the art commercially available CFD codes can be used but with a much reduced scope for refinements and control over the modelling components, due to the “closed source” nature of such codes. Parallel processing could improve the practicality of more accurate, but computationally demanding, techniques such as LES. On the other hand, cost-efficient techniques (e.g. RANS) should be examined more closely in terms of their potential by further validation, since encouraging performance has been reported in certain cases.

CHAPTER 3

EXPERIMENTAL METHODS

3.1 INTRODUCTION

The experimental aspect of the research was conducted in the Hyder laboratory of the Hydro-Environmental Research Centre at Cardiff University. This section is dedicated to the overview of experimentation facilities and sampling instruments. The prototype model characteristics and operation methods are detailed in section 3.2. Sections 3.3 and 3.4 deal with the data acquisition, sensitivity analyses and preliminary tests associated with Acoustic Doppler Velocimetry and Tracer Experimentation respectively.

3.2 LABORATORY MODEL

The laboratory model was designed in 2002 for the study of CT flow and mixing processes, where previous experimentation focused primarily on the evaluation of different baffling configurations on hydrodynamics and the derivation of RTD curves at the outlet (Rauen, 2005).

Even though the geometrical features of the experimentation unit are of particular interest, a description of how water recirculates into the contact tank is preceded by highlighting some considerations that influence the experimental procedure.

3.2.1 The Hydraulic Circuit

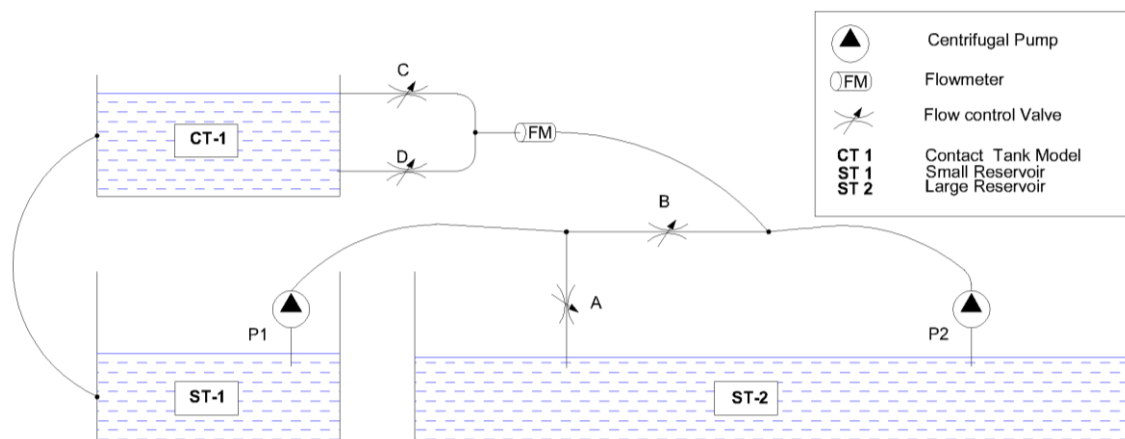


Figure 3.1 Hydraulic Circuit Diagram

The hydraulic circuit describes how water recirculates into the tank, the route followed and the equipment used to control, monitor and alter hydraulic conditions within the CT physical model. Figure 3.1 indicates the main components of the system.

There are three tanks in the circuit; CT-1 is the contact tank model, while ST-1 and ST-2 are two reservoirs for water supply and storage. ST-1 is made out of steel and is the main support tank of the model and has dimensions $2.0 \times 1.5 \times 1.5$ m with an approximate capacity of 4.5 m^3 . There is a PVC pipe of 40 mm internal diameter which draws water through a pump and transfers it either to CT-1 or ST-2 depending on the valve configuration. Water from the outlet of CT-1 is diverted to ST-1 by a flexible plastic pipe of 140 mm internal diameter.

The ST-2 reservoir supports the majority of the flumes and physical models in the Hyder laboratory. It has an approximate capacity of 48 m^3 and was incorporated in the hydraulic circuit to ensure the feasibility of experimentation with tracers. Ideally, when conducting tracer experiments, it is desirable to allow for a sufficient retention time before the re-introduction of water to CT-1. Thus, dyed water will not return to CT-1 in time to interfere with the results of an on-going tracer test. This could not have been achieved with the limited volume offered by ST-1 alone, as the recirculation time would be too short. On the other hand, for ADV measurements, the use of ST-2 was not necessary and ST-1 sufficed as the sole supply reservoir for the system.

There are 2 centrifugal pumps, *P1* and *P2*, each one used to acquire water from ST-1 and ST-2 respectively. They were both manufactured by Clarke International; model CPE20A1, with specifications of 1.5 kW (2.0 hp) and a discharge (*Q*) range of 1.66–6.25 l/sec. For ADV measurements, only *P1* was in operation, transferring water to CT-1. During tracer experiments, *P1* transferred water from ST-1 to ST-2, while *P2* in turn pumped it towards CT-1's inlet. An electromagnetic flowmeter (manufactured by Euromag International; model MUT 1100/J) was placed upstream of the inlet and was connected to an MC106 converter displaying the discharge value in m^3/h . According to the flowmeter manufacturer, the uncertainty of the measure is equal to 0, 2% of the read value. As shown in Figure 3.1, there are 4 Flow Control Valves (FCV) in the system. FCVs A and B regulate whether the flow from ST-1 will be directed towards ST-2 or CT-1 respectively. C and D are used to control the flow and the type of inlet (pipe / channel).

3.2.2 The Physical Model

The contact tank model (CT-1) is designed after the CT operated by Yorkshire treatment at Embsay water treatment works. CT-1 is not as accurate, geometrically, as

the scaled model tank used by Teixeira (1993), but its versatility provides the potential for examining more complex hydrodynamic features. The tank itself has dimensions $3.0 \times 2.0 \times 1.2$ m and is primarily fabricated out of steel, designed specifically for research purposes associated with CTs. Lateral parts of the North and South wall are made out of glass which enable the observation of hydrodynamic and mixing effects. The baffling configuration is particularly flexible, as internal baffles are made out of plywood and their arrangement can be altered with relative ease. In addition, the design features two inlet options, an open channel entry or a pipe inlet which can be controlled through FCVs C and D mentioned previously. Figures (3.2 – 3.4) depict the main features of the tank geometry.

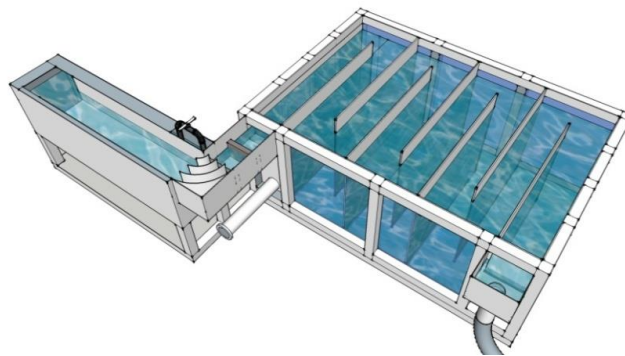


Figure 3.2 Three-Dimensional sketch of CT-1

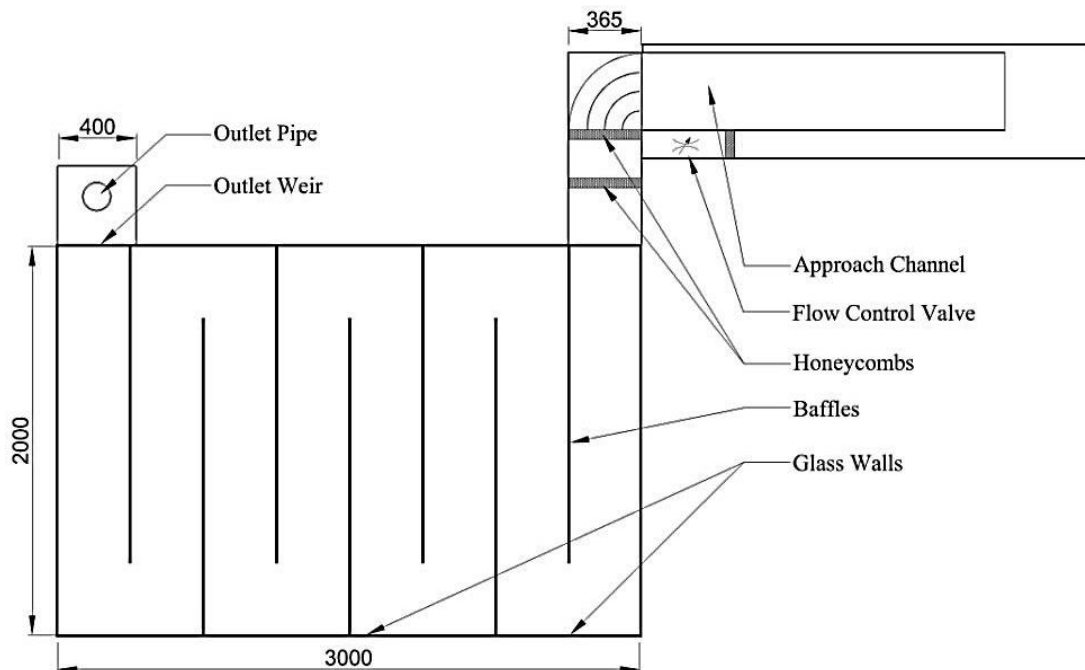


Figure 3.3 Plan View of CT-1 and main dimensions

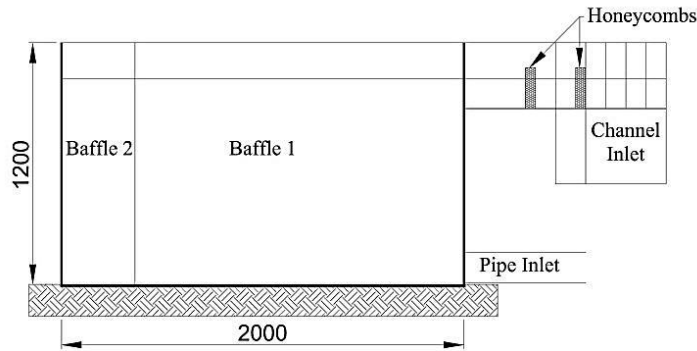


Figure 3.4 Cross-Section of CT-1 halfway through the 1st Compartment

The channel inlet consists of a deep section, a 90° bend and a shallower channel of width 0.365m (W_c) and depth 0.30m (H_I) prior to the CT-1 entrance as shown in Figures 3.2 and 3.3. The end of the pipe from ST-1 or ST-2, depending on the experiment type, is submerged in the deep end of the channel. The flow follows a pattern through honeycomb devices aiming to create uniform flow conditions upon entry to CT-1. In line with the centre of the shallow approach channel there is a plastic inlet pipe as indicated in the cross section of Figure 3.4. A tracer injection mechanism was incorporated by Rauen (2005) that consists of a diffuser, a control valve with a connection for a syringe and three injection needles placed around the 152 mm internal diameter pipe.

The outlet section consists of a weir that can be altered depending on the desired water level. The water downstream of the weir drops into a steel box where the 140 mm diameter return pipe to ST-1 is connected. An additional drainage pipe in the bottom of the tank also leads to ST-1 which is used for the replacement of water in case of high background concentration levels (>10 ppb) or when the model is not operated frequently.

An 8 compartment baffle configuration was adopted for the experimental campaign of hydrodynamics and solute transport. This setup, which can be seen in Figure 3.3, is a characteristic example of a serpentine CT design. The tank is divided into 8 compartments of equal width, by positioning 7 smooth baffles made out of plywood with dimensions 0.12×1.63×1.20 m and an in-between distance of W_c (= 0.365 m).

Two separate experiments were carried out: (a) Velocity and turbulence measurements to study the hydrodynamics and (b) Tracer experiments observing the transport of a

conservative scalar through the tank. The flow rate produced during physical model experimentation by the centrifugal pumps was $Q = 4.72$ l/s using the approach channel as an inlet and was closely monitored for its consistency through the flowmeter. In accordance with the dimensions of CT-1 and the volumetric flow rate, the theoretical residence time $T=V/Q$ was $T = 1265$ s. Based on Q , the water level (H_t) was measured at 1.02 m, while the bulk velocity (U_b) was 12.5mm/s. The average Reynolds number (Re), according to the hydraulic radius of the compartment and U_b , was $Re \approx 6750$. The sampling points for each of the experiments are illustrated in Figure 3.5.

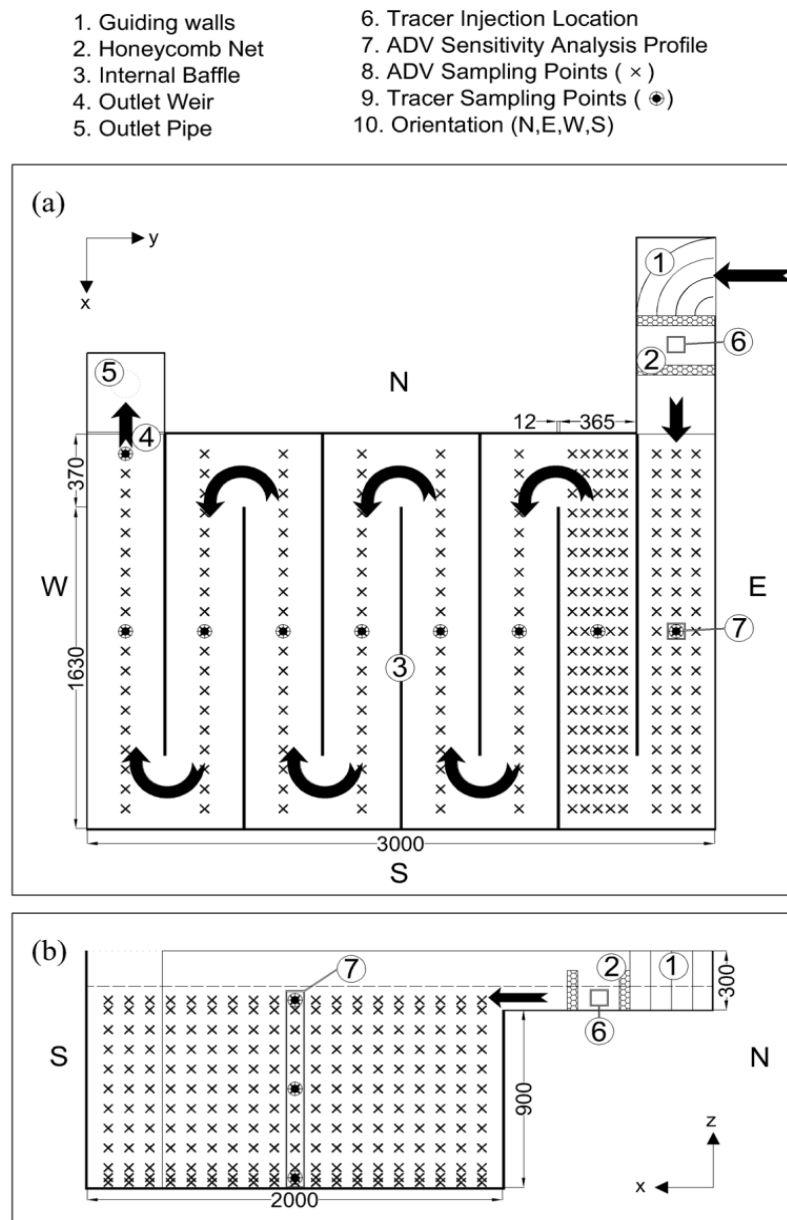


Figure 3.5 (a) Schematic view of laboratory model tank configuration including vectors indicating main streamwise flow direction ; (b) channel inlet and compartment 1 cross-section (dimensions in mm). Experimental data sampling points are illustrated in both sketches.

Different baffling arrangements were investigated previously as part of a study examining the hydraulic efficiency improvement potential. Configuration CT-1 was briefly examined using two inlet designs (channel and pipe) and another four distinct baffling arrangements (Figure 3.6) were considered, taking advantage of the physical model versatility. The experimental data comprises of tracer RTD curves at the outlet of the tank for each configuration and indicative ADV measurements for the characterization of the flow in each case.

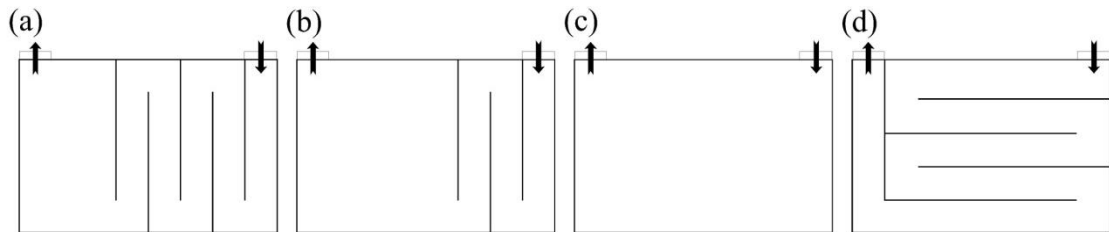


Figure 3.6 Baffling Configurations examined in previous studies (adopted from Rauen, 2005): (a) MS1, (b) MS2, (c) MS3 and (d) CT-O.

3.3 ACOUSTIC DOPPLER VELOCIMETRY

Velocity and turbulence measurements are essential for laboratory- and field-scale research for the understanding of hydrodynamics subject to various geometries and/or under different flow conditions. Common approaches include Laser Doppler Anemometry (LDA), Particle Image Velocimetry (PIV), Hot Wire Anemometry and Acoustic Doppler Velocimetry (Garcia et al., 2005). For the geometry and size of CT-1, the application of ADV is one of the techniques suitable for the acquisition of accurate velocity quantities and the capture of turbulence statistics.

In terms of its performance, the temporal and spatial resolution is inferior compared to the LDA method, but the accuracy of ADV measurements is comparable and within close agreement to the corresponding LDA ones (Lohrmann et al., 1994). Some of the advantages over LDA include greater operational simplicity and versatility at lower cost (Garcia et al., 2005). Further comparisons with LDA and other methods have been discussed and reported by additional studies (Kraus et al., 1994; Finelli et al., 1999; Voulgaris and Trowbridge, 1998; Lane et al., 1998) suggesting an encouraging performance of the ADV approach. For example, Lohrmann et al. (1994) managed to characterise turbulent velocity fluctuations at frequencies of up to the maximum sampling rate and velocities of as low magnitude as 0.4 mm/s. Lane et al. (1998)

highlighted some positive aspects of ADVs, i.e. measurement of all three velocity dimensions simultaneously and sampling remotely from the sensor with minimal intrusion to flow conditions.

However, there are speculations over the underestimation of velocity components for readings in close proximity to wall or bed boundaries (Voulgaris and Trowbridge, 1998; Finelli et al., 1999). The exact distance threshold where such inaccuracies take effect has not yet been defined, but caution is advised for readings in the region within 45 mm off solid boundaries (Chanson, 2008).

As mentioned in the literature review, hydrodynamic measurements in CTs have been limited to the LDA experiment of Teixeira (1993) and the ADV results of Rauen (2005). This section will be describing operational and processing aspects of the Nortek ADV probe utilised to investigate flow hydrodynamics in the CT-1 configuration.

3.3.1 ADV Principle of Operation

The sampling location for the standard down-looking Nortek ADV probe (Serial Number N0093) is offset approximately 5 cm away from the transmitter and has a cylindrical volume of 6 mm diameter and 9 mm height (Nortek-AS, ADV Operation Manual, 1997). Care must be taken on the orientation and tilt angle of the ADV during experimentation, as the velocity data is transformed into a Cartesian system of coordinates based on the orientation of the receivers. Depending on the configuration, a trigonometric transformation may be required during post-processing and this could lead to velocity resolution errors if not taken into consideration. Ideally the ADV positioning should be decided *a-priori*, to ensure the consistency of the coordinate system at all sampling points.

The ADV probe emits acoustic pulses via its central beam at a pre-defined frequency, which propagate through the water and are reflected by suspended matter in the sampling volume. The echo is in turn monitored by the receiver beams where the Doppler shift is measured, as shown in Figure 3.7. Meanwhile, the probe itself is connected to a laboratory PC with dedicated software (adv.exe) configuring and controlling the operation.

In accordance with the frequency shift in each axis, the corresponding velocity component is calculated. However, the ADV signal obtained by receivers incorporates the combined effects of turbulent velocity fluctuations, Doppler noise, signal aliasing, turbulent shear and other disturbances (Chanson, 2008). Consequently, raw ADV data of turbulent velocities without any post-processing should never be trusted as they can be severely misleading. Therefore, the output has been designed to include additional parameters which can be associated with the quality of the measurements, i.e. the signal strength, the Signal-to-Noise Ratio (*SNR*) and correlation percentage (*COR*). These can be used to neutralize disturbances and evaluate the measurement validity (Wahl, 2000; Nikora and Goring, 1998) following a post-processing procedure which can be optimized through appropriate software.

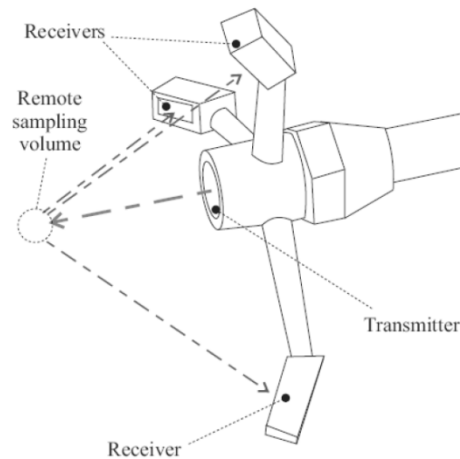


Figure 3.7 Representation of a 3-receiver ADV probe, its sampling volume and acoustic pulses (adopted from Chanson, 2008)

3.3.2 Initialization and Data Acquisition

An ADV data acquisition sensor does not require re-calibration, because it is initially performed by the manufacturer, and it remains robust as long as the acoustic receivers are not damaged (Nortek-AS). The working order of the equipment can be periodically verified using diagnostic software (*advcheck.exe*). This feature enables the inspection of the measurement region with respect to signal amplitudes sampled by each of the three probe receivers. Amplitude peaks among the 3 beams should ideally coincide or be within a certain range, particularly in the region of pulse transmission, sampling volume and boundary locations. Initially, using these preliminary tests, it was found that the amplitude varied substantially between the beams, but it was later deduced that deviations from the standard were the result of a faulty PC monitor which somehow

interfered with the signal. Once the monitor was replaced, no anomalies were encountered in subsequent tests.

The configuration of the probe had to be reviewed depending on the conditions expected at the sampling volume and was conducted through the ADV software (adv.exe). Firstly, the instrument maximum sampling rate (*SR*) of 25 Hz was selected as high frequencies are desirable for the characterization of turbulence (Lohrmann et al., 1994). Parameters such as temperature and salinity were defined as 20 °C and 0 ppt respectively, in agreement with the system water characteristics. Based on these, the software calculated the speed of sound as 1482 m/s for consideration during post-processing. A velocity range value of ± 10 cm/s was prescribed for compartments 1 and 2 due to the high velocities and unsteadiness expected by the inlet configuration. For compartments 3 onwards the range was reduced to ± 3 cm/s.

In terms of positioning inside the tank, the ADV system was attached to a movable rack with millimetre scales, aiding manual displacements between sampling points. The sensor was orientated accordingly to ensure the collapse between the coordinate system of the velocity output and the axes, defined in Figure 3.5.

During experimentation, the instantaneous readings were transferred automatically to the laboratory PC and were simultaneously exported to the output file (*.adv). This information included velocity fluctuations in the x, y and z directions, *SNR* and *COR* values in every receiver. Readings could be monitored with respect to time during data acquisition and provided a preliminary quality indication based on the *SNR* and *COR* values displayed.

By definition, *SNR* represents the strength of the received echo sampled from the probe which is influenced by the concentration of suspended scatters in the flow. In line with this principle, a high concentration of particles in the sampling volume enhances the signal strength and reduces the extent of background noise. In contrast, a low *SNR* is associated with noisy data, with high uncertainty, even after post-processing. To counteract the occurrence of low *SNR*, frequent addition of seeding material into the system is recommended as it increases the concentration of suspended scatters. A silicate powder of neutrally buoyant hollow spheres of 10 μm diameter (Spheri-
cel-

110P8) was introduced at regular intervals of typically about an hour, as a seeding material, when the average *SNR* during experimentation dropped below 10 – 20 db.

The correlation percentage (*COR*) is considered an indicator of measurement quality, calculated from the signals that the sensor receives. A high *COR* suggests low noise and implies reliable velocity measurements. This was highlighted during the experiments, as the *SNR* exceeding 15-20 db when introducing seeding material was accompanied with a distinct increase of *COR* which converged to the maximum (100%). On the other hand, factors such as extremely turbulent regimes can lead to signal decorrelation that would invariably be detrimental to *COR*. Nonetheless, throughout the ADV measurements, and with the aid of frequent seeding material injections, the average *COR* was kept within 75-100%. This range was deemed sufficient for the purposes of this study as a minimum *COR* of 70% is recommended for turbulence statistics, and a 40% for mean velocities (Martin et al., 2002).

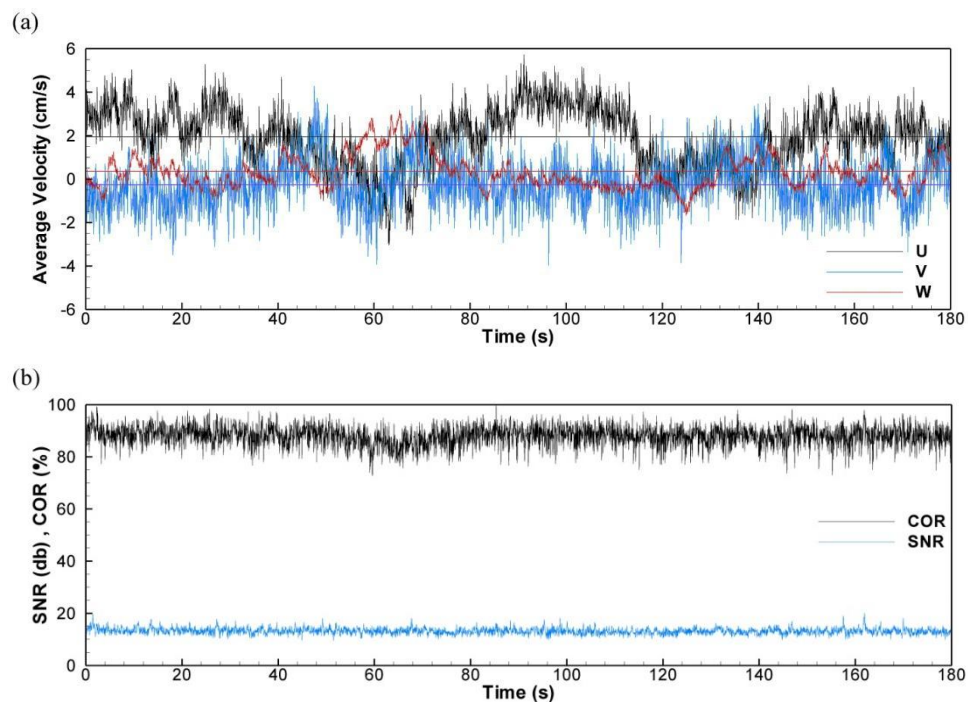


Figure 3.8 Unfiltered ADV data series obtained during data acquisition at a sampling point in compartment 1. (a) Horizontal (U), Transverse (V) and Vertical (W) velocity fluctuations. The mean value of each velocity is indicated by the straight line; (b) Signal-to-Noise Ratio and (SNR) average correlation percentage (COR).

3.3.3 Post Processing

According to the manufacturer, an accuracy of $\pm 1\%$ is expected following post-processing for measurements, if the data series is averaged over a sufficient amount of time to ensure the effects of noise are balanced out. Therefore all ADV output was

imported to suitable software (WinADV, version 2.029) for filtering and the calculation of velocity and turbulence statistics. The software is a Windows-based viewing and post-processing utility of ADV files, developed in the US Bureau of Reclamation's Water Resources Research laboratory (Wahl, 2000).

For the steady flow of CT-1, the first part of signal analysis was the removal of samples with average *COR* and *SNR* less than 70% and 5-15 db respectively or obvious communication errors. The data series was then subjected to a spike detection algorithm developed by Goring and Nikora (2002) which was integrated in the processing options of WinADV. Every sampling point data series was subsequently processed to produce summary statistics that were automatically exported either to spreadsheets (MS-Excel) for further analysis or to flow visualization software (Tecplot 10).

The statistics calculated, contained average velocities, Root-Mean-Squared (RMS) turbulence levels, covariance, skewness and kurtosis of the velocity data series (Wahl, 2000). As an example, assume that the data series of Figure 3.8 was imported to WinADV. Sampling took place over 180 s with a frequency of 25 Hz which means that the series consists of 4500 points. Assume that following the filtering stage, N_m data points (typically 90-99% of the unprocessed series) remain to compute the statistics. If v is the instantaneous velocity measured in the x direction, then the mean horizontal velocity (U) was calculated as:

$$U = \frac{\sum_{n=1}^{N_m} v}{N_m} \quad (3.1)$$

The horizontal RMS of turbulence velocity fluctuations $\overline{u'}$ was given by:

$$\overline{u'} = \sqrt{\frac{\sum_{n=1}^{N_m} v^2 - \left(\sum_{n=1}^{N_m} v\right)^2 / N_m}{N_m - 1}} \quad (3.2)$$

which could in turn be used to either calculate the turbulence intensity in one direction (e.g. $I_x = |u'/U|$) or the overall Turbulent Kinetic Energy (k) through

$$k = \frac{1}{2} \left((\overline{u'})^2 + (\overline{v'})^2 + (\overline{w'})^2 \right) \quad (3.3)$$

where $\overline{v'}$ and $\overline{w'}$ is the RMS turbulence in the y and z directions respectively. The covariance between velocities was of interest for the analysis of Reynolds stresses. For example, between U and V components, the covariance can be estimated as:

$$\overline{u'v'} = \frac{\sum_{n=1}^{N_m} uv}{N_m} - \frac{\sum_{n=1}^{N_m} v \sum_{n=1}^{N_m} v}{N_m(N_m-1)} \quad (3.4)$$

where v is the instantaneous velocity measured in the y direction (Wahl, 2000). The investigation of other statistics (skewness, kurtosis) was beyond the scope of the experimentation but information with regards to their significance and calculation can be found in Wahl (2000).

3.3.4 Sensitivity Analysis

Vertical profiles were examined for a central location in compartment 1, indicated in Figure 3.5, with each data point repeatedly measured using multiple sampling intervals. These profiles were part of a sensitivity analysis to identify the optimal time for reliable hydrodynamic result acquisition. The durations tested in the analysis were 1, 2, 3 and 5 minutes respectively. Focus was given on both velocity and turbulence statistics while accuracy was quantified by comparing RMS values of velocity and turbulence as shown in Figure 3.9.

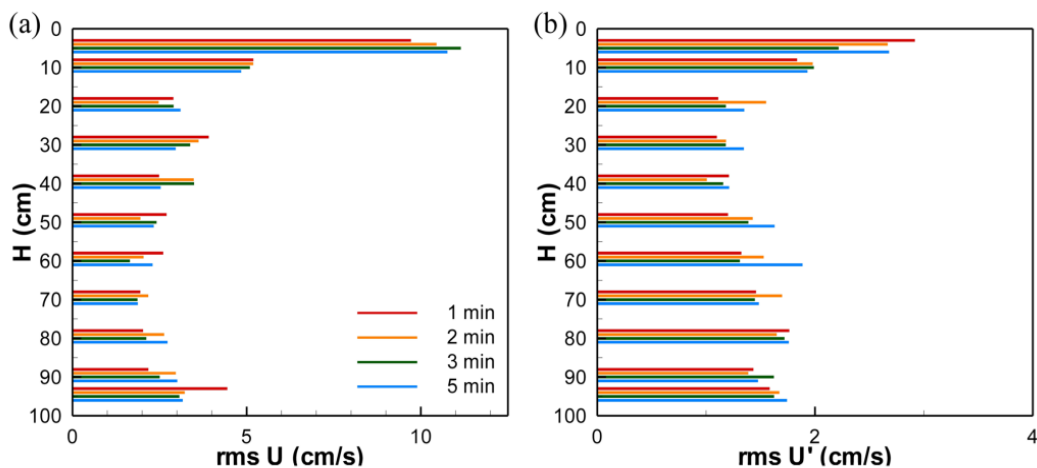


Figure 3.9 Root Mean Squared profiles of: (a) Mean (U), and (b) Turbulent (u') Horizontal Velocities

Figure 3.9(a) illustrates the processed results with respect to the horizontal velocity component U . By calculating the percentile error against the 5 min data points, the 3 min performed best with an average error of 8%, followed by the 2 min which had an error of 11%, and lastly the 1 min with approximately 20%. A similar pattern is

observed for the RMS turbulence in Figure 3.9(b). A large fraction of the deviations is attributed to mean velocities at mid-depth, which are part of a slow flow region. Even so, the measurements for 3 and 5 min were in close agreement and thus, a sampling duration of 3 min was considered sufficient. It should be noted that this approach was more conservative than that of Rauen (2005) where a sampling interval of 2 min was chosen.

The sensitivity analysis of covariance was inconclusive, indicating no correlation between the different sampling duration profiles. Perhaps the characterization of Reynolds stresses would benefit from a combination of longer monitoring (>10 min), greater SNR levels (>20 db) or an ADV probe with a higher sampling frequency to neutralize the impact of background noise and other disturbances. However, such analyses were beyond the scope of this study, but could be examined in further detail through additional hydrodynamic measurements at a later stage.

The ADV sampling campaign (≈ 3400 measurements) formed a database which consisted of mean velocity, turbulence intensity and TKE parameters for every compartment of the CT-1 configuration. These measurements were crucial for the understanding of CT flow hydrodynamics discussed in Chapter 5 and the validation of numerical simulations investigated in Chapter 6.

3.4 TRACER EXPERIMENTATION

As shown in Chapter 2, dye tracing has been frequently reported in research and performance assessments of CT units. Tracer injection techniques can be used to characterise the solute transport patterns within a water body between two points, i.e. the injection and the monitoring location. Fluorescent dyes especially, can be easily detectable by instruments known as Fluorometers, which are calibrated to associate fluorescence intensity with the actual tracer concentration. The instrument operation involves a photomultiplier which measures the amount of light emitted by the analysed sample at an emission wavelength, following an excitation by an internal light source (Turner Designs, Digital Fluorometer AU Manual, 1998).

In the study of Smart and Laidlaw (1977) several fluorescent dyes were compared with regards to their suitability as tracers under a range of conditions of temperature, pH and salinity. These included Amino G acid, Photine CU, Fluorescein, Lissamine FF,

Pyranine, Rhodamine B, Rhodamine WT and Sulpho-rhodamine B. Rhodamine WT, used for all CT-1 tracer injections, was one of three recommended dyes for water tracing. As an orange dye, there is lower background fluorescence at the Rhodamine colour wave band, permitting the acquisition of higher sensitivities. Nevertheless, a background fluorescence level can always be detected in the system water due to natural fluorescence or suspended sediments in the flow. This leads to a background concentration which should be accounted for during post-processing so that it does not distort the tracer analysis conclusions. The impact of pH on Rhodamine is negligible for the range of 5.0 - 9.0 (Smart and Laidlaw, 1977); for the system water of CT-1 those limits were never exceeded. Water temperature variations do not arise during the CT-1 system operation, so their contribution on tracer results were classed as insignificant as well. The effect of salinity applies only when tracers are used in estuarine and marine environments, or in blackish groundwater, which was not the case within the laboratory setting.

Fluorometer equipment consisted of three sets of Cyclops-7 submersible sensors and Databank Handheld Dataloggers all manufactured by Turner Designs. Cyclops-7 has the capability to detect Rhodamine concentrations within a dynamic range of 0.01 – 1000 parts per billion (ppb). Dataloggers simultaneously act as power supply and data storage for the fluorescence sensors and can store up to 10000 readings with a minimum time interval of 1 sec.

3.4.1 Tracer Dilutions and Fluorometer Calibration

Rhodamine WT is supplied as a liquid solution of 20% active ingredient (AI). Using a series of dilutions, a variety of tracer solutions can be produced, either for the fluorometer calibration or the tracer injections. As an example, the preparation procedure of a 100 ppb Rhodamine WT solution is as follows:

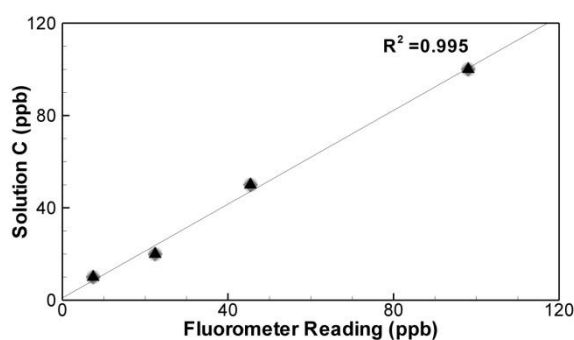
- 1) 1 ml of Rhodamine WT dye is diluted into a 100 ml volumetric flask and then filled to the mark with distilled water. Mixing results in 10ml/L but since only 20% of that is the fluorescent tracer (AI) it yields 2 ml/L (ppt). This is solution #1.
- 2) 1 ml of #1 is diluted into a 100 ml volumetric flask as before with distilled water. Complete mixing of the container produces a 20 ppm solution (#2).
- 3) 5 ml of #2 are diluted into a 1L flask with system water to the mark. The outcome is a 100 ppb Rhodamine WT solution (#3).

Similar steps were taken for the preparations of 10, 20, and 50 ppb solutions. The preparation method for a 500 ppm tracer solution consists of:

- 1) 5 ml of 20% AI dye diluted into a 100 ml volumetric flask to the mark with distilled water resulting into a 10 ppt AI solution (#4)
- 2) 100 ml of #4 diluted into a 2L flask with system water to the mark. Thorough mixing leads to a 500ppm Rhodamine WT solution (#5).

50 ml of #5 were used for each injection which translates to 25mg Rhodamine WT mass for each experiment. In addition, a 4 ppt solution was also used for initial “black box” type experiments to confirm that no deviations arise between the produced RTD curves and results when altering injection concentration levels. Dye solutions were preserved in amber glass bottle containers away from sunlight and in room temperature conditions.

The calibration process involves setting the blank and standard levels of concentration encountered during the experiment. The instruments were calibrated using 2 solutions; (a) blank system water with no tracer concentration (0 ppb) and (b) a 100 ppb tracer solution which was manufactured internally (Solution #3). Other solutions of 10, 20, 50 and 100 ppb were prepared to reaffirm the working order of the fluorometers by producing the calibration curve of Figure 3.10, which plots the correlation between the fluorometer readings and the actual concentration values. The linear regression curve that best fits the data was later used to correct the fluorescence readings during the tracer analysis.



C (ppb)	Fluorometer Reading (ppb)		
	1	2	3
10	7.41	8.00	7.89
20	22.4	22.33	22.39
50	45.43	45.15	45.41
100	98.05	98.75	98.86

Figure 3.10 Calibration Curve and Readings for known concentrations for each of the 3 fluorometers.

3.4.2 Tracer Data Analysis Procedure

Tracer injections were performed in the centre of the volume located between 2 honeycomb devices in the approach channel, avoiding disturbance of inflow conditions

(Figure 3.5). The 50 ml tracer solution was introduced to the system through a syringe. The injection duration had to be instantaneous and therefore occurred as quickly as possible, typically lasting below 10 s. The 10 s interval is less than the $1/50^{\text{th}}$ T threshold recommended by Thirumurthi (1969) for gulp injection experiments. The fluorometers were affixed accordingly at the gauge points investigated, before experimentation using the same movable rack described for the ADV readings. Readings were stored for at least 500 seconds prior to any injection and continued until the storage limit, of the databank was reached (10000 readings).

Typically, at any time, there would be 50 m^3 of water flowing within the hydraulic circuit; approximately 6 m^3 in CT-1, 4 m^3 in ST-1 and 40 m^3 in ST-2. The standard injection of 25mg Rhodamine WT would theoretically increase the overall concentration by approximately 0.5 ppb, as it remains in the system unless the water is replaced. Therefore, the water should mix for a sufficient amount of time so that the background concentration becomes uniform across the whole hydraulic circuit, before a subsequent experiment. However, once it exceeded a certain level (≈ 10 ppb), following a series of tracer experiments, the system was drained and replaced with blank water (≈ 0 ppb). The system would be in operation for at least 40 minutes prior to an injection in order to converge to steady state flow conditions. During this time, background concentration, average discharge, water level and injection time were monitored so that they could be accounted for in the post-processing of the tracer samples.

The readings of a “black-box” type experiment are utilized herein for the understanding of the post-processing analysis. 50ml of a 4ppt tracer solution were injected in the inlet and the concentration was gauged at the outlet. Once the Databank was full, readings from the fluorometer were transferred to the laboratory computer and an output file was compiled. The format of the output was: record number, time and sensor reading. The concentration-time diagram, otherwise referred to as C_{pulse} curve (Levenspiel,1999), illustrated in Figure 3.11(a), displays the fluorometer readings as exported from the Datalogger with respect to the sampling duration.

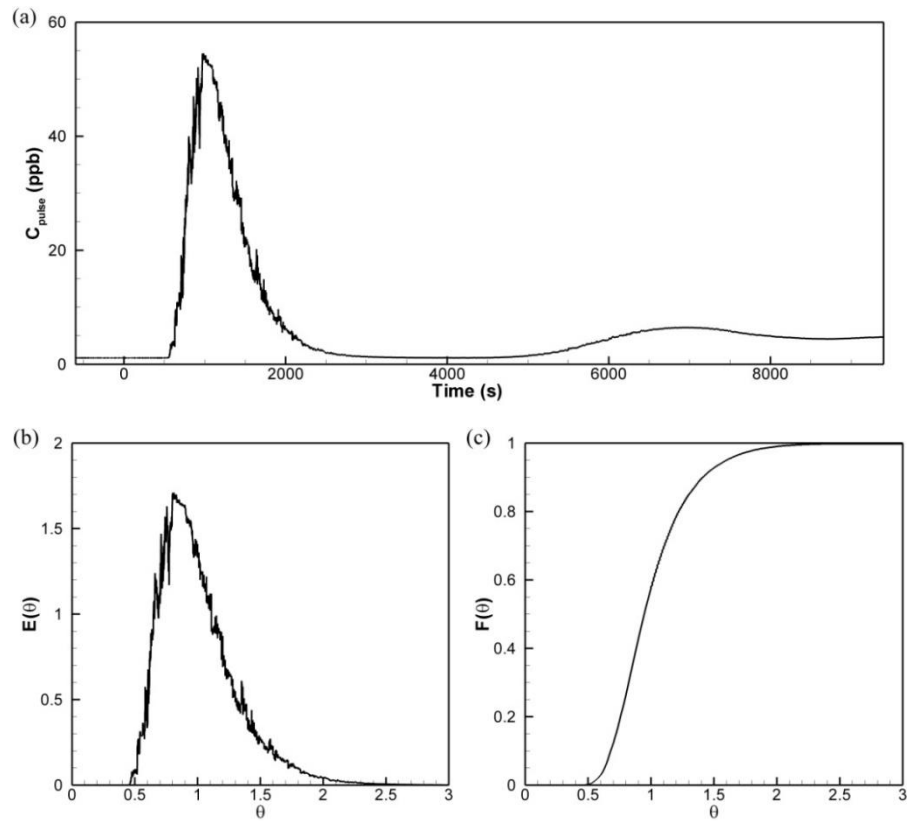


Figure 3.11 (a) C_{pulse} curve from a black box experiment with an injection concentration of 4ppt at the inlet. Corresponding curves after the analysis: (b) Residence Time Distribution (RTD) Curve and (c) Flow – Through (FTC) Curve

The standard procedure was to filter initially the background concentration and discount results before the tracer injection. Values following the reappearance of tracer in the sampling point are also removed to not interfere with calculations. For the curve in Figure 3.11a, background concentration was at 1.12 ppb, injection time was 600 sec (in Figure 3.11a it is indicated as $t=0$ s) and the reappearance of tracer at the gauge point occurs after approximately 4600 sec. This means that the RTD curve analysis is based on the data points between 600 & 4600 sec and the background concentration of 1.12 ppb should be subtracted from the concentration values.

The concept of the E curve, in other words residence time distribution with respect to time in seconds, can be acquired by simply changing the concentration scale so that the curve area is equal to unity (Levenspiel, 1999). In essence, readings must be divided by the area of the C_{pulse} curve as:

$$Area = \int_0^{\infty} C dt = \sum_i C_i \Delta t_i \quad (3.6)$$

$$E_i = \frac{C_i}{\sum_i C_i \Delta t_i} \quad (3.7)$$

Standard practise recommends time to be measured in terms of the theoretical retention time $\theta = t/T$. This normalization process enables the comparison of different CTs, or similar CTs operated under different flow rates, and aids in the interpretation of any deviations. The normalized RTD function, $E(\theta)$, can be described by:

$$E_{\theta} = T \times E_i = \frac{C_{pulse}}{C_0} = \frac{C_{pulse}}{M/V} \quad (3.8)$$

Where M is the tracer mass injected and V is the tank volume. Throughout the experiment, mass conservation must be satisfied and any deviations encountered should be justified. The mass balance can be expressed through the recovery rate index (REC) expressed by equation (2.2). Tracer mass recovered and REC was calculated according to the C_{pulse} curve using the following formulas:

$$M_{rec} = Q \times \Delta t_i \times \sum_i C_i \quad (3.9)$$

$$REC = \frac{M_{rec}}{M} \quad (3.10)$$

Ideally the REC value should be 1. Discrepancies from this value must be kept to a minimum for the curves to be acceptable. Therefore, an experiment was considered valid only when $0.85 < REC < 1.15$ as recommended by Stamou and Adams (1988). In cases when the value was not within that range, results were discarded and the experiment was repeated. The REC value was then used as a correction factor for the RTD as shown by equation (2.3).

Table 3.1 REC values for Outlet Tracer Experiments

Experiment Number	REC
1	0.967
2	0.997
3	0.958
4	1.103
5	1.046
6	0.929

For the black-box experiment example, the corrected E_{θ} curve produced is given in Figure 3.11(b), where the difference between the C_{pulse} curve and the final RTD curve is illustrated. The REC value of the particular experiment was 0.967 which is within the limits recommended by Stamou and Adams (1988).

The information carried by E_θ enables the plot of the corresponding Flow-Through Curve (FTC). FTCs illustrate the extent of tracer dye that has gone through a gauge point at any given moment during the experiment in a scale of 0 to 1:

$$F_\theta = \int_0^\theta E_\theta d\theta \quad (3.11)$$

The curve of Figure 3.11(b) is the result of the integration of E_θ to produce the corresponding FTC. The reproducibility of the normalized curves is examined in Figure 3.12.

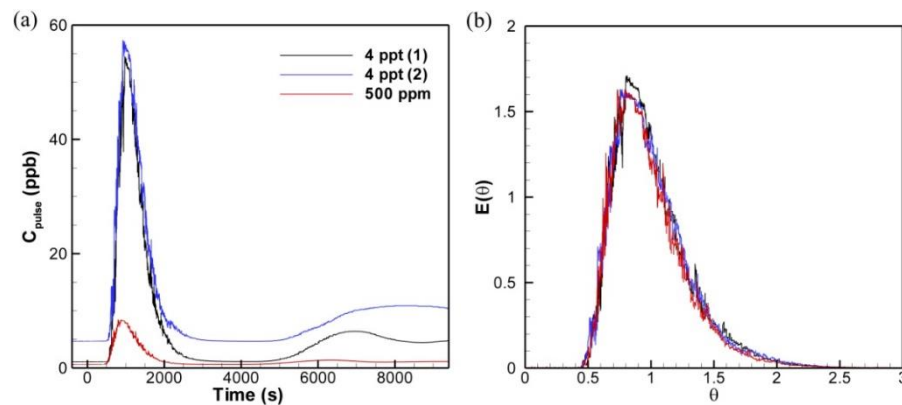


Figure 3.12 Reproducibility of RTD curves: (a) C_{pulse} curves for 3 experiments at the outlet and (b) corresponding normalized RTD curves.

Subsequent experiments were conducted at the outlet using 4 ppt and 500 ppm tracer injection concentrations respectively examining the shape of the normalized RTD curves. In both cases, even though the C_{pulse} curves (Figure 3.12a) may differ significantly, the corresponding E_θ plots (Figure 3.12b) essentially collapse. Any tracer experiments that followed adopted a Rhodamine WT injection concentration of 500 ppm as it appears sufficient to be detected by the fluorometer even at the outlet of CT-1. It should be acknowledged that tracer experiments were repeated at least once to confirm the consistency of the normalised curves.

3.4.3 Hydraulic Efficiency Indicators

A qualitative observation of E_θ and F_θ curves can provide an insight to the conditions within CTs. However, the interpretation of the shape of a curve is not always straightforward as argued by Levenspiel (1999). As discussed in Chapter 2, HEIs associated with the description of certain flow conditions within hydraulic systems can be extracted to further understand or quantify mixing processes and the short-circuiting

occurrence. Table 3.2 depicts significant time landmarks of a tracer experiment necessary for the estimation of HEIs.

Table 3.2 Definition of time-specific parameters

Parameter	Description
t_i	Initial tracer appearance time
t_{10}	Time to passage of 10% tracer mass
t_{50}	Time to passage of 50% tracer mass
t_{90}	Time to passage of 90% tracer mass
t_p	Peak concentration time
t_g	Mean residence time

t_i , t_{10} , t_{50} and t_{90} , can be directly drawn from the FTC curve with respect to time. t_p corresponds to the time when the maximum concentration is encountered in the RTD. t_g can be calculated as:

$$t_g = \frac{\sum_i t_i C_i}{\sum_i C_i} \quad (3.12)$$

The HEIs of Table 3.3 are either normalised versions of the variables in Table 3.1 or supplementary short-circuiting and mixing indexes frequently used to evaluate the hydraulic performance of CTs. More information on the adequacy of individual HEIs is discussed in the studies of Teixeira and Siqueira (2008) and Marske and Boyle (1973).

Table 3.3 Hydraulic Efficiency Indicator Definition

HEI	Type	Definition
t_{10}/T	Short-circuiting	Normalised t_{10}
t_i/T	Short-circuiting	Index of Short Circuiting
t_p/T	Short-circuiting	Index of Modal Detention Time
t_{50}/T	Short-circuiting	Index of Mean Detention Time
t_g/T	Short-circuiting	Index of Average Detention Time
t_{90}/T	Mixing Processes	Normalized t_{90}
t_{90}/t_{10}	Mixing Processes	Morril Index (Mo)
σ^2	Mixing Processes	Dispersion Index
d	Mixing Processes	Dispersion Coefficient

Under an ideal scenario, all short-circuiting indicators indicated in Table 3.3 should converge to the value of 1.0. With regards to the mixing processes HEIs, t_{90}/T and Mo should converge to 1.0 while σ^2 and d to 0. The dispersion index σ^2 , introduced in Chapter 2, was defined as the ratio of the temporal RTD function variance σ_t^2 to the squared mean residence time (t_g^2) and can be estimated as

$$\sigma_t^2 = \left(\frac{\sum t^2 c}{\sum c} \right) - \left(\frac{\sum t c}{\sum c} \right)^2 \quad (3.14)$$

$$\sigma^2 = \frac{\sigma_t^2}{t_g^2} \quad (3.15)$$

σ^2 is a more thorough representation of the mixing phenomena in the flow, compared to other indicators since it is drawn from the whole RTD curve (Teixeira and Siquiera, 2008). In turn, the dispersion coefficient d can be calculated using σ^2 through equation (2.6).

3.5 CHAPTER SUMMARY

This chapter reports on the contact tank physical model (CT-1) design and methodology followed to study hydrodynamics and solute transport in CTs experimentally. The geometry and physical model operation details are presented in section 3.2 which provides an overview of the hydraulic circuit and the main features of the tank. The CT design analysed for this study adopts an 8 compartment baffling configuration with an open channel inlet and a sharp-crested weir as an outlet. The experimental campaign comprised of approximately 3400 ADV measurements and 25 tracer gauging stations.

Section 3.3 details the specifications of the Nortek ADV probe, highlighting the capabilities of the instrument but also taking into consideration any uncertainties associated with the sampling technique. The ADV data post-processing procedure was conducted using freely available software, WinADV, and was further examined using MS Excel and Tecplot 10. Production of turbulence and velocity information is also explained indicating the main equations to produce statistics from the samples. Lastly, results are presented from a sensitivity analysis verifying the sufficiency of a 3 min sampling duration for the desired hydrodynamic quantities.

Tracer experiment materials and methodology are expanded in section 3.5. The laboratory equipment consisted of three Turner Designs Cyclops-7 fluorometers and the use of Rhodamine WT liquid as a tracer. The experiments involved instantaneous injections of 25mg 500 ppm tracer solutions, and gauging at various locations inside the tank. The fluorometer output was analysed to produce Residence Time Distribution (RTD) curves and Hydraulic Efficiency Indicators (HEIs). A “black-box” experiment was used as an example in this study to describe the experiment process and aspects that were taken into account when producing the results. The methodology described herein was used to produce the results discussed in Chapter 5 and the validation of the numerical modelling simulations in Chapter 6.

CHAPTER 4

NUMERICAL MODELLING GOVERNING EQUATIONS AND METHODS

4.1 INTRODUCTION

Computational modelling of flow and solute transport processes in CTs constitutes a major aspect of this study and the associated numerical and theoretical framework is presented within this Chapter. Initially, section 4.2 describes the main governing equations and assumptions in the solution of the Navier-Stokes Equations for hydrodynamics, solute transport equations and accompanied with other theoretical considerations. In section 4.3 details of the algorithms and techniques implemented for the numerical solutions are provided including an overview of the steps taken to perform CFD simulations.

4.2 NUMERICAL MODELLING EQUATIONS

This section provides details of the theoretical background and the governing equations that dictate numerical modelling of flow and transport in CT geometries examined in Chapters 6 and 7.

4.2.1 Hydrodynamic modelling

The fundamental principle of any CFD model is the conservation of energy, mass and momentum, i.e. the conservation laws of physics. In fluid flow, these laws are represented through the Navier-Stokes (N-S) equations which in their original form encompass all known internal and external effects on the motion of a fluid. However, depending on the specifications of each particular problem, certain simplifications are normally made in order to allow the usage of CFD methods on practical applications.

The most demanding approach is the Direct Numerical Simulation (DNS) as it attempts to completely resolve the equations taking into consideration all influential scales of fluid motion. For fully developed flows this requires excessively high resolution of grid size and time step which becomes impractical for engineering applications. In 1963, Smagorinsky proposed the Large-Eddy Simulation method. LES simulations apply a spatial filtering procedure and explicitly simulate large scale eddies, accountable for the majority of momentum transport and turbulent diffusion (Ferziger and Peric, 1996), while the smaller-scales which are statistically more universal are estimated through approximate models known as Sub Grid Scale (SGS) models. Application of LES on CT modelling can be found in Kim (2011) for a small scale ozone contactor model

using a high performance supercomputer. With on-going advances of computer processing capabilities, which constantly reduce the computational time, LES could be more widely tested for engineering purposes in the near future. However, the most practical method to presently calculate turbulent flow is the time averaging of the N-S equations to yield the Reynolds Averaged N-S (RANS) equations. This suggests a statistical method where the instantaneous values of velocity and pressure are separated into mean and fluctuating components. Due to the non-linearity of the N-S equations, averaging leads to unknown correlations between scalar quantities known as Reynolds Stresses (Rodi, 1993). The determination of these parameters is achieved through the application of approximate models, i.e. turbulence modelling. RANS limitations include the inability of capturing instantaneous flow dynamics and the inadequacy to model anisotropic flows when an eddy-viscosity formulation is implemented. Nonetheless, the approach has been widely applied in the literature for CT problems due to the low computational cost but also its capability to produce accurate results when suitable turbulence models are adopted.

4.2.2 Governing Equations

The Reynolds averaged Navier-Stokes (RANS) equations for continuity and momentum conservation were used to describe the flow hydrodynamics within the geometries examined. Closure to the effects of turbulence was provided by implementing the standard k- ϵ model (Rodi, 1993) to compute the Reynolds Stresses. The SSIIM model (Olsen, 2011) was employed to perform the RANS simulations of hydrodynamics using a finite-volume approach on a structured non-orthogonal grid. The particular code has been successfully applied previously in the relevant studies of Kim (Kim, 2011; Kim et al., 2010) for similar flows and geometries. In order to reduce the computational load of the simulations, the flow field was assumed to be steady-state and incompressible. The influence of temperature was also beyond the context of this research.

The continuity equation of an incompressible fluid can be described in Cartesian notation form as:

$$\frac{\partial U_i}{\partial x_i} = 0 \tag{4.1}$$

Where U_i is the time averaged velocity vector and x_i is the Cartesian vector component with an index $i = 1, 2$ and 3 , as introduced in Chapter 2. According to the general continuity equation, the change of mass in a control volume is equal to the difference of the total mass which enters and leaves through the faces of the volume. For a steady flow as described by equation (4.1), the rate at which mass enters a control volume is equal to the rate at which mass exits the volume.

The second law is the transport of momentum, which for the purposes of this study can be transformed from equation (2.21) and be written as:

$$\frac{\partial U_i}{\partial t} + U_j \frac{\partial U_i}{\partial x_j} = -\frac{1}{\rho} \frac{\partial p}{\partial x_i} + \frac{\partial}{\partial x_i} \left(\nu \frac{\partial U_i}{\partial x_j} - \overline{u'_i u'_j} \right) \quad (4.2)$$

u' is the turbulent fluctuation of the corresponding velocity component, based on the Reynolds' theory, according to which the velocity, pressure and scalar quantities are differentiated into mean and fluctuating quantities (Rodi, 1993).

There are four terms presented in equation (4.2). The first term is the transient of the velocity. It represents the local acceleration of a fluid particle at a point with respect to time. However, in cases where a steady state hydrodynamic solution is required, the simulations are independent of the time parameter and therefore this term can be ignored. Once the simulation is converged, the steady state results can be exported and be used subsequently for time-dependent processes such as the transport of solutes under an assumption that their transport has a negligible impact on the flow field. This practise has been also reported in the literature (e.g. Rauen, 2005; Kim, 2011) for the comparison of flow and tracer transport in water treatment facilities under certain operational conditions. The second term represents the acceleration of a fluid particle along a flow pathline (in the x,y or z direction) with respect to distance, i.e. advective effect to the transport of momentum.

The third term describes the pressure gradient with respect to each direction. As argued by Patankar (1980), one of the main challenges for the estimation of a flow field is obtaining the pressure distribution across the computational domain. Due to the complex three-dimensionality of the flow and the vertical accelerations that occur in the CT under investigation, a hydrodynamic pressure distribution is expected. This issue was addressed in this study using the Semi-Implicit Method for Pressure Linked

Equations (SIMPLE) algorithm as described by Patankar and Spalding (1972). However, in the absence of significant three-dimensionality, a hydrostatic approach can reduce the computational effort of the simulations while still providing realistic approximations. This could be applied successfully in CT geometries where the flow is predominantly two- or one-dimensional. The fourth term of the momentum equation encompasses the effects of convection and diffusion (viscous term). It can be observed that this parameter is not only dependant on the fluid characteristics through the kinematic viscosity, but also on the turbulence stresses which highlights the requirement of the closure model.

The structure of the momentum equation (4.2) can be adopted for the description of other transport processes through a more generalized form, as given by Patankar (1980) for a scalar φ :

$$\frac{\partial \varphi}{\partial t} + U_i \frac{\partial \varphi}{\partial x_i} = \frac{\partial}{\partial x_i} \left(D \frac{\partial \varphi}{\partial x_i} \right) + S \quad (4.3)$$

where D is the diffusion coefficient and S is a source term. It comprises of transient, advective, diffusion and source terms respectively. Therefore, for the momentum formulation, the pressure gradient corresponds to the source term of S , and the effects of turbulence and diffusion are represented by the D coefficient.

In general, the transport processes which were involved in the simulation of hydrodynamics (and in extension solute transport as discussed in a later section) could be reduced to the form of equation (4.3) by appropriate modifications of the φ , D and S parameters. Typical examples for the hydrodynamic simulations include the transport of turbulent kinetic energy or energy dissipation rate associated with turbulence modelling.

4.2.2.1 Turbulence Modelling

The standard k - ϵ is one of the most widely applied two-equation turbulence models and has been tested against a wide range of conditions since its development by Launder and Spalding (1972) as also suggested by the frequency of its application in CT studies in Table 2.2.

According to the RANS theory, the instantaneous value of velocities U_i , pressure p and scalar quantities φ can be separated into average and turbulent components as indicated in equation (4.4) to (4.6)

$$U_i = \bar{U}_i + u_i' \quad (4.4)$$

$$p = \bar{p} + p' \quad (4.5)$$

$$\varphi = \bar{\varphi} + \varphi' \quad (4.6)$$

The correlations between fluctuating components either among velocities $\overline{u_i' u_j'}$ or between velocity and scalar quantities $\overline{u_i' \varphi'}$ constitute the unknown parameters occurring from the N-S averaging process. The Reynolds stress term $\overline{u_i' u_j'}$ can be approximated using the Boussinesq approximation (Rodi, 1993):

$$-\overline{u_i' u_j'} = \nu_t \left(\frac{\partial U_j}{\partial x_i} + \frac{\partial U_i}{\partial x_j} \right) + \frac{2}{3} k \delta_{ij} \quad (4.7)$$

where δ_{ij} is the Kronecker delta, k is the turbulent kinetic energy introduced in Chapter 3 and ν_t is the eddy viscosity coefficient. Eddy viscosity (or turbulence viscosity) is a parameter that is extensively used in RANS turbulence models. Unlike the molecular kinematic viscosity (ν), the eddy viscosity is not a fluid property but is directly related to the local state of turbulence and varies along the flow field. The whole eddy viscosity concept stems from an analogy between molecular and turbulent motions initiated by Boussinesq (1877) which led to the formulation of equation (4.7). ν_t can be evaluated as

$$\nu_t = C_\mu \frac{k}{\varepsilon} \quad (4.8)$$

where C_μ is a constant and ε is the turbulent energy dissipation rate. If P_k defines the production of k , and expressed as

$$P_k = \nu_t \frac{\partial U_j}{\partial x_i} \left(\frac{\partial U_j}{\partial x_i} + \frac{\partial U_i}{\partial x_j} \right) \quad (4.9)$$

then k and ε are modelled by the following differential equations:

$$\frac{\partial k}{\partial t} + U_j \frac{\partial k}{\partial x_j} = \frac{\partial}{\partial x_j} \left(\frac{\nu_t}{\sigma_k} \frac{\partial k}{\partial x_j} \right) + P_k - \varepsilon \quad (4.10)$$

$$\frac{\partial \varepsilon}{\partial t} + U_j \frac{\partial \varepsilon}{\partial x_j} = \frac{\partial}{\partial x_j} \left(\frac{\nu_t}{\sigma_\varepsilon} \frac{\partial \varepsilon}{\partial x_j} \right) + C_{\varepsilon 1} \frac{\varepsilon}{k} P_k + C_{\varepsilon 2} \frac{\varepsilon^2}{k} \quad (4.11)$$

The constant values of the k - ε turbulence model are (Rodi, 1993) $C_\mu = 0.09$, $C_{\varepsilon 1} = 1.44$, $C_{\varepsilon 2} = 1.92$, $\sigma_k = 1.0$, $\sigma_\varepsilon = 1.3$.

Equations (4.10) and (4.11) are structured according to the general transport equation of Patankar (1980), i.e. equation (4.3). They are interconnected as ε and k are each integrated in the k - and ε -equation as a part of the source terms. Both equations form the framework of the k - ε model and are solved iteratively until the k and ε field converges across the computational domain. During the simulation, the eddy viscosity ν_t is calculated for every iteration using equation (4.8) and is then inserted in the momentum equations' diffusive term. Equation (4.2) is transformed accordingly to represent the turbulent terms through the eddy viscosity formulation as

$$\frac{\partial U_i}{\partial t} + U_j \frac{\partial U_i}{\partial x_j} = -\frac{1}{\rho} \frac{\partial p}{\partial x_i} + \frac{\partial}{\partial x_i} \left[(\nu + \nu_t) \frac{\partial U_i}{\partial x_j} \right] \quad (4.12)$$

where kinematic and eddy viscosities are added together to yield the effective viscosity thereby assuming isotropic turbulence since it retains the same values for the x , y and z direction momentum equations.

4.2.2.2 Boundary Conditions

At the start of the hydrodynamic simulations, zero initial conditions are set, which implies that the variables U , V , W and P within the domain are set to zero, a practise adopted from Patankar (1980) and Roache (1998) while the k and ε parameters were established according to the inflow. In addition, the numerical model is subjected to the specification of appropriate conditions at cells adjacent to the domain boundaries. Within the scope of the current study, different boundary types were identified for the consideration of inlet, outlet, free-surface and solid wall effects. Focus is also given on the application of empirical wall-functions near solid surfaces, which are necessary for the accuracy of the k - ε turbulence model in certain regions of the domain. Appropriate treatment of these boundaries is crucial for the validity of numerical simulations and as such, the main details are explained in this section.

a) Dirichlet boundary

For the simplest boundary condition type, namely the Dirichlet boundary, variables are specified with a value on the boundary of the domain. This type is used for the inflow

boundary condition with the mean velocity over the entire inlet area of the flow field, and wall boundaries with no-slip conditions.

b) Neumann boundary

The Neumann condition involves a derivative of a solution to be taken on the domain boundary. This approach is used at outflow surfaces with zero gradient, which is the case for the numerical model of the CTs considered. At outlet sections the Neumann approach was prescribed for all variables, so that the respective gradient normal to the boundary was set to zero.

A combination of the Neumann and Dirichlet conditions is implemented for the variables depending on the boundary effects. At the inlet, a Dirichlet condition was set for velocity components, where a uniform horizontal velocity is assumed dependent on the flow rate Q as $U_{in}=Q/A_{in}$, where U_{in} is the inlet horizontal velocity component and A_{in} is the area covered by the inlet surface. On the other hand, transverse (V) and vertical (W) velocity components were considered negligible and equal to zero. For the pressure (p), a zero-gradient Neumann condition was assumed while the turbulence parameters (k , ε) were estimated based on U_{in} . For solid boundaries, the Neumann condition applied for p and ε , whereas the remaining variables were set to zero ($U = V = W = k = 0$).

c) Free-surface boundary

The free surface was modelled as a rigid, frictionless lid, so that the value of the mean vertical velocity was set to zero at the surface (Dirichlet), while the Neumann boundary condition was applied for the other hydrodynamic variables. Therefore, at the free surface these variables are calculated assuming:

$$\left. \frac{\partial U}{\partial z} \right|_{z=H} = \left. \frac{\partial V}{\partial z} \right|_{z=H} = \left. \frac{\partial P}{\partial z} \right|_{z=H} = \left. \frac{\partial k}{\partial z} \right|_{z=H} = \left. \frac{\partial \varepsilon}{\partial z} \right|_{z=H} = 0 \quad \text{and} \quad W = 0 \quad (4.13)$$

where H is the flow depth. This approach was considered sufficient as variations on the water surface of the laboratory model during experimentation were negligible across the whole geometry, once steady-state conditions were achieved.

d) Wall-function boundary

As argued by Versteeg and Malalasekera (1995), a significant advantage of the $k-\varepsilon$ model lies in the treatment of turbulence near wall boundaries. The use of empirical wall functions is implemented for cells adjacent to these regions, thus eliminating the need for a higher resolution grid for the viscous sub-layer that would substantially increase the computational time. These functions replace the source terms of the governing equations near the wall boundaries as described by Olsen (2011). The default wall law applied in the CFD model was developed by Schlichting (1979):

$$\frac{U}{U_*} = \frac{1}{\kappa} \ln \left(\frac{30 y^+}{k_s} \right) \quad (4.14)$$

$$U_* = \sqrt{gHS_f} \quad (4.15)$$

$$S_f = \frac{U^2 n^2}{H^{2/3}} \quad (4.16)$$

$$k_s = \left(\frac{26}{M} \right)^6 \quad (4.17)$$

where U_* is the shear velocity, κ is von Karman's constant with a value of 0.4, y^+ is the distance of the particular computational point from the wall and k_s is Nikuradse's surface roughness height. For the shear velocity calculation, S_f is the friction slope and g is the gravitational acceleration. For the roughness height estimation, the Stricklers number was used (M) which is equal to the inverse of the Mannings number n ($M=1/n$). For simulations of field scale CT flow n was assumed to be in the range of 0.012-0.020 which is an approximation influenced by the recommendations of Chow (1959). A value of $n = 0.012$ was adopted in previous studies for the simulation of the flow in the laboratory CT model. However, a different approach was prevalent for the CT-1 simulations, since a smooth wall law was imposed for near boundary cells of $y^+ < 30$. The following wall functions were applied (Olsen, 2011):

$$\frac{U}{U_*} = \frac{1}{\kappa} \ln \left(\frac{E U_* y^+}{k_s} \right) \quad \text{if} \quad \frac{E U_* y^+}{k_s} > 11 \quad (4.18)$$

$$\frac{U}{U_*} = \frac{E U_* y^+}{k_s} \quad \text{if} \quad \frac{E U_* y^+}{k_s} < 11$$

where E is empirically given the value of 9.0. A smooth-wall approach for the laboratory model was deemed appropriate as dictated by the plywood floor and baffles that featured negligible roughness k_s .

4.2.3 Solute transport modelling

Solute transport modelling provides the potential of examining how tracers, disinfectants or pathogens mix and flow through different hydrodynamic conditions. As the primary goal of contact tank design is ultimately disinfection, such simulations can be analysed or refined to quantify the impact of given hydrodynamic conditions on disinfectant or pathogen transport throughout the tank. An in-house code developed by Stoesser (2001) and Kim (2011) was used and refined as part of this investigation. Details of the theoretical background associated with the solute transport simulations are discussed below.

4.2.3.1 Principal Equations and Considerations

The governing equation for scalar transport modelling is the advection-diffusion equation (2.22) which was introduced in Chapter 2. According to the Reynolds stress theory, it can be rewritten as:

$$\frac{\partial \varphi}{\partial t} + U_i \frac{\partial \varphi}{\partial x_i} = \frac{\partial}{\partial x_j} \left(D \frac{\partial \varphi}{\partial x_i} - \overline{u'_i \varphi} \right) + S_\varphi \quad (4.19)$$

where $-\overline{u'_i \varphi}$, once multiplied with the density ρ , represents the turbulent mass flux. This component is the scalar version of the unknown parameters arising from the averaging of fluctuating quantities during the derivation of RANS equations. Similarly to the momentum equations' requirement for a closure model to account for the effects of turbulent fluctuations, the transport of scalars is subject to the same issue due to the turbulent mass flux term. This term could alternatively be approximated as

$$-\overline{u'_i \varphi} = D_t \frac{\partial \varphi}{\partial x_i} \quad (4.20)$$

where D_t is defined as the turbulent mass diffusivity which is dependent on the flow turbulence intensity rather than the characteristics of the scalar. The gradient-diffusion hypothesis was adopted for the estimation of D_t as

$$D_t = \frac{v_t}{Sc} \quad (4.21)$$

where Sc is the turbulent Schmidt number. The benefit of the gradient-diffusion hypothesis lies in the lack of additional transport equations, because it relies on the eddy viscosity parameter obtained previously divided by the Schmidt number, typically in the range of 0.7 - 1.0. In accordance with Rodi (1993), it is not unrealistic to adopt a constant Sc number, as the parameter has been found to show little variation across a flow, even in complex fluid simulations. The estimation of an appropriate Schmidt number has been a subject of controversy (Combest et al., 2011) and a sensitivity analysis should normally be performed. An estimate of $Sc = 0.7$ was considered for this study according to the recommendations of Launder (1978) and the previous studies of Kim (Kim, 2010; Kim et al., 2013a). A Sc value of 0.7 yielded the best agreement against the experimental results in the validation study of Chapter 6, but it should be noted that the results in preliminary simulations were equally satisfactory for a value of 1.0.

A limitation of the gradient-diffusion hypothesis is the assumption of isotropic turbulence which in turn can be a source of errors in the presence of highly anisotropic flow. However, isotropic turbulence is an overall assumption of the numerical simulations, which is justified on the grounds of simplicity and reduced computational load. An additional assumption which is adopted is the treatment of solutes as passive, i.e. the solute has a negligible impact on the hydrodynamics. Based on this, converged velocity and eddy viscosity values of a previous steady-state hydrodynamic simulation are imported and remain unaltered throughout the transient simulations. For the tracer analysis, this complies well as fluorescent dyes such as Rhodamine WT are selected because they have a negligible impact on flow conditions. This assumption is expanded herein to the simulation of microorganism and disinfection by-product transport, since the whole concept of hydraulic efficiency is already established on the agreement that pathogens are following the path of soluble tracers in disinfection reactors. It should be remarked that this condition is realistic specifically when the turbulence diffusivity D_t is by far greater than the molecular diffusivity D , which would be the case in fully developed turbulent flow encountered in field-scale CTs or the laboratory model of the experimental investigation.

4.2.3.2 Initial Conditions and Source Term Imposition

As with the hydrodynamic simulations, initial and boundary conditions are required to simulate solute transport. Two distinct types of simulations are contemplated in the results; (a) the simulation of tracer injection experiments and the (b) simulation of disinfection processes. A Dirichlet condition is generally established at the inlet for solute concentrations which is dependent on whether it is an instantaneous injection (tracer experiment) or a constant feed of a reactive solute until steady-state conditions are established (disinfection simulation). The same boundary type (Dirichlet) is applied for solid surfaces which are characterized by no solute flux and the concentration of all solutes is set to zero. At the free surface and outlet sections the Neumann boundary approach is applied, so that the normal gradient of the solute concentrations at the corresponding boundary are set to zero. Additional yet more specific considerations for tracer injection and disinfection simulations are respectively outlined below.

a) Conservative Tracer Simulations

The transport of a conservative tracer is simulated by solving the advection-diffusion equation which can be written for these particular simulations as:

$$\frac{\partial c_T}{\partial t} + U_j \frac{\partial c_T}{\partial x_j} = D_T \frac{\partial^2 c_T}{\partial x_j^2} \quad (4.22)$$

where in comparison with equation (4.19) molecular diffusion is considered negligible ($D \approx 0$) and the Source term S_ϕ is equal to zero, due to the conservative nature of the tracer simulated. The tracer injection simulation follows the studies of Falconer and Ismail (1997), Stamou (2002) and Rauén (2005). Therefore, in accordance with the Chapter 3 laboratory tracer experiment description, an injection time of 10s is considered. Therefore, from simulation time $t = 0$ until $t = 10$ s a constant tracer concentration of C_{in} was introduced. For $t > 10$ s and the remainder of the simulation C_{in} was set to zero. The actual magnitude of the initial concentration C_{in} is irrelevant as the simulation results were subject to the same post-processing procedure as experimental data to produce normalized RTDs and HEIs respectively. The performance of this approach to reproduce the experimental findings is discussed in Chapter 6.

b) Disinfection Simulations

Significant reactions of interest to this investigation were previously outlined as disinfectant decay, the inactivation of pathogens and the production of potentially carcinogenic DBPs. These processes are interconnected as discussed in Chapter 2 where the decay of chlorine influences the microbial inactivation since disinfectant concentration distribution is determinant for pathogen inactivation rates (e.g. Equations 2.9 – 2.14). Similarly, it can be observed that chlorine concentration levels are crucial parameters for the production of DBPs.

For each of these processes the source term of equation (4.19) had to appropriately be altered to simulate the mass loss/production occurring during the transport of disinfectant, microorganisms and DBPs. For example, assuming a first-order decay of chlorine, the Chick-Watson model for a pathogen such as *G. Lamblia* and the production of TTHMs through a model from Singer's (1994) study, i.e. equation (2.16), the transport equations would in turn have the following form:

$$\frac{\partial C_{Cl}}{\partial t} + U_i \frac{\partial C_{Cl}}{\partial x_i} = D_T \frac{\partial^2 C_{Cl}}{\partial x_j^2} - k_b C_{Cl} \quad (4.23)$$

$$\frac{\partial N}{\partial t} + U_i \frac{\partial N}{\partial x_i} = D_T \frac{\partial^2 N}{\partial x_j^2} - k' C_{Cl}^n N \quad (4.24)$$

$$\frac{\partial C_{DBP}}{\partial t} + U_i \frac{\partial C_{DBP}}{\partial x_i} = D_T \frac{\partial^2 C_{DBP}}{\partial x_j^2} + m C_{Cl}^a t_c^b \quad (4.25)$$

Where C_{Cl} is the chlorine concentration (mg/l), k_b is the first order bulk decay rate, N is the microorganism number, C_{DBP} the DBP concentration in $\mu\text{g/l}$, t_c is the contact time at that point, m represents various parameters included in by-product models such as temperature, organic carbon while a and b are exponents of C_{Cl} and contact time t_c respectively. The latter depend on the prevalent operational conditions of disinfection. Equations (4.23)-(4.25) are examples of the kinetic models incorporated in the solute transport simulations. The use of alternative or more sophisticated models is also discussed in Chapter 7.

The transport of disinfectant, microorganisms and by-products is simulated simultaneously as the three processes are interconnected through their source terms. The approach of Greene et al. (2006), where a first-order decay model of chlorine was incorporated in the inactivation source term is also examined. However, separating the

chlorine decay as a distinct transport equation results in further insights with regards to the interaction between chlorine and pathogen inactivation or by-product production processes, rather than solely providing an indication of microorganism survival level. In addition, the approach utilized in this study provides a structured framework for the development and testing of different decay, inactivation and DBP formation models.

Typically, a constant feed of chlorine C_{Cl} and microorganisms N is introduced at the inlet throughout the simulation. At $t = 0$ s the concentrations across the domain are zero ($C_{Cl} = N = C_{DBP} = 0$) along with the by-product concentration at the inlet ($C_{DBP} = 0$). The simulation is run until equilibrium is reached between chlorine – microorganisms – DBPs across the computational domain.

The effect of turbulence on the chemical reactions is considered negligible as chemical time scales are significantly larger compared to the mixing and turbulence time scales (slow chemistry). Under this scenario, micro-mixing is fast enough so that the composition variables can be approximated by their mean values, meaning that the scalar covariances between reactants are zero. For more information about the closure of chemical source terms the interested reader is directed to the work of Fox (2003) and Pope (2000).

4.3 NUMERICAL METHODS

While the previous section contains information on the main variables, governing laws and boundary conditions necessary, this part expands on the methodology relevant to the space and equation discretisation and subsequent numerical solution across the domain. The term discretisation implies the replacement of continuous information contained in the exact solution of the differential equations with discrete values leading to the formation of a computational grid. There are different ways of discretizing the differential equations, namely the finite difference method (FDM), the finite element method (FEM) and the Finite Volume Method (FVM). Each of them has merits and drawbacks and the type of approach selected depends on the specifications of the problem. The FEM is usually the most flexible but a computationally demanding approach as it relies on unstructured grids, whereas the FDM is the simplest approach but is constrained by uniform structured meshes making it less flexible. The FVM features characteristics from both methods even though it has been referred to be more

closely related to the finite difference scheme. The key difference of the FVM is its foundation on the conservation laws of physics rather than pure continuum mathematics concepts (Roache, 1998). The computational models set up for this study are designed according to the FVM concept and some relevant details of the numerical techniques are presented here for completeness. More information on the development and the principles of numerical models based on FVM can be found in Patankar (1980), Stoesser (2001), Olsen (2011), Vesteeg and Malalasekra (2006).

4.3.1 The Control-Volume Formulation

The finite volume method is applied on three-dimensional non-uniform computational grids to predict the distribution of the aforementioned variable quantities within the CFD models of CTs. The control-volume formulation dictates that the calculation domain is divided into a number of non-overlapping control volumes which encompass all the grid points of the simulation. In turn, the differential equation is integrated over each control volume (Patankar, 1988). There are piecewise profiles expressing the variation of a scalar φ between grid points to evaluate the associated integrals. The result is a discretisation equation which connects the values of φ for a number of grid points. All the differential equations examined in section 4.2 had the form of the general transport equation (4.3) which if discretized using the FVM in a structured 3-D domain for a variable φ , could be written as:

$$a_P \varphi_P = a_E \varphi_E + a_W \varphi_W + a_N \varphi_N + a_S \varphi_S + a_T \varphi_T + a_B \varphi_B + b \quad (4.26)$$

Where P is the grid point calculated during that iteration and E, W, N, S, T and B are the surrounding points of P in the x , y and z directions as illustrated in Figure 4.1.

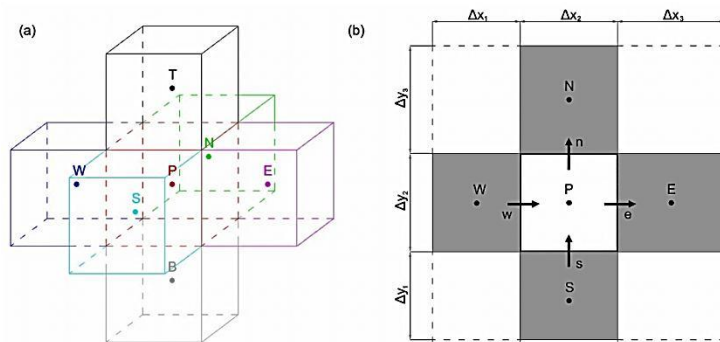


Figure 4.1 Examples of structured Finite Volume Method discretization grids (a) 3-D uniform computational grid and (b) plan view of non-uniform computational mesh

Coefficients a and b account for transient, diffusive, advective and source-term contributions to the transport of φ and are calculated as:

$$a_E = D_e A(|Pe_e|) + \llbracket -F_e, 0 \rrbracket \quad (4.27a)$$

$$a_W = D_w A(|Pe_w|) + \llbracket F_w, 0 \rrbracket \quad (4.27b)$$

$$a_N = D_n A(|Pe_n|) + \llbracket -F_n, 0 \rrbracket \quad (4.27c)$$

$$a_S = D_s A(|Pe_s|) + \llbracket F_s, 0 \rrbracket \quad (4.27d)$$

$$a_T = D_t A(|Pe_t|) + \llbracket -F_t, 0 \rrbracket \quad (4.27e)$$

$$a_B = D_b A(|Pe_b|) + \llbracket F_b, 0 \rrbracket \quad (4.27f)$$

$$a_P = a_E + a_W + a_N + a_S + a_T + a_B + a_P^0 - S_P \Delta x \Delta y \Delta z \quad (4.27g)$$

$$b = S_C \Delta x \Delta y \Delta z + a_P^0 \varphi_P^0 \quad (4.27h)$$

where $a_E, a_W, a_N, a_S, a_T, a_B$ are the control-volume surface integrands, $\Delta x, \Delta y$ and Δz is the control volume grid spacing in the x, y and z directions respectively. More parameters are introduced in equations (4.27a-h). φ_P^0 is the central cell's scalar value obtained from the previous iteration and combined with a_P^0 derived from the formula below,

$$a_P^0 = \frac{\rho_P^0 \Delta x \Delta y \Delta z}{\Delta t} \quad (4.28)$$

the term $a_P^0 \varphi_P^0$ corresponds to the control volume's internal energy. The parameters S_P and S_C are connected with the scalar source term S_φ from the governing equations as:

$$S_\varphi = S_C + S_P \varphi_P \quad (4.29)$$

The source term is separated into S_C and S_P through a linearization process which is in detail described in Patankar (1980). This procedure had to be undertaken for the k, ε turbulence quantities and the non-conservative solute transport simulations. Moreover, for tracer injections which occur at a given point just downstream of the inlet, the concentration value is introduced by modifying equation (4.29) for the particular cell during the injection interval to $S_C = 10^{30} C_{in}$ and $S_P = -10^{30}$ where 10^{30} is given as a large enough value to make the other terms of the discretisation equation negligible yielding the desired concentration value.

D and F correspond to the conductance and fluxes at control volume surfaces with neighbouring cells. The conductance is given for each neighbouring cell as

$$D_e = \frac{\Gamma_e \Delta y \Delta z}{(\delta x)_e} \quad (4.30a)$$

$$D_w = \frac{\Gamma_w \Delta y \Delta z}{(\delta x)_w} \quad (4.30b)$$

$$D_n = \frac{\Gamma_n \Delta z \Delta x}{(\delta y)_n} \quad (4.30c)$$

$$D_s = \frac{\Gamma_s \Delta z \Delta x}{(\delta y)_s} \quad (4.30d)$$

$$D_t = \frac{\Gamma_t \Delta y \Delta x}{(\delta z)_t} \quad (4.30e)$$

$$D_b = \frac{\Gamma_b \Delta y \Delta x}{(\delta z)_b} \quad (4.30f)$$

whereas the fluxes F as:

$$F_e = \rho f_e \Delta y \Delta z \quad (4.31a)$$

$$F_w = \rho f_w \Delta y \Delta z \quad (4.31b)$$

$$F_n = \rho f_n \Delta x \Delta z \quad (4.31c)$$

$$F_s = \rho f_s \Delta x \Delta z \quad (4.31d)$$

$$F_t = \rho f_t \Delta x \Delta y \quad (4.31e)$$

$$F_b = \rho f_b \Delta x \Delta y \quad (4.31f)$$

where Γ_e and $\Delta y \Delta z$ is the diffusion coefficient and the area of the control volume surface at e. $(\delta x)_e$ represents the distance between the grid points P and E, f_e is the flux component in the x direction as computed at the particular surface. Similar notation applies for the other surfaces at equations (4.30b-f) and (4.31b-f). These can be represented in a generalized notation as $f_{i+1/2}$ for a surface between grid points (i) and (i+1), where the variable components are f_i and f_{i+1} respectively.

These values are in turn used to calculate the local Peclet number Pe which is for each control volume surface calculated by dividing the surface flux F by the conductance D . The Peclet number is determinant for the evaluation of the $A(|Pe|)$ function, which is derived according to the differentiation scheme applied for the particular scalar ϕ between the grid points. Essentially, the objective of these schemes is to obtain realistic approximations of the surface integrals, i.e. $f_{i+1/2}$. Relevant to the study are the second-order central, first-order upwind, hybrid, power law and the Hybrid Linear/Parabolic Approximation (HLPA) differencing schemes. The second-order central and upwind differencing schemes are discussed here since they are integral components of the Hybrid and HLPA method.

The second order central differencing scheme interpolates the value of f at the cell face linearly so that:

$$f_{i+1/2} = \frac{1}{2}(f_i + f_{i+1}) \quad (4.32)$$

This results to an $A(|Pe|)$ function of :

$$A(|Pe|) = 1 - 0.5|Pe| \quad (4.33)$$

According to the upwind scheme, $f_{i+1/2}$ is equal to the value of f at the grid point at the upwind side of the face as

$$f_{i+1/2} = \begin{cases} f_{i+1} & \text{if } Pe \geq 0 \\ f_i & \text{if } Pe < 0 \end{cases} \quad (4.34)$$

and

$$A(|Pe|) = 1 \quad (4.35)$$

The Hybrid (Spalding, 1972) method combines the central differencing and upwind schemes in a manner that can be described as

$$f_{i+1/2} = \begin{cases} f_i & \text{if } Pe < -2 \\ \frac{1}{2}(f_i + f_{i+1}) & \text{if } |Pe| \leq 2 \\ f_{i+1} & \text{if } Pe > 2 \end{cases} \quad (4.36)$$

where

$$A(|Pe|) = \llbracket 0, 1 - 0.5|Pe| \rrbracket \quad (4.37)$$

A similar but more sophisticated approach is the power-law scheme which was developed by Patankar (1979), which similarly to the hybrid, for $|Pe| > 10$ it follows the upwind scheme, but for $|Pe| \leq 10$ a power-law interpolation is undertaken between f_i and f_{i+1} to evaluate $f_{i+1/2}$. The resultant $A(|Pe|)$ function is given by :

$$A(|Pe|) = \llbracket 0, (1 - 0.1|Pe|)^5 \rrbracket \quad (4.38)$$

The HPLA method combines a second-order upstream weighted approximation and the upwind differencing scheme (Stoesser, 2001; Kim, 2011) for the determination of $f_{i+1/2}$. HPLA was introduced by Zhu (1991) and was adopted on the grounds of being low

diffusive and unconditionally stable. The approximation of the control volume surface flux is given by:

$$f_{i+1/2} = f_i + \gamma(f_{i+1} - f_i) \left(\frac{f_i - f_{i-1}}{f_{i+1} - f_{i-1}} \right) \quad (4.39a)$$

$$\gamma = \begin{cases} 1 & \text{if } 0 < \frac{f_i - f_{i-1}}{f_{i+1} - f_{i-1}} < 1 \\ 0 & \text{otherwise} \end{cases} \quad (4.39b)$$

The power law scheme is applied for water flow calculations whereas hybrid and HPLA are numerically applied for the solute transport simulations coupled with an implicit Euler scheme to integrate the equation in time.

4.3.2 Pressure-Momentum Coupling

For the solution of the momentum equations, a major challenge is exhibited by the pressure gradient which as discussed in the previous section would correspond to the source term of the generalized transport equation (4.3). However, even though the momentum equation is discretized using the control-volume formulation in the format of equation (4.26), the source parameters S_C and S_P do not incorporate the effects of the pressure gradient when obtaining parameters b and α_P (Patankar, 1980). This gives rise to an additional unknown term which is added to the discretisation equations of the momentum equations for a non-staggered grid as:

$$a_P u_P = \sum a_{nb} u_{nb} + b + (p_e - p_w) \Delta y \Delta z \quad (4.40a)$$

$$a_P v_P = \sum a_{nb} v_{nb} + b + (p_n - p_s) \Delta x \Delta z \quad (4.40b)$$

$$a_P w_P = \sum a_{nb} w_{nb} + b + (p_t - p_b) \Delta y \Delta x \quad (4.40c)$$

where nb denotes the neighbouring grid points and the last term represents in each case the pressure force acted on the control volume for the particular direction. In order to estimate the pressure gradients, the SIMPLE algorithm was adopted which is a process where the pressure is initially guessed and iteratively corrected until a converged solution is obtained that satisfies the continuity equation. The main sequence of the algorithm operations is outlined below.

For the purposes of the algorithm the pressure term becomes:

$$p = p^* + \acute{p} \quad (4.41)$$

which means that it is divided into a guessed pressure p^* and a pressure correction \acute{p} . Using an initial estimate of the guessed pressure p^* equations (4.40a-c) are used to obtain an imperfect velocity field by obtaining some preliminary velocity components u^* , v^* and w^* . The next step is using these velocities to estimate the pressure correction. For this, the continuity equation is incorporated in a discretisation equation to obtain \acute{p} as:

$$a_p \acute{p}_p = \sum a_{nb} \acute{p}_{nb} + b \quad (4.42)$$

where for incompressible flow,

$$b = \rho[(u_w^* - u_e^*)\Delta y\Delta z + (v_n^* - v_s^*)\Delta x\Delta z + (w_t^* - w_b^*)\Delta x\Delta y] \quad (4.43)$$

The acquired values of \acute{p} are firstly applied in equation (4.41) to compute the new pressure p for the next iteration. Also, velocity components (u^* , v^* and w^*) obtained in the beginning of the iteration are subjected to the following velocity-correction equations to derive a corrected velocity field:

$$u_p = u_p^* + d_u(\acute{p}_w - \acute{p}_e) \quad (4.44a)$$

$$v_p = v_p^* + d_v(\acute{p}_s - \acute{p}_n) \quad (4.44b)$$

$$w_p = w_p^* + d_w(\acute{p}_b - \acute{p}_t) \quad (4.44c)$$

where

$$d_u = \frac{\Delta y\Delta z}{a_p} \quad (4.45)$$

with similar calculations for d_v and d_w respectively. Once those velocities are obtained the FVM method is applied to calculate the new values for the turbulence quantities. The pressure field obtained from equation (4.41) is then treated as the revised guessed pressure and the whole process is repeated until a converged solution is found corresponding to a pressure correction $\acute{p} \approx 0$.

In order to aid the convergence of the numerical models, relaxation factors were imposed. For the pressure-correction equation the factor corresponded to a value of 0.2. For velocity and turbulence quantities the values of 0.8 and 0.5 were adopted respectively. For the remaining scalar quantities considered (e.g. solute concentrations) the relaxation factors established were equal to unity.

4.3.3 Solution Techniques

The result of the previous analysis focused on the discretisation of the governing equations of fluid flow and solute transport. The consequence of this process is a system of linear algebraic equations of the form $[A]\varphi = [b]$ which needs to be solved. The complexity of the system is in line with numerical characteristics such as simulation dimensionality, number computational points and discretisation practises (Versteeg and Malalasekera, 1995). Generally, the techniques can be separated into direct and iterative approaches. A typical example of direct solution is calculating the inverse of matrix $[A]$ and solving the system for the value of φ by Gaussian elimination. The storage requirements for the equation systems resulting from the computational domain of this study make this approach highly impracticable for standard processors. On the other hand, iterative methods are relying on the repeated application of simple algorithms until convergence is achieved through multiple iterations. A simple technique of this type is the Gauss-Seidel method which assuming a 3-D problem with a discretized equation of (4.26) the new value of φ_P is calculated by using the previously known estimate or guess (depending on the iteration number), which restates (4.26) as

$$a_P\varphi_P = a_E\varphi_E^* + a_W\varphi_W^* + a_N\varphi_N^* + a_S\varphi_S^* + a_T\varphi_T^* + a_B\varphi_B^* + b \quad (4.46)$$

where φ_E^* , φ_W^* , φ_N^* , φ_S^* , φ_T^* and φ_B^* are previous estimates of φ in the neighbouring grid points. A more sophisticated approach is the line-by-line or the Alternate-Direction Implicit (ADI) method which requires the Tri-Diagonal Matrix Algorithm (TDMA). The 3-D problem is split into a series of 1-D problems by treating implicitly the points located in one direction at a time, and taking the neighbouring values in the other directions explicitly from the previous iteration results, i.e.:

$$-a_E\varphi_E + a_P\varphi_P - a_W\varphi_W = a_N\varphi_N^* + a_S\varphi_S^* + a_T\varphi_T^* + a_B\varphi_B^* + b \quad (4.47a)$$

$$-a_N\varphi_N + a_P\varphi_P - a_S\varphi_S = a_E\varphi_E^* + a_W\varphi_W^* + a_T\varphi_T^* + a_B\varphi_B^* + b \quad (4.47b)$$

$$-a_T\varphi_T + a_P\varphi_P - a_B\varphi_B = a_E\varphi_E^* + a_W\varphi_W^* + a_N\varphi_N^* + a_S\varphi_S^* + b \quad (4.47c)$$

The system of equations is then solved using TDMA. The implicit nature of the ADI method shows a higher convergence rate making it more efficient than the Gauss-Seidel approach. This method was used for the hydrodynamic simulations and was aided using appropriate relaxation factors for smoother convergence. A stronger implicit process (SIP) was also used for the solution of the discretisation equations for the solute transport approach as proposed and expanded by Stone (1968).

4.3.4 CT Flow and Transport Simulation Procedure

The main sequence of operations followed when undertaking CFD simulations to acquire disinfection efficiency data is illustrated in the flow chart of Figure 4.2. These can be classified into three categories of pre-processing, processing and post-processing.

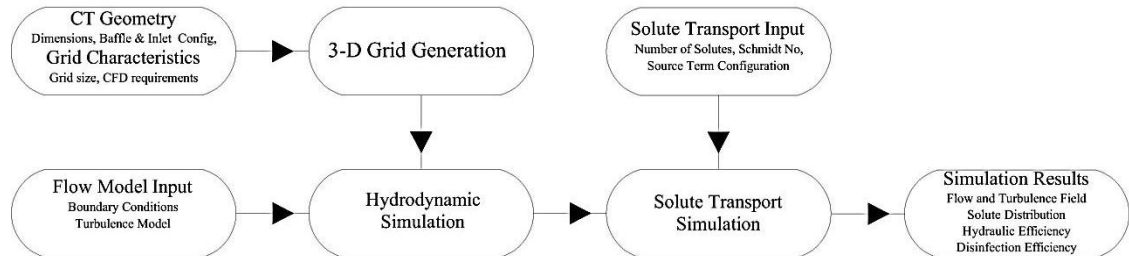


Figure 4.2 Flow Chart illustrating the sequence of operations performed for the acquisition of Flow and Disinfection Predictions

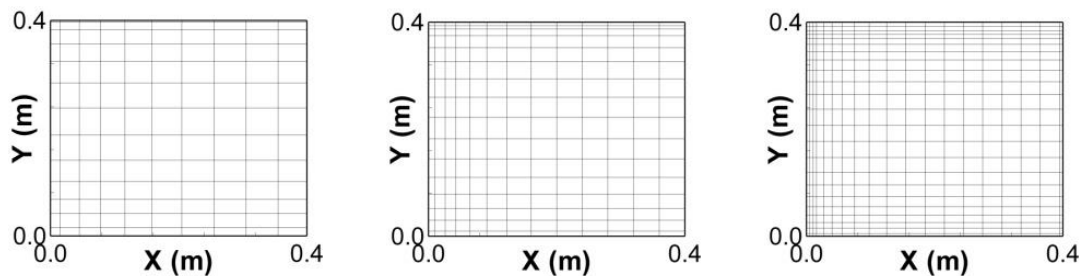


Figure 4.3 Different mesh resolution examples produced from the grid generator program

Pre-processing operations import necessary information and parameters to the main solver prior to the initialization of any simulation. In this case, these are the CT geometry, computational grid characteristics and more specific CFD model input. The CT geometry information comprises of tank dimensions, then baffle number, location orientation, size and specification of inlet and outlet locations. The grid characteristics input includes minimum and maximum computational cell size and factors of grid step increase away from boundaries in instances of non-uniform mesh (Figure 4.3). This information is fed into a mesh generator algorithm developed in Fortran 95 to calculate grid spacing and produce coordinate files for the computational grid points in a format compatible to the numerical model codes. For pure hydrodynamic simulations the CFD model input specifies boundary conditions such as discharge, wall roughness and blocked cells due to baffling configuration. For solute transport simulations, the inlet or the tracer injection concentration data must be additionally specified while the flow and turbulence field which was obtained previously as output of a hydrodynamic simulation must be available.

Processing operations are the hydrodynamic and solute transport simulations, where the governing equations are discretized based on the Finite Volume Method and solved using numerical techniques. The output of the simulation is designed in a way to produce files compatible for visualisation software (Tecplot 10) and spread sheets (MS Excel) for post-processing. These software packages are extensively used to analyse and acquire the findings discussed in subsequent chapters.

4.4 CHAPTER SUMMARY

An overview of the computational modelling approach is presented in this chapter. The governing formulas were identified as the Reynolds-Averaged Navier-Stokes (RANS) differential equations which are based on the conservation of continuity and momentum. The momentum equations were coupled with a standard two-equation k- ϵ model to provide a closure to the turbulence uncertainty. The transport of a solute was dictated by the Advection-Diffusion equation which is outfitted with appropriate source terms to describe the chemical species conservation, decay or production as it flows through the contact tank geometry. Assumptions were made to reduce the computational load of the simulations such as by modelling the water flow as incompressible and the scalar transport according to the gradient-diffusion hypothesis.

The discretisation of the governing equations was performed using the Finite Volume Method in a regular, orthogonal, non-staggered three-dimensional grid. The Semi-Implicit Method for Pressure Linked Equations algorithm was implemented to couple the mean velocity and pressure fields until a realistic pressure field was established to satisfy the continuity equation. The Power-Law formulation was used for the interpolations of the convective term in the hydrodynamic simulation whereas for solute transport a combination of the Hybrid and the Hybrid Linear/Parabolic Approximation differentiation scheme was adopted. The algebraic solutions of the systems of equations developed from the discretization of the governing equations were derived using the TDMA or the SIP numerical techniques for the hydrodynamic and solute transport simulations respectively.

Towards the end, the sequence of operations for the simulation of flow and transport characteristics are depicted to produce output compatible for visualization and processing software for the subsequent analysis of simulation predictions.

CHAPTER 5

EXPERIMENTATION RESULTS

5.1 INTRODUCTION

This chapter focuses on the results of experiments derived from the ADV and Rhodamine WT tracer injection campaign. The main objectives were (i) to obtain accurate and reliable data of the hydrodynamics and passive tracer transport characteristics for a scaled CT as well as to identify short-circuiting and internal recirculation patterns, (ii) provide evidence of the strong interlink between the hydrodynamics and tracer transport in baffled CTs, (iii) quantify the effect of the complex hydrodynamics and mixing processes on hydraulic efficiency indicators (HEIs), and (iv) evaluate the reliability of the theoretical models to predict the hydraulic efficiency parameters for baffled disinfection tanks. Results were obtained by following the methodology described in Chapter 3. Findings relevant to the hydrodynamic conditions encountered in the laboratory model are examined in section 5.2. Section 5.3 expands the analysis to tracer findings and focus is given on the relationship between hydrodynamics and solute transport inside CTs.

5.2 HYDRODYNAMIC CHARACTERISTICS OF CT-1

The main findings obtained from the data set comprised of the ADV measurements (Figure 3.5) in the CT laboratory model introduced in Chapter 3 (CT-1) are discussed herein. A general overview of the flow patterns in each compartment is given in section 5.2.1 for an initial appreciation of the overall hydrodynamic conditions. The analysis becomes more quantitative in sections 5.2.2 and 5.2.3, where the mean velocity and turbulence field is examined in-depth at specific locations across the tank. Results are compared against available experimental data from previous studies which are currently limited to Teixeira (1993) and Rauen (2005) according to the literature review of Chapter 2. Teixeira's (1993) LDA experiment results were acquired from a CT model which even though presents certain similarities to CT-1, it features some design characteristics such as inlet configuration and baffle thickness which differentiate the two. Rauen (2005) obtained ADV measurements for alternative baffling configurations including CT-1, but for a 30% lower flow rate. Comparisons with previous data were primarily undertaken to encourage the verification of the measurements, since the main objective of the particular experiments is to provide a reliable data set for the validation of CFD approaches rather than solely the study of hydrodynamics in CT geometries.

5.2.1 Compartmental Flow Pattern Analysis

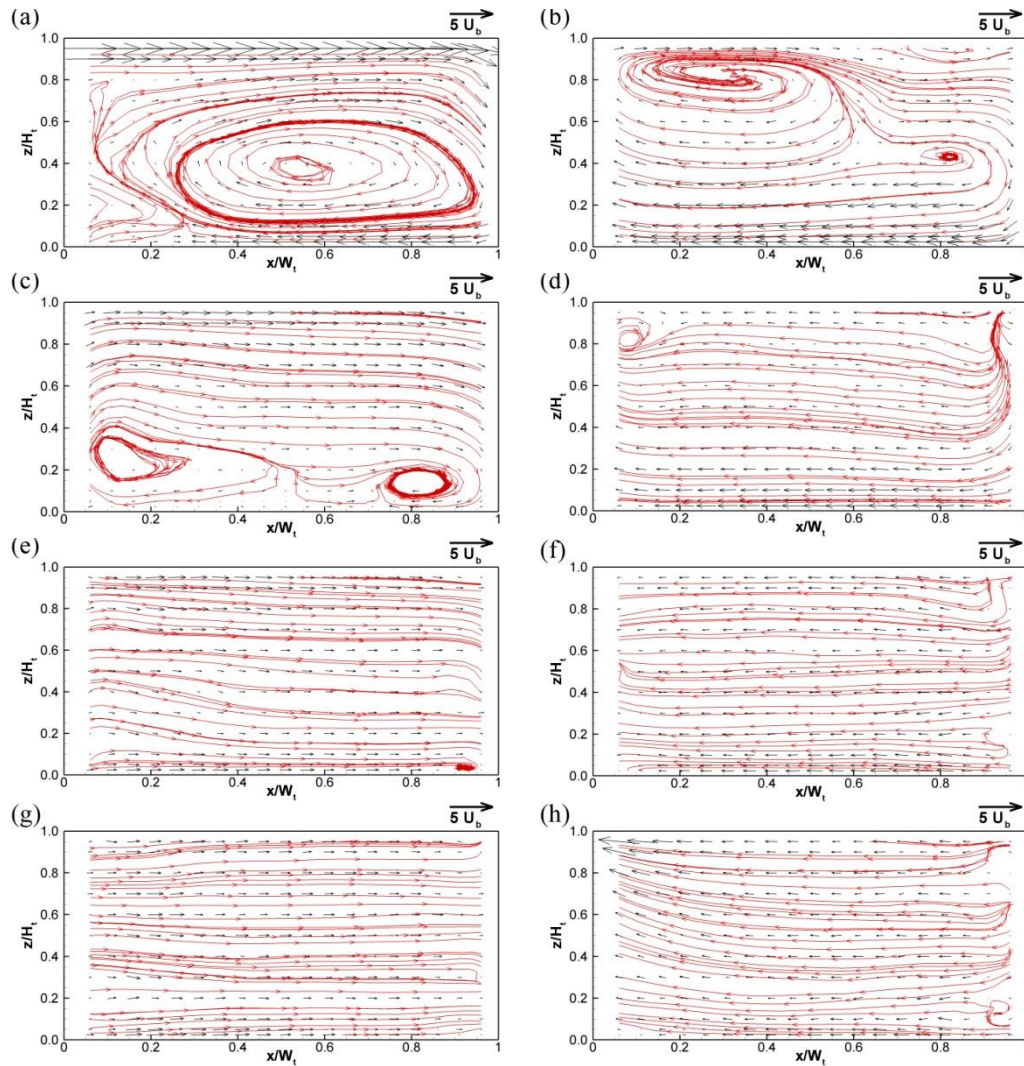


Figure 5.1 Streamlines and vectors indicating the flow pattern and normalised velocity magnitude as observed from the ADV investigation in each of the 8 compartments of CT-1. The longitudinal profiles are taken from the centreline of the compartments and are plotted as viewed from the east side of the tank defined in Figure 3.5.

Under a plug flow regime, the fluid flows through the reactor in an orderly manner with no fluid element overtaking or mixing with any other element ahead or behind. This theory allows lateral mixing but not longitudinal mixing or diffusion along the flow path. These conditions should ensure the same contact time in the tank for all fluid elements. The flow pattern corresponding to this regime suggests an absence of recirculation zones, a scenario that is physically unfeasible in reactor geometries featuring variable inlet and outlet conditions and baffling configurations where fluid flow meanders around them.

Figure 5.1 presents streamlines indicating the route followed once system water enters from the approach channel as produced according to the Tecplot software interpretation algorithm. The streamlines are derived from the ADV measurements acquired in the centreline of compartments 1-8. It is apparent that the first compartment is dominated by one large recirculation zone and significant two-dimensionality in the longitudinal plane. This flow pattern is a result of the inlet configuration which causes the system water to enter the first chamber by means of a high momentum jet which results in the 2D profile at the x-z plane of the first compartment. It is formed when the water jet gets deflected from the opposite wall and then again from the compartment bed. In contrast, the entire contact tank is 2-dimensional in the x-y plane, i.e. the flow meanders horizontally through the tank. Hence there is significant three-dimensionality close to the inlet, which is where the flow recovers from 2D in the longitudinal to 2D in the horizontal plane.

This process begins already in compartment 1 and is illustrated in Figure 5.2, where streamlines produced by ADV measurements highlight secondary recirculation in the horizontal plane ($z/Ht = 0.5$). Multiple secondary circulation cells in the centre of the compartment are identified and stronger flow is observed near the sidewalls as indicated by the vectors of normalized velocity.

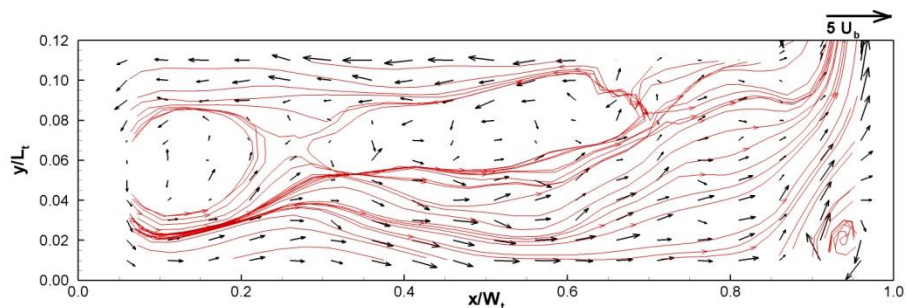


Figure 5.2 Flow pattern of compartment 1 at the horizontal plane of $z/Ht = 0.5$. This is further illustrating the hydrodynamic complexity downstream of the inlet when combined with the vertical recirculation zone of figure 5.1(a).

The conditions of compartment 1, result in subsequent recirculation zones occurring in compartments downstream (Figure 5.1b) which combined with the expected horizontal recirculation zones around baffle lees demonstrate the complexity of the tank hydrodynamics. For compartments 2 and 3 (Figure 5.1b-c) vertical recirculations continue to occupy a significant extent of the compartment volume which undoubtedly encourages short-circuiting by accelerating the velocities along the main flow path. The transition to 2-D flow is apparent between compartments 3 and 4 as the pattern appears

uniform across the depth onwards until the outlet. Nonetheless, there are still some minor disturbances near the baffle lee edges where flow begins to meander ($0.0 < x/W_t < 0.15$ and $0.85 < x/W_t < 1.00$) which are to be expected. The adoption of the baffling configuration does promote uniformity as observed in latter compartments where the influence of the inflow jet diminishes and is replaced by quasi 2-D conditions.

The flow structure in compartments 1 and 2 is of particular interest due to the recirculation produced from the inlet water jet, as it utterly contradicts the desirable plug flow regime that is usually the objective when designing CTs. In spite of this, the current inlet configuration is quite common in field-scale CTs (e.g. Embsay CT) and studies (Stamou, 2008) scarcely report on the influence of the inlet arrangement on the hydrodynamics which is side-tracked by baffling configuration optimizations. To better understand the impact of the inlet on the flow pattern downstream more longitudinal profiles are depicted for compartments 1 and 2 in Figure 5.3.

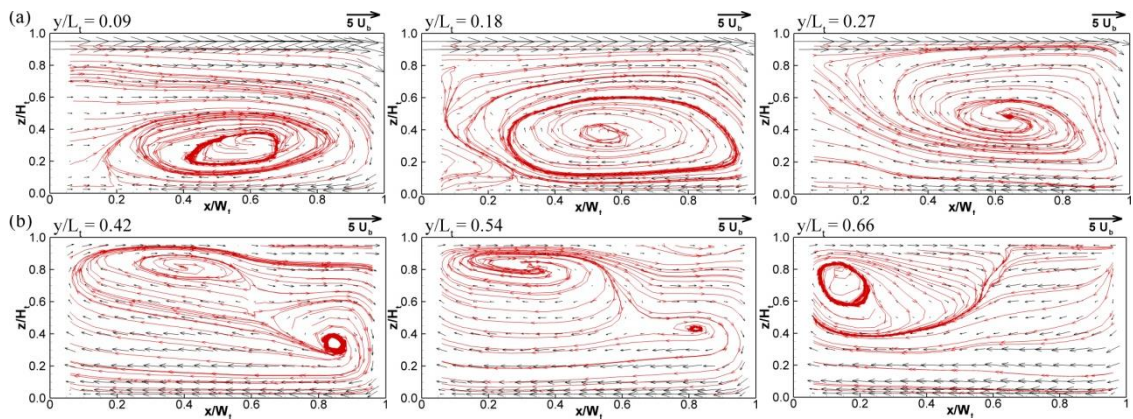


Figure 5.3 (a) Compartment 1 and (b) compartment 2 recirculation zones in x-z planes . Based on the obtained flow pattern the vertical recirculation zone occupying the majority of compartment 1 volume also expands to the first half of compartment 2 and results in a subsequent dead zone in the second half of the compartment. The profiles are plotted as viewed from the east side of the tank defined in Figure 3.5.

By observation, the vertical recirculation zone dimensions vary across the compartment width. Closer to the side wall ($y/L_t=0.09$), the recirculation is centred approximately at $x/W_t = 0.50$ and $z/H_t = 0.25$, whereas the recirculation area is encompassed in the region of $0.15 < x/W_t < 0.85$ and $0.0 < z/H_t < 0.50$. In the centreline of the compartment, the recirculation occupies a greater area ($0.10 < x/W_t < 1.00$ and $0.0 < z/H_t < 0.65$) and its centre has shifted to ($x/W_t = 0.55$, $z/H_t = 0.35$). The same pattern applies close to the baffle separating the 2 compartments, where the recirculation zone is now located in the upper layer of the profile and is centred at (0.65, 0.45). Based on the transition between the profiles in compartment 1, it can be argued that the recirculation at compartment 2,

which at $y/L_t = 0.42$ is centred at (0.85, 0.35) is part of the first compartment's recirculation. However, it is noticed that this does not occupy the whole compartment width as shown by the profile at $y/L_t = 0.66$, where a different recirculation is dominant, centred at (0.15, 0.70), suggesting strong three-dimensionality even in the transition between compartments 2 and 3.

The previous studies of Teixeira (1993) and Rauen (2005) acknowledged the first compartment flow complexity on the particular configuration, but not of the second compartment where it was described as transitional between 3-D and 2-D flow. These results herein indicate that significant three-dimensionality persists until compartment 3 as shown also by the compartment's longitudinal profile at $y/L_t = 0.96$ (Figure 5.1c)

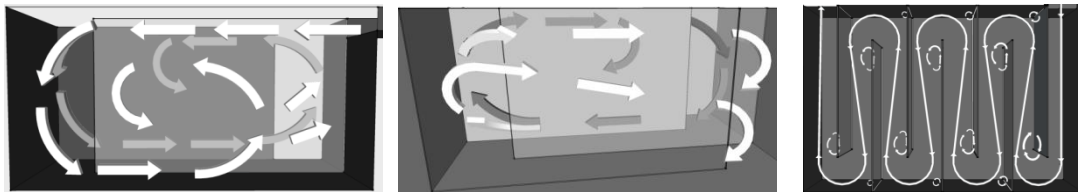


Figure 5.4 Main CT flow patterns in 3-D sketch form a) 1st and 2nd Compartments: White arrows correspond to flow in the 1st compartment and dark grey in the 2nd. b) 2nd and 3rd Compartments; white arrows represent the 3rd compartment flow and dark grey the 2nd. c) System plan view including the main flow streamline and 2-D recirculation zones.

The sketch in Figure 5.4 summarises the main characteristics of the flow pattern in the CT-1 laboratory model. Accordingly, it (a) illustrates the 1st and 2nd compartment vertical quasi 2D recirculations. In the 2nd compartment, the flow short-circuits close to the bed, which is a result of the recirculation in the first compartment, because the water jet deflected at the end wall of compartment 1 moves near the bottom of compartment 2 (see sketch in Figure 5.3b). There is also vertical recirculation in the second half of the 2nd compartment, whilst in the first half of the compartment the flow exhibits strong 3-dimensionality, which is further promoted from horizontal dead zones resulting from flow separation at the baffle edge (see Figure 5.3c). Figure 5.3(c) only illustrates significant horizontal dead zones for simplicity and therefore the three-dimensionality indicated by Figures 5.3(a-b) is not included.

5.2.2 Mean Velocity and Turbulence Characteristics

With regards to the CT hydrodynamics, attention is given on (a) the impact of recirculation zones on local acceleration which lead to the exacerbation of short-circuiting effects, (b) the transition from 3-D to quasi-2D flow in the x-y plane in latter

compartments and (c) the hydrodynamics deviation from an ideal plug flow regime. Comparisons are also made with the previous quantitative results obtained by Rauen for CT-1 under different operational conditions and Teixeira (1993), who carried out an extended analysis of the flow field assessed by use of LDA in a contact tank with similar design characteristics to the CT-1 setup.

5.2.2.1 Overview of Velocity Results

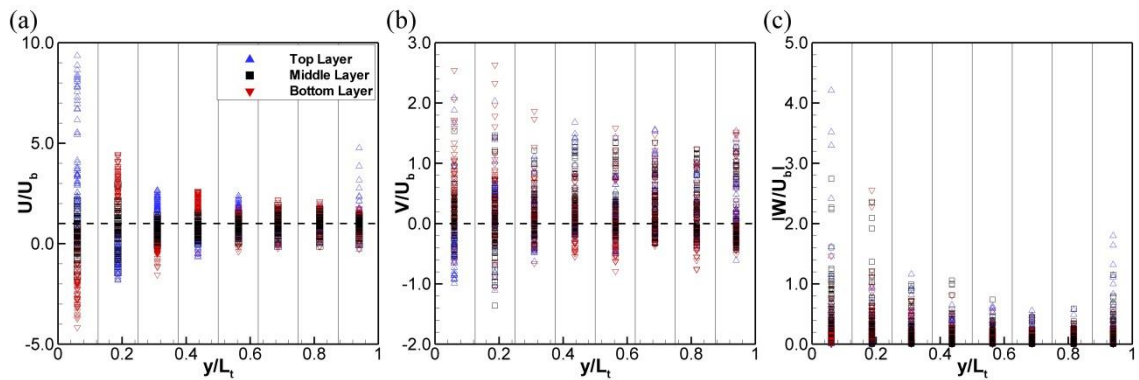


Figure 5.5 Normalized velocity measurements plotted with respect to the tank length. (a) Horizontal velocities where the positive values are towards the flow direction (streamwise), (b) transverse velocities and (c) magnitude of vertical velocity measurements. The dashed line implies the plug flow velocity magnitude. Vertical grid lines indicate the different compartments.

The occurrence of recirculating flow structures is concurrent with the presence of a pronounced advective flow path, in which the average velocity is faster than the cross-sectional mean velocity U_b (Thackston et al., 1987). As observed in the previous section, these occurrences were particularly prevalent in the first three compartments of CT-1 due to the inlet configuration. Therefore, it is interesting to examine their impact on the velocity measurements. Figure 5.5(a) presents streamwise horizontal velocity results for all ADV sampling points across the compartments. It can be deduced that the inflow water jet results into significantly greater horizontal velocities at the top layer of compartment 1 compared to U_b . This is where the highest velocity in the tank is measured ($U_{max} = 9.52 U_b$), 852% greater than what would be expected from a near-plug flow scenario. The desired plug flow velocity is illustrated by the dashed line which highlights a consistent velocity of U_b in the streamwise direction and 0 velocities in the transverse and vertical directions. The deviation from this line is remarkable in compartments 1-3, but significant improvement is noticed in compartments 4-7. In the 8th compartment higher streamwise velocities at the top layer are a result of the outlet weir.

Reverse flow (i.e. $U/U_b < 0$) is encountered in many locations across the tank. It initially occurs in the bottom of the first compartment and alternates in subsequent compartments with the top layer, a direct consequence of vertical recirculations. The magnitude of reverse flow diminishes gradually in the same manner that streamwise velocity converges to U_b as y/L_t increases. For example, in the 1st compartment the maximum reverse velocity is approximately $4.30 U_b$ whereas in the 2nd it is reduced by 47% to $2.26 U_b$. At the 3rd compartment a further 32% reduction is noticed ($U_{rev,3} = 1.54 U_b$). At compartment 8 it is almost negligible ($U_{rev,8} = 0.27 U_b$) and it is limited to some minor horizontal recirculation zones either at corners or behind baffles.

A large fraction of the three-dimensionality can be signified by the high magnitude of the vertical velocity (Figure 5.5c) in compartments 1-2, an effect once again of the water jet deflections against the side walls and the unavoidable reverse flow that these entail. The average magnitude of vertical velocities in the initial three compartments is 0.56 , 0.43 and $0.21 U_b$ respectively. This supports the theory that compartment 2 flow is similarly three-dimensional, with only 25% reduction in vertical velocities. The transition between 3-D and 2-D conditions is placed in the 3rd compartment which is characterized by an approximate 100% reduction of vertical velocity magnitude. In compartment 7 the minimum compartment vertical velocity mean is calculated as $0.09 U_b$ prior to an increase to $0.20 U_b$ in compartment 8 due to the outlet geometry (Figure 5.5c).

5.2.2.2 Deviation from Plug Flow Profile

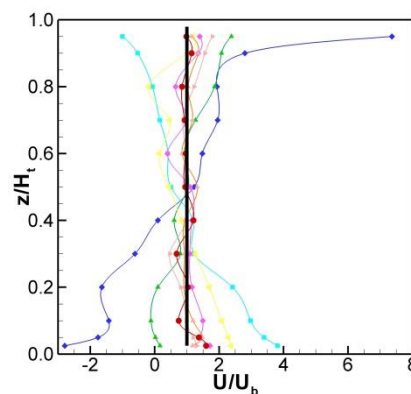


Figure 5.6 Vertical profiles of U/U_b in the centre of each compartment. Positive velocities follow the streamwise direction in each compartment. The theoretical plug flow velocity profile is presented for comparison

Figure 5.6 quantifies afore-made statements of strong 2D recirculation, particularly in compartments 1 and 2 but also provides evidence of the flow's considerable deviation

from plug flow (here indicated by the solid line of magnitude U_b across the entire depth). Whilst in compartment 1 the surface and near bed layer flow exceed velocities of 8 and -3 times the plug flow velocity, with the maxima in the top and bottom layers of compartment 2 still being around 4 and -2 times plug flow velocity. The latter is quite remarkable given the significant distance to the inlet. In compartment 8, the measured velocity profile almost coincides with the plug flow line.

The convergence to plug flow is quantitatively assessed at the vertical profiles in the centre of each compartment (Figure 5.6) by adopting the methodology of Rauén (2005) of calculating the mean deviation of the measured velocities against a plug flow scenario:

$$\sigma_c = \frac{\sum_{i=1}^{12} \left| \frac{U_{c,i} - U_b}{U_b} \right|}{12} \quad (5.1)$$

where i is a layer index and $U_{c,i}$ the corresponding velocity measurement for the particular compartment (c). The maximum value of i is 12 since this is the number of ADV measurements on each vertical profile. Table 5.1 shows results for each sampling point of the vertical profiles in Figure 5.6. In turn, Figure 5.7 compares the depth-mean deviation coefficient σ_c with the findings of previous work.

Table 5.1 Calculation of mean plug flow deviation coefficient for the vertical profiles of Figure 5.6

z/H_t	$ U - U_b/U_b $							
	Comp 1	Comp 2	Comp 3	Comp 4	Comp 5	Comp 6	Comp 7	Comp 8
0.025	2.99	3.09	0.83	1.53	0.40	0.84	0.26	0.71
0.050	1.89	2.64	0.98	1.45	0.28	0.52	0.59	0.47
0.100	1.53	2.19	0.88	1.24	0.06	0.60	0.28	0.20
0.200	1.76	1.60	0.89	0.82	0.13	0.24	0.03	0.11
0.300	0.66	0.31	0.14	0.34	0.50	0.17	0.01	0.27
0.400	0.10	0.27	0.35	0.12	0.08	0.24	0.01	0.29
0.500	1.31	0.46	0.11	0.52	0.02	0.18	0.41	0.02
0.600	1.58	0.56	0.01	0.84	0.03	0.58	0.09	0.03
0.700	2.10	0.83	0.36	0.52	0.06	0.05	0.26	0.00
0.800	2.07	0.92	0.99	0.81	0.31	0.30	0.12	0.09
0.900	3.00	0.43	1.22	0.09	0.67	0.45	0.45	0.23
0.950	7.90	0.07	1.55	0.27	0.92	0.49	0.23	0.06
Mean (σ_c)	2.24	1.12	0.69	0.71	0.29	0.39	0.23	0.21

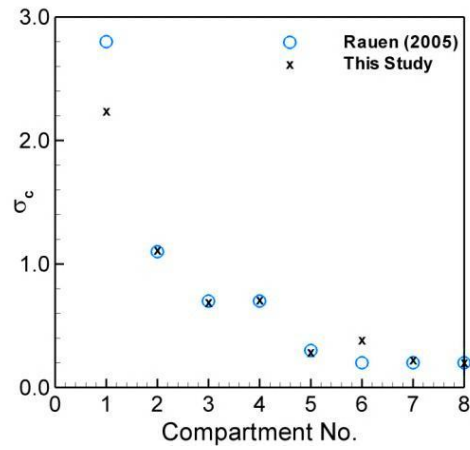


Figure 5.7 Plug Flow deviation coefficient with respect to compartment number

The comparison indicates that despite the lower flow rate in Rauen’s (2005) investigation, the deviation from plug flow is not altered as most points coincide, suggesting that the overall flow structure is not significantly affected. The convergence to plug flow is remarkable once a transition to 2-D flow is established in compartments 3-8. However, the deviation between compartments 6 and 8 is almost negligible which could mean that the only possibility for further optimization of the hydrodynamics would be a transition to 1-D flow, i.e. conditions which could perhaps be accommodated by a long narrow channel or pipe flow.

5.2.2.3 Turbulence Kinetic Energy

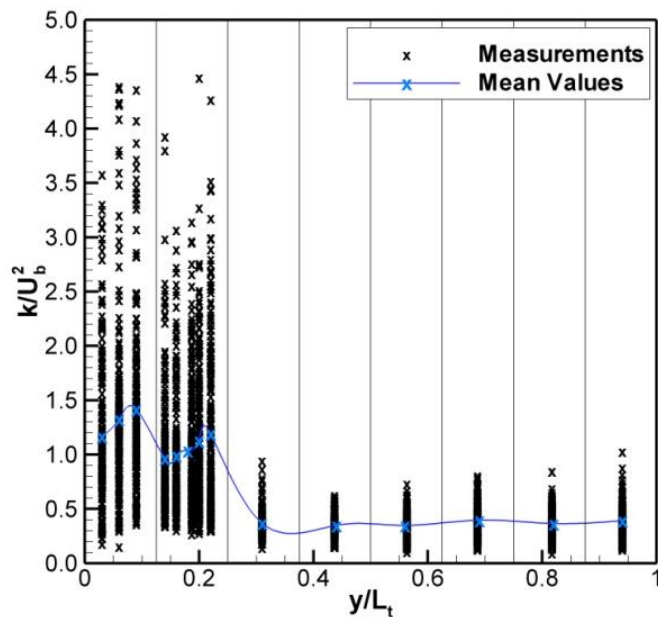


Figure 5.8 Normalised turbulence kinetic energy (k/U_b^2) along the tank, calculated from the RMS fluctuations of velocity obtained from the ADV experimentation

The calculation of turbulence quantities relies on statistics of velocity fluctuations monitored from the duration of ADV sampling (equations 3.2-3.4). The turbulence kinetic energy in particular is of interest in this case, since it is the quantity approximated by the k- ϵ turbulence model in the computational simulations (Chapter 6). The estimation of the second model parameter from ADV measurements, i.e. the turbulent energy dissipation rate (ϵ), requires the accurate production of energy spectra which would need higher sampling frequency or duration which was not further examined within the scope of this study.

Figure 5.8 plots the turbulent kinetic energy values obtained for each of the longitudinal profiles. The average k levels appear to be conservative in the initial two compartments with an overall average of $1.15 k/U_b^2$. However, the measurements later in the flow path notoriously deviate from this, as following a rapid decay of 67% in the transition between compartment 2 and 3 the mean turbulence level appears to be consistent at $0.37 k/U_b^2$. The results are remarkably scattered for compartments 1 and 2. The greater levels of turbulence in these compartments can be attributed to shear, wall and bed generated turbulence. Wall and bed - generated turbulence is caused by the approach channel water jet as it is deflected from the opposite wall and the tank bottom in compartments 1 and 2. The shear-generated turbulence is more pronounced between the water jet flow path and the vertical recirculation zones formed. As the influence of the jet diminishes towards the end of compartment 2, the turbulence kinetic energy is characterized by the rapid decay at the transition between compartments 2 and 3.

In subsequent compartments, even though the turbulence levels appear more consistent, higher kinetic energy is encountered in cases of local acceleration as the flow meanders through the baffling configuration. However, the deviation from the mean k values is nowhere near as significant as it is near the presence of the current inlet configuration. Indicatively, the standard deviation of the measurements in compartments 1 and 2 is $0.752 k/U_b^2$, whereas for compartments 3-8 it is only $0.130 k/U_b^2$, demonstrating a much more uniform turbulence field.

With respect to the impact of turbulence on the operation of CTs, it can be argued that high levels of turbulence could lead to better mixing conditions (e.g. across the compartments' cross-section) of chemical species encouraging more uniform

distribution throughout the CT flow. In that respect, the higher mean levels of turbulence in compartments 1 and 2 are beneficial. However, this is greatly hindered by the high standard deviation of k in the volume encompassed by these compartments, which is characterized by excessively higher turbulence near solid and free-surface boundaries in comparison with other regions. The state of turbulence is crucial on scalar transport and for the purposes of CT operation the aim should primarily be to retain it uniform across the geometry with a view to promoting even mixing.

5.2.2.4 Correlation with Previous Data

The experimentation in contact tank hydrodynamics has almost entirely been undertaken in rectangular small-scale contact tanks, where the CT-1 baffling configuration was of particular interest as it is representative of the serpentine CT design commonly adopted in water treatment works. Therefore, the validity of this study's measurements can be further verified using the past work available in the literature (Rauen, 2005; Teixeira, 1993; Shiono and Teixeira, 2000).

Previous ADV measurements in the CT-1 configuration focused on the production of velocity vertical profiles to compute the deviation from plug flow (Figure 5.7), and a longitudinal velocity profile in compartment 1 examining the vertical recirculation zone. Figure 5.9 compares the results between this study and Rauen (2005) by means of vector and contour plots. The water jet is apparent at $z/H_t > 0.90$ and the high-velocity reverse flow near the bed in both cases is situated between $0.3 < x/W_t < 1.0$ and $0.0 < z/H_t < 0.25$. Overall, a good agreement can be observed between the two and any discrepancies are attributed to the impact of the different flow rate on the flow structure.

Experimental findings reported in Teixeira (1993) and Shiono and Teixeira (2000) for a couple of accurate geometric small-scale models (1:4 and 1:8) of the Embsay water disinfection tank are also of relevance to this study. The results of the smaller model (1:8) are mostly discussed on the grounds of similarity between the hydrodynamics developed in the two models. Though the tank geometry of CT-1 is similar to the one (referred here as ST) investigated by Shiono and Teixeira (2000), there are a couple of important differences, which are: Firstly, the ST tank (1:8) was smaller and the cross-sectional Re was approximately half of the current study, i.e. $Re_{ST} \approx 3500$. Though both, the model of this study and the ST model were Froude models of the prototype Embsay tank, the Re numbers are unequal (due to the Fr- Re conflict of hydraulic models), and

hence it is interesting to see how this affects the turbulence statistics. Secondly, the ST tank featured a different inlet configuration, whilst in the present study the flow enters the contact tank rather undisturbed with a honeycomb net that promotes flow uniformity; a sharp crested rectangular weir is located before the tank entrance in the ST model. Other noteworthy differences between the two models is the normalized baffle thickness of the ST tank which is approximately 5 times greater than CT-1 and the compartment width of the ST is 15% narrower as a result of the baffle thickness. The impact of the narrower compartment width undoubtedly results in an increased compartment cross-sectional velocity which is, however, neutralized in this analysis through the normalization process with the cross-sectional bulk velocity U_b .

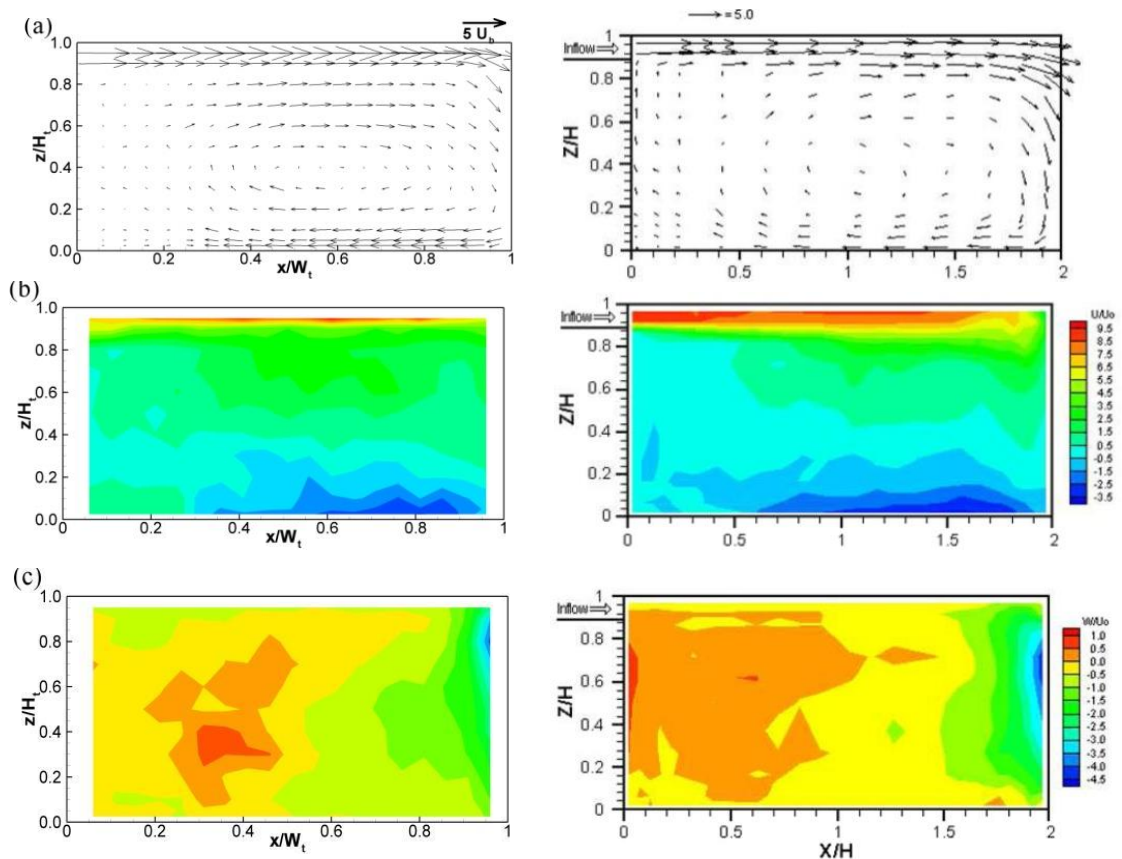


Figure 5.9 Normalised mean velocities measured in this study (on the left) and Rauen (2005) (right) for: a) Vector plot of the resultant velocity field; b) horizontal velocity (U/U_b) and c) vertical velocity (W/U_b) contour plots.

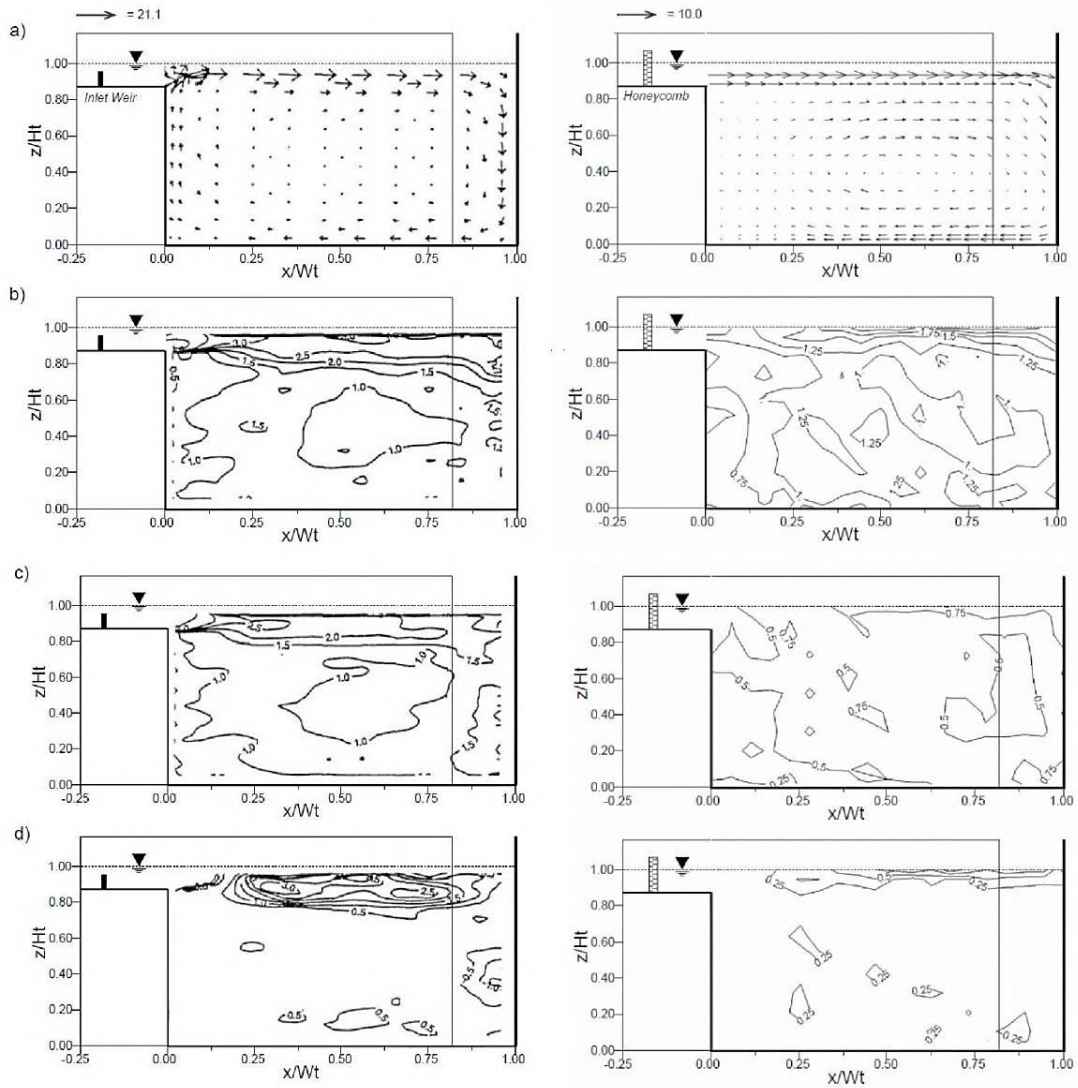


Figure 5.10 Mean flow and turbulent parameters graphical comparison a) velocity vector plots, b) contour plot of turbulent intensity u'/U_b , c) w'/U_b and d) Reynold's stress $\overline{uw'}/U_b^2$

Figure 5.10 presents velocity vectors and contour lines of the streamwise turbulence intensity and the primary Reynolds stress in the centre plane of the first compartment. In the left column the results of the present study are depicted whilst in the right column the results of the ST study are shown. For consistency, all quantities were normalised based on tank dimensions W_t , L_t , H_t or bulk velocity U_b . In the ST model the vertical recirculation zone covers the whole length of the compartment and has its centre at approximately $x/W_t = 0.5$, $z/H_t = 0.5$. In the present model the recirculation zone only occupies the region between $0.20 < x/W_t < 1.00$ and is centred at $(0.60, 0.40)$ for the particular longitudinal profile. The region between $0.00 < x/W_t < 0.20$ and $0.00 < z/H_t < 0.80$ is dictated by very low flow velocities and can arguably be classified as a dead zone.

The difference in the flow patterns between the two models can be explained by the difference in inlet configuration. The weir in the approach channel of the ST leads to a more intensified jet entering the first chamber of the tank. Accordingly, the inflow horizontal velocity reaches a maximum magnitude of $U_{max,ST} = 21.1U_b$, (as compared to $U_{max,CT-1} = 9.52 U_b$), hence this jet adds considerably more momentum to the inlet flow compared to the tank under investigation in this study, resulting in the larger recirculation zone. This illustrates how minor changes in the inlet can have a large effect on the compartment hydrodynamics.

In the second and third row of Figure 5.10 streamwise and vertical turbulence intensities, u'/U_b and w'/U_b , are plotted. Overall, the turbulence levels are significantly higher in the ST model, which is a direct result of higher momentum of the jet, generating a significantly stronger shear layer between the high momentum near surface flow and the recirculation zone underneath it. In terms of turbulence intensity magnitudes the ST tank features approximately three times higher streamwise turbulence near the water surface than the present tank, however in the remaining tank volume turbulence intensity levels are of similar magnitude at similar locations. The shear layer is visible from the shear stress contour lines as depicted in the bottom row of Figure 5.10. Again, near the water surface significantly greater magnitudes of $-\overline{uw}/U_b^2$ are found in the ST than in the present model, whilst in the rest of the tank magnitudes of the shear stress are similar.

With regards to compartments 2-8, the ST tank layer-averaged velocities were plotted as shown in Figure 5.11(a) for measurements in the centreline of the tank width ($x/W_t = 0.50$). The ADV measurements which correspond to these layers for CT-1 are also plotted herein for comparison suggesting a satisfactory agreement between the velocity data sets and implying very similar flow patterns in both CT laboratory models. Figure 5.11(b) compares turbulence intensity (u'/U_b) results with respect to tank length for the ST model and CT-1 respectively. In terms of turbulence decay, the higher levels of turbulence are apparent for ST in compartments 1 and 2. The rapid decay which was placed in the end of compartment 2 for CT-1 commences earlier in the ST model as clearly seen between $0.12 < y/L_t < 0.30$. In subsequent compartments the turbulence intensity appears to be consistent in both cases between $0.5 - 0.6 u'/U_b$.

Observed hydrodynamic conditions are significant for the transport of a scalar, or in the context of water treatment facilities the transport of pathogens. Effects of hydrodynamics on scalar transport are examined by the tracer analysis expanded in the next section.

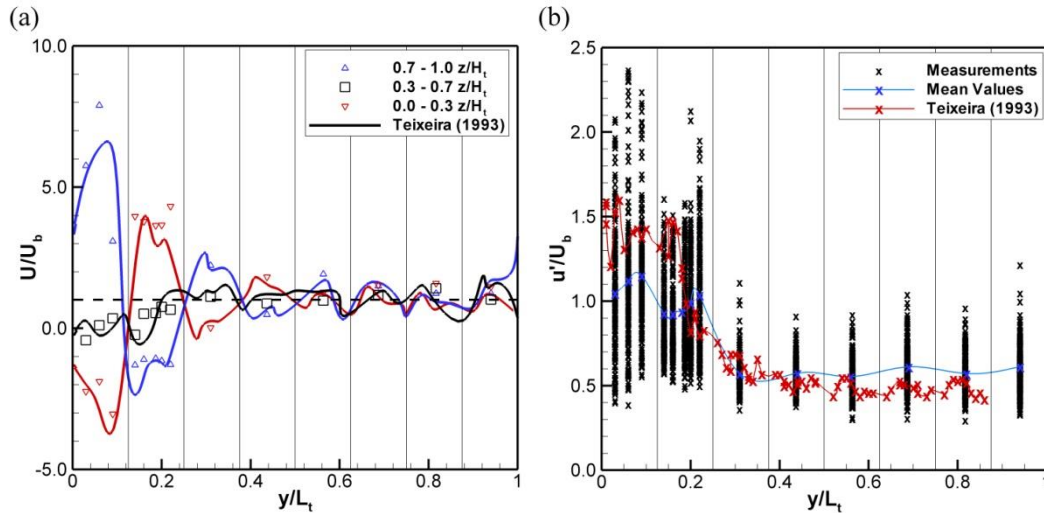


Figure 5.11 Correlation of (a) mean velocity and (b) turbulence intensity results with the available data of Shiono and Teixeira (2000)

5.3 TRACER ANALYSIS OF CT-1

The experimental tracer analysis of CT-1 was based on the 25 tracer sampling points distributed evenly across the outlet and the centre of each compartment as shown in Figure 3.5. A general discussion of how tracer disperses and mixes in CT-1 is made in section 5.3.1, according to the RTD curves produced with respect to the theoretical retention time. In section 5.3.2 the RTDs are normalized with respect to the retention time for each individual monitor point and attention is shifted towards the impact of hydrodynamic conditions on the RTD of the tracer. A connection with hydraulic efficiency is made in 5.3.3 with the derivation of disinfection-related Hydraulic Efficiency Indicators (HEIs) assessing the deviation of the flow from optimum conditions. In section 5.3.4, the performance of the dispersion model to produce hydraulic efficiency parameters is examined by comparing the experimental findings against plug flow using theoretical or previously measured conditions of dispersion.

5.3.1 RTD Curve Analysis of Mixing Conditions

A holistic approach on tracer analysis was adopted, where instead of simply treating the CT reactor as a “black box”, sampling points were primarily situated in the interior of

the tank. These data sets provide an indication of the mixing conditions that prevail during the operation of such facilities at water treatment works. Figure 5.12 depicts vertically averaged normalized RTD curves for each of the CT-1 compartments as well as the outlet monitor point with regards to the tank theoretical retention time T .

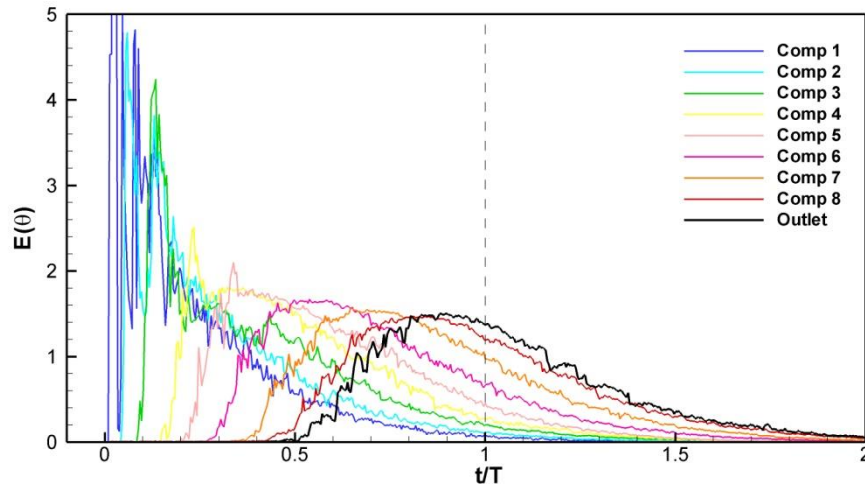


Figure 5.12 Residence Time Distribution (RTD) curves for each compartment normalized with respect to the theoretical retention time T .

The shape of the normalized RTD appears to vary significantly between compartment 1 and the outlet. In compartments 1 and 2, the curve is highly skewed to the right side, an indication of extensive mixing conditions which detains tracer longer than expected in these compartments as shown by the strong tailing effects. Even for $\theta = 1.0$, there is still traceable concentration in compartments 1-2. From compartment 3 onwards the tailing effects do not seem to change significantly, a sign of more desirable mixing conditions, which appears to be concurrent with the absence of three-dimensionality discussed previously in the hydrodynamic results.

Effects of short-circuiting become apparent by the early concentration peaks in some of the curves. This is obvious in compartments 1-4 in Figure 5.12. Even though these diminish in compartments 4-8, the overall impact of short-circuiting can be noticed at the outlet by the deviation of the outlet curve peak and the theoretical retention time. Specifically, the value of t_p is monitored at 0.87θ rather than 1θ , a detrimental consequence of the tank hydraulic inefficiency.

5.3.2 Impact of Flow Patterns on Solute Transport

As mentioned previously, the occurrence of recirculating flow structures is concurrent with the presence of a pronounced advective flow path, in which the average flow

velocity is faster than the cross-sectional mean velocity U_b (Thackston et al., 1987). The significance of the above statement for solute transport would be that some pathogens (or tracer particles) that are being transported in this flow path are advected much faster through the system than the average residence time T , i.e. they short-circuit. On the other hand, increased velocities in one area of the tank leads to excessive shear and turbulence and thus other pathogens are being transported by means of turbulent diffusion into recirculation or dead zones and remain in the system for a longer period of time than T . Quantitative evidence of this behaviour is provided in the following.

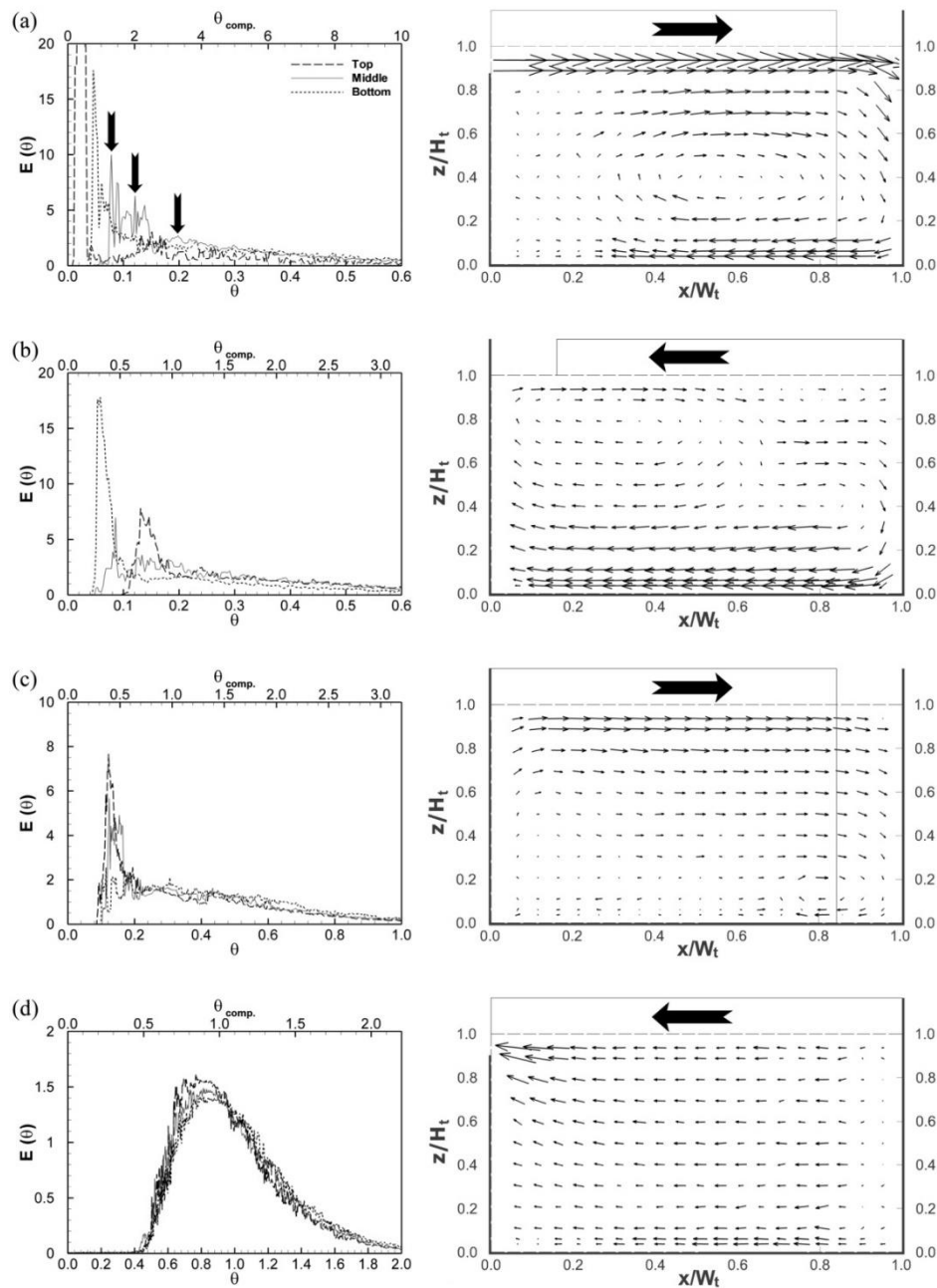


Figure 5.13 RTD curves vs Compartment flow patterns. a) 1st compartment, b) 2nd compartment, c) 3rd Compartment, d) 8th Compartment. Fluorescence peaks indicating flow recirculation are marked in the 1st compartment RTD Curve.

Figure 5.13 presents RTD curves of the tracer in the centre of compartments 1,2,3 and 8 (left column) and the respective flow fields in the centre plane for each compartment (right column). Figure 5.13 suggests that convection is the main mode of solute transport as shown by the tracer RTD curves. This is best illustrated by the first row of Figure 5.13. The tracer that was injected at the inlet is advected with the inlet jet flow, and hence the tracer curve has a significant peak ($E(\theta)=76.8$ at $\theta= 0.0195$), i.e. it appears almost instantly in the top layer of the compartment. Then, part of it is deflected from the wall towards the bottom of the compartment, which is derived from the peak in the RTD curve of the bottom location ($E(\theta)=19.3$ at $\theta= 0.0446$) and is then transported into the recirculation zone where the concentration peak appears last ($E(\theta) = 6.5625$ at $\theta = 0.1003$). The vectors on the right and illustrate the quasi 2D recirculation. In addition, the RTD curve near the surface exhibits several distinct secondary peaks (indicated by the arrows), suggesting that some tracer recirculates through the first compartment multiple times. This behaviour was also observed by Kim et al (2010b), who showed that tracer circuits multiple times in large recirculation zones.

In the 2nd compartment, the tracer initially appears near the bed, which is a result of the recirculation in the 1st compartment, because some tracer that is deflected at the end wall of compartment one gets advected near the bottom into compartment two (see sketch in Figure 5.3b), which is where the velocities are highest (Figure 5.6). There is also vertical recirculation in the second half of the compartment, whilst in the first half the flow exhibits the strong three-dimensionality due to the horizontal recirculation resulting from separation at the baffle edge. In the 3rd compartment, the tracer appears first at the free surface, a result of the recirculation in compartment two. The tracer RTD curves in compartment 3 exhibit similar trends as in the first two, i.e. distinct peaks near the surface and bottom due to recirculating flow, however, the tracer appears to be better mixed as the peaks occur at approximately the same time. From the vector plot on the right hand side it is seen that the flow still features recirculation regions, however, the velocities are lower, i.e. the recirculation has less momentum in transporting tracer.

As a comparison, in compartment 8 recirculations seem absent and the tracer RTD curves almost collapse. However, all three curves exhibit strong tailing behaviour, i.e. the curve is non-Gaussian and skewed towards higher residence times, a sign of significant internal recirculation, which is the result of the complex two and three-

dimensional flow in previous compartments (particularly in compartment 1 where the tracer circuits through the recirculation zone multiple times as discussed for Figure 5.12).

5.3.3 Hydraulic Efficiency Characterization

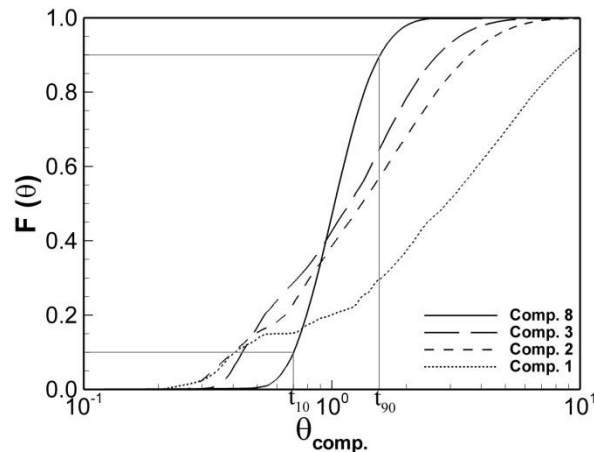


Figure 5.14 Vertically Averaged F curves for sampling points at compartments 1, 2, 3 and 8 as measured experimentally. Specifically for the compartment 8 F curve, t_{10} and t_{90} values are indicated to demonstrate how they are obtained for HEI calculation.

Qualitative analyses of the hydraulic performance of CTs based on normalised RTD curves usually involve an assessment of the degree of similarity between the results obtained for a given tank and the corresponding reference curve, i.e. for plug flow or plug flow with dispersion. In addition to this, the tracer curve analysis here is complemented by the calculation of Hydraulic Efficiency Indicators (HEI). Standard indicators previously introduced in Chapter 3 are considered for the performance assessment of CT units i.e. t_{10} , t_{90} , σ^2 , and MO . The indicator t_{10} serves as a measure for severity of short-circuiting whereas t_{90} highlights the extent of internal recirculation. The MO (Morrill index) along with the dispersion index σ^2 indicate the amount of mixing in the disinfection tank.

The HEIs t_{10} and t_{90} and thus MO can be obtained from the cumulative tracer curve $F(\theta)$, which, for compartments 1, 2, 3 and 8, is depicted in Figure 5.14. The thin horizontal lines indicate that 10% and 90% of the tracer respectively have reached compartment 8 in the respective dimensionless time θ (i.e. t_{10} and t_{90}). The steeper the curve, the better the performance, i.e. tracer dispersion is small, and whilst this is true for the tracer in compartment 8, the $F(\theta)$ curves for the other compartments are quite gently sloped, i.e. early exit of 10% of the tracer and a significant residence time of 90% of the rest of the

tracer. Obviously, and due to the flow and transport characteristics elucidated before, the $F(\theta)$ curve of the tracer in compartment 1 is particularly flat, a sign of poor hydraulic performance.

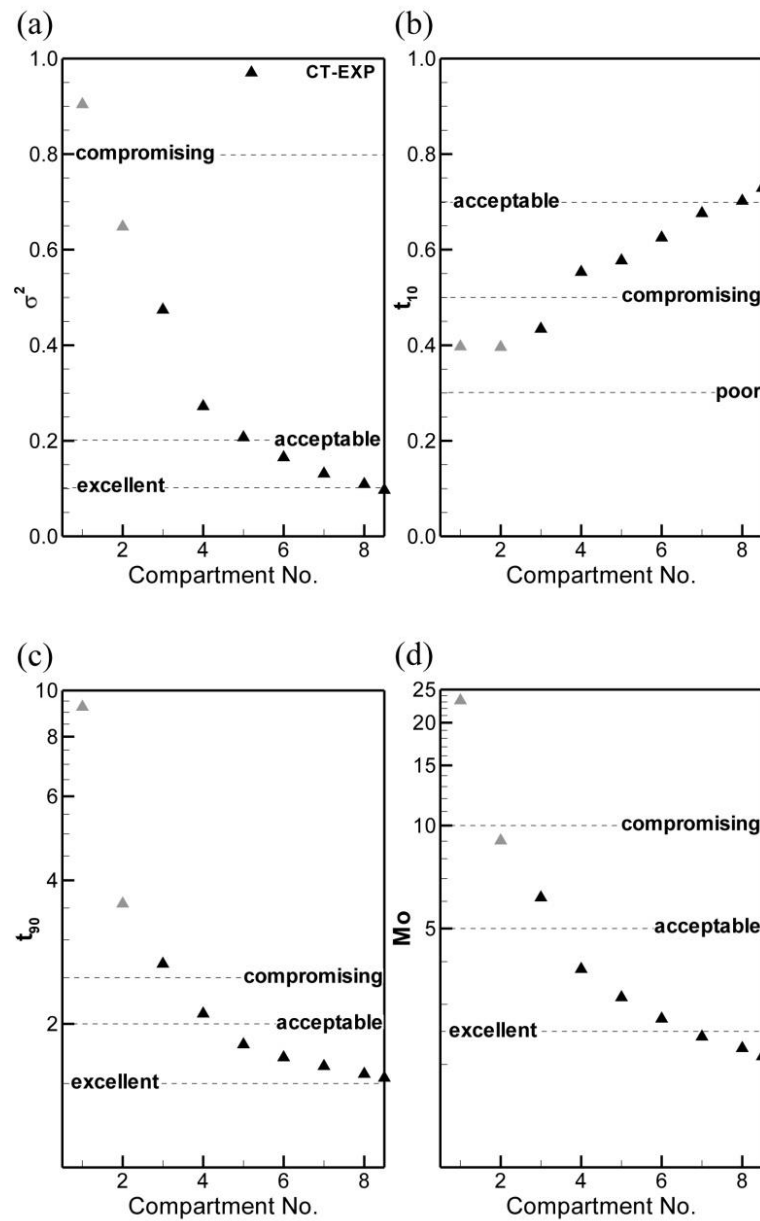


Figure 5.15 HEI indicators as a function of distance from the inlet (here in terms of compartment number) obtained experimentally. The hydraulic performance of the tank is indicated for each HEI ranging between poor, compromising, acceptable and excellent. Grey data points indicate results which are influenced by tracer mass re-appearance.

Figures 5.15(a) and 5.15(d) show a plot of σ^2 and Mo as a function of compartment number, where both HEIs appear to be particularly high in compartments 1-4 and decrease exponentially towards the outlet. These two indicators reflect the complex hydrodynamics close to the inlet and the transition to quasi two-dimensional flow in the horizontal plane from compartment 3 onwards. In Figure 5.15(b-c) t_{10} and t_{90} are plotted

against the compartment number. While t_{10} increases gradually with compartment number, t_{90} decreases rapidly and reaches an asymptotic value. The number of compartments hence plays an important role in the efficiency and functionality of the contact tank. An easy way to assess the design efficiency is the four-tier hydraulic performance colour code as proposed by Van der Walt (2002), which classifies the disinfection tank design as “poor”, “compromising”, “acceptable” and “excellent” for each of the four HEIs. For the tank under investigation in this study, all indicators suggest the design to be “acceptable” but only from the 6th compartment onwards. Noteworthy is the fact that the “excellent” threshold is surpassed only at the outlet ($\sigma^2 = 0.095$, $t_{10} = 0.73$, $t_{90} = 1.50$, $Mo = 2.05$), justifying the need for 8 compartments for the current configuration. In addition, the “compromising” values of t_{10} and t_{90} between compartments 1 and 3 reaffirm the previous observations of increased short-circuiting and tracer entrapment due to the inflow water jet that is dominant in those chambers.

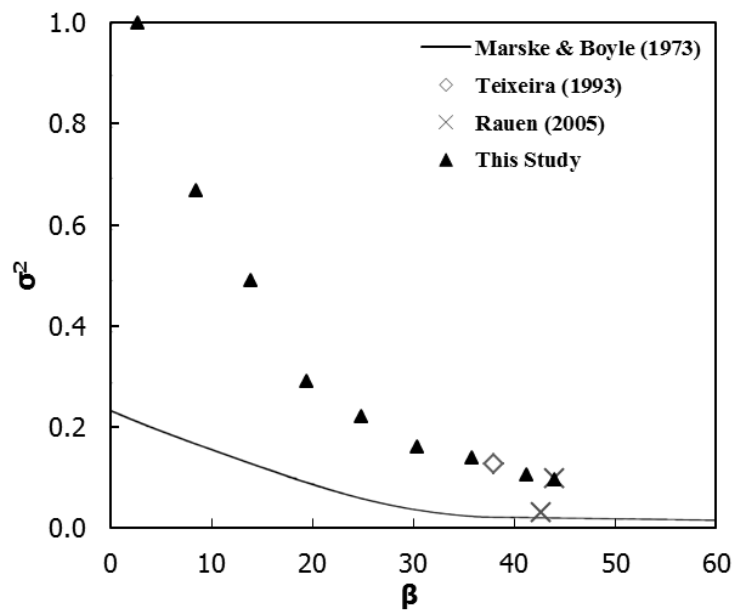


Figure 5.16 Dispersion Index with respect to tank length to width ratio (β) according to the tracer experiments of the present work, Marske and Boyle (1973), Teixeira (1993) and Rauen (2005)

HEI results for serpentine CTs are generally limited to outlet tracer tests in the literature such as for the study of Marske and Boyle (1973). Further HEI data could be obtained from the available RTD curves of Teixeira (1993). Figure 5.16 includes all available σ^2 values from the previous experiments along with a distribution curve derived from several field scale CTs as published by Marske and Boyle (1973). In contrast to Figure 5.15, Figure 5.16 plots the results with respect to the length to width ratio (β) to make the comparison of different tanks against the CT-1 model feasible. The ST tank ($\sigma^2 =$

0.126) seems to be less efficient than the current CT, which could be associated with the worse hydrodynamics in compartment 1. Rauen (2005) undertook a series of experiments in the same model yielding almost identical results for the HEI ($\sigma^2 = 0.095$, $t_{10} = 0.70$, $t_{90} = 1.48$, $Mo = 2.12$) as in the present study providing further verification of the reproducibility of the RTDs and the normalization process.

The distribution of the dispersion index of the present study is considerably above the one of Marske and Boyle (1973), particularly in the early compartments of the tank, suggesting poorer performance. It is speculated that not only flow-length-to-width-ratio influences the performance of such tanks but also other geometrical features. Indeed, when Rauen (2005) changed the baffling configuration, the HEIs obtained were $\sigma^2 = 0.055$, $t_{10} = 0.78$, $t_{90} = 1.32$, $Mo = 1.69$, i.e. overall superior performance. Other factors could include the tank depth, as the investigation of Marske and Boyle does not report on details of the vertical tank dimensions which could imply that the tanks of that study had negligible depth compared to the other dimensions and therefore predominantly 2-D flow.

5.3.4 Comparison against Theoretical Dispersion Models

The dispersion index σ^2 is particularly interesting in this analysis due to its connection with the dispersion number d through equation (2.6). The value of d is in turn related to the longitudinal dispersion coefficient D_L ($= dU_bL$), which is used to predict theoretically the depth-mean concentration-time series of a conservative tracer under idealized flow conditions, using Levenspiel's (1999) equation:

$$C = \frac{M}{A\sqrt{4\pi D_L t}} e^{\left[-\frac{(x-Ut)^2}{4D_L t}\right]} \quad (5.2)$$

where A is the compartment cross-sectional area and x is the distance from the injection point. In equation (5.2) the effects of hydrodynamic complexity in the CT are included in the turbulent dispersion number D_L , which is, however, neither constant nor known *a-priori* and hence must be calibrated or determined through an empirical formula. For open-channels with a logarithmic velocity profile, D_L can be computed as (Elder, 1959):

$$D_L = 5.93U_*H_t \quad (5.3)$$

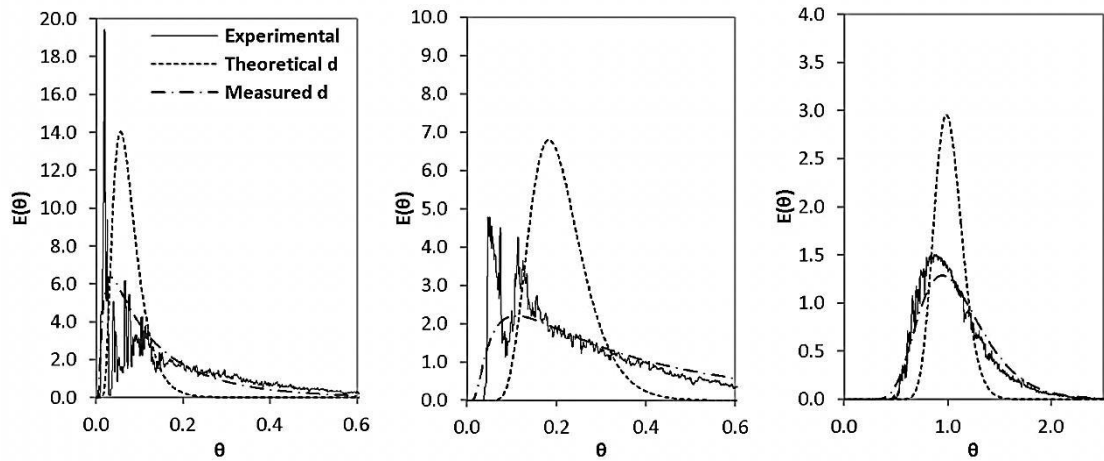


Figure 5.17 Theoretical and Dispersion Calibrated RTD curve predictions against experimental measurements: (a) 1st compartment, (b) 2nd compartment and (c) 8th Compartment

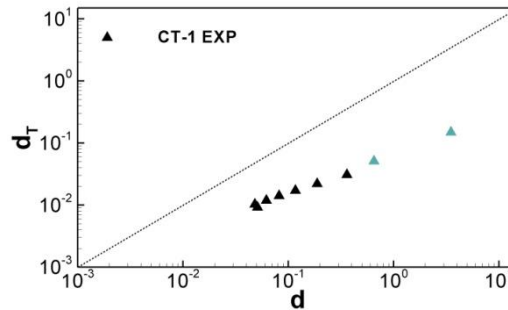


Figure 5.18 Deviation between measured (d_M) and theoretical (d_T) dispersion number prediction. The compartment number of the measured dispersion numbers is indicated in the figure.

Figure 5.17 portrays RTD curves for compartments 1, 2 and 8. The dashed line denoted “Theoretical d ” represents the curve as calculated through equation (5.2) using an uncalibrated dispersion number D_L computed using equation (5.3), the dash-dotted line denoted “Measured d ” represents the RTD curve as calculated through equation (5.2), but using the measured σ^2 values (Figure 5.16) to obtain d to compute D_L . The solid line represents the vertically averaged measured RTD curve.

The two different d values are compared directly in Figure 5.18. It is obvious that the measured d values are consistently and significantly greater than the theoretically obtained ones, implying gross under-predictions of the dispersion in the tank. As a result, there are marked differences between “Theoretical d ” and experimental RTD curves, particularly in compartments 1 and 2. Even with *a-priori* knowledge of the longitudinal dispersion number the experimental curves cannot be matched due to the strong multi-dimensionality of the flow. Clearly, both theoretically and experimentally obtained dispersion numbers cannot account for these effects.

However, the peak of the calibrated curve coincides with the measured peak in terms of dimensionless time θ , a sign that the t_{10} predictions might be reasonably good. Similar behaviour is observed for compartment 2. Whilst “Theoretical d” RTD curve predictions don’t agree well with the observed curve, the predicted RTD curve using the experimentally obtained longitudinal dispersion number match the measured RTD curve quite well, in terms of both the location of the peak and the tailing of the curve, suggesting that short-circuiting and internal recirculation is captured reasonably well. Finally, the predictions for compartment 8: the dispersion model seems to predict a reasonable RTD shape with an experimentally determined dispersion number, which demonstrates the potential of the theoretical approach. However, the relatively poor agreement of the RTD curve obtained using a theoretical value for d suggests that it is imperative that dispersion number values have to be known *a-priori*.

Table 5.2 Morrill index (Mo) as predicted by using the theoretical model and as obtained experimentally in tabulated form.

Comp.	Morrill Index		
	CT-1 EXP	Theoretical d (Error %)	Measured d (Error %)
1	23.24	2.74 (88.2)	78.42 -(237.4)
2	9.03	1.78 (80.3)	12.77 -(41.3)
3	6.15	1.56 (74.6)	7.28 -(18.5)
4	3.80	1.46 (61.6)	4.19 -(10.1)
5	3.14	1.40 (55.5)	3.44 -(9.5)
6	2.72	1.35 (50.3)	2.84 -(4.3)
7	2.41	1.32 (45.2)	2.61 -(8.4)
8	2.23	1.30 (41.9)	2.30 -(3.3)
Outlet	2.05	1.28 (37.6)	2.27 -(10.7)

From the RTD curves of Figure 5.17, the HEIs can be derived, here only for the Morrill Index and these are summarized in table 5.2. For CT-1, the theoretical results (without *a-priori* knowledge of the dispersion number) translate to an excellent performance ($Mo < 2.5$) from the 2nd compartment onwards. This is in vast conflict with the experiments which are indicating poor to compromising conditions until the 4th compartment. Even though the relative error between the data sets steadily decreases as more plug flow like conditions occur, theoretical predictions appear inadequate to produce a reasonable estimation. Clearly, application of the theoretical equation including unknown dispersion numbers to design contact tanks can lead to substantial under-design implications. On the other hand, if the dispersion number is known *a-priori* then a very good estimate for the tank performance is obtained already from compartment 3 onwards.

5.4 CHAPTER SUMMARY

In this Chapter a discussion is made on velocity and tracer results at various locations of CT-1 obtained experimentally. The velocity measurement data were analysed to identify short-circuiting and internal recirculation, which are accountable for disinfection performance deficiencies. Based on the tracer residence time distribution curves, disinfection-related hydraulic efficiency indicators (HEIs) were obtained to assess the contact tank's performance. In terms of the hydrodynamics, comparisons were made with data from the previous studies of Teixeira (1993) and Rauen (2005). It is shown that the inlet configuration has a marked influence on the hydrodynamics in the early compartments of the tank, causing significant recirculation zones in a large portion of the compartment and leading to subsequent three-dimensionality of the flow even up to compartments 2-3. Similarly, the inlet conditions cause elevated levels of turbulence kinetic energy and its sources (shear, bed and wall) were identified. Based on these hydrodynamic measurements in CT-1, the inflow resembled a jet due to the approach channel design, which results in stronger recirculation and up to three times higher turbulence levels in compartment 1.

The correlation between the hydrodynamics and the tracer RTD curves obtained in each compartment suggest that advection is the main mode of tracer transport, demonstrating the strong interlink between the hydrodynamics and solute transport. The calculation of various HEIs from accumulated tracer curves obtained for each compartment allowed monitoring contact tank performance as a function of distance from the inlet or compartment number, respectively. The obtained HEIs were compared to previous studies and were subjected to a four tier tank performance code, categorising it into categories ranging from excellent to poor. For the 8 compartment CT-1 model under investigation here, the HEIs suggest poor disinfection performance in the early part of the tank, while excellent performance for some HEIs is reached only very close to the outlet.

Considering that the baffled design opts for plug flow conditions throughout the tank volume, the experimental results were compared with predictions of a purely theoretical approach based on the dispersion model. This model takes into consideration complex hydrodynamic conditions, through a dispersion number, the value of which is unknown a-priori and needs to be estimated. It is shown that with a-priori knowledge of the

dispersion number, HEIs can be predicted reasonably accurately. However, it is also demonstrated that HEI predictions without a-priori knowledge of the dispersion number can be grossly erroneous. Hence, assessment of existing or design of new contact tanks, for which the hydrodynamics depart from plug flow conditions, either require a-priori known input into theoretical modelling approaches or more sophisticated (multi-dimensional) modelling techniques. This outcome acts as a prelude for the three-dimensional CFD approach which is evaluated in Chapter 6.

CHAPTER 6

NUMERICAL SIMULATIONS

6.1 INTRODUCTION

This Chapter focuses on the results of computational fluid dynamics (CFD) simulations of flow and solute transport in CTs. Three-dimensional numerical model simulations of flow and transport characteristics have been conducted using a RANS equation approach described in Chapter 4. A description of the CT computational model setup and preliminary mesh convergence analysis is included in Section 6.2. Section 6.3 centres upon the agreement between simulated velocity and solute transport results against laboratory data to evaluate the validity and the predictive capabilities of the numerical model. Experimental data were obtained from the velocity and tracer transport measurement campaign which was the subject of Chapter 5. The geometry of the computational CT model is then altered in section 6.4 to examine the effects of geometrical scale as well as different inlet and baffling configurations on the hydrodynamics and mixing properties.

6.2 CONTACT TANK NUMERICAL MODEL SETUP

A certain degree of preliminary processes are necessary to perform CFD analyses. A flow chart depicting this process is given in Figure 4.2. As an example, some important details for the setup of the CT-1 numerical model are expanded below.

The geometry and boundary conditions expanded below is chosen to replicate the laboratory experiments. At the inlet surface, a Dirichlet boundary condition is applied for the velocity and turbulence parameters. Transversal V and vertical W velocity components are set to zero and a uniform streamwise velocity U is assumed with a magnitude based on the experimental study flow rate. A Neumann condition with mass conservation is imposed at the outlet surface for all variables. The water surface is treated as a rigid, frictionless lid, with no shear stress. The side walls, tank bottom and internal baffles are considered smooth to match the low roughness surfaces of the laboratory model, and low Reynolds number wall functions are employed. However, properties of these conditions had to be altered when modifying the CT geometry. For example, for field-scale circumstances the wall-function of equation 4.14 is imposed instead of the smooth-wall law of equation 4.18.

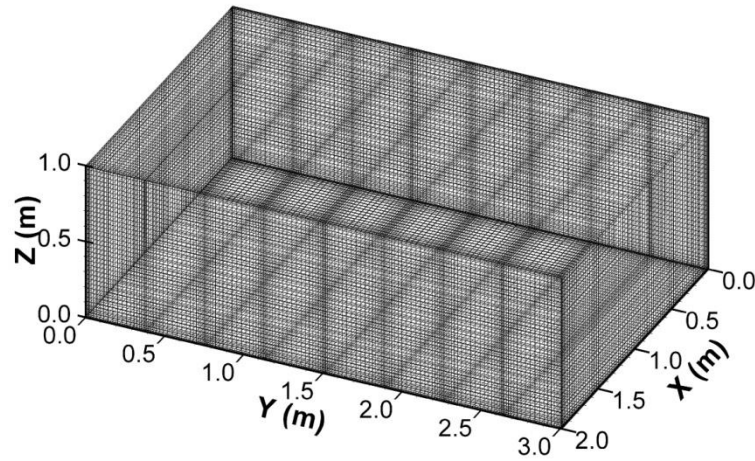


Figure 6.1 3-D Mesh (MM) used for hydrodynamic and solute transport simulations

Grid independency can be considered as a quality indicator for RANS simulations (Kim et al., 2013). Therefore, successively finer meshes were preliminary tested to ensure that the simulation results converged and were considered independent of the grid size. Table 6.1 provides the details of the 4 progressively finer grids used in this study. The grids are denoted CM (Coarse Mesh), MM (Medium Mesh), FM (Fine Mesh) and RM (Refined Mesh). All grids feature a refinement near the side walls, baffles and an inlet arrangement (Figure 6.1) to ensure proper resolution of the steep gradients. The RM, as the most time consuming approach, was only run in for the hydrodynamic simulations to verify the FM’s mesh convergence. The computational time of the FM simulation was approximately 1.5h while running on a Windows operating system with a 2.83GHz processor and 3.24 GB RAM. The MM simulation converged in less computational time (≈ 0.5 h) while RM and CM run for 24h and 0.1h, respectively.

Table 6.1 Mesh Resolutions of numerical models.

Mesh	Dimensions (i, j, k)	Min. cell Dimension (mm)	Max. cell Dimension (mm)	Compartment Width (cells)	y ⁺ (mm)	Total Numerical Points
RM	360 x 127 x 64	1	20	45	0.5	2,926,080
FM	161 x 77 x 42	10	30	20	5	520,674
MM	113 x 57 x 33	20	40	14	10	212,553
CM	97 x 45 x 23	30	50	12	15	100,395

The potential to produce predictions of satisfying quality using the aforementioned grid resolutions was assessed by comparing vertical velocity and turbulence kinetic energy profiles for certain points inside CT-1. Some evidence of this is demonstrated in the validation section which follows. In general, all grids except from CM show

encouraging performance, while the majority of the results in this chapter are presented for the FM mesh characteristics, unless stated otherwise.

6.3 NUMERICAL RESULT VALIDATION

Generally, the validation procedure is greatly influenced by the experimental data availability. Typically, previous studies on contact tank hydrodynamics and tracer transport have simply relied on the reproduction of the outlet RTD curve as discussed in Chapter 2. Unfortunately, this practise can be sometimes misleading due to the uncertainty of the interpretation of RTD curves pointed out by Levenspiel (1999). Comparisons with hydrodynamics have been limited to velocity measurements in the studies of Khan et al. (2006) and Rauen (2005) without any reference to the turbulence data obtained experimentally. In contrast, a more elaborate approach is followed here as the laboratory work provided a comprehensive data set of velocity and turbulence readings for hydrodynamics. In order to validate solute transport, CFD predictions are compared with the RTD data derived from multiple locations in the interior of the tank, instead of being limited to comparisons against outlet RTD results.

6.3.1 Hydrodynamics

A major advantage of computational over physical modelling is the wealth of data that can be extracted in the post-processing stage. This is better observed in Figure 6.2, where computational results from across the domain have been plotted against actual measurements, with a view to highlighting the overall agreement between the two data sets. A quick inspection suggests that the computational simulations yield encouraging results as the experimental data in all the compartments is within the range predicted by the simulations. In terms of velocity measurements the CFD produces extensively higher velocities in compartment 8 which was not identified by the ADV results. This is due to the region where such velocity magnitudes develop being very close to the free surface near the outlet weir, where ADV measurements are not feasible using the available down-looking probe. This is further reflected by the high k levels near the outlet which were not captured by the experimental investigation at these locations. Similar issues arise in compartments 1 and 2, as even though the average values are in good agreement with the experimental readings, intensified turbulence is predicted in near-wall regions where ADV measurements become unreliable due to the close

proximities to solid surfaces. On the other hand, k levels in compartments 4-7 are predicted within the range obtained from the measurements, suggesting an encouraging performance of the $k-\varepsilon$ model to provide a closure to the turbulence uncertainty.

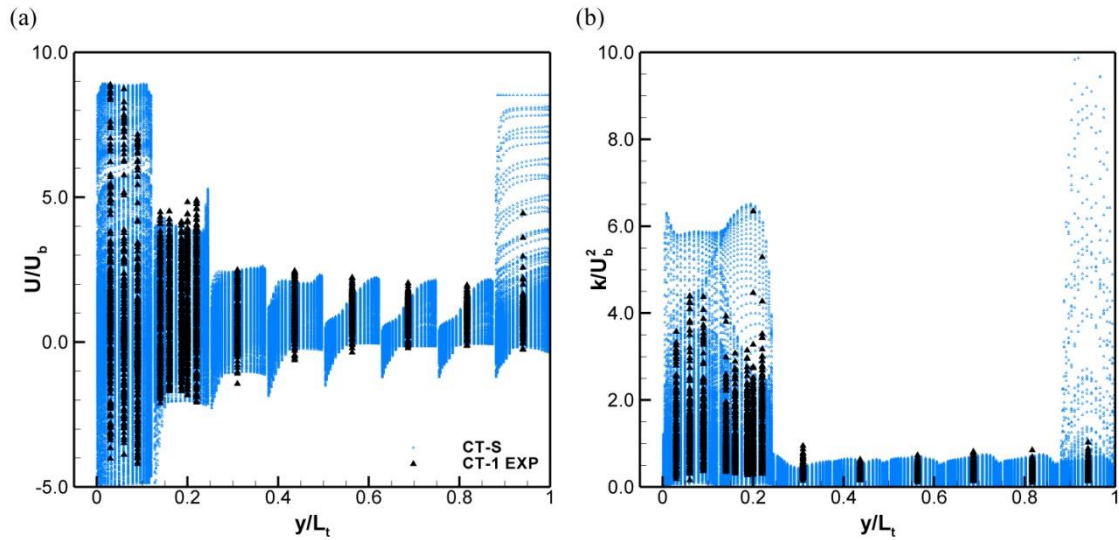


Figure 6.2 Normalised (a) Streamwise velocity (U/U_b) and (b) turbulence kinetic energy (k/U_b^2) data available from simulations with the FM mesh and experimentally.

The accuracy of the CFD model in reproducing the hydrodynamics of the experiments is examined in Figures 6.3 - 6.5. Figure 6.3(a) presents vertical velocity profiles of the streamwise velocity in the centre (i.e. $y/L_t = 0.06, 0.18, 0.94$ and $x/W_t = 0.5$) of compartments 1, 2 and 8. The figure includes experimental measurements (CT-EXP) and numerical predictions (CT-S) of the simulations for three different grids i.e. FM, MM and CM. The velocity is normalized using the cross-sectional bulk velocity U_b . A fairly good agreement between the simulations and ADV measurements can be observed in all 3 compartments, particularly for CT-S-MM and CT-S-FM simulations. CT-S-CM underestimates the high velocity near the water surface in compartment 1, but grid refinement eliminates this deviation. All three simulations pick up the strong backflow near the bottom of compartment 1. In compartment 2, the flow is still under the influence of the jet-type inflow and both predicted velocity profiles CT-S-FM and CT-S-MM agree fairly well with the ones measured. The flow is predicted to be quite uniform by the 8th compartment and simulations are reasonably accurate for all three grids.

Figure 6.3(b) presents the k/U_b^2 profiles along the centreline of the three selected compartments. CT-S-MM and CT-S-FM are able to predict well the magnitude of the k -peak created by the jet-type inflow and also the lower portion of the profile in the first compartment. The turbulence decays gradually from the inlet until halfway through

compartment 8 and all simulations, regardless of the grid, are able to match to a satisfying degree the k profile's shape and magnitudes, in compartments 2 and 8. Some discrepancies arise in the reproduction of the near-bed k profile of the 2nd compartment, but this could be attributed to ADV readings which for that location might be impaired by the close proximity to the bed surface as discussed in Chapter 3.

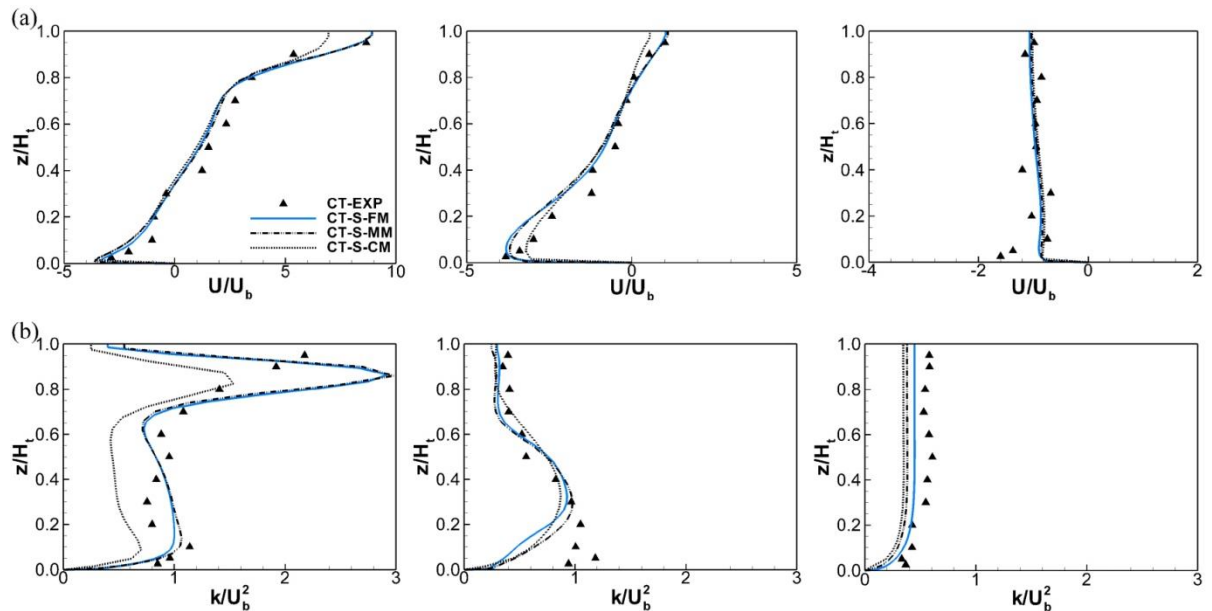


Figure 6.3 (a) Profiles of the streamwise velocity and (b) profiles of the turbulent kinetic energy k in the centre of the 1st(left), 2nd (middle) and 8th (right) compartment

Further evidence of the good performance of this CFD simulation is provided when comparing velocity and turbulence profiles against ADV data in horizontal planes for $z/H_t = 0.05, 0.50$ and 0.95 respectively and at the centreline of the tank width ($x/W_t = 0.50$) as in Figure 6.4. On the horizontal plane the available data is quite limited, particularly in compartments 3-8 as focus was primarily given on obtaining vertical longitudinal profiles to characterize the three-dimensionality of the problem. Nonetheless, the velocity predictions fit well with the measurements in all compartments while the turbulence results are in good agreement for compartment 3 onwards. Some deviations in the 1st and 2nd compartments is a consequence of the flow unsteadiness developed downstream of the inlet which is obviously not reproduced by the steady-state RANS approach adopted herein.

In general, the accurate representation of the turbulence field was considered determinant for the reliability of the solute transport and kinetic processes. For the flows developed in CTs, turbulent diffusion is a crucial factor for scalar transport and therefore its good approximation is essential for subsequent solute transport simulations.

The connection of turbulent diffusion (D_t) with turbulence quantities such as k is apparent from the eddy viscosity formulation of equation (4.8). However, previous computational studies (Khan et al., 2006; Rauen, 2005) have relied simply on the validation of velocity field rather than considering the effect of turbulence for its impact on tracer transport. On the other hand, this study provides evidence (Figure 6.3b, 6.4b) of the k - ϵ model's potential to reproduce the turbulence levels using a steady-state approach for such CT flow conditions.

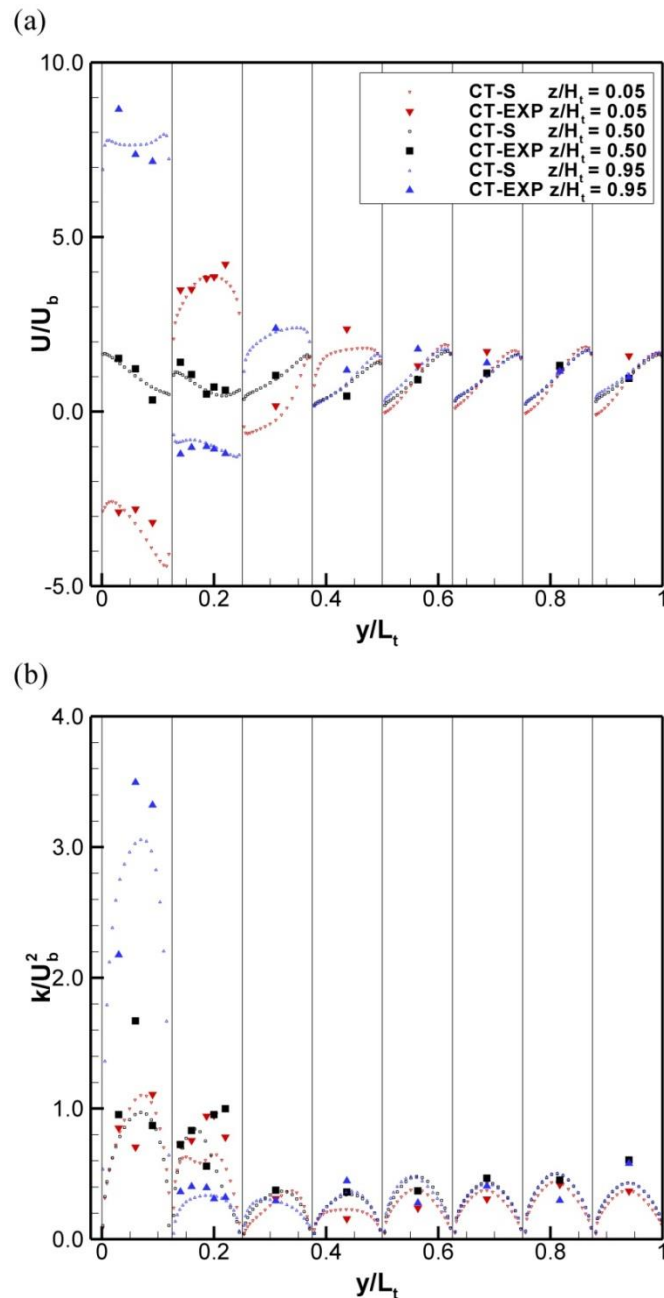


Figure 6.4 Comparison of horizontal profiles of (a) streamwise velocity and (b) turbulence kinetic energy against available experimental data at 3 different vertical planes ($z/H_t = 0.05, 0.50$ and 0.95) where $x/W_t = 0.50$.

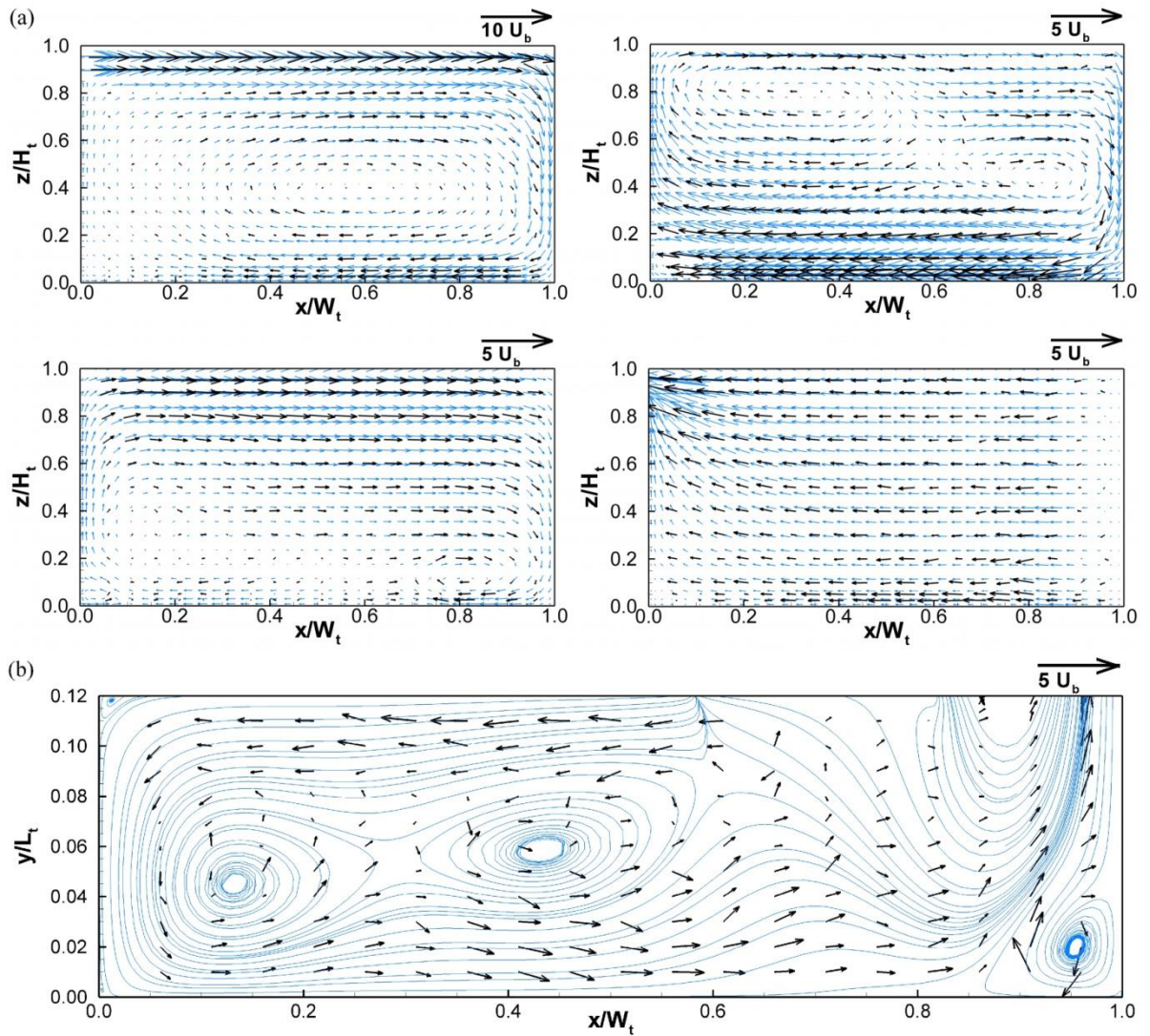


Figure 6.5 (a) Velocity vectors in the centre-plane of Compartments 1 (first row left),2 (first row right), 3(second row left) and 8 (second row right). The blue vectors represent the CT-S-FM simulation results and the black vectors represent the ADV (CT-EXP) data (b) Horizontal profile of flow at mid-depth ($z/H_t = 0.50$) for CT-S-FM streamlines and CT-EXP measurement vectors in compartment 1.

Figure 6.5(a) presents vector plots of CT-EXP measurements (black vectors) and the CT-S-FM simulation (blue vectors) along the longitudinal centre-planes of compartments 1, 2, 3 and 8 ($y/L_t = 0.06, 0.18, 0.30$ and 0.96). As discussed from the hydrodynamic results of Chapter 5, the water enters the first compartment in the form of a high velocity jet, which primarily creates a 2-D recirculation zone occupying the region between $0.20 < x/W_t < 1.00$ and $0.00 < z/H_t < 0.80$ (Figure 4(a), 1st row left). The strong jet and the subsequent deflection off the wall opposite of the inlet lead to vertical non-uniformity of the streamwise velocity and recirculation in subsequent compartments. In the second compartment (Figure 6.5a, 1st row right) the highest velocities are near the bottom where two counter-rotating eddies form and in

compartment 3 (Figure 6.5a, 2nd row left) the highest velocities are again near the surface and a relatively weak circulation cell is observed near the bed. The flow is quite uniform by the 8th compartment, except in the region close to the outlet, which is where flow accelerates. The purpose of Figure 6.5 is to compare the predicted velocity vectors and flow patterns with the measured data which was more extensively discussed in section 5.2.1. It is apparent that the CFD model has the capability of capturing fairly accurately the time-averaged hydrodynamics in the CT. In Figure 6.5(b), streamlines produced by CT-S-FM simulation highlight secondary recirculation in the horizontal plane ($z/H_t = 0.5$). Multiple secondary circulation cells in the centre of the compartment are identified and stronger flow is observed near sidewalls. The CFD model is able to pick up this trend and the simulated flow patterns agree well with the measurements (also see Figure 5.2).

6.3.2 Tracer Transport

The simulated concentration levels were monitored in the centre of each compartment, i.e. at the same sampling locations as in the experiments which are indicated in Figure 3.5. The readings have been normalized using the theoretical residence time T to produce RTD curves. The RTD predictions are discussed below followed by a subsequent HEI analysis for the assessment of the simulations with respect to the ability of deriving reliable estimates of hydraulic efficiency.

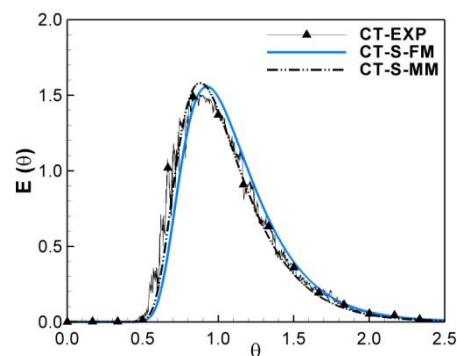


Figure 6.6 RTD curves produced at the outlet for experimental and computational data. Further refinement of the computational grid does not produce noticeable difference.

Figure 6.6 presents RTD curves at the outlet of CT-1 for CT-S-FM, CT-S-MM simulations and CT-EXP respectively. The shape of the curve is adequately reproduced by the RANS simulations, regardless of the grid and without additional calibration of the input parameters. The steep increase and the slight tailing of the curve are in excellent agreement, whilst the peak is underestimated by less than 5%.

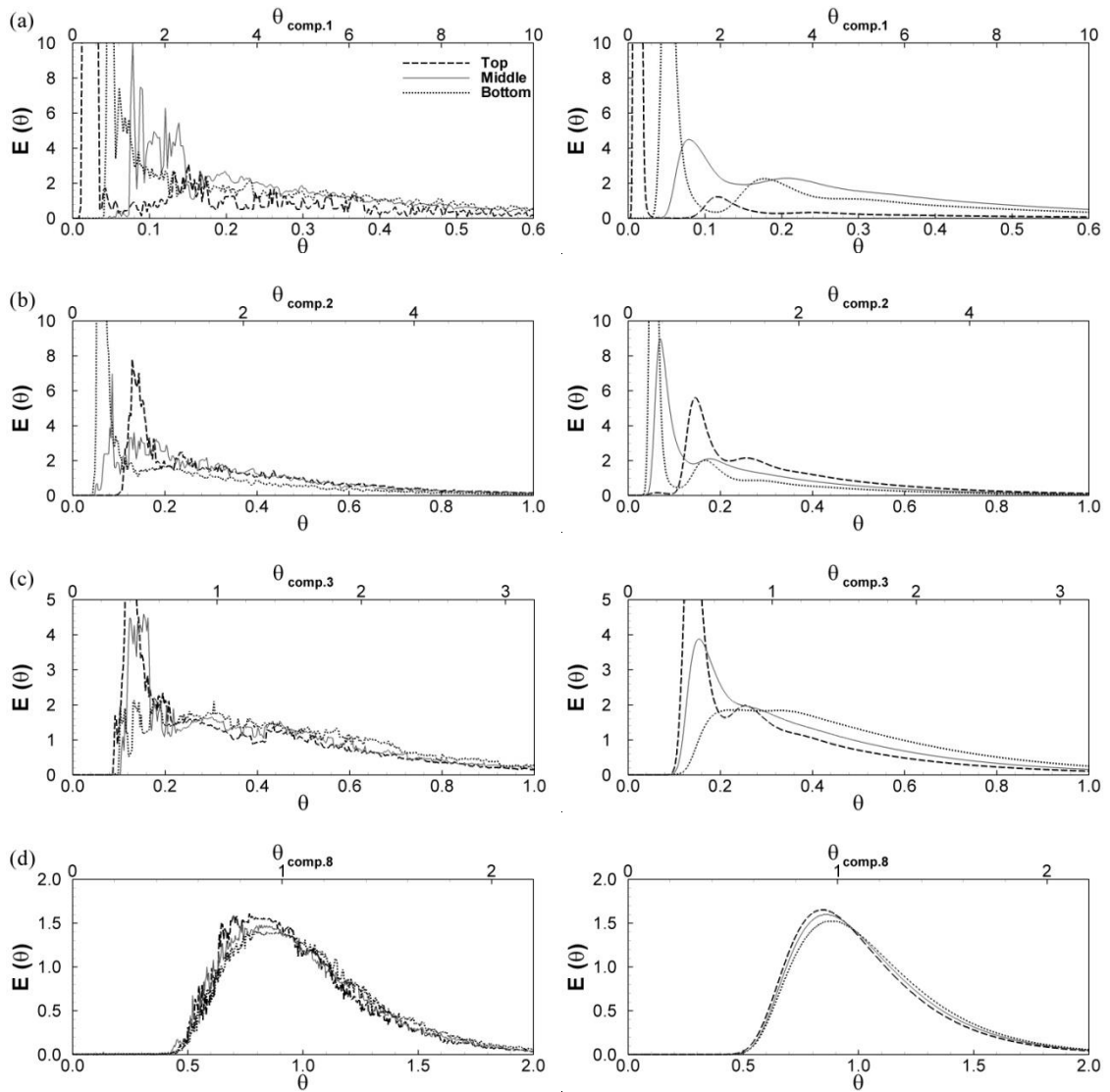


Figure 6.7 RTD curves produced for experimental and computational data (FM) at compartments (a) 1, (b) 2, (c) 3, and (d) 8: experimental RTDs (left), computational RTDs (right)

In chapter 5, advection was identified to be the main mode of tracer transport in CT-1, confirming the strong interlink between hydrodynamics and solute transport. This phenomenon is clearly illustrated by the RTD curves produced for three vertical locations along the centreline, i.e. top, middle and bottom ($z/H_t = 0.05, 0.50$ and 0.95), of compartments 1-8. In accordance with Figure 5.13(a), tracer injected at the inlet is advected with the jet and hence a significant peak ($E(\theta) = 76.81$) is almost instantly ($\theta = 0.020$) observed near the water surface of the compartment. Part of the tracer is then deflected from the wall towards the bottom of the compartment and is transported along the large recirculation zone, which is derived from the associated curve peak ($E(\theta) = 19.29$), occurring slightly later ($\theta = 0.045$) than the peak near the surface. Finally, the tracer is entrained into the recirculation zone where the concentration peak ($E(\theta) = 10.09$) appears last ($\theta = 0.073$).

The simulated peaks and their occurrence agree quite well: near the surface i.e. $E(\theta) = 94.60$ and $\theta = 0.013$, near the bottom, i.e. $E(\theta) = 21.4$, $\theta = 0.051$ and at mid-depth, i.e. $E(\theta) = 4.49$, $\theta = 0.079$. In the 2nd compartment (Figure 5.13b) the highest peak occurs first near the bed, $E(\theta) = 18.51$, $\theta = 0.057$ where the highest velocities occur, then in the middle of the compartment, $E(\theta) = 6.97$, $\theta = 0.083$, which is a result of the first of the two counter-rotating eddies that transports some tracer into the middle of the compartment and finally near the surface, $E(\theta) = 8.63$, $\theta = 0.088$. Again, the numerical simulation is able to capture this behaviour, as demonstrated by the realistic prediction of peaks and their occurrence.

The numerically predicted RTDs are much smoother than the measured distributions, with the latter exhibiting the unsteadiness of the flow. In fact, the flow in contact tanks is governed by large-scale flow unsteadiness as has been reported recently by Kim et al. (2010b, 2013), who showed that vortex shedding from baffle edges can dominate the flow and influence the transport of scalars in such tanks. The concentration fluctuations in compartment 1 (Figure 6.7a) suggest such unsteadiness in the flow which is not captured by the RANS simulation. However, for compartment 3 (Figure 6.7c), as flow becomes more uniform and the initial three-dimensionality caused by jet mixing diminishes, RANS simulations produce more accurate RTD predictions which consistently improve towards compartment 8 (Figure 6.7d) implying that despite the inability to capture the detailed unsteady flow dynamics due to the nature of the simulation, the overall behaviour of the scalar transport is well predicted herein.

Further insights into the mixing processes can be deduced by the cumulative RTD curves (F) in compartments 1, 2 and 8 of the CT-1 tank using numerical data (Figure 6.8) and the experimental data of Figure 5.14 which is incorporated for comparison. The solid grey line at $\theta = 1$ represents an ideal transport scenario, i.e. under plug flow conditions and the steeper the curve the better the performance of the CT. By the 8th compartment the F-curve is quite steep, resembling plug flow, and the curves of simulation and experiment almost coincide. The discrepancies between the curves are largest for compartment 1, which is due to the aforementioned significant unsteadiness that cannot be reproduced by the RANS model. Already in compartment 2 a much better agreement between simulation and experiment is observed. In compartments the CT suffers from severe short-circuiting and internal recirculation, which is evidenced in

the F-curve by the early occurrence of tracer (i.e. $\theta \ll 1$) and the long tail of the F-curve, i.e. $\theta \gg 1$.

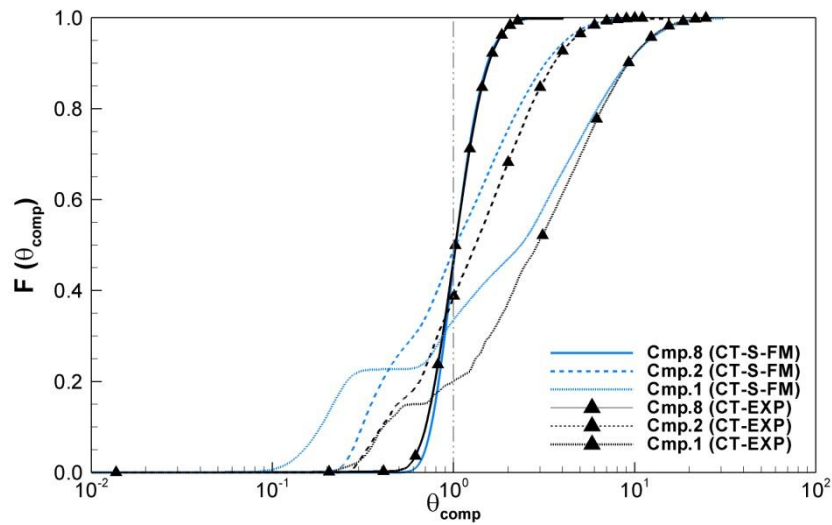


Figure 6.8 Cumulative tracer distribution (F) in compartments 1, 2, and 8 as produced experimentally and computationally

This is better quantified in the so-called hydraulic efficiency indicators (Figure 6.9), which are discussed further below. Simulation HEIs were deduced from E and F curves such as the ones shown in Figures 6.6 - 6.8.

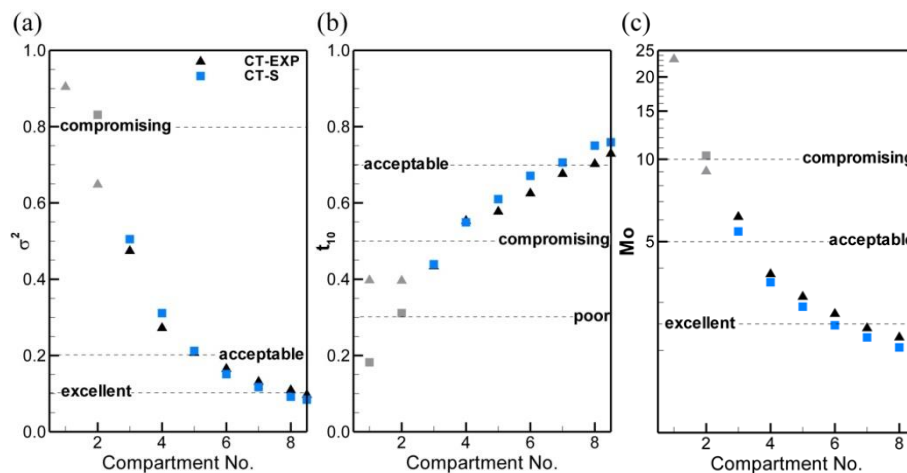


Figure 6.9 Simulation HEI prediction and comparison against experimental results from Chapter 5.

Overall, numerical model predictions provide a reliable indication of the hydraulic efficiency demonstrated by the close agreement against measured results. The non-ideal nature of hydrodynamics and mixing processes is observed inside the tank, where compromising or even poor performance is encountered at some tracer sampling points in a similar manner as the experimental results. HEIs drawn from compartments 1-2 (marked grey in the figure) are considered unreliable as the monitor points are inside

recirculation zones where tracer mass reappears multiple times during the sampling duration (due to convection), thus distorting the accuracy of RTD curves and their corresponding HEIs.

6.4 APPLICATIONS OF CFD MODELLING IN CTs

The comparison of experimental and computational results presented in the previous sections, indicates the ability of the current CFD approach to predict flow and solute transport conditions within serpentine disinfection tank facilities. This can be refined to produce design specific parameters (i.e. HEIs) that can either aid in the assessment of a design prior to construction, or the optimization of an existing design through retrofitting by evaluation of potential improvements computationally. Some different CT geometries are tested in this manner using the RANS approach, as the performance of the model to reproduce the experimental results can be promising even for practical applications due to the low-computational effort necessary. The applications considered refer to common design aspects which once addressed properly could result in improved disinfection efficiency; namely (a) alternative baffling or (b) inlet configurations and (c) CT reactor model scale.

6.4.1 Effect of Baffling Configuration

As discussed previously (Chapter 2), one of the most influential CT design parameters is the tank length to width (β) ratio. The increase of the β has been associated with the standard serpentine baffling configuration in CTs such as the one outfitted in the CT-1 model. The impact of the optimized baffling configurations has been extensively examined previously experimentally (Hart, 1979; Falconer and Tebbutt, 1988) as well as computationally (Stamou, 2002; Stamou, 2007; Gualtieri, 2007) to extract RTDs and HEIs at the outlet. In many cases such studies were crucial for the optimization of field-scale models (Falconer and Tebbutt, 1988; Stamou, 2002). Considering the wealth of information that is available in the literature, the baffling configuration optimization was not a major aspect of this investigation. However, previous experimental results (Rauen, 2005) with different baffling configurations on the laboratory model present an opportunity to test the robustness of the RANS simulation approach used to predict HEIs, especially since these results have not been reproduced computationally previously.

The alternative baffling configurations were introduced in Chapter 3 in Figure 3.6, denoted as MS-1, MS-2, MS-3 and CT-O. Figure 6.10 presents the outlet RTD predictions produced computationally, illustrating how the shape is improved once the baffling configuration is gradually optimised.

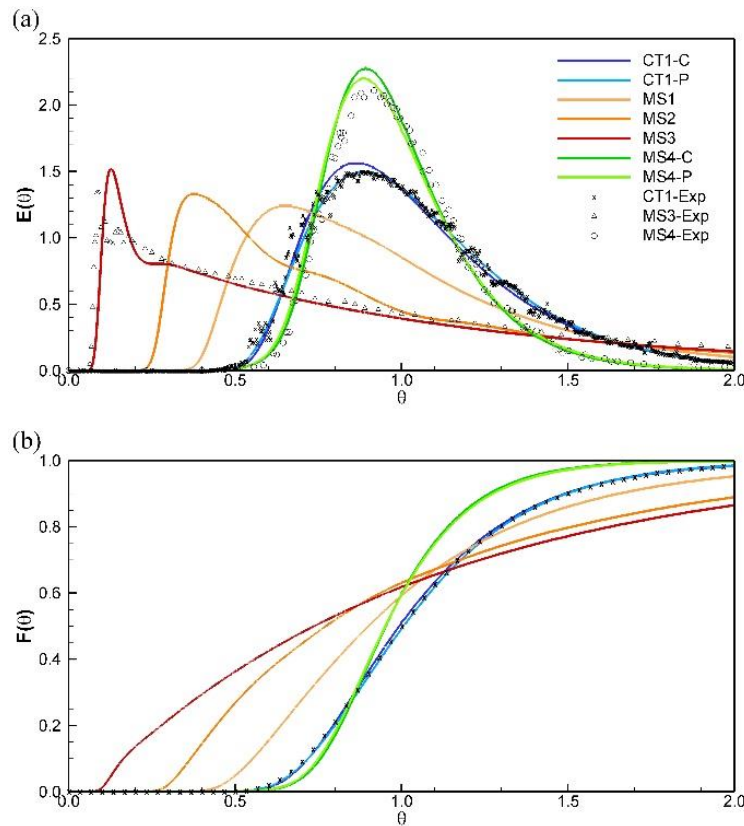


Figure 6.10 CFD predictions of Outlet (a) E_0 and (b) F curves for the different baffling configurations examined experimentally by Rauén (2005) and (Angeloudis et al., 2014)

It is of interest to assume that the original design was MS-3, i.e. the CT model without any baffles. Under such circumstances, the flow is completely three-dimensional with a very poor hydraulic efficiency as the peak of the curve appears unacceptably early ($t_p = 0.123$). MS-2 and MS-1 configurations are in between the MS-3 and CT-1 baffling configurations. These feature only 3 (MS-2) and 5 (MS-1) of the final 7 baffle configuration (CT-1) respectively.

An attempt to neutralize the inlet effect on the flow through a subsequent optimized baffling was CT-O (Figure 3.6d). The baffle opposite of the approach channel confines the vertical recirculation zone to the width of the compartment, rather than allowing it to occupy the entire length of the compartment as in CT-1. The tank is divided into 6 compartments instead of 8, as the cross-baffling design enables longer compartments

that occupy more volume reducing the compartment number, while maintaining the meandering flow structure of serpentine CTs.

Table 6.2 Outlet Experimental and Computational HEIs obtained for different Baffling Configurations

HEI	CT-1		CT-O		MS-1		MS-2		MS-3	
	CFD	EXP								
σ^2	0.085	0.095	0.048	0.055	0.198	0.224	0.401	0.306	0.637	0.534
t_{10}	0.73	0.73	0.76	0.78	0.53	0.50	0.39	0.37	0.17	0.16
t_{90}	1.46	1.50	1.29	1.32	1.76	1.69	2.06	1.81	2.07	1.84
Mo	2.00	2.05	1.68	1.69	3.30	3.38	5.31	4.89	12.4	11.5

The performance of the numerical models to reproduce the results for different baffling configurations is assessed in Table 6.2 through comparisons of experimentally and computationally derived HEIs. Firstly, the short-circuiting indicator t_{10} is predicted accurately in all 5 cases and deviations are typically below 5%. In terms of the mixing indicators, the best agreement is observed for the optimal baffling configuration of CT-O, followed closely by CT-1. However for MS-1, MS-2 and MS-3 despite the good estimate of short-circuiting (t_{10}), the deviation in the dispersion index (σ^2) reaches even 25% for MS-2 and MS-3 suggesting that tracer mixing processes in these geometries are not reproduced as well as for CT-1 and CT-O. It is speculated that for CT-1 and CT-O the initial flow unsteadiness is neutralized by the baffles which encourages flow uniformity early in the flow-path enabling the steady state simulation to provide a good approximation of the flow and turbulence field. For MS-1, MS-2 and MS-3 no significant measures are taken to neutralize the flow unsteadiness which results in discrepancies from the steady-state CFD predictions.

This also relates to the findings of Kim et al. (2013b) where it was argued that employing the gradient diffusion hypothesis to model an unsteady process through a steady state flow field, accurate predictions of tracer RTD curves can be achieved, but only for certain flows. In other cases, the turbulent Sc requires calibration, especially for flows that are dominated by large-scale turbulence structures. For narrow compartment tanks (e.g. CT-1, CT-O), the hydraulic efficiency predictions are quite accurate with the standard value of the Sc , whereas Sc had to be decreased substantially to provide accurate results for wide compartment tanks. Better results for MS-1, MS-2 and MS-3 which feature wider compartment could therefore be achieved by calibration of the Sc number unless more sophisticated simulation approaches are considered. Undertaking

such investigations was not contemplated further as additional information can be found in Kim et al. (2013b).

6.4.2 Effect of Inlet Configuration

A major observation of Chapter 5 was that the flow in the tank under investigation (CT-1) was found to be extensively three-dimensional due to the existing inlet configuration, resulting in short-circuiting and internal recirculation, particularly in the first three compartments. Near the inlet, the tracer residence time distribution curve analysis and HEIs suggested poor disinfection performance confirming the detrimental impact of the present design.

Once preliminary simulations were undertaken to reproduce the laboratory model experimental data (CT-EXP) and confirmed the satisfactory numerical model predictive capabilities, further simulations were then carried out to investigate the effect of alternative inlet configurations on the hydrodynamics and solute transport. Two additional cases are presented herein:

- A vertically expanded inlet design (Half Depth Inlet, HDI) which spans from $z/H_t = 0.50$ to 1.00 in the first compartment and
- A more idealized scenario where flow enters over the entire depth, i.e. a Full Depth Inlet (FDI) configuration, i.e. $z/H_t = 0.00$ to 1.00 .

Both cases utilized the same mesh resolution as CT-S-FM, with alterations in the boundary conditions to accommodate dimension changes and a uniform velocity profile based on the 4.72 l/s flow rate.

The hydrodynamic effects of the inlet configuration is shown in a quantitative way in Figure 6.11, where profiles of the vertical streamwise velocity in the centre of compartments 1, 2, 4, and 7 are plotted for three inlet configurations. The strong secondary flow in the first compartment is absent in the FDI flow and much weaker in the HDI flow. By the 4th compartment the HDI configuration exhibits the same profile as the FDI flow suggesting quasi plug flow conditions, whilst the flow of the original configuration (CT-1) is still non-uniform over the depth. All profiles essentially coincide by the 7th compartment a sign that the influence of the inlet is no longer apparent on the hydrodynamics.

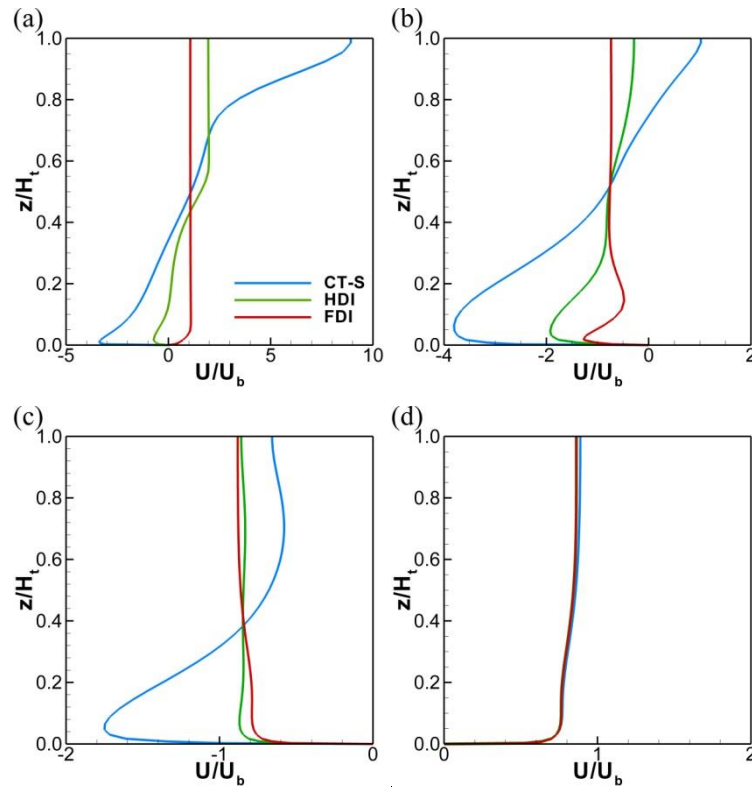


Figure 6.11 Streamwise velocity profiles in the 1st (a) 2nd (b) 4th (c) and 7th (d) compartment for original inlet (CT-1), half depth inlet (HDI) and full depth inlet (FDI) configurations.

A visualization using streamtraces of the flow in the three CTs is provided in Figure 6.12. The streamtraces are coloured by the velocity magnitude. The strong multi-dimensionality of the flow in the original configuration (CT-1, Figure 6.12a) can be discerned. The flow enters the CT-1 tank as the surface jet and it creates the strong, primarily 2D vertical recirculation zone, though some three-dimensionality below the entrance is observed in the streamlines. The flow gets deflected off the opposite wall and it continues to affect the flow profile until the 6th compartment as suggested by the vertical profiles of figure 6.11. The HDI flow features some three-dimensionality, especially visible near the downstream end of compartment 1, but recovers much quicker towards plug-flow type conditions. The FDI flow converges to uniformity from the beginning, small recirculation zones are observed behind baffles and in the corners of the tank (which is seen in the small top-view figure inserted at the top right) which are predominantly limited to the x-y (horizontal) plane. These are also present in the HDI and CT-S flows, but less significant (and almost absent in the early compartments of the CT-S where the flow is influenced strongly by the inlet jet) due to the three-dimensionality of the flow for these configurations.

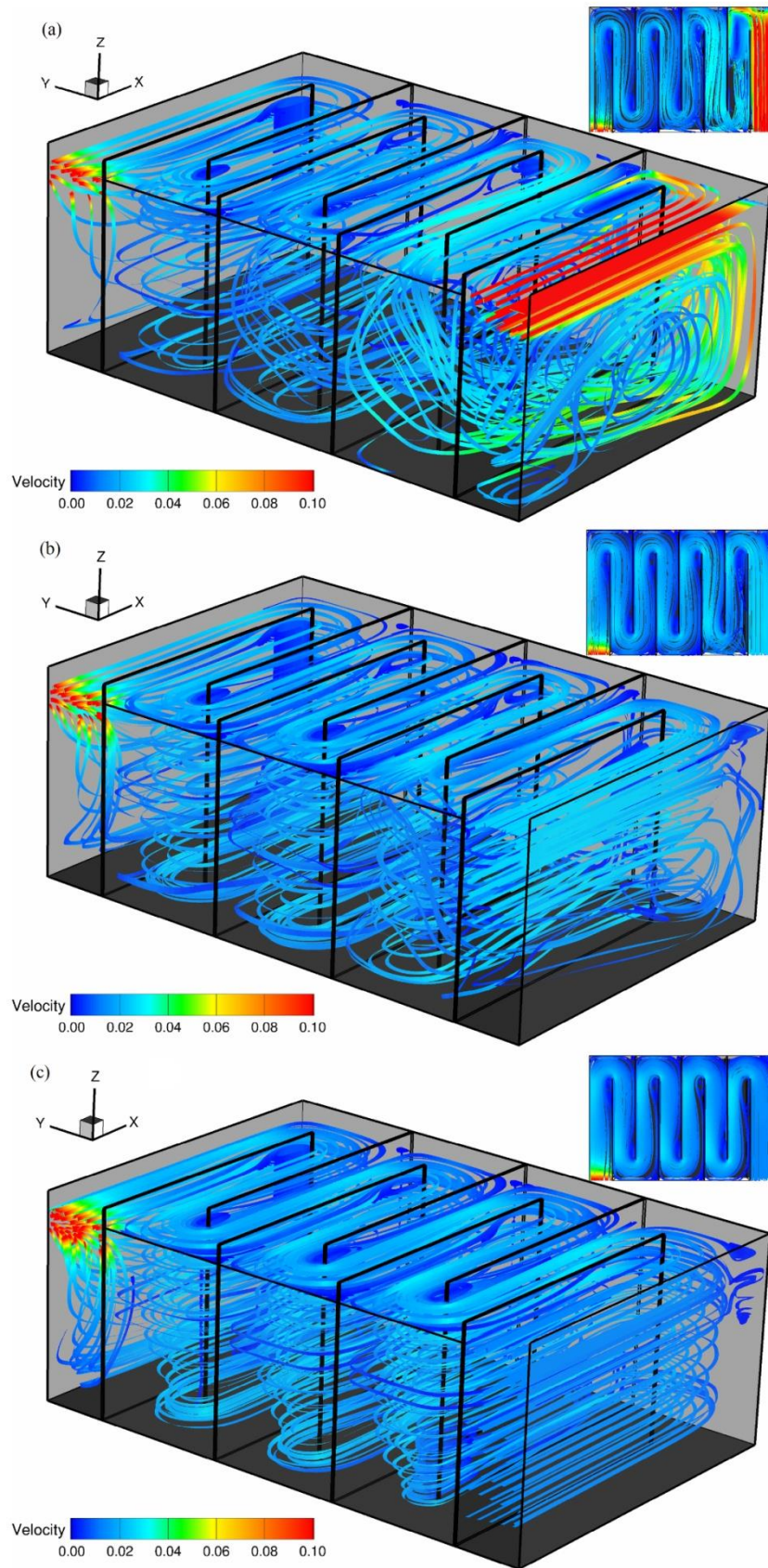


Figure 6.12 3-D and plan view visualization of fluid flow using streamtraces in (a)CT-S (b) HDI and (c) FDI design models respectively. The streamtraces are coloured with regards to their velocity magnitude

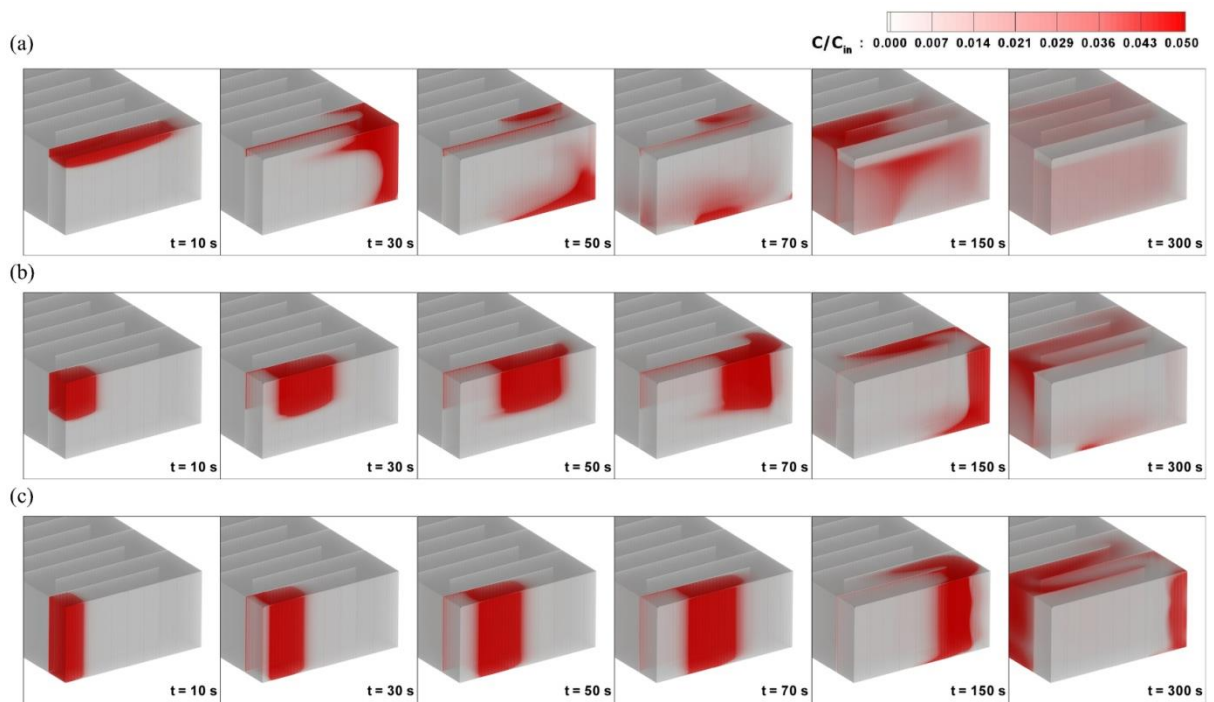


Figure 6.13 Contour profiles of tracer distribution in the initial at $t = 10, 30, 50, 70, 150$ and 300 sec following injection (a) Current configuration simulation (CT); (b) Half Depth Inlet (HDI) configuration; (c) Full Depth Inlet (FDI) configuration.

The previous discussion on CT-1, HDI and FDI hydrodynamic differences have an inevitable impact on the solute transport. An appreciation of how the tracer is transported through the early compartments of the CTs under the influence of the three different flows developed in each case is provided in Figure 6.13, which presents 3D views of the tracer concentration at different instants in time after the injection at $t = 0.0$ sec. The effect of the inlet condition is most visible at $t = 10$ s (i.e. the end of the injection period) during which some tracer has already reached the exit of compartment 1 in the CT-1 tank, whilst the tracer in the FDI design resembles a plug flow cloud. At $t = 70$ s, some tracer is being advected near the bottom back towards the inlet of the first compartment of the CT-1 tank while the rest is already halfway through the second compartment. At the same instant, the bulk of the tracer is still in the first compartment of the HDI tank but only a fraction of tracer mass has passed half of compartment 1 in the FDI tank. At the theoretical retention time of the first compartment, i.e. $T_1 \approx 150$ s (i.e. $\approx T/8$), a lot of the tracer is still recirculating in compartment 1 in the CT-1 design, whilst some tracer has already reached the exit of compartment 3. The HDI tank exhibits similar behaviour as the CT-1 tank but less pronounced. At $t = 150$ s, some tracer starts to recirculate in compartment 1, other has reached the exit of compartment 2. The tracer in the FDI design starts to deviate from plug flow at $t = 150$ s as the tracer is spread in the streamwise direction due to the horizontal recirculation behind baffle

walls. At $t = 300\text{s}$ the tracer in the CT-1 tank is well mixed and spread over the first four compartments. Simultaneously, in the HDI design, tracer is spread mainly over compartments 2 and 3 with some still circulating through compartment one. In the FDI design, the bulk of the tracer occupies half of compartments 2 and 3 but some tracer is detained in the first compartment's corner recirculation zones. Clearly, even though the jet-type inflow condition promotes short-circuiting in the early compartments, it also leads to rapid mixing as opposed to trapping of tracer in the horizontal recirculation of the FDI design. The HDI design has a bit of both short-circuiting and internal circulation.

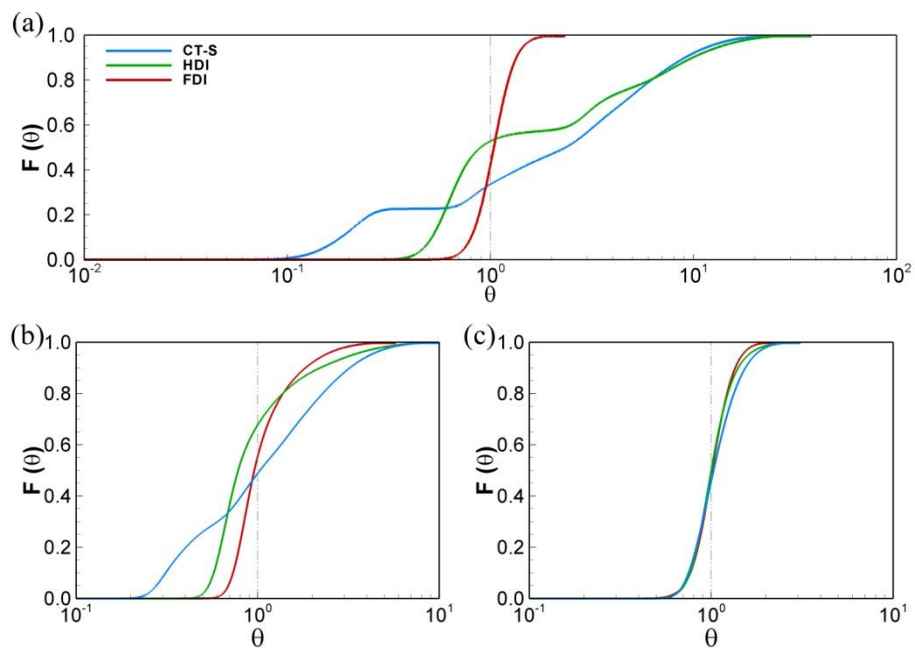


Figure 6.14 F curves of CT-S, FDI and HDI for compartments (a)1, (b) 2, (c) 8.

A quantification of how the transport of the tracer is affected by the inlet arrangements is provided by the simulated F curves in figure 6.14a-c. A plug flow transported tracer leads to the ideal F-curve (dashed line) i.e. the entire tracer mass appears at $\theta = 1.0$, i.e. the theoretical retention time, for which disinfection efficiency is maximized. Clearly, the F-curve of the FDI design is closest to a straight line in every compartment, and the $F(\theta)$ values are consistently closer to $\theta = 1.0$ than in the other cases. In compartment 1 (Figure 6.14a) the effect of short-circuiting and internal recirculation, i.e. when some tracer mass passes through compartment 1 quickly and some tracer mass stays in the compartment for a significant amount of time, is reflected in the flatness of both the CT-1 and HDI curves. However, already in compartment 2 the HDI curve resembles more the FDI curve, suggesting that the influence of the inlet configuration is relatively weak,

whilst the curve of CT-1 is still quite flat. Close to the outlet of the contact tank, i.e. the 8th compartment (Figure 6.14c), the curves essentially coincide for all inlet scenarios until 70% of mass has gone through ($F(\theta) = 0.7$), suggesting that the inlet configuration does not play a big role in terms of short-circuiting for tanks with a long flow path (distance between inlet and outlet). Some noticeable difference arises between $F(\theta) = 0.7$ and 1.0, e.g. which reflects the tanks behaviour in terms of internal recirculation. The FDI curve converges to unity first, followed by HDI and then lastly by CT-1, suggesting that tracer is trapped inside the system for greater time in the HDI design and even more so in CT-1 design.

Table 6.3 Disinfection Indicators at the Outlet for different inlet configurations of the laboratory model.

HEI	CT-1		HDI	FDI
	(EXP)	(CFD)	(CFD)	(CFD)
σ^2	0.095	0.085	0.071	0.049
t_{10}	0.729	0.730	0.769	0.773
t_{90}	1.541	1.463	1.386	1.338
Mo	2.051	1.995	1.803	1.731

The predicted outlet HEIs in comparison to CT-1 are presented in tabular form in table 6.3. In addition, the effect of inlet configuration on the distributions of HEIs as a function of distance from the inlet is also plotted in Figures 6.15(a-d). In the early compartments (1-3), the FDI design suggests significantly better hydraulic performance than the CT-1 design, which is because the flow is almost plug-flow already in the 1st compartment. The HDI design is only slightly better than CT-1 in compartments 1 and 2, but almost identical to the FDI design from compartment 4 onwards. The inlet configuration improves local short-circuiting effects (higher t_{10} in compartments 1-3) but this is not obvious in latter compartments where t_{10} is only marginally greater than the one of CT-1 and almost identical at the outlet. Similar to CT-1, the HDI configuration also suffers from very high t_{90} -values in early compartments, indicating that tracer is trapped in the recirculation zones. However, at the outlet both FDI and HDI designs perform better in terms of t_{90} than the CT-1 design. The inlet design is particularly influential to the mixing conditions as the relevant indicators (σ^2 and Mo) are improved by the HDI and FDI modifications. Noteworthy is the behaviour of the FDI design in terms of all HEIs exhibiting excellent performance in the first compartment, and a sudden drop to acceptable (even poor for t_{10}) for compartments 2-5, until the HEIs suggest excellent performance again. This can be explained by the fact that the flow is completely undisturbed in compartment 1, but then features more

pronounced 2D horizontal recirculation zones behind the baffles and in compartment corners (see top views of the flow depicted in the upper right corner of Figure 6.12). Whilst contact tanks designed similar to CT-1 would require at least 8 compartments to reach the excellent threshold for all indicators, it is surpassed by the 7th compartment in the HDI design and by the 6th compartment in the FDI design.

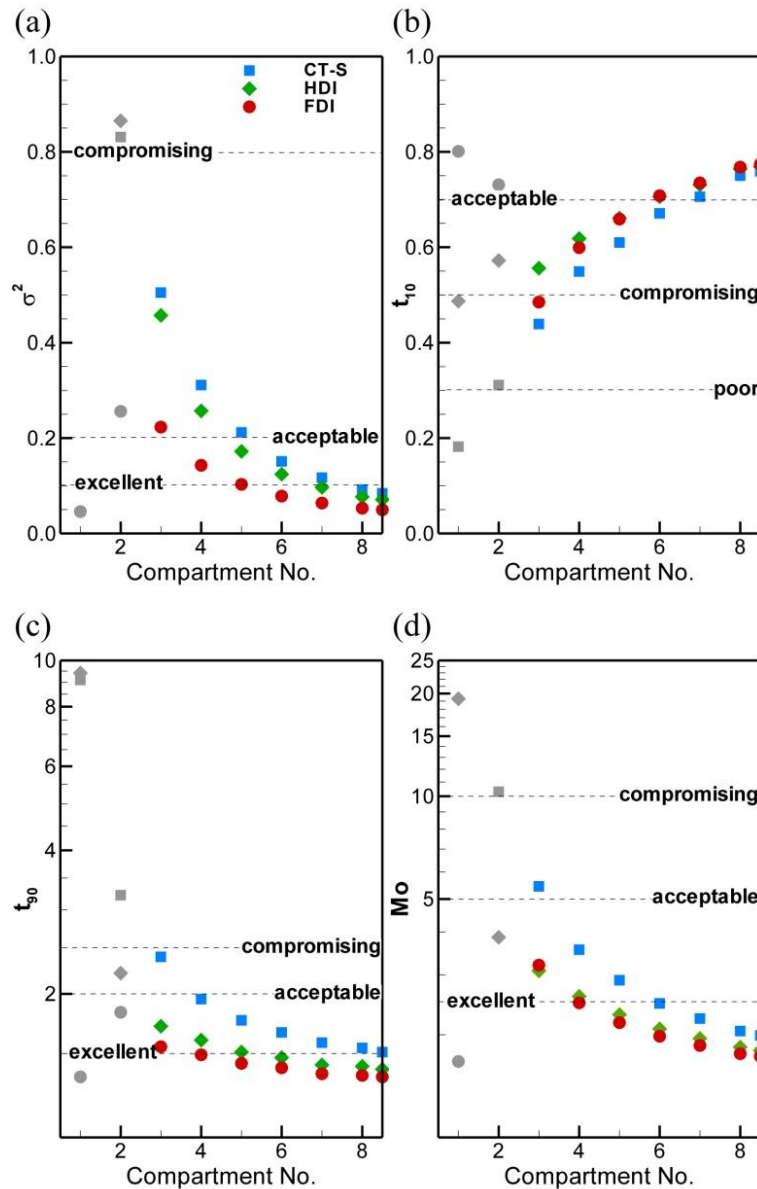


Figure 6.15 HEI indicator prediction across the CT model computational domain. Flow path normalized with respect to the compartment number for σ^2 , t_{10} , t_{90} and Mo . Results from the three different inlet configurations (CT-1, HDI and FDI) are reported illustrating the efficiency improvement shown by each of the indicators. Unreliable results due to tracer recirculation are highlighted in grey marker

Finally, the analysis above demonstrates that the CT-1 and FDI flows are quite different, especially in the early compartments, which is where they should be considered 3D- and 2D- flows, respectively. It is shown that disinfection efficiency is influenced quite significantly by the three-dimensionality of the flow and hence it is

deemed appropriate that the modelling approach reflects this. Treating the design of CT-1 as a 2D problem could result in an under-design because hydraulic efficiency is likely to be overestimated as seen in Figures 6.15.

6.4.3 Effect of Geometry Up-scaling

The extrapolation of scaled model experimental findings to larger, field-scale tanks is an important aspect that requires careful consideration. This is because of the dynamic scaling of free-surface flows, for which a Froude-number-model ($Fr_{Model} = Fr_{Prototype}$) is required. However this leads to $Re_{Model} < Re_{Prototype}$, as both dimensionless numbers can only be matched for the full scale tank (see Table 6.4). A Froude-scale model leads to an overestimation of boundary-generated turbulence, but an underestimation of friction effects (Falconer and Liu, 1987) and, important here, to an underestimation of turbulence driven mixing. To investigate the effect of the Fr-Re conflict on contact tank performance the numerical model, previously validated using the available experimental data, is employed to calculate flow and tracer transport in a prototype-scale version of CT-1. The geometric scale is $\lambda = 6:1$, i.e. the prototype is six times larger than the laboratory model and this it is denoted as CT-6. Table 6.4 provides parameters and important dimensionless numbers of the CT-1 and CT-6 tanks. The flow conditions in the original scale model were dictated by Froude-scaling and the prototype size of the tank is $18.0\text{m} \times 12.0\text{m} \times 6.12\text{m}$ with a flowrate of $Q = 0.415\text{m}^3/\text{s}$. This yielded $Re_{CT-6} \approx 15Re_{CT-1}$ and in terms of theoretical retention times $T_{CT-6} \approx 2.5T_{CT-1}$.

Table 6.4 Model parameters according to geometric and dynamic similarity

Model	Geometric Similarity (λ)	Bulk Velocity (cm/sec)	Froude Number	Reynolds Number	Residence Time (min)
CT-1	1	1.25	0.004	6,750	21
CT-6	6	3.10	0.004	99,480	50

Figure 6.16 presents velocity vectors and contour lines of the normalized turbulent kinetic energy k in the centre plane of the first compartment ($y/L_t = 0.06$) of the CT-1 laboratory experiment and the numerical models of CT-1 and CT-6. It is apparent that CT-1 and CT-6 feature a very similar flow structure, despite the difference in the Reynolds number. The distribution and magnitude of the turbulent kinetic energy of CT-1 and CT-6 is also very similar, despite the great difference in the Reynolds number between the two tanks. A more quantitative comparison of velocity and k is provided in

Figure 6.17, which presents measured and simulated velocity (CT-1 and CT-6) and normalized turbulent kinetic energy profiles at the tracer sampling locations (i.e. in the centre of the compartment) of compartments 1, 2 and 8. As stated previously, the effect of up-scaling is quite insignificant for the time-averaged flow and plays a minor role in the turbulence characteristics. This complies well with recent experimental findings of Teixeira and Rauen (2013) which suggest that the dynamic similitude of Froude small-scale models is retained as long as turbulent flow exists in the model ($Re \geq 3795$), which is the case of the present study.

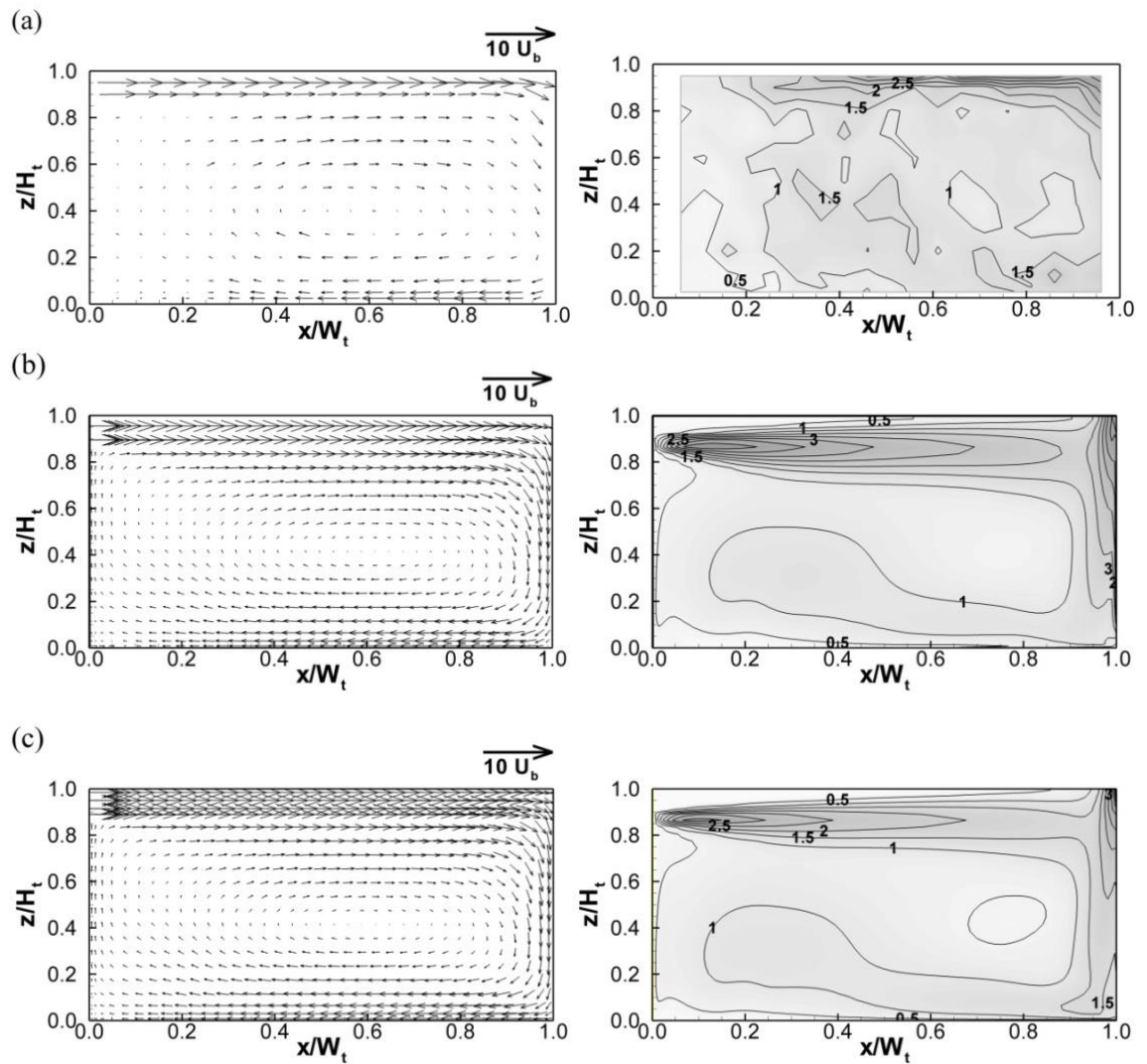


Figure 6.16 Mean flow and turbulent parameters graphical comparison. Normalised velocity (U/U_b , W/U_b) vector plots and Normalized Turbulent kinetic energy (k/U_b^2) contour plots in the centerline of compartment 1 for (i) CT-1 experimental measurements, (ii) Numerical simulation of CT-1, (iii) Simulation up-scaled (6:1) CT-6 model.

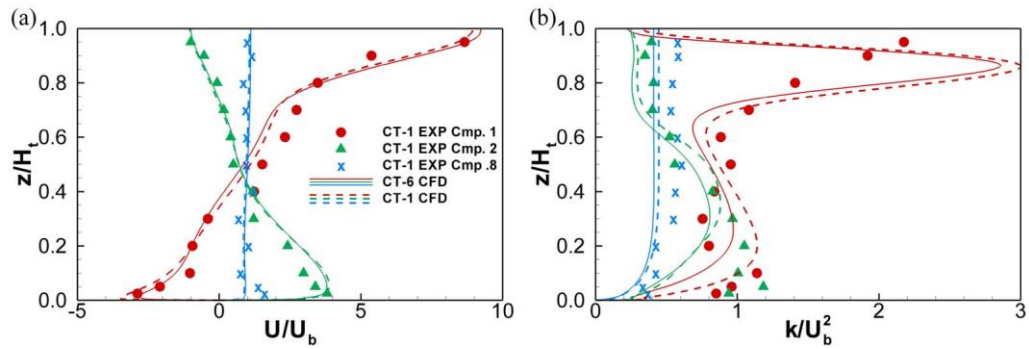


Figure 6.17 Vertical profiles of a) U/U_b and b) k/U_b^2 in compartments 1, 2 and 8 as measured experimentally in CT-1 and computationally in CT-6. Positive are considered the velocities that follow the streamwise direction in each compartment.

The proof of the insignificance of up-scaling, here only by a factor 6 though (as this is close to the scale typically encountered at water treatment works), is an important finding, because it shows that the hydrodynamics and to a certain extent the scalar transport of large-scale tanks can be extrapolated from small-scale model data. This is also shown in Table 6.5, which is an expanded version of the theoretical and experimental approach comparison discussed in Chapter 5. The deviation of the field-scale model *Mo* to the CT-1 experimental results is approximately only by 1% greater than the simulation results, an additional indication of the validity of the small-scale model results to practical situations.

Table 6.5 Theoretical, Experimental and CFD prediction of Morrill Index (*Mo*)

Compartment Number	Morrill Index (<i>Mo</i>)				
	CT-1 EXP	PF-TD (Error %)	PF-MD (Error %)	CT-6 CFD (Error %)	CT-1 CFD (Error %)
1	23.24	2.74 (88.2)	78.42 (-237.4)	58.70 (-152.6)	50.15 -(115.8)
2	9.03	1.78 (80.3)	12.77 -(41.3)	10.82 -(19.8)	10.34 -(14.5)
3	6.15	1.56 (74.6)	7.28 -(18.5)	5.66 (8.0)	5.44 (11.5)
4	3.80	1.46 (61.6)	4.19 -(10.1)	3.61 (5.0)	3.55 (6.6)
5	3.14	1.40 (55.5)	3.44 -(9.5)	2.86 (8.7)	2.88 (8.0)
6	2.72	1.35 (50.3)	2.84 -(4.3)	2.45 (9.8)	2.47 (9.1)
7	2.41	1.32 (45.2)	2.61 -(8.4)	2.21 (8.5)	2.23 (7.3)
8	2.23	1.30 (41.9)	2.30 -(3.3)	2.03 (9.1)	2.05 (8.1)
Outlet	2.05	1.28 (37.6)	2.27 -(10.7)	1.97 (3.9)	1.99 (2.9)

The application of the three-dimensional CFD methods seems much more reliable (Table 6.5) for the assessment of CT units compared to the theoretical approaches considered previously (PF-TD, PF-MD). This is to be expected as the theoretical assumption of near-plug flow conditions is flawed for the majority of the geometries explained herein, making the three-dimensional numerical approach far superior. The CT-6 simulations demonstrate that an additional advantage of CFD is the direct study of

field scale models, while also producing the same findings suggested by the scaled model experimental study.

6.5 CHAPTER SUMMARY

In this Chapter a RANS based CFD technique was employed to predict flow and tracer transport processes in serpentine CTs. The CFD model was first validated by comparing simulated velocity and tracer predictions with experimental data. The analysis was then extended to investigate the effect of different geometry variations such as inlet and baffling configurations on flow, or the effect of scaling and the applicability of the experimental studies in small-scale models to larger CT flows.

In the validation phase it was found that the RANS model is able to reproduce the time-averaged flow in the CT very well and a good prediction of scalar transport throughout the tank was achieved. This is also reflected in the good match of simulated RTD, F curves and HEIs with the experimental ones. The performance of the model was also validated against available data in the literature by testing different baffling configurations and highlighting in the meantime the influence of such modifications on the tank hydraulic efficiency and particularly short-circuiting.

Attention was then shifted to simulations with varying inlet configurations for the laboratory model. These indicated improved hydrodynamics, e.g. quasi 2D flow for the FDI design, and transport characteristics as demonstrated by improved HEIs mainly by reduction of flow complexity inside the tank. However, the benefit of such modifications does not primarily lead to short-circuiting mediation so much as the reduction of tailing effects as shown by cumulative RTD curves. Some other noteworthy highlights of this chapter are outlined as follows:

- The inlet and baffling modifications are significant in the sense that the same hydraulic efficiency level as achieved at the outlet of the original design could be achieved earlier in the flow path, which, in practise, could correspond to improved mixing and accommodating optimized disinfection conditions.
- Numerical simulations of hydrodynamics and tracer transport in an up-scaled tank verify the validity of the findings from the small-scale tank. These simulations provide evidence that the Fr-Re conflict can be negligible for the flow conditions developed in the small-scale model.

- It is shown that the hydraulic efficiency is influenced quite significantly by the flow-dimensionality developed in the reactor and hence it is deemed appropriate that the modelling approach reflects this. Treating the design of CT-1 as a 2D problem, which was the case of some studies in the literature, could in some instances result in an overestimation of hydraulic efficiency.

The hydrodynamic and solute transport results of the CT geometries investigated herein are integral for the analysis of Chapter 7 where the connection of the CT configuration with certain major disinfection processes is examined.

CHAPTER 7

DISINFECTION KINETICS

7.1 INTRODUCTION

This chapter expands on the analyses of computational fluid dynamics (CFD) simulations of reactive processes. The focus of these simulations aims at identifying the connection between hydraulic conditions discussed in Chapter 6 for different CT geometries with certain disinfection chemistry processes by integrating the mathematical models of reaction kinetics within the solute transport modelling. An additional challenge arises, with regards to the assessment of the reactive reactions to obtain useful information of the disinfection operation. Section 7.2 highlights the kinetic processes of significance for this study and the modelling approach followed for each case. Section 7.3 highlights results of reactive simulations for different chlorine CT geometries and examines the potential of CFD to be used for more chemistry related analysis than simply extracting HEIs.

7.2 KINETICS OF INTEREST

The main objective of the methodology implemented in Chapter 6 was to assess CTs through HEIs obtained from predicted RTD curves. HEIs can provide a reasonable estimate of the expected hydraulic performance of the CTs; however, these cannot predict parameters specific to disinfection such as the optimum disinfectant dosage, pathogen survival level or potential of by-product formation. This could be invaluable information for the operation and design of CTs which is often determined empirically using approaches such as the *Ct* concept. In section 2.4, the literature review associated with mathematical models related to disinfection demonstrates that significant advances have been reported in predicting the disinfectant decay, pathogen inactivation and by-product formation reaction progress (e.g. Haas and Karra, 1984; Gyürék and Finch, 1998; Brown et al, 2011) respectively. Some representative models for each of these processes are incorporated herein by adjusting solute transport equation source terms accordingly as described in the numerical modelling methodology of Chapter 4.

7.2.1 Disinfectant Decay

The reactive simulations were conducted under a chlorine disinfection scenario. In this case, as soon as free chlorine is introduced it reacts with both organic and inorganic substances, leading to a process of decay. This decay rate can normally be described by means of a first-order kinetic model as:

$$\frac{\partial C_{Cl}}{\partial t} = -k_b C_{Cl} \quad (7.1)$$

where C_{Cl} is the Chlorine concentration, k_b is the disinfectant bulk decay rate. The value of k_b is generally dependent on water quality as well as disinfection conditions and can therefore vary significantly. In spite of this, a k_b value equal to $2.77 \times 10^{-4} \text{s}^{-1}$ was set for all simulations, i.e. a realistic estimate of decay rate for raw water. Typically the range of the rate can vary between 0.5×10^{-4} and $5 \times 10^{-4} \text{s}^{-1}$ in accordance with Brown et al. (2011).

As it was discussed in Chapter 2, previous studies (e.g. Brown et al., 2010; Kohpaei and Sathasivan, 2011) illustrate that the initial introduction of chlorine in CT systems is subject to fast-reacting compounds. This is associated with a period of more rapid chlorine decay, typically within the first 5 minutes of chlorination, and has been reported to correspond to a 37-53% decrease from the initial dosage concentration (Brown et al., 2010). In order to account for these effects on chlorine consumption, apart from the decay rate of equation (7.1) an additional source term is adopted for the chlorine decay simulations:

$$\frac{\partial C_{Cl}}{\partial t} = -k_{FR} C_{FR} C_{Cl} - k_b C_{Cl} \quad (7.2)$$

Where C_{FR} is the concentration of fast reacting compounds and k_{FR} is the consumption rate of chlorine due to these compounds respectively. C_{FR} itself is modelled to follow a first-order decay and is negligible after 5 min of contact time, minimizing the influence of fast reactants for the remainder of the simulation. The above chlorine consumption rate is a combination of the first order decay rate model which is assumed to remain consistent across the domain and a second order reaction model as in Kohpaei and Sathasivan (2011).

7.2.2 Pathogen Inactivation

Ultimately, pathogen inactivation is the core objective of disinfection, and a quantitative indication of the survival level expected at the outlet of the CT could encourage or aide geometry modifications with a view to process optimization. It is interesting to observe the effect of the geometry on the inactivation process under identical chlorine disinfection operational conditions within the CT flow, a scenario which is difficult to accommodate for experimental investigations. Some examples of this practise have

been reported through numerical simulations by Huang et al. (2004) and Wols et al. (2011) for ozone contactors represented by 2-D computational domains.

The pathogen inactivation rate within the current investigation is incorporated in the simulation by differentiating the Chick-Watson law (equations 2.8-2.9) with respect to time as

$$\frac{\partial N}{\partial t} = -k' C_{Cl}^n N \quad (7.3)$$

where N is the pathogen population and n is a coefficient of dilution, approximately equal to 1 for chlorine disinfection (Zhang et al., 2000). The decay rate k' is deduced through a complicated function that is influenced by disinfection parameters such as microbe type, water chemical composition, disinfectant, temperature and pH. This should be adjusted accordingly for practical situations. This study considers the inactivation of the *Giardia Lamblia* protozoa, a particularly chlorine resistant type of drinking water pathogen commonly chosen as an indicator of pollution (AWWA, 1991). For *G.lambli*a, k' is given the value of $18.4 \text{ l mg}^{-1} \text{ h}^{-1}$ at $25 \text{ }^\circ\text{C}$ and a pH value of 7.0 (Johnson, 1997).

7.2.3 Disinfection By-Products

Recent concerns over the formation of potentially carcinogenic by-products during chlorination have led to practises requiring DBPs to be constrained within certain limits in the finished water. Similarly to the previously discussed kinetic processes, a wide range of mathematical models have been developed to predict the development of DBPs (Sadiq and Rodriguez, 2003). The incorporation of such models on CT CFD simulations has been limited to 2-D practises (Zhang et al., 2000) and not extensively discussed in the literature. The prediction of *TTHM* was considered in this study, by including an appropriate model (Singer, 1994) when simulating their transport and formation through the CT system:

$$TTHM = 0.00306[(TOC)(UV_{254})]^{0.44}(Cl_2)^{0.409}(Te)^{0.665}(pH - 2.6)^{0.715}(Br + 1)^{0.036}(t)^{0.265} \quad (7.4)$$

where *TTHM* is the total trihalomethane concentration in $\mu\text{g/l}$, *TOC* is the total organic carbon concentration in mg/l , UV_{254} is the ultraviolet absorbance at 254 nm in cm^{-1} , C_{Cl} is the chlorine concentration in mg/l , Te is the temperature in $^\circ\text{C}$, Br is the bromide ion

concentration in mg/l and t is the contact time at the particular location. Table 7.1 depicts the water quality parameter input for the simulation of by-product formation (equation 7.4), as adopted from the study of Zhang et al. (2000). A major assumption which should be remarked with regard to the input resides within the consideration of the Total Organic Carbon as a constant during the simulation, which is further discussed in the subsequent section over the implications of such a simplistic approach in the results.

Table 7.1 Water Quality Parameters Input

Parameters	Values	Units
Total Organic Carbon (<i>TOC</i>)	4.48	mg/l
Ultraviolet Absorbance at 254 nm (<i>UV₂₅₄</i>)	0.06	cm ⁻¹
Water Temperature (<i>Te</i>)	18	°C
Bromide Ion Concentration (<i>Br</i>)	0.036	mg/l
pH	7	-

The reaction modelling methodology followed within this chapter is tailored to the transport of free chlorine disinfectant, *G.Lambli*a pathogen population and Total THM (*TTHM*) by-product transport. However, the same framework can be adjusted for other disinfectants, pathogens or by-products by imposing appropriate kinetic models to the source terms accordingly.

7.3 ANALYSIS OF KINETICS THROUGH CFD MODELLING

In contrast to the methodology associated with obtaining HEIs for the hydraulic efficiency assessment of CTs, which is well documented and widely applied in the industry, there are no clearly defined approaches on analysing the CFD results featuring kinetic models. In the literature, apart from Zhang et al. (2000), numerical modelling studies of reactive flows in CTs have been limited to pathogen inactivation with the disinfectant decay being treated as a first-order reaction throughout the disinfection process (Wols et al, 2011; Greene et al., 2006; Huang et al., 2004). The simulation results were assessed at sampling locations (e.g. at the outlet) providing an indication of the microorganism survival ratio. Greene et al. (2006) compared the CFD predictions of inactivation against theoretical reaction models (i.e. complete micro-mixing and complete segregation) demonstrating an encouraging performance of the CFD model. Wols et al. (2011) proceeded into baffling configuration modifications and (ozone) disinfection efficiency prediction, evaluating a variety of CFD disinfection models and

recommended methods were the flow field in the contactor is accurately accounted for. The two superior approaches in terms of performance were identified as a Lagrangian particle tracking or a direct Eulerian inactivation method, which is of interest as the latter is adopted for the current analysis.

The practise of monitoring survival ratio stems from practical situations where such parameters are extracted by analysing the water chemistry during the treatment process. Results of this kind were reported by Haas et al. (1995) which were then incorporated in the published work of Greene et al. (2006) alongside their numerical model predictions. The analysis of system water samples has been also conducted to obtain data for the by-product formation and chlorine consumption at water treatment works as illustrated in the study of Brown et al. (2011), where empirical models are developed to predict THMs throughout the processes at water treatment works (equation 2.18).

A novel experimental technique for the assessment of pathogen inactivation (*E.Coli*) was outlined by Asraf-Snir and Gitis (2011) which involves fluorescent labelling of microorganisms and injecting them as tracers in a bench-scale reactor, operating with a constant feed of chlorine. In their experiments it was argued that the residence time of a solute within a reactor is affected by the size of the solute particles. Some of the aspects of their investigation are particularly relevant to this study, firstly because it is the only reported application of reactive tracer experiment methodology to serpentine CTs and secondly due to some experimental considerations that serve as an example of how CFD, and specifically RANS approaches, can more practically be used as an optimization tool for disinfection processes.

Namely, the hypothesis that the solute particle size is determinant to the outlet RTD shape is largely dependent on the hydrodynamic conditions established in the reactor. This applies under specific circumstances where molecular diffusion is comparable or larger than the turbulent diffusion, a condition which is encountered in laminar flows. This was the case in the study of Asraf-Snir and Gitis (2011) as based on the specifications of flow and scale of their laboratory model, the Reynolds number is extremely low (<100). In contrast, the flow developed in field scale models is characterised by a turbulent flow regime, where the effect of particle size on solute transport can be considered negligible compared to turbulent diffusion. This is an

example of how the scale of laboratory models can be unsuitable to reproduce the flow conditions encountered in practise.

According to the experimental study of Teixeira and Rauen (2013), the threshold for maintaining dynamic similitude between small and full-scale water treatment tanks is a minimum of $Re \geq 3795$. However, even if the dynamic similitude is retained and the Reynolds number is within an acceptable range, an inevitable consequence of the reactor scale difference is that the tank retention time would be distorted. This can be observed in Table 6.4 where to achieve Froude similitude between CT-1 and CT-6 the theoretical residence time was altered from 21 to approximately 50 min. On the other hand, disinfection reactions are heavily dependent on contact time (or theoretical retention time) while the hydrodynamics developed at the particular geometry are crucial for the reactant mixing. By adjusting the flow rate to match the contact time, the hydrodynamic flow structure is modified and the dynamic similitude between small-scale and field-scale model is lost. As a result, the disinfection under a specific contact time can only accurately be examined at full-scale conditions since only then the scaling effects associated with the hydrodynamics, surface roughness and contact time are absent. This is an advantage of developing a CFD methodology to simulate the disinfection efficiency directly at field-scale CTs, a practise which can be more flexible, adaptable and inexpensive than conducting experimental investigations at such facilities.

Two different numerical approaches are contemplated for the reactive simulations discussed below. The first one features instantaneous injections of microorganisms similarly to Asraf-Snir and Gitis (2011), but applied for turbulent flow regimes where molecular diffusion is negligible. The latter involves the simulation of disinfectant decay, microorganism survival ratio and by-product formation under a hypothesis of a constant introduction of chlorine and *G.Lamblia* concentrations at the inlet. The simulations are run until a steady state is achieved for chlorine, *G. Lamblia* and *TTHMs* across the whole computational domain. The CT geometries involved vary in terms of their design in an attempt to examine whether the hydraulic efficiency findings obtained previously (Chapter 6) correspond to the same order of disinfection performance estimated by the reactive simulations. Apart from the original setup (CT-1), inferior (MS-3) and superior (CT-O) baffling configuration CT geometries are included. In addition, the simulations of the laboratory model geometry with different inlet

configurations (HDI and FDI) are also considered. In all cases the FM grid characteristics (Table 6.1) were adopted for the computational grids introduced in Chapter 6. Based on these meshes, the maximum duration of the solute transport simulation time was limited to 6 hours, demonstrating the practical potential of such approaches.

7.3.1 Reactive Tracer Simulations

Two different reactive tracer scenarios are attested, each one for the assessment of inactivation and by-product formation processes respectively. A first-order decay of chlorine is assumed for simplicity (equation 7.1), as the objective of these simulations is mainly to compare the CT geometries rather than deduce disinfection operational information.

a) Pathogen Inactivation Potential

There are two stages associated with the simulation of this reactive experiment, where a concentration of *G.Lambli*a population is simulated as the tracer quantity. At first, a chlorine concentration of 1.5 mg/l is introduced at the inlet of the MS-3, CT-1, HDI, FDI and CT-O models respectively, until the disinfectant distribution across the domain converges to a steady-state condition. Once this is established, a concentration of *G.Lambli*a is set at the inlet boundary for $t = 10$ s to simulate the injection. Figure 7.1 shows RTD response curves at the outlet of the contactor. The steady-state flow velocity and turbulence field for each design was imported from the previous hydrodynamic simulations discussed in chapter 6 with an inlet flow rate of 4.72 l/s.

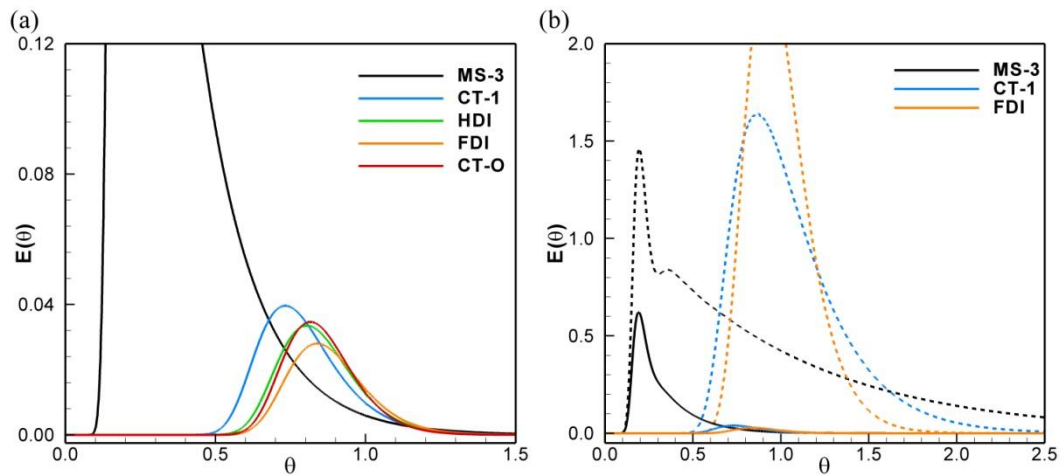


Figure 7.1 *G.Lamblia* concentration RTD curves; (a) Results for different CT designs and (b) comparison with conservative tracer curves

Taking into account the chlorine reactions with microorganisms, the *G.Lamblia* concentration injected is not conserved; this is reflected by an area below the normalized RTD curve unequal to unity (Figure 7.1a). Another observation is that the total RTD area varies for each configuration, a phenomenon attributed to the influence of mixing on inactivation reactions. The disinfection efficiency is quantified for each of the CT geometries by comparing the areas between reactive and conservative tracer RTDs as shown in Figure 7.1b. The percentage of tracer (*G.Lamblia*) loss since the injection is provided in table 7.2, calculated by subtracting the normalized area of the microorganism RTD from unity (i.e. the conservative tracer RTD curve area).

Table 7.2 *G.Lamblia* tracer mass loss during the experiment and RTD peak time (t_p) for conservative and reactive tracer respectively

CT Design	Conservative tracer t_p (θ)	<i>G.Lamblia</i> tracer t_p (θ)	<i>G.Lamblia</i> inactivation (%)
MS-3	0.195	0.192	87.71
CT-1	0.866	0.733	98.72
HDI	0.884	0.804	98.98
FDI	0.923	0.838	99.13
CT-O	0.890	0.817	99.00

The impact of the flow field on the inactivation is remarkable. MS-3, as the most inefficient design corresponds to an 87.7% *G.Lamblia* inactivation, which is substantially worse against the remaining configurations. The difference between CT-1 and MS-3 demonstrates how significantly a serpentine design enhances the contactor inactivation potential. Subsequent inlet and baffle (FDI, CT-O) modifications further improve the CT-1 inactivation process from a 1-log *G.Lamblia* disinfection (90.0-

98.9%) to a 2-log level (99.0-99.9%), even though the disinfectant mass remains the same.

These results also indicate that FDI performs better than CT-O, a noteworthy finding due to the ambiguity of the HEIs presented in Chapter 6 (Tables 6.2-6.3) where it is difficult to determine which of the two configurations is more hydraulically efficient. FDI has a marginally superior t_{10} value (0.773 against CT-O's 0.762) whereas t_{90} , Mo and σ^2 are all inferior to the CT-O HEIs. In contrast, even though HDI has a t_{10} value (=0.769) greater than CT-O, the mass loss percentage in table 7.2 does not reflect a superiority of the HDI design. The above is an example that indicators alone are not always sufficient in determining the optimal contactor performance.

HEIs like t_{10} , t_{90} , Mo and σ^2 were not applicable in reactive tracer experiments as these are comparable only if tracer mass is conserved. However, peak concentration times (t_p) were calculated for comparison against the conservative tracer predictions (Table 7.2) to indicate how the shape of the RTDs is altered by the pathogen reactions with chlorine. - Even for the most efficient configurations, t_p deviates from the residence time, a sign that some overall short-circuiting is unavoidable. This deviation is even more pronounced in the *G.Lambli*a tracer simulations since the peak concentration appears even earlier than for the conservative tracer results, which illustrates why neutralizing short-circuiting effects is crucial for the microorganism inactivation. By examining the RTDs of Figure 7.1a the greatest area of the plots is placed at a contact time of $\theta < 1.0$ whereas for $\theta \geq 1.0$ the *G.Lambli*a population converges faster to zero, perhaps due to its sufficient exposure to chlorine past that point.

b) By-Product Formation Potential

For the assessment of by-product formation, 2.0 mg/l of free chlorine were introduced for an interval of 10s (≈ 100 mg of Cl_2) at each of the 5 different CT models. The concentration of *TTHMs* at the inlet was set to 0 $\mu\text{g/l}$. Kinetic processes that are involved in the scalar transport source terms were (a) a first order decay of chlorine (equation 7.1) and (b) the formation of *TTHMs* which is calculated through equation (7.4). Specifically, the simulation time at every time-step of the iterative process is used as the t parameter in the by-product formation equation. In the meantime, Chlorine and

TTHM concentrations are monitored at the outlet to derive RTD information. Figure 7.2 presents sample E_θ and F curves of Chlorine concentrations for MS-3, CT-1 and FDI.

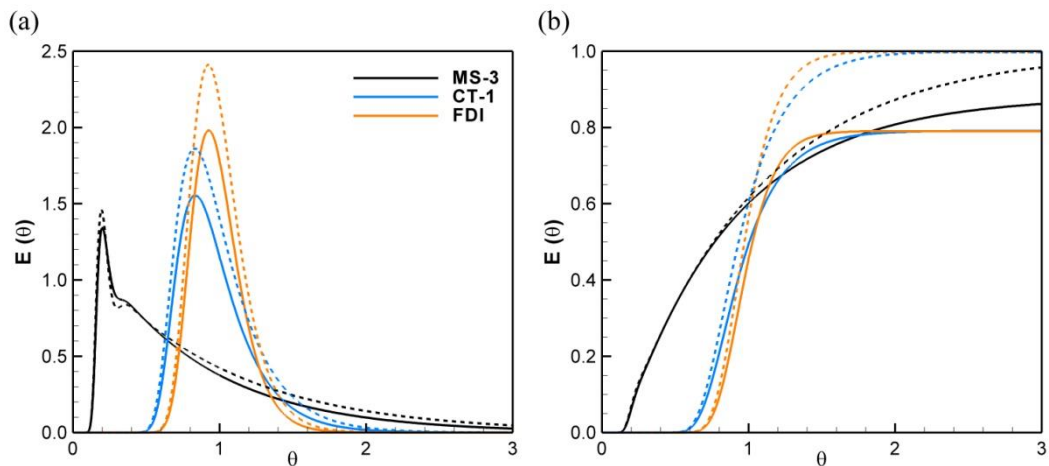


Figure 7.2 Chlorine concentration RTD curve comparison against conservative tracer results from Chapter 6; (a) E_θ and (b) cumulative F curves

The disinfectant mass recovered for the configurations which adopt baffling configurations to counter the short-circuiting effect (CT-1, CT-O, HDI and FDI) is between 78-80% with no significant variation. However, for the MS-3 design, mass accumulated at the outlet (Figure 7.2b) amounts to 88%; approximately 10% greater than in any other configurations. It is speculated that this is a consequence of the severe short-circuiting of MS-3 which encourages the disinfectant to exit the system prematurely, instead of attempting to maximize the contact time with organic material carried by the water.

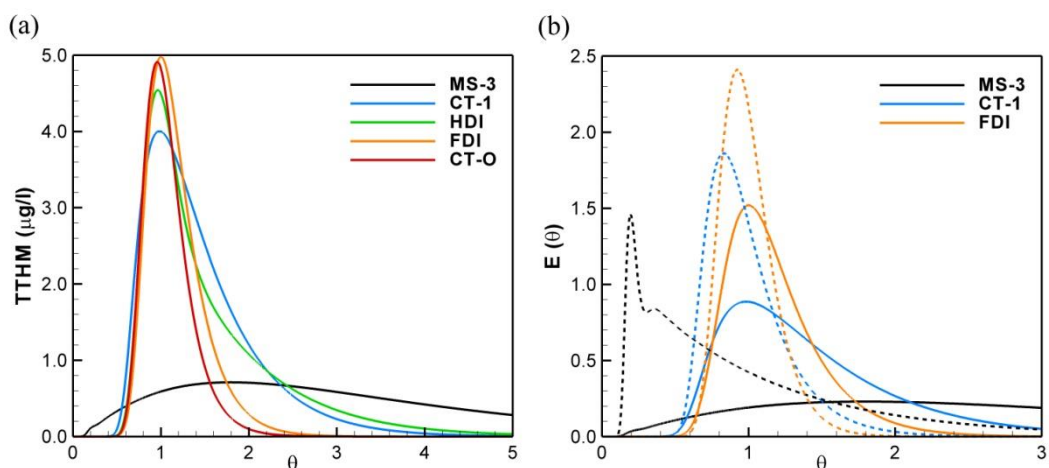


Figure 7.3 Outlet by-product concentration RTDs; (a) TTHM concentration-time and (b) normalised (TTHM and conservative) E_θ curves

Figure 7.3a depicts concentration-time plots of estimated *TTHMs* at the outlet of the CTs produced by the 100 mg of chlorine injected at the beginning of the simulations.

Using equation (3.9), the Cl_2 and $TTHM$ mass recovered was calculated and is shown in table 7.3 to highlight the influence of the geometry on by-product formation.

Table 7.3 Cl_2 and TTHM mass recovered at CT Outlets

CT Design	Cl_2 Mass Injected (mg)	Cl_2 Mass Recovered (mg)	Cl_2 consumption (%)	TTHMs Accumulated (mg)
MS-3	100.0	88.06	11.94	7.41
CT-1	100.0	78.14	21.86	12.20
HDI	100.0	77.82	22.18	11.77
FDI	100.0	79.05	20.95	7.87
CT-O	100.0	79.89	20.11	6.67

The CT-O design performs best with the lowest $TTHM$ production potential compared to the other designs. This can be justified by the lack of extensive tailing associated with the particular baffling configuration. The FDI design, by neutralizing the vertical recirculation zones at compartments 1-3, does not detain chlorine in those regions as long as in CT-1 or HDI which results in lesser RTD tailing and therefore reduced $TTHM$ formation. However, despite MS-3's strong tailing effects the accumulated mass is not as high as in CT-1 or HDI. This is attributed to the short-circuiting of the majority of disinfectant at low contact times, which leads to lower chlorine concentrations and $TTHM$ formation inside the tank.

The main outcome of these two non-conservative tracer simulations is that depending on the reaction studied, the RTD shapes and areas will be modified accordingly. For *G.Lambli*a inactivation the contact time is beneficial and therefore the tailing effects which were encountered in the conservative tracer RTDs are not appearing, whereas short-circuiting effects are more pronounced (Figure 7.2b). In contrast, for $TTHMs$, greater contact time corresponds to higher by-product formation and tailing effects become more significant (Figure 7.3b).

7.3.2 Simulation of Steady-State Disinfection Processes

In order to estimate expected disinfection performance of a variety of CT designs under operational conditions, simulations where chlorine and microorganisms are continuously introduced into the CT geometry are considered. A flowrate of 2.86 l/s was assumed for MS-3, CT-1, HDI, FDI and CT-O accordingly, to accommodate a retention time of 35 min, i.e. a realistic estimate for chlorination at water treatment works. A concentration of fast reactants (C_{FR}) is assumed in the inlet water chemistry, which decays logarithmically due to reactions with chlorine and becomes negligible for

$t > 5$ min. The aim of this modelling strategy is to reproduce the initial rapid chlorine consumption that has been occurring at water treatment works (Brown et al., 2011) using the parallel chlorine decay model of equation 7.2. In terms of *G.lamblia*, a 3-log inactivation target was set, i.e. a common compliance standard for potable water. A constant reactive tracer experiment is modelled prior to the disinfection simulation to calculate an acceptable approximation of the contact time (average residence time) at each computational cell based on the concentration distribution. The contact time estimate is imported in the *TTHM* source term, but is also invaluable to provide an overview of the disinfection progress in the post-processing analysis.

The inlet concentration boundary conditions remain unchanged throughout the whole simulation, assuming $C_{Cl} = 2$ mg/l, $C_{FR} = 1$ mg/l and $C_{TTHM} = 0$ µg/l. For *G.Lamblia*, instead of providing an actual concentration, a dimensionless value of 1 is set that represents the population survival ratio (N/N_0), which can directly be used to determine the log-inactivation.

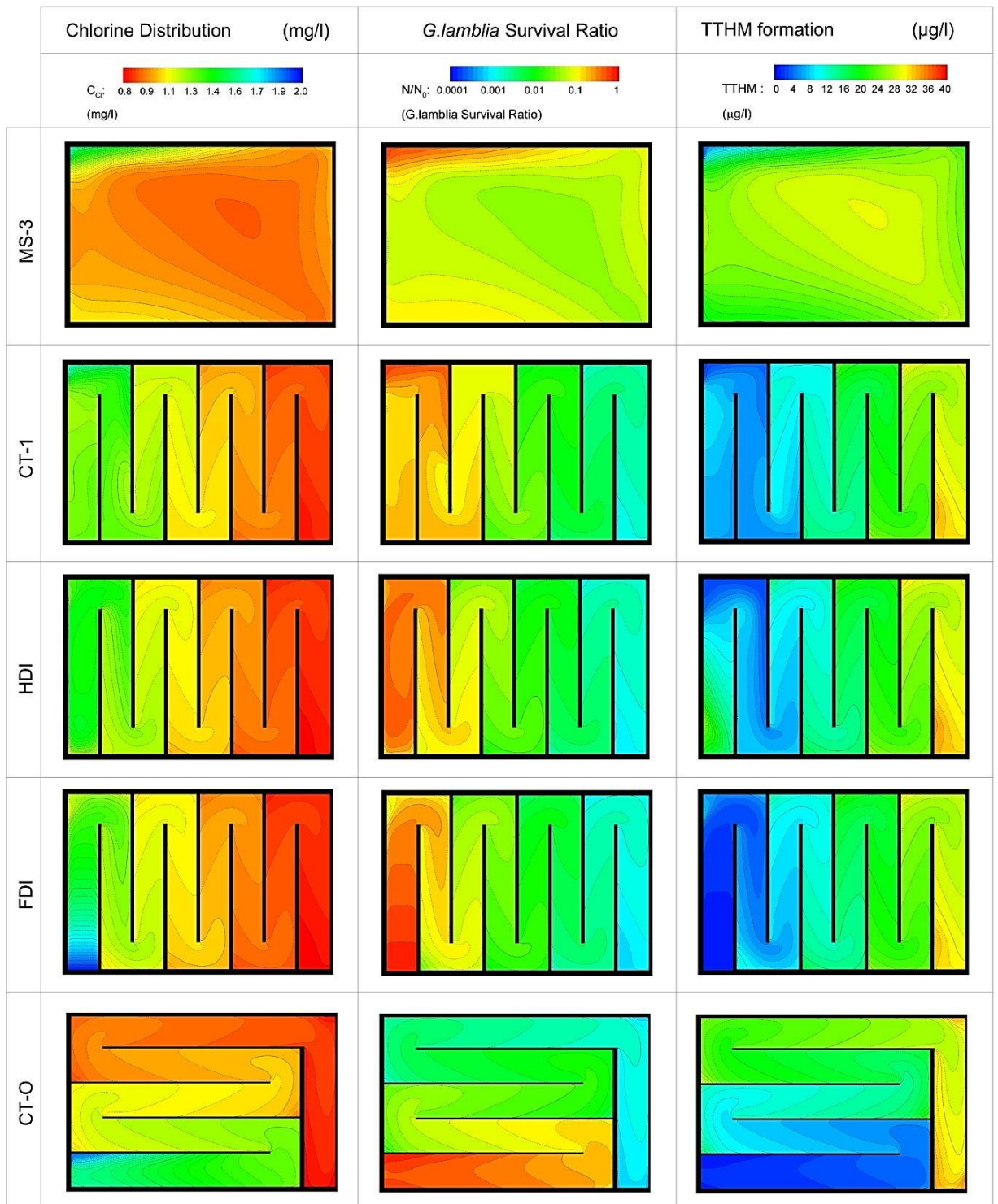


Figure 7.4 Contour plots of Disinfectant Distribution, *G.lamblia* Inactivation and total Trihalomethane formation as predicted from the CFD simulation of the disinfection processes for each of the CT designs . The plots are obtained at half-depth, i.e. $z/H = 0.50$

Figure 7.4 presents contour plots of C_{Cl_2} , *G.lamblia* N/N_0 and $TTHM$ at mid water depth, which provide an appreciation of the strong interconnection between hydrodynamics and chemical reaction kinetics. For MS-3 the disinfectant concentration remains quite low across the geometry, apart from some regions early in the flow path highlighted in

the contour plot, due to the effects of short-circuiting and three-dimensional mixing. This leads to a lower level of inactivation at the outlet and an overall uncertainty over the main flow pattern developed. For CT-1 and HDI, it can be observed that once the flow is characterized by a recovery from the initial three-dimensionality (i.e. compartment 3 onwards), chlorine is distributed more evenly across the compartment. This corresponds to a gradual inactivation of pathogens and a controlled accumulation of by-products which is only partially hindered by the flow separation in baffle edges and corners. In contrast, in compartment 1, due to severe recirculation, there is a distinctively higher survival ratio of *G.lamblia* in regions where the flow short-circuits and a reduced survival ratio in the centre of the recirculation zones as the disinfectant is detained longer than expected. A similar pattern arises with *TTHMs*, as an accumulation of by-products in major recirculation zones is apparent, such as in the vertical ones formed in compartments 1-3 for CT-1 and HDI. However, in the absence of inlet design disturbances, the disinfection processes in FDI occur consistently from the inlet to the outlet, influenced only by baffle edges and compartment corners. With the optimized baffling configuration, CT-O also yields similar results to FDI, constituting it even more promising due to the difficulty of establishing the FDI's inlet flow with a uniform cross-sectional disinfectant concentration in practical situations.

Under the current disinfection conditions, the CT designs correspond to mean *G.lamblia* N/N_0 at the outlet of 3.9×10^{-2} , 1.5×10^{-3} , 1.1×10^{-3} , 8.9×10^{-4} and 8.3×10^{-4} for MS-3, CT-1, HDI, FDI and CT-O respectively, suggesting increased inactivation through improved hydrodynamics. Accordingly, for by-product formation the average *TTHM* concentrations reported in each case are 27.71, 30.17, 30.86, 31.17 and 31.53 $\mu\text{g/l}$ respectively. A more holistic overview of the disinfection with respect to contact time is given in Figure 7.5 where C_{Cl} , N/N_0 and *TTHM* are plotted as a function of normalized contact time θ at computational cells (each data point represents a location in the tank).

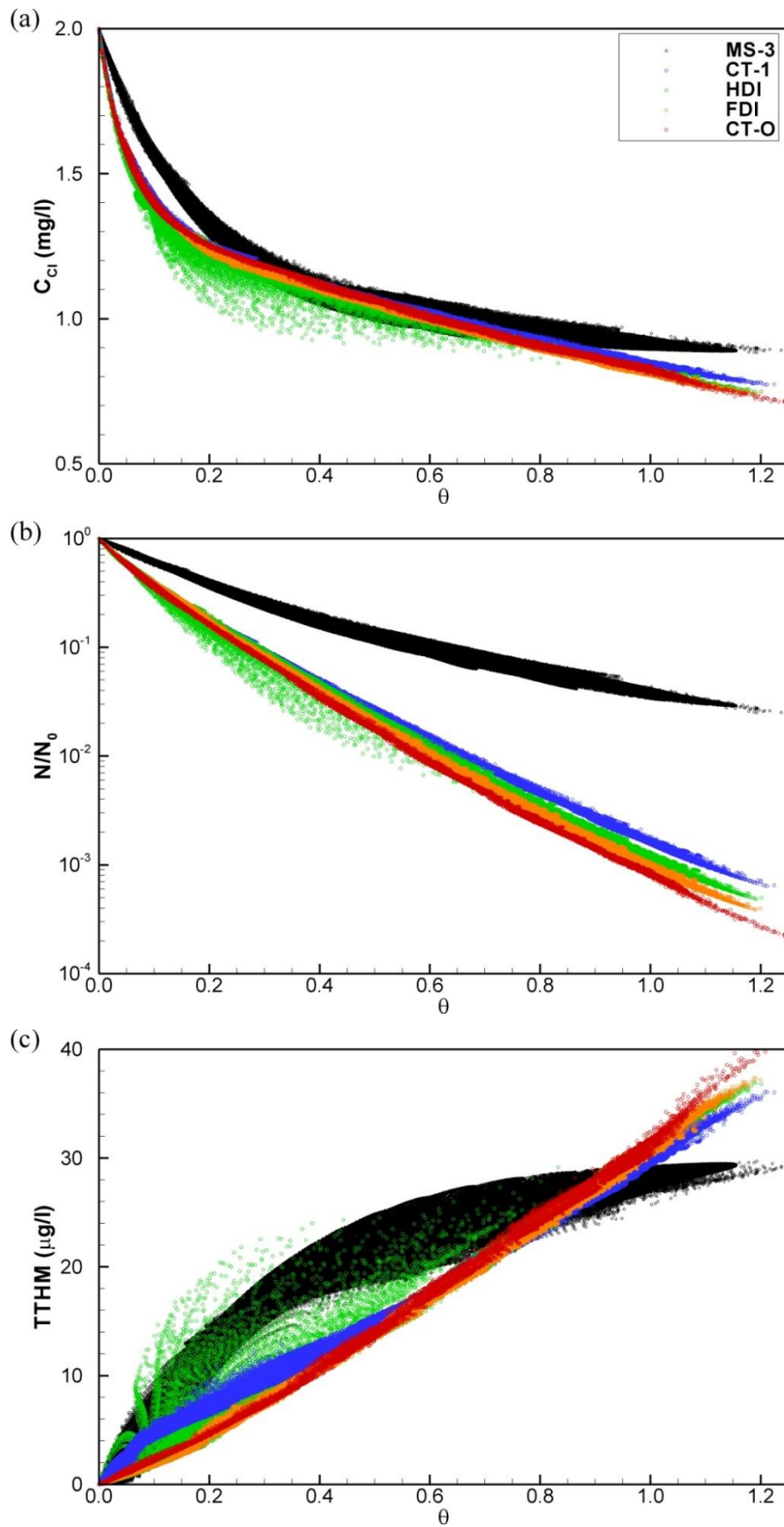


Figure 7.5 Disinfection Performance with respect to contact time based on computational cells of CFD simulations: (a) Chlorine Concentration (C_{Cl}), (b) *G.lamblia* Survival Ratio (N/N_0) (c) Total Trihalomethane (TTHM) formation. The figure indicates that despite disinfection occurring under identical conditions of operation and water quality, the CT geometrical differences have a distinctive impact on the kinetics.

The unbaffled tank (MS-3), fails notoriously in meeting the 3-log inactivation highlighting once more how detrimental the hydraulic efficiency can be on the reactions undertaken in the contactor. The chlorine and *TTHM* concentration range with respect to time is greater than in the other designs, which suggests non-uniform contact time along the main flow-path.

As Figure 7.5a illustrates, the effect of inlet configuration on chlorine decay is small. However, HDI and CT-1 data points are more scattered compared to FDI. From Figure 7.5b it is seen that 3-log inactivation is surpassed in all baffled configurations, however for CT-1 only at a few locations very close to the outlet. The optimized designs (HDI, FDI and CT-O) exhibit superior disinfection performance at many locations. The highest inactivation is achieved near the bottom close to the outlet weir, within a minor low-velocity recirculation zone (see Figure 6.5a). The production of by-products (Figure 7.5c) suggests a steady accumulation of *TTHM* over time. The HDI design appears to produce high levels of *TTHM* in the recirculation of compartment 1, which is due to the low turbulence recirculation region entrapping significant concentrations of disinfectant for long periods of time, also shown in Figure 6.13b ($t = 300\text{s}$). There, the combination of high C_{Cl} concentration and contact time in that recirculation zone results in early by-product production. In contrast for CT-1, which also features a similar recirculation zone (Figure 6.5a), the contact time in compartment 1 is lower due to rapid mixing by the jet flow, and therefore the formation of by-products is not as significant. For FDI, a higher production of by-products is observed for locations in corner recirculation zones, which is expected from the tracer transport simulation (e.g. Figure 6.13c, $t = 300\text{s}$). This highlights that any low-velocity recirculation zone causes the production of by-products. Similar concentrations of *TTHM* are observed at the outlet for the different configurations.

A more quantitative indication of the inactivation and by-product formation process is given in table 7.4 where average values of N/N_0 and C_{TTHM} are calculated at intervals of 0.10θ showing the differentiation of disinfection progress as a consequence of the CT geometry modifications. Unfortunately, a remarkable flaw of the direct Eulerian method is the calculation of disinfection-related processes based on an averaged residence time at each computational cell. Therefore, for a more accurate prediction the full distribution of chlorine exposure times should be taken into account, which is the main advantage of using Particle-Tracking techniques (Wols et al., 2011). On the other hand, the

availability of RTD curves from the simulation of conservative tracer injections in Chapter 6 can be useful to estimate the range of variation of disinfection performance at CT outlet sampling points using interpolation and regression analysis techniques. Results of such an approach are indicated in table 7.5.

Table 7.4 Average Values of G.Lamblia Survival Ratio and TTHM Concentration with respect to mean residence time.

θ	G.Lamblia Survival Ratio (N/N ₀)					TTHM Concentration (µg/l)				
	MS-3	CT-1	HDI	FDI	CT-O	MS-3	CT-1	HDI	FDI	CT-O
0.00	1.0000	1.0000	1.0000	1.0000	1.0000	0.00	0.00	0.00	0.00	0.00
0.10	0.6400	0.3612	0.3765	0.4048	0.4327	3.22	3.29	3.57	1.62	2.99
0.20	0.4213	0.1839	0.1849	0.1939	0.2053	6.45	6.58	6.35	3.77	5.99
0.30	0.2858	0.0638	0.0908	0.0788	0.0974	9.67	9.87	13.21	8.24	8.98
0.40	0.2089	0.0417	0.0457	0.0398	0.0462	12.90	13.17	14.12	10.35	11.98
0.50	0.1526	0.0281	0.0217	0.0227	0.0219	16.12	16.46	15.17	13.13	14.97
0.60	0.1176	0.0148	0.0097	0.0115	0.0104	19.35	19.75	17.45	17.18	17.96
0.70	0.0903	0.0092	0.0045	0.0059	0.0054	21.28	23.04	19.69	20.29	22.45
0.80	0.0702	0.0051	0.0037	0.0032	0.0029	22.62	26.15	24.10	24.34	25.66
0.90	0.0534	0.0031	0.0023	0.0019	0.0016	25.04	26.98	26.46	27.02	28.87
1.00	0.0418	0.0018	0.0013	0.0011	0.0009	26.58	30.20	29.17	30.41	32.07
1.10	0.0340	0.0011	0.0008	0.0006	0.0005	27.41	34.52	33.33	34.81	36.33
1.20	0.0275	0.0007	0.0005	0.0004	0.0003	28.57	36.81	35.49	37.88	39.63

Table 7.5 Estimation of G.Lamblia N/N₀ and TTHM at the outlet for t₁₀ and t₉₀ with the aid of regression analyses of CFD results extracted from Figure 7.5 (e.g. Table 7.4)

CT Design	t ₁₀	t ₉₀	G.Lamblia Survival Ratio		TTHM Concentration (µg/l)	
			t ₁₀ N/N ₀	t ₉₀ N/N ₀	t ₁₀ TTHM	t ₉₀ TTHM
MS-3	0.17	2.07	0.4797	0.0033	5.47	43.53
CT-1	0.73	1.46	0.0079	0.0002	20.71	43.65
HDI	0.77	1.39	0.0043	0.0002	25.08	42.39
FDI	0.77	1.34	0.0039	0.0002	22.32	42.78
CT-O	0.76	1.29	0.0037	0.0002	24.37	42.37

The indicators t₁₀ and t₉₀ are considered, due to their significance they have for current practises to assess disinfection efficiency (e.g. C×t₁₀ concept). For microorganism N/N₀, it could be argued that the minimum contact time survival ratio is the most important prediction as it highlights the lowest disinfection efficiency achieved in the contactor due to the implications of short-circuiting. In contrast, the highest by-product concentrations at maximum contact time are of interest, a consequence of the entrapment of disinfectant at dead zones for higher residence times. For MS-3 at the outlet t₁₀ value approximately 48% N/N₀ is estimated; a sign of notoriously inefficient disinfection. The use of internal baffles directly neutralizes this issue from 48% to 0.79%, while additional modifications reduce it to 0.37% for t₁₀.

With regards to TTHM production, the concentrations predicted for t_{90} do not reflect any remarkable deviations. However, in reactive tracer injections, significant differences were encountered in terms of the mass production but it is speculated that in the more hydraulically efficient designs (FDI,CT-O) the by-product mass is more concentrated yielding similar levels as the inefficient designs (MS-3, CT-1). It should be also noted that the TTHM simulations of this work do not consider the fact that chlorine reacts partly with total organic carbon (*TOC*). According to Brown et al. (2010), who investigated THM formation at water treatment facilities, their production is not constant but flattens out due to reduced availability of *TOC* as chlorine decays over time. A better understanding of the relationship of *TOC* and chlorine could improve the accuracy of these simulations. Similarly, more sophisticated inactivation kinetics models can be adopted, such as the Hom model (equation 2.14) incorporated in a separate study by Greene (2002) to replace the less versatile Chick-Watson law. Further refinements were not tested within the scope of this investigation but can be the subject of subsequent research.

7.4 CHAPTER SUMMARY

Disinfection processes can typically be modelled through mathematical functions that include several parameters such as reactant type, water chemical composition, reactant concentration or exposure time, temperature and pH. It is therefore vital to select appropriate models that consider all influential parameters that affect the disinfection reactions. However, the development of reaction predictive models is usually based on still water tests where the influence of water movement is essentially insignificant. Conservative tracer experiments discussed in Chapter 6 highlight the remarkable impact of different geometry on the solute mixing processes constituting links between kinetic and hydraulics desirable. Results herein acknowledged this challenge of accurately taking into account the hydrodynamic regime impact on chemical reactions, by combining CFD with mathematical disinfection models.

Previous CT-related studies have considered incorporating disinfection models in CFD modelling practises, but these were often assuming two-dimensional flow or only considering the microorganism inactivation, allowing room for improvements. The kinetic processes of chlorine decay, microorganism inactivation and by-product formation were modelled on a three-dimensional domain for 5 different geometry

configurations (MS-3, CT-1, HDI, FDI and CT-O) of the laboratory model discussed in Chapters 3, 5 and 6. Numerical model boundary conditions were modified to simulate two types of reactive tracer experiments each tailored to the investigation of pathogen inactivation and by-product formation respectively. A steady-state disinfection scenario which simultaneously models the transport of chlorine, *G.Lamblia* population and *TTHMs* was also contemplated. The main outcomes of the analysis undertaken from the CFD simulations included the following:

- On a discussion with regards to a reactive tracer experimental investigation (Asraf-Snir and Gitis, 2011) in a serpentine CT, it is speculated that reactive tracer experiments are highly dependent on the actual contact time which is inevitably altered when up-scaling a CT model that retains dynamic similarity with the original design. In contrast, for conservative tracer experiments, HEIs can be normalized with respect to time and RTD information can be extrapolated as long as dynamic similitude is satisfied between the laboratory and field-scale geometries. This suggests that reaction-related experiments should be conducted either at field-scale models to avoid the loss of dynamic similarity or, alternatively, be simulated numerically through CFD methods.
- For scalar quantities that decay as they flow through the CT volume (e.g. Pathogen populations), short-circuiting has a detrimental effect which can translate to insufficient inactivation levels for pathogens downstream. This is quantitatively shown when comparing *G.Lamblia* population survival ratio at the outlet of a poorly designed tank (MS-3) against a tank with a reasonable baffling configuration to counter short-circuiting (e.g. CT-1). On the other hand, the low contact times of short-circuiting are linked with low DBP formation, whereas the higher contact times which are indicated by extensive RTD tailing correspond to greater DBP concentrations.
- Low-velocity recirculation zones entrap disinfectant longer and result in greater DBPs compared to rapid-mixing recirculation zones. A characteristic example is the comparison between the vertical recirculation zones developed in compartment 1 for CT-1 and HDI respectively. For HDI, where lower velocities are developed in the recirculation zone, significantly greater residence time is estimated, which combined with the high chlorine concentrations near the inlet corresponds to high DBP concentration occurrences early along the flow-path.

- HEIs are sometimes insufficient and ambiguous in determining the optimal inactivation potential of CT designs. This is illustrated by the t_{10} indicator which is greater for HDI and FDI configurations and yet CT-O performs better according to the disinfection simulations. Nonetheless, RTD curves from conservative tracer experiments can be used to estimate the range of the disinfection parameters at tracer sampling locations using interpolation and regression analysis techniques. In this manner, the current Eulerian simulation output is processed to yield results typically obtained from Lagrangian particle tracking methods.

It is shown that a 3-D CFD model can aid in the design of a CT by providing reliable predictions of complex flows, pathogen inactivation and a means to regulate the formation of potentially carcinogenic DBPs. There is a need to further refine the numerical methodology with more sophisticated kinetic models; however these are subject of on-going research. Such refinements could provide a more accurate assessment of newly designed or retrofitted CTs.

CHAPTER 8

CONCLUDING REMARKS

8.1 SUMMARY

This thesis discussed the potential of optimizing the water disinfection undertaken in contact tank (CT) facilities by means of complementary experimental and numerical modelling techniques. Three-dimensional Computational Fluid Dynamics models were set up to simulate the hydrodynamic and solute transport processes in serpentine contact tanks. The simulation capability to reproduce the actual conditions was initially assessed through comparisons against laboratory results. Experimental data availability comprised of hydrodynamic and solute transport measurements that were either collected solely for the particular investigation or encountered in the relevant literature. The CFD approach was subsequently refined with appropriately selected kinetic models, describing the processes of disinfectant decay, pathogen inactivation and the formation of potentially carcinogenic Disinfection By-Products (DBPs).

A review of the main results obtained and the conclusions derived from this study is presented below.

8.2 CONTRIBUTION TO CONTACT TANK RESEARCH

During its course, this study spanned several scientific domains as necessitated by the nature of the problem. Considering the aims outlined at the beginning of this report, the achievements of the study can be classified under three major topics which are (a) an experimental hydrodynamic and solute transport investigation in a small-scale CT, (b) the implementation of a numerical approach (CFD) to accurately reproduce and predict hydrodynamic and mixing conditions in CT geometries and (c) the potential of developing links between numerical models and kinetic processes occurring within CT flow.

a) Experimental Study of Flow and Transport Characteristics in a Scaled CT

Hydrodynamic and conservative tracer concentration readings were obtained experimentally (Chapter 3) at various locations of a scaled physical model of a contact tank. The velocity measurement data were analysed to identify short-circuiting and internal recirculation, which are accountable for disinfection performance deficiencies (Chapter 5). Based on the tracer residence time distribution curves, disinfection-related hydraulic efficiency indicators (HEIs) were obtained to assess the contact tank's

performance. In terms of the hydrodynamics, comparisons were made with data from relevant studies encountered in the available literature. The conclusions from the experimental of this research are summarised as:

1. It is shown that the inlet configuration has a marked influence on the hydrodynamics in the early compartments of the tank, causing significant recirculation zones in a large portion of the compartment and leading to subsequent three-dimensionality. Inlet conditions led to elevated levels of turbulence primarily as a result of interactions with bed and side boundaries.
2. The correlation between the hydrodynamics and the tracer RTD curves obtained in each compartment demonstrate that advection is the main mode of tracer transport and demonstrates the strong interlink between the hydrodynamics and solute transport.
3. The impact of the inlet geometry can be remarkably detrimental to the CT's hydraulic efficiency, as HEIs suggest poor disinfection performance in the early part of the tank, gradually improving once more uniform conditions prevail later in the flow path.
4. The application of the dispersion model which assumes plug flow as the dominant regime notoriously overestimates the system hydraulic efficiency. However, it is shown that with *a-priori* knowledge of the actual dispersion conditions, HEIs can be predicted reasonably accurately.

Hence, numerical assessment of existing or design of new contact tanks, for which the hydrodynamics depart from plug flow conditions, either require *a-priori* known input into theoretical modelling approaches or more advanced numerical modelling techniques.

b) Computational Modelling of Flow and Mixing Processes in CTs

A RANS based CFD technique (Chapter 4) was employed to predict flow and tracer transport processes in serpentine CTs (Chapter 6). The CFD model was first validated by comparing simulated velocity and tracer predictions with experimental data. The analysis was then extended to investigate the effect of different geometry variations such as inlet and baffling configurations on flow, or the effect of scaling and the

applicability of the experimental studies in small-scale models to larger CT flows. The main findings are outlined as follows:

1. The 3-D numerical model was able to reproduce the time-averaged flow very well and a good prediction of scalar transport throughout the tank was achieved. Testament of the ability of the modelling approach is also reflected in the good match of simulated Residence Time Distribution curves and Hydraulic Efficiency Indicators with the experimental ones. The performance of the model was subsequently validated against available data in the literature by testing different baffling configurations and highlighting the influence of such modifications on the tank hydraulic efficiency and particularly short-circuiting.
2. The benefit of inlet design modifications does not primarily lead to short-circuiting mediation so much as the reduction of tailing effects and uneven mixing as shown by cumulative RTD curves. The inlet and baffling modifications are significant in the sense that the same hydraulic efficiency level as achieved at the outlet of the original design could be achieved earlier in the flow path, which, in practise, could accommodate optimized disinfection conditions.
3. Numerical simulations of hydrodynamics and tracer transport in an up-scaled tank verify the validity of the findings from the small-scale tank. These simulations provide evidence that the Fr-Re conflict can be negligible for the flow conditions developed in the small-scale model.
4. Disinfection efficiency is influenced quite significantly by the flow-dimensionality developed in the reactor and hence it is deemed appropriate that the modelling approach reflects this. Treating the design of a serpentine contact tank as a 2D problem, which was the case of some studies in the literature, could in some instances result in an overestimation of hydraulic efficiency.

The close agreement between hydrodynamic and solute transport results of the CT geometries predicted through numerical modelling combined with the low computational demand of the CFD method for current processing capabilities could suggest that such an approach can readily be implemented for practical situations.

c) CFD Modelling of Disinfection Kinetics in CTs

The focus of these simulations was to link the hydraulic conditions of different CT geometries with certain disinfection chemistry processes by adding the reaction kinetics

to the CFD modelling approach. An additional challenge is presented, with regards to the analysis of the reactive reactions to obtain useful information associated with the disinfection processes. This was addressed by reviewing previous experimental and numerical work for relevant applications and accordingly testing different CT geometries under a range of disinfection and reaction scenarios. The main conclusions from this are:

1. It is speculated that reactive tracer experiments are highly dependent on the actual contact time which is inevitably altered when up-scaling a CT model that retains dynamic similarity with the original design. As a result it is desirable that reaction-related experiments should be conducted either at field-scale models to avoid uncertainties from loss of flow dynamic similarity or, alternatively, be simulated at normal-scale numerically through CFD methods.
2. For scalar quantities that decay as they flow through the CT volume (e.g. Pathogen concentrations), short-circuiting has a detrimental effect which can translate to insufficient inactivation levels for pathogens downstream. In contrast, for by-product formation, the low contact times of short-circuiting are linked with low DBP formation, whereas the greater residence time which is indicated by extensive RTD tailing corresponds to greater DBP production. For example, low-velocity recirculation zones which entrap disinfectant longer result in greater DBPs compared to rapid-mixing recirculation zones which have lower residence time.
3. Conservative HEI indicators are sometimes insufficient and ambiguous in determining the optimal inactivation potential of CT designs. Nonetheless, the RTD curves of conservative experiments can be used in conjunction with Eulerian reactive simulations to determine the range of the disinfection parameters at sampling locations using interpolation and regression analysis techniques.

It was illustrated how a 3-D CFD model can aid in and/or guide the design of a CT by providing reliable predictions of complex flows, pathogen inactivation and a means to regulate the formation of potentially carcinogenic DBPs. Disinfection models incorporated in computational modelling methodology could replace the current practises of obtaining hydraulic efficiency indicators which are often questionable over their significance in the disinfection processes.

8.3 RECOMMENDATIONS FOR FUTURE INVESTIGATIONS

The following recommendations with regards to future research are proposed:

- Experimental investigation of chemical reaction kinetics (reactant decay, pathogen inactivation and DBP formation) in a CT model of known hydrodynamic and mixing conditions to provide a complete database to validate CFD modelling of disinfection. Such a study can be conducted within the geometry of existing contact tank model at Cardiff University by means of reactive tracer experiments, supplementing the already available experimental results of hydrodynamics and solute transport with reaction kinetics data which can subsequently be used to refine and validate CFD modelling approaches of reactive processes.
- Perform hydrodynamic measurements in field-scale models, which have yet to be reported in the available literature. These results would satisfy the need to provide experimental evidence that can be used for comparisons against field-scale hydrodynamic simulations. These measurements apart from velocity should additionally focus on the reproduction of the turbulence structure within the contact tank geometry. The turbulence field is crucial for the determination of the associated velocity-field and the transport and mixing of solutes.
- The use of the Gradient-Diffusion Hypothesis and the assumption of isotropic turbulence across the whole domain of the CT geometry is a simplification which was adopted to reduce the computational load in this study when simulating hydrodynamics and solute transport. More rigorous approaches could be tested to determine the anisotropic turbulence diffusivity through algebraic models and calculate the individual Reynolds stresses rather than relying on the eddy viscosity formulation and the uncertainty included with the turbulent Schmidt number estimation. The effect of the turbulence anisotropy on reaction kinetics should also be incorporated in the modelling practises.
- Currently, the only practical method to numerically model the CT flow in field-scale contact tanks is through RANS simulations. More accurate techniques that can account for the flow unsteadiness (LES, DNS) have yet to be reported for the

original scale of such problems. This is due to the highly turbulent nature of the flow developed within the geometries which requires impractically high mesh resolutions for the discretization of the domain. This corresponds to a computational load which can be particularly time-consuming even for the flow field developed in the small-scale model (CT-1) contemplated within this study. However, with ongoing advances in the processing capabilities of high performance computers, such LES and DNS simulations could become practically feasible in the near future. These simulations would provide a greater insight on the turbulence structure developed in water treatment facilities.

- The application of particle tracking methodology involves the numerical introduction of particles into the flow while their trajectories through the reactor are tracked over time using a Lagrangian approach. Such an approach has only been reported previously for microorganism population transport in an ozone contactor (Wols et al., 2010). The exposure of the microorganisms can be estimated according to each individual trajectory to estimate disinfection efficiency variation. This is a promising approach which could also be adopted to estimate the production of DBPs. It would be interesting to investigate how Lagrangian simulation results compare with the disinfection efficiency predictions estimated using the Eulerian approach.
- Refine kinetic models for a more informative estimation of disinfection parameters. An example would be the transport and decay of Total Organic Carbon (TOC) as chlorine reacts with it to produce DBPs. A similar approach could be adopted for any other parameters that are involved in the pathogen inactivation or by-product transport source terms.

8.4 PUBLICATIONS RELATED TO THIS WORK

Peer-Reviewed Journals

Angeloudis, A., Stoesser, T., Kim, D. and Falconer, R.A., (2014). *Flow, Transport and Disinfection Performance in Small- and Full- Scale Contact Tanks. Journal of Hydro-Environment Research (in press).*

Angeloudis, A., Stoesser, T., Kim, D., Falconer, R.A., (2013). *Modelling of Flow, Transport and Disinfection Kinetics in Contact Tanks. Water Management – Proceedings of the ICE, (in press).*

Rauen, W. B., Angeloudis, A., Falconer, R. A., (2012). *Appraisal of Chlorine Contact Tank Modelling Practices. Water Research, 46(18): 5834-5847*

Conference Proceedings

Angeloudis, A., Stoesser, T., Falconer, R.A., (2014). *Disinfection Kinetics in CFD Modelling of Solute Transport in Contact Tanks. Proceedings of the 3rd European IAHR Congress, Porto (submitted).*

Angeloudis, A., Stoesser, T., Kim, D., Falconer, R.A., (2013). *CFD Study of Flow and Transport Characteristics in Baffled Disinfection Tanks. Proceedings of the 2013 IAHR World Congress, Tsinghua University Press, Chengdu*

Angeloudis, A., Rauen, W. B., Falconer, R. A. (2012). *Disinfection Contact Tanks: Contemporary Design and Modelling Considerations. Proceedings of the 2nd European IAHR Congress, Munich.*

REFERENCES

American Water Works Association, (1990). *Water Quality and Treatment: a Handbook of Community Water Supplies*. McGraw-Hill.

Amini, R., Taghipour, R., Mirgolbabaei, H., (2011). Numerical Assessment of Hydrodynamic Characteristics in Chlorine Contact Tank. *International Journal for Numerical Methods in Fluids*, 67, 885-898.

Amy, G. L., Chadik, P. A., Chowdary, Z. K., (1987). Developing Models for Predicting Trihalomethane Formation Potential and Kinetic. *Journal of the American Water Works Association*, 79(7), 89-97.

Angeloudis, A., Rauen, W. B., Falconer, R. A. (2012). Disinfection Contact Tanks: Contemporary Design and Modelling Considerations. *Proceedings of the 2nd European IAHR Congress, Munich*.

Angeloudis, A., Stoesser, T., Kim, D., Falconer, R.A., (2013). CFD Study of Flow and Transport Characteristics in Baffled Disinfection Tanks. *Proceedings of the 2013 IAHR World Congress, Tsinghua University Press, Chengdu*

Angeloudis, A., Stoesser, T., Kim, D., Falconer, R.A., (2014). Modelling of Flow, Transport and Disinfection Kinetics in Contact Tanks. *Proceedings of the ICE – Water Management (in press)*.

Angeloudis, A., Stoesser, T., Falconer, R.A., (2014). Disinfection Kinetics in CFD Modelling of Solute Transport in Contact Tanks. *Proceedings of the 3rd European IAHR Congress, Porto (submitted)*.

Angeloudis, A., Stoesser, T., Kim, D. and Falconer, R.A., (2014). Flow, Transport and Disinfection Performance in Small- and Full- Scale Contact Tanks. *Journal of Hydro-Environment Research (in press)*.

Asraf-Snir, M., Gitis, V., (2011). Tracer Studies with Fluorescent-dyed Microorganisms- A new Method for Determination of Residence Time in Chlorination Reactors. *Chemical Engineering Journal*, 166, 579-585.

Boussinesq (1877). Essai sur la Théorie des Eaux Courantes. (Essay on the Theory of Water Flow.) Mémoires présentés par divers savants à l'Académie des Sciences, Paris, France, 23, ser 3, 1, supplement 24, 1281-1302 (in French).

Brown, D., West, J. R., Curtis, B. J., Bridgeman, J., (2010). Modelling THMs in Water Treatment and Distribution Systems. Proceedings of the Institution of Civil Engineers, Water Management, 163(WM4), 165-174.

Brown, D., Bridgeman, J., West, J. R., (2011). Predicting Chlorine Decay and THM Formation in Water Supply Systems. Reviews in Environmental Science and Biotechnology, 10(1), 79-99.

BSI (2003). Wastewater Treatment Plants – Part 14: Disinfection. British Standard BS EN 12255-14. [WWW] <URL <http://www.bsonline.bsi-global.com/server/index.jsp>> [Accessed 20/06/13]

Chanson, H., (2008). Acoustic Doppler Velocimetry (ADV) in the Field and in Laboratory: Practical Experiences. International Meeting on Measurements and Hydraulics of Sewers. Hydraulic Model Report No. CH70/08, Div. of Civil Engineering, The University of Queensland, Brisbane Australia.

Chick, H., (1908). An Investigation of the Laws of Disinfection. Journal of Hygiene, 8, 92-158

Chow, V. T. (1959). Open-Channel Hydraulics. McGraw-Hill, New York.

Cockx, A., Do-Quang, Z., Line, A., Roustan, M., (1999). Use of Computational Fluid Dynamics for Simulating Hydrodynamic and Mass Transfer in Industrial Ozonation Towers. Chemical Engineering Science, 54, 5085-5090.

Coker, A. K. (2001). Modelling of Chemical Kinetics and Reactor Design. Gulf Publishing Company, Houston.

Combest, D. P., Ramachandran P. A., Dudukovic M. P., (2011). On the Gradient Diffusion Hypothesis and Passive Scalar Transport in Turbulent Flows. Industrial & Engineering Chemistry Research, 50, 8817-8823.

Courtis, B. J., West, J. R., Bridgeman, J., (2009). Temporal and Spatial Variations in Bulk Chlorine Decay within a Water Supply System. *Journal of Environmental Engineering*, ASCE, 135(3), 147-152.

Deardorff, J. W., (1970). A Numerical Study of Three-Dimensional Turbulent Channel Flow at Large Reynolds Numbers. *Journal of Fluid Mechanics*, 41, 453-480.

Deborde, M., von Gunten, U., (2008). Reactions of Chlorine with Inorganic and Organic Compounds During Water Treatment – Kinetics and Mechanisms: A critical Review. *Water Research* 42(1-2), 13-51.

European Water Platform / Water supply and sanitation Technology Platform, 2011. *Water Treatment: Recommendations for Research and Technology Development. Scientific Publication Water Quality VI.* [WWW] <URL [http://www.wsstp.eu/files/WSSTPX0001/communication_tools/scientific_publication/Scientific Publication Water Quality VI.pdf](http://www.wsstp.eu/files/WSSTPX0001/communication_tools/scientific_publication/Scientific_Publication_Water_Quality_VI.pdf)> [Accessed 04/02/12].

Falconer, R. A., (1990). Engineering Problems and the Application of Mathematical Models Relating to Combating Water Pollution. *Municipal Engineer* 7, 281-291.

Falconer, R. A., Ismail, A. I. B. M., (1997). Numerical Modeling of Tracer Transport in a Contact Tank. *Environment International*, 23(6), 763-773.

Falconer, R. A., Liu, S. Q., (1987). Mathematical-Model Study of Plug Flow in a Chlorine Contact Tank. *Journal of the Institution of Water and Environmental Management*, 1(3), 279-290.

Falconer, R. A., Liu, S. Q., (1988). Modelling Solute Transport Using the QUICK Scheme. *Journal of Environmental Engineering*, 114(1), 3-20.

Falconer, R. A., Tebbutt, T. H. Y., (1986). A Theoretical and Hydraulic Model Study of a Chlorine Contact Tank. *Proceedings of the Institution of Civil Engineers, Part 2- Research and Theory*, 81, 255-276.

Finch, G. R., Daniels, C. W., Black, E. K., Schaefer F. W., Belosevic, M., (1993). Dose Response of *Cryptosporidium Parvum* in Outbred Neonatal CD-1 Mice. *Applied and Environmental Microbiology*, 59(11), 3661-3665.

Ferziger, J.H., Peric, M. (2002). *Computational Methods for Fluid Dynamics*. Springer-Verlay, third-edition.

Finelli, C. M., Hart, D. D., Fonseca, D.M. (1999). Evaluating the Spatial Resolution of an Acoustic Doppler Velocimeter and the Consequences for Measuring Near-Bed Flows. *Limnology and Oceanography*, 44, 7, 1793-1801.

Fox, R. O., (2003). *Computational Models for Turbulent Reacting Flows*. Cambridge University Press, Oxford, UK.

Garcia, M. G., Cantero M. I., Nino, Y., Garcia M. H. (2005). Turbulence Measurements with Acoustic Doppler Velocimeters. *Journal of Hydraulic Engineering*, 131(12), 1062-1073.

Goring, D. G., Nikora, V. I. (2002). Despiking Acoustic Doppler Velocimeter Data. *Journal of Hydraulic Engineering, ASCE* , 128, 1, 117-126.

Greene, D. J., (2002). *Numerical Simulation of Chlorine Disinfection Processes in Non-Ideal Reactors*. PhD Thesis, Drexel University

Greene, D. J., Farouk, B., Haas, C. N., (2004). CFD Design Approach for Chlorine Disinfection Processes. *Journal of the American Water Works Association*, 96(8), 138-150.

Greene, D. J., Haas, C. N., Farook, B., (2007). Computational Fluid Dynamics Analysis of the Effects of Reactor Configuration on Disinfection Efficiency. *Water Environment Research*, 78, 909-919.

Gualtieri, C., (2006). Numerical Simulation of Flow and Tracer Transport in a Disinfection Contact Tank. *Proceedings of the 3rd Biennial Meeting of the International Environmental Modelling and Software Society*, Vermont.

Gualtieri, C., (2007). Analysis of the Effect of Baffles Number on a Contact Tank Efficiency with Multiphysics 3.3. *Proceedings of the COMSOL User Conference 2007*, Napoli.

Gyürék, L. L., Finch, G. R., (1998). Modeling Water Treatment Chemical Disinfection Kinetics. *Journal of Environmental Engineering, ASCE*, 124(9), 783-793.

- Haas, C. N., Karra, S. B., (1984). Kinetics of Microbial Inactivation by Chlorine. *Water Research*, 18(11), 1443-1449.
- Haas, C. N., Joffe, J., Anmangandla, U., Hornberger, J. C., Health, M. S., Jacangelo, J., Glicker, J., (1995). Development and Validation of Rational Design Methods of Disinfection. American Water Works Association Research Foundation: Denver, Colorado.
- Hannoun, I. A., Boulos, P. F., (1997). Optimizing Distribution Storage Water Quality: A Hydrodynamic Approach. *Applied Mathematical Modelling*, 21(9), 495-502.
- Hart, F. L., (1979). Improved Hydraulic Performance of Chlorine Contact Chambers. *Journal of the Water Pollution Control Federation*, 51(12), 2868-2875.
- Hart, F. L., Vogiatzis, Z., (1982). Performance of Modified Chlorine Contact Chamber. *Journal of the Environmental Engineering Division, ASCE*, 108(EE3), 549-561.
- Hom, L. W., (1972). Kinetics of Chlorine Disinfection in an Ecosystem. *Journal of the Sanitary Engineering Division*, 98(1), 183-194.
- Huang, T., Brouckaert, C. J., Docrat, M., Pryor, M., (2002). A Computational Fluid Dynamic and Experimental Study of an Ozone Contactor. *Water Science and Technology*, 46(9), 87-93.
- Huang, T., Brouckaert, C. J., Pryor, M., Buckley, C. A., (2004). Application of a Computational Fluid Dynamics Modelling to an Ozone Contactor. *Water SA*, 30, 51-56.
- Johnson, P., Graham, N., Dawson, M., Barker, J., (1998). Determining the Optimal Theoretical Residence Time Distribution for Chlorine Contact Tanks. *Journal of Water Services Research and Technology – Aqua*, 47(5), 209-214.
- Khan, L. A., Wicklein E. A., Teixeira, E. C., (2006). Validation of a Three-Dimensional Computational Fluid Dynamics Model of a Contact Tank. *Journal of Hydraulic Engineering* 132(7), 741-746.
- Kim, D. I., (2007). Development and Application of Integrated Ozone Contactor Design and Optimization Tools. PhD Thesis, Georgia Institute of Technology.

- Kim, D. I., Elovitz, M., Roberts, P. J., Kim, J. H., (2010a). Using 3DLIF to investigate and improve performance of a multicompartment ozone contactor. *Journal of American Water Works Association*, 99(8), 77-91.
- Kim, D., (2011). Large Eddy Simulation of Flow in Water and Wastewater Disinfection Reactors. PhD Thesis, Georgia Institute of Technology.
- Kim, D., Kim, J. H., Stoesser, T., (2009). LES and RANS Modelling of Flow in an Ozone Contactor: Mean and Instantaneous Turbulent Flow Characteristics. *Proceedings of the 33rd IAHR Congress*, Vancouver.
- Kim, D., Kim, D., Kim, J. H., Stoesser, T., (2010b). Large Eddy Simulation of Flow and Tracer Transport in Multichamber Ozone Contactors. *Journal of Environmental Engineering*, 136(1), 22-31.
- Kim, D., Stoesser, T., Kim, J. H., (2013a). The Effect of Baffle Spacing on Hydrodynamics and Solute Transport in Serpentine Contact Tanks. *Journal of Hydraulic Research*, iFirst, 2013, 1-11.
- Kim, D., Stoesser, T., Kim, J. H., (2013b). Modeling Aspects of Flow and Solute Transport Simulation in Water Disinfection Tanks. *Applied Mathematical Modelling*, in press.
- Kohpaei, A. J., Sathasivan, A., (2011) Chlorine Decay Prediction in Bulk Water Using the Parallel Second Order Model: An Analytical Solution Development. *Chemical Engineering Journal*, 171(2011): 232-241
- Kraus, N. C., Lohrmann, A., Cabrera, R. (1994). New Acoustic Meter for Measuring 3D Laboratory Flows. *Journal of Hydraulic Engineering*, ASCE, 120, 3, 406-412.
- Lam, C. K. G., Bremhorst, K., (1981). A Modified Form of the k - ϵ Model for Predicting Wall Turbulence. *Journal of Fluids Engineering*, ASME, 103, 456-460.
- Lane, S. N., Biron, P. M., Bradbrook, K. F., Butler, J. B., Chandler, J. H., Crowell, M. D., McLelland, S. J., Richards, K. S. and Roy, A. G. (1998). Three-Dimensional Measurement of River Channel Flow Processes Using Acoustic Doppler Velocimetry. *Earth Surface Processes and Landforms*, 23, 1247-1267.

- Launder, B. E. (1978). Heat and Mass Transport. Turbulence, Chapter 5, P. Bradshaw, ed., Springer, Berlin.
- Launder, B. E. and Spalding, D. B. (1972). Lectures in Mathematical Models of Turbulence. Academic Press, London.
- Launder, B. E., Sharma, B. I., (1974). Application of the Energy Dissipation Model of Turbulence to the Calculation of Flow Near a Spinning Disk. Letters in Heat and Mass Transfer, 1, 131-138.
- Lee, S., Shin, E., Kim, S. H., Park, H., (2011). Dead Zone Analysis for Estimating Hydraulic Efficiency in Rectangular Disinfection Chlorine Contactors. Environmental Engineering Science, 28(1), 25-33.
- Levenspiel, O., (1999). Chemical Reaction Engineering. 3rd ed., John Wiley & Sons, New York.
- Liem, L. E., Stanley, S. J., Smith, D. W., (1999). Residence Time Distribution Analysis as Related to Effective Contact Time. Canadian Journal of Civil Engineering, 26(4), 135-144.
- Lohrmann, A., Cabrera, R. and Kraus, N. C. (1994). Acoustic-Doppler Velocimeter(ADV) for Laboratory Use. Proceedings of Fundamentals and Advancements in Hydraulic Measurements and Experimentation. Buffalo, USA.
- Lohrmann, A., Cabrera, R., Gelfenbaum, G. and Haines, J. (1995). Direct Measurements of Reynolds Stress with an Acoustic Doppler Velocimeter. Proceedings of the IEEE 5th Working Conference on Current Measurement. St. Petersburg, USA.
- Louie, D. S., Fohrman, M. S., (1968). Hydraulic Model Studies of Chlorine Mixing and Contact Chambers. Journal of the Water Pollution Control Federation, 40(2-1), 174-184.
- Marske, D. M., Boyle, J. D., (1973). Chlorine Contact Chamber Design – A Field Evaluation. Water and Sewage Works, 120(1), 70-77.

- Martin, V., Fisher, T. S. R., Millar, R. G., Quick, M. C. (2002). ADV Data Analysis for Turbulent Flows: Low Correlation Problem. Proceedings of the ASCE Specialty Conference on Hydraulic Measurements and Experimental Methods. Estes Park, USA.
- Menter, F. R., (1994). Two-Equation Eddy-Viscosity Turbulence Models for Engineering Applications. *Journal of the American Institute of Aeronautics and Astronautics*, 32(8), 1598-1605.
- Nieuwenhuijsen, M. J., Toledano, M. B., Bennett, J., Best, N., Hambly, P., Hoogh, C., Wellesley, D., Boyd, P. A., Abramsky, L., Dattani, N., Fawell, J., Briggs, D., Jarup, L., Elliott, P., (2008). Chlorination By-Products and Risk of Congenital Anomalies in England and Wales. *Environmental Health Perspectives*, 116(2), 216-222.
- Nikora, V. I. and Goring, D. G. (1998). ADV Measurements of Turbulence: Can We Improve Their Interpretation. *Journal of Hydraulic Engineering, ASCE*, 124, 6, 630-634.
- Olsen N.R.B, (2011). A Three-Dimensional Numerical Model For Simulation Of Sediment Movements In Water Intakes With Multiblock Option, Department Of Hydraulic And Environmental Engineering The Norwegian University Of Science And Technology.
- Patankar, S. V., (1980). *Numerical Heat Transfer and Fluid Flow*. Taylor & Francis.
- Patankar, S. V. and Spalding, D. B. (1972). A Calculation Procedure for Heat, Mass and Momentum Transfer in Three-Dimensional Parabolic Flows. *International Journal of Heat and Mass Transfer*, 15, 1787-1972.
- Peplinski, D. K., Ducoste, J. J., (2002). Modeling of Disinfection Contactor Hydraulics Under Uncertainty. *Journal of Environmental Engineering, ASCE*, 128(11), 1056-1067.
- Pope, S. B., (2000). *Turbulent Flows*. First edition, Cambridge University Press, Oxford, UK.
- Powell, J. C., Hallam, N. B., West, J. R., Forster, C. F., Simms, J., (2000). Factors which Control Bulk Chlorine Decay Rates. *Water Research*, 34(1), 117-126.

- Rauen, W. B., (2001). Effects of Scale and Discharge on the Dynamic Similitude and Chlorine Disinfection Efficiency of Scaled-Down Models of Contact Tanks. M.Sc. Dissertation, Department of Environmental Engineering, UFES, Brazil (in Portuguese).
- Rauen, W. B., (2005). Physical and Numerical Modelling of 3-D Flow and Mixing Processes in Contact Tanks. PhD Thesis, Cardiff University.
- Rauen, W. B., Lin, B., Falconer, R. A., Teixeira, E. C., (2008). CFD and Experimental Model Studies for Water Disinfection Tanks with Low Reynolds Number Flows. Chemical Engineering Journal, 137(3), 550-560.
- Rauen, W. B., Angeloudis, A., Falconer, R. A., (2012). Appraisal of Chlorine Contact Tank Modelling Practices. Water Research, 46(18): 5834-5847
- Roache, P. J., (1998). Fundamentals of Computational Fluid Dynamics. Hermosa Publishers, New York.
- Rodi, W., (1993). Turbulence Models and Their Application in Hydraulics. 3rd ed., Taylor&Francis.
- Sadiq, R., Rodriguez, M. J., (2004). Disinfection By-Products (DBPs) in Drinking Water and the Predictive Models for their Occurrence: a Review. Science of the Total Environment, 321(1-3), 21-46.
- Schlichting, H. (1979). Boundary-Layer Theory. McGraw-Hill.
- Shiono, K., Teixeira, E. C., (2000). Turbulence Characteristics in a Baffled Contact Tank. Journal of Hydraulic Research, 38(4), 271-278.
- Singer, P. C., (1994). Control of Disinfection By-Products in Drinking Water. Journal of Environmental Engineering, 120(4), 727-744.
- Smagorinsky, J. S., (1963). General Circulation Experiments with the Primitive Equations. Part I: Basic Experiments. Monthly Weather Review, 91, 99-164.
- Smart, P. L. , Laidlaw, I. M. S. (1977). An Evaluation of Some Fluorescent Dyes for Water Tracing. Water Resources Research, 13, 1, 15-33.

- Spalding, D.B. (1972). A novel finite-difference formulation for differential expressions involving both first and second derivatives. *Int. J. Num. Methods Eng.*, 4, 551.
- Stamou, A. I., (2002). Verification and Application of a Mathematical Model for the Assessment of the Effect of Guiding Walls on the Hydraulic Efficiency of Chlorination Tanks. *Journal of Hydroinformatics*, 4(4), 245-254.
- Stamou, A. I., (2008). Improving the Hydraulic Efficiency of Water Process Tanks using CFD Models. *Chemical Engineering and Processing: Process Intensification*, 47(8), 1179-1189.
- Stamou, A. I., Adams, E. W., (1988). Study of the Hydraulic Behaviour of a Model Settling Tank Using Flow-Through Curves and Flow Patterns. Report no. SFB 210/E/36, University of Karlsruhe, Karlsruhe, Germany.
- Stamou, A. I., Noutsopoulos, G., (1994). Evaluating the Effect of Inlet Arrangement in Settling Tanks Using the Hydraulic Efficiency Diagram. *Water SA*, 20(1), 77-83.
- Stevenson, D. G., (1995). The Design of Disinfection Contact Tanks. *Journal of the Chartered Institution of Water and Environmental Management*, 9, 4, 146-152.
- Stoesser, T., (2001). Development and validation of a CFD-code for turbulent open-channel flows. PhD Thesis, University of Bristol.
- Stone, H.L. (1968). Iterative Solution of Implicit Approximations of Multidimensional Partial Differential Equations. *SIAM Journal on Numerical Analysis*, 5(3), 530-558.
- Teixeira, E. C., (1993). Hydrodynamic Processes and Hydraulic Efficiency of Chlorine Contact Units. PhD Thesis, University of Bradford.
- Teixeira, E. C., Chacaltana, J. T. A., Pacheco, C. G., Siqueira, R. N., (2004). Use of Flow Through Curves to Calibrate and Validate Numerical Models of Solute Transport in Contact Tanks. *Proceedings of the 6th International Conference on Hydroinformatics*, Singapore.
- Teixeira, E. C., Siqueira, R. C. N., Rauen, W. B., (2002). Automation of Acquisition and Processing of Flow-Through Curves. *Proceedings of the 5th International Conference on Hydroinformatics*, Cardiff, UK.

- Teixeira, E. C., Siqueira, R. N., (2008). Performance Assessment of Hydraulic Efficiency Indexes. *Journal of Environmental Engineering*, 134(10), 851-859.
- Teixeira, E. C., Rauen, W. B., (2013). Effect of Scale and Discharge Variation on Similitude and Solute Transport in Water Treatment Tanks. *Journal of Environmental Engineering*, doi:10.1061/(ASCE)EE.1943-7870.0000772.
- Templeton, M. R., Hofmann, R., Robert, C. A., (2006). Case Study Comparisons of Computational Fluid Dynamics (CFD) Modeling versus Tracer Testing for Determining Clearwell Residence Times in Drinking Water Treatment. *Journal of Environmental Engineering and Science*, 5(6), 529-536.
- Thackston, E. L., Shields, F. D., Schroeder, P. R., (1987). Residence Time Distributions of Shallow Basins. *Journal of Environmental Engineering*, 113(6), 1319-1332.
- Thayanity, M., (1984). Hydraulic Design Aspects of Chlorine Contact Tanks. MSc Thesis , University of Birmingham.
- Thirumurthi, D., (1969). A Break-Through in Tracer Studies in Sedimentation Tanks. *Journal of the Water Pollution Control Federation*, 41(11), R405-R418.
- Trussell, R. R., Chao, J. L., (1977). Rational Design of Chlorine Contact Facilities. *Journal of Water Pollution Control Federation*, 49(4), 659-667.
- UNESCO (2012). Managing Water under Uncertainty and Risk. The United Nations World Water Development Report 4, Volume 1. [WWW] <URL <http://unesdoc.unesco.org/images/0021/002156/215644e.pdf>> [Accessed 20/06/2013]
- Van der Walt, J. J., (2002). The Modelling of Water Treatment Process Tanks. PhD Thesis, Rand Afrikaans University.
- Versteeg, H. K. and Malalasekera, W. (1995). An Introduction to Computational Fluid Dynamics: the Finite Volume Method. Longman Scientific and Technical, Essex, UK.
- Voulgaris, G. and Trowbridge, J. H. (1998). Evaluation of the Acoustic Doppler Velocimeter (ADV) for Turbulence Measurements. *Journal of Atmospheric and Oceanic Technology*, 15, 272-289.

- Wang, H., (1995). Numerical Modelling of Flow and Disinfection Processes in Chlorine Contact Tanks. PhD Thesis, University of Bradford.
- Wang, H., Falconer, R. A., (1998a). Simulating Disinfection Processes in Chlorine Contact Tanks using Various Turbulence Models and High-Order Accurate Difference Schemes. *Water Research*, 32(5), 1529-1543.
- Wang, H., Falconer, R. A., (1998b). Numerical Modeling of Flow in Chlorine Disinfection Tanks. *Journal of Hydraulic Engineering*, 124(9), 918-931.
- Wang, H., Shao, X., Falconer, R. A., (2003). Flow and Transport Simulation Models for Prediction of Chlorine Contact Tank Flow-Through Curves. *Water Environment Research*, 75(5), 455-471.
- Wahl, T., (2000). Analyzing ADV data using WinADV. Proceedings of Joint Conference of Water Resources Engineering and Water Research Plan Management, Minneapolis, USA
- Watson, H. E. (1908). A Note on the Variation of Disinfection with Change in the Concentration of the Disinfectant. *Journal of Hygiene*, 8, 536-542.
- Wilson, J. M., Venayagamoorthy, S. K., (2010). Evaluation of Hydraulic Efficiency of Disinfection Systems Based on Residence Time Distribution Curves. *Environmental Science & Technology* 44(24), 9377-9382.
- WHO (2011) Guidelines for Drinking-Water Quality. Vol. 1, 4th ed., World Health Organization. [WWW] <URL http://whqlibdoc.who.int/publications/2011/9789241548151_eng.pdf> [Accessed 20/06/2013]
- Wols, B. A., Hofman J. A. M. H., Uijttewaal W. S. J., Rietveld, L. C., van Dijk, J. D., (2010). Evaluation of Different Disinfection Calculation Methods Using CFD. *Environmental Modelling & Software*, 25 (2010): 573-582
- Xu, Q., (2010). Internal Hydraulics of Baffled Disinfection Contact Tanks Using Computational Fluid Dynamics. MSc Thesis, Colorado State University.

- Yang, C. Y., Cheng, B. H., Tsai, S. S., Wu, T. N., Lin, M. C., Lin, K. C., (2000). Association Between Chlorination of Drinking Water and Adverse Pregnancy Outcome in Taiwan. *Environmental Health Perspectives*, 108(8), 765-768.
- Yu, X., Mazurek, K. A., Putz, G., Albers, C., (2010). Physical and Computational Modelling of Residence Flow Development Time in a large Municipal Disinfection Clearwell. *Canadian Journal of Civil Engineering*, 37(9), 931-940.
- Zhang, G., Lin, B., Falconer, R. A., (2000). Modelling Disinfection By-products in Contact Tanks. *Journal of Hydroinformatics*, 2(2), 123-132.
- Zhang, J.-M., Lee, H. P., Khoo, B. C., Teo, C. P., Haja, N., Peng, K. Q., (2011). Modelling and Simulations of Flow Pattern, Chlorine Concentration and Mean Age Distributions in Potable Water Service Reservoir of Singapore. *Journal of Environmental Engineering, ASCE*, 137(7), 575-584.
- Zhang, J., Tejada-Martinez, A. E., Zhang, Q., (2013). Reynolds-Averaged Navier-Stokes Simulation of the Flow and Tracer Transport in a Multichambered Ozone Contactor. *Journal of Environmental Engineering*, 2013, 139, 450-454.
- Zhu, J., (1991). A Low-diffusive and Oscillation-free Convection scheme. *Communications in Applied Numerical Methods*, 7, 225-232.

NOMENCLATURE

A	Compartment cross-sectional wetted area
b	Mass source term contributions to discretized equation
Br	Bromide ion concentration
$C_{\varepsilon 1}, C_{\varepsilon 2}$	Coefficients of k- ε turbulence model
C_{μ}	Constant used for the estimation of the eddy viscosity parameter
C_0	Average tracer concentration based on the mass injected
C	Concentration value
C_{Cl}	Chlorine concentration at a computational point
C_{DBP}	Disinfection by-product concentration at a computational point
Cl	Chlorine dosage
d	Dispersion number
D	Conductance coefficient
D_t	Turbulent mass diffusivity
D_L	Longitudinal dispersion coefficient
DCAA	Dichloroacetic acid concentration
DE	Disinfection Efficiency
E	Empirical constant for the near-wall boundary conditions
$E(\theta)$	Normalised Concentration RTD
$f_{i+1/2}$	Approximations of surface integrals
F	Fluxes at computational control volume surfaces with neighbouring cells
$F(\theta)$	Normalised mass cumulative RTD
g	Gravitational acceleration
H	Flow depth
H_t	Tank height
H_i	Inlet channel height

K	Turbulent kinetic energy
k'	Empirical microorganism inactivation constant
k_b	Bulk decay constant
k_{bf}	Bulk decay for fast reactants
k_{bs}	Bulk decay for slow reactants
k_s	Nikuradse's surface roughness height
k_{tc}	Coefficient of proportionality between TTHM production - Cl consumption
L	Flow path length
L_t	Tank length
M	Tracer Mass
Mo	Morril Index
n	Manning's number
N	Microorganism population at time t
N_m	Number of data points with ADV measurements
N_0	Initial Microorganism population
P, p	Pressure
P^*	Guessed pressure
\acute{p}	Pressure correction
P_k	Production of k parameter
Pe	Peclet Number
Q	Discharge / Flow rate
Re	Reynolds Number
REC	Mass Recovery Index
S	Source term
Sc	Schmidt number
S_ϕ	Volumetric source term
S_f	Friction slope

t	Time expressed in hours
t_c	contact time
t_{10}	Time to 10% passage of tracer mass
t_{50}	Time to 50% passage of tracer mass
t_{90}	Time to 90% passage of tracer mass
t_p	Peak concentration time
t_g	Time to the centroid of the residence time distribution
T	Theoretical/Hydraulic residence time
T_e	Temperature
TCAA	Trichloroacetic acid concentration
TOC	Total organic carbon concentration
TTHM	Trihalomethane concentration
u^*	Preliminary velocity estimation
U_b	Bulk Velocity
U_i	Time-averaged velocity in the i -direction
U_{max}	Maximum streamwise velocity magnitude
U_{rev}	Reverse velocity
u_i'	Fluctuating velocity in the i -direction
UV_{254}	Ultraviolet absorbance at 254 nm
v	Instantaneous velocity measured in the y direction
ν_t	Eddy viscosity
V	Tank Volume
W	Tank Width
W_c	Compartment width
x	Horizontal direction coordinate
x_i	Coordinates in tensor notation
y	Transverse direction coordinate

y^+	Distance of computational point from the wall
z	vertical direction coordinate
α	Coefficient of discretized governing equation
β	Tank length-to-width (L/W) ratio
δ_{ij}	Kronecker delta
$\Delta\theta$	Normalized time Interval
ε	Turbulent energy dissipation rate
θ	Non-dimensional time-parameter
θ_{10}	Normalized t_{10} with respect to time
θ_{90}	Normalized t_{90} with respect to time
κ	von Karman's constant
ν	kinematic viscosity
ρ	Fluid specific mass
σ^2	Dispersion index
σ_c	Plug flow deviation coefficient
σ_t^2	Variance of residence time distribution
$\sigma_\kappa, \sigma_\varepsilon$	Coefficients of k- ε turbulence model
u	Instantaneous velocity measured in the x direction
φ	Scalar quantity

ABBREVIATIONS

ADI	Alternating Direction Implicit
ADV	Acoustic Doppler Velocimetry
AI	Active Ingredient
AWWA	American Water Works Association
CFD	Computational Fluid Dynamics
CT	Contact Tank
COR	Correlation Index
DBP	Disinfection By-Products
DE	Disinfection Efficiency
DIVAST	Depth Integrated Velocities and Solute Transport
DNS	Direct Numerical Simulation
FCV	Flow Control Valves
FDM	Finite Difference Method
FEM	Finite Element Method
FTC	Flow Through Curve
FVM	Finite Volume Method
HEI	Hydraulic Efficiency Indicator
HLP	Hybrid Linear/Parabolic method
LDA	Laser Doppler Anemometry
LES	Large Eddy Simulation
LIF	Laser Induced Fluorescence
MCL	Maximum Contaminant Level
PIV	Particle Image Velocimetry
QUICK	Quadratic Upstream Interpolation for Convective Kinematics
RANS	Reynolds Averaged Navier-Stokes

RMS	Root Mean Square
RTD	Residence Time Distribution
SGS	Sub-grid Scale
SIMPLE	Semi-Implicit Method for Pressure Linked Equations
SIP	Stronger Implicit Process
SNR	Signal-to-Noise Ratio
SR	Sampling Rate
SWTR	Surface Water Treatment Rule
TDMA	Tri-Diagonal Matrix Algorithm
TKE	Turbulence Kinetic Energy
THM	Trihalomethanes
UV	Ultraviolet Radiation
WHO	World Health Organisation